Deeply Virtual Compton Scattering off Helium-4

Mohammad Hattawy

IPNO-T-15-02

Université Paris-Sud XI

École Doctorale MIPEGE

THÈSE DE DOCTORAT

Soutenue le 14 Septembre 2015 à Orsay par

Mohammad Hattawy

pour obtenir le titre de Docteur ès Sciences de l'Université Paris Sud XI

Specialité : Physique Nucléaire

Sujet :

Deeply virtual Compton scattering off ^4He

Directeur de thèse: **Michel Guidal**
Encadrant de thèse: **Raphaël Dupré**
Institut de Physique Nucléaire d'Orsay

Jury :

Président :	M. Bernard Pire	-	CPhT (Palaiseau, France)
Directeur :	M. Michel Guidal	-	IPNO (Orsay, France)
Rapporteurs :	M. Michel Garçon	-	CEA-Saclay (Gif sur Yvette, France)
	Mme. Kawtar Hafidi	-	ANL (Argonne, IL, USA)
Examinateurs :	M. Raphaël Dupré	-	IPNO (Orsay, France)
	M. Sergio Scopetta	-	INFN (Pérouse, Italie)

Acknowledgements

I would like to express my deep acknowledgements to many great people who supported me during the past three years and contributed in making my study possible.

My deepest appreciation goes to my supervisors **Raphaël Dupré** and **Michel Guidal**. Raphaël you taught me how to express ideas and simplify any crisis situation. Your patience and support helped me overcome all the work issues during my study. Thanks a lot for answering my countless questions. Michel, in addition to your support, insightful comments and encouragement, I will never forget your calm mood with all the administrative processing. To both of you, I deeply appreciate your belief in me and I hope that one day I will become a good advisor to my students as both of you were to me.

To **the members of the jury**, I am deeply grateful to you for the enthusiasm that you have shown to participate in the my committee. Also, I warmly thank you for the fruitful comments and recommendations. In particular, special thanks to Michel Garçon and Kawtar Hafidi for reading every letter in my dissertation.

My sincere gratitude goes to **Silvia Niccolai and her nice family** for the continuous support. I will never forget your comments and suggestions on my presentations. I would like also to thank all the members of **PHEN group at IPNO**. Big thanks to Carlos Munoz, Gabriel Charles (you do not need to swear on everything you say), Ani Simonyan for sharing the office, Rafayel Paremuzyan, Jean-Pierre Didelez, Eric Voutier, Camille Desnault, Brice Garillon, Hyon-Suk Jo, Baptiste Guegan and Alejandro Marti.

I would like to thank all the members of **EG6 group** at JLab. I warmly appreciate the help of Stepan Stepanyan, Nathan Baltzell, Lamiaa El Fassi, F.-X. Girod and Cristina Moody. I greatly value the countless discussions and your advises during our weekly meetings. I appreciate **Vadim Guzey** and **Simonetta Liuti** for the fruitful discussions during the last few months of my study.

I would like to thank my professors at **Birzeit University**. My deep thanks to W. Khater, A. Shawabka, R. Rihan, H. Jaqaman and W. Karain. Special thanks to A. Abdel-Latif.

I greatly value the help of **my friends** in Paris whom gave me the family feeling. Monem, Rustom, Elli, Roukoz, Omar, Mounzer, Abdel-Majid, Moustafa and Mohammad, I will never forget you. Deep thanks to Ayman and Reem for almost daily asking about me.

Most importantly, this work would not be possible without the love and the support of **my family**. I dedicate this work to my parents, brothers and sisters. I love you guys and still waiting to see my nephews. To my extended family, thanks a lot for asking about me. I warmly appreciate the generosity of my relatives in Amman for the great hospitality during my visits.

Finally, I appreciate the financial support from **le Consulat Général de France à Jérusalem**, **le Campus France**, **l'Uinversité Paris Sud XI** and **l'Institut de Physique Nucléaire d'Orsay**.

Contents

Introduction

The nucleons are the origin of 99% of the mass of the visible universe. It has received a great attention during the last five decades, both experimentally and theoretically, to better understand its complicated nature. In 1961, the nucleons were found to have an extended internal structure by R. Hofstadter *et al.* [1] with the first electron-proton Elastic Scattering (ES) measurement, at SLAC [2]. In 1964, M. Gell-Mann [3] and G. Zweig [4] independently proposed the quark model, in which hadrons are assumed to be made of quarks held together by the strong interaction. Inclusive reactions, such as Deep Inelastic Scattering (DIS), provide access to the momentum distributions of the internal constituents of the nucleons. It was found, after the first electron-proton DIS measurement at SLAC [5] that the quarks carry only about half of the energy-momentum of the proton, while the other half is carried by other non-charged carriers. This has inspired R. Feynman [6] and J. D. Bjorken [7] to introduce the parton model. According to this model, the nucleons are composed of point-like quasi-free partons, the quarks and the gluons. These quarks are of two types: the valence quarks, which give rise to the quantum numbers of the hadron, and the sea quarks, that are produced by gluon splitting into quark-antiquark pairs and form the complex structure of the nucleon.

The ES and the DIS processes contain one-dimensional information about the partonic structure of the nucleon, accessing the transverse charge distribution and the longitudinal momentum distribution, respectively. However, more information lies in the correlations between the space and momentum degrees of freedom of the partons. Such correlations are encoded in the Generalized Parton Distributions (GPDs). The GPDs can be interpreted as the transverse spatial distributions of partons that carry a certain fraction of longitudinal momentum. Hard exclusive processes, such as Deeply Virtual Compton Scattering (DVCS), $eN \rightarrow eN\gamma$, and Deeply Virtual Meson Production (DVMP), $eN \rightarrow eNm$ where m is a meson, are the main tools to explore the GPDs of the nucleons. From the theoretical point of view, DVCS is considered the cleanest way to access the GPDs.

In 1983, the European Muon Collaboration has discovered that the inclusive DIS structure functions of the bound nucleons inside nuclei are different from the ones in a free nucleon [8]. This effect has been more precisely investigated to understand its origins, at CERN, SLAC, DESY(HERMES), Fermilab, and JLab. Correlations were established with nuclear properties, such as the mass and the nuclear density, but there is still no widely accepted explanation for this phenomenon. The nuclear DVCS opens a new avenue to explore the nature of medium modifications at the partonic level, generalizing the EMC effect in terms of the three-dimensional GPDs instead of the one-dimensional DIS structure functions. We can measure two DVCS channels off a given nuclear target: the coherent and the incoherent channel. One can measure nuclear GPDs from the coherent channel, where the target nucleus remains intact, while from the incoherent channel, where the nucleus breaks and the DVCS takes place on a bound nucleon, one can access the nucleon GPDs.

The ^{4}He nucleus is of particular interest to study nuclear GPDs as its partonic structure is described by only one chirally-even GPD. It is also a simple few-body system and has a high density that makes it the ideal target to investigate nuclear effects on partons. The Thomas Jefferson National Accelerator Facility, known also as Jefferson Lab (JLab), offers unique opportunities to perform our reaction of interest as it provides longitudinally-polarized high-energy electron

beams. The experimental Hall B of JLab houses the CLAS detector, which is a nearly 4π-detector. The experiment described in this thesis is JLab-E08-24, which was carried out in 2009 by the CLAS collaboration during the "EG6" run. In this experiment, a 6 GeV longitudinally-polarized electron beam was scattered onto a 6 atm ^4He gaseous target. During this experiment, in addition to the CLAS detector, a Radial Time Projection Chamber (RTPC), to detect low-energy nuclear recoils, and an Inner Calorimeter (IC), to improve the detection of photons at very forward angles, were used.

This thesis is organized as follows:

- In chapter 1, the available theoretical tools to study hadronic structure are presented, with an emphasis on the nuclear effects and GPDs.
- In chapter 2, the characteristics of the CLAS spectrometer are reviewed.
- In chapter 3, the working principle and the calibration aspects of the RTPC are discussed.
- In chapter 4, the identification of the final-state particles and the Monte-Carlo simulation are presented.
- In chapter 5, the selection of the DVCS events, the background subtraction, and uncertainty studies on the measured beam-spin asymmetries are presented.
- In chapter 6, the DVCS beam-spin asymmetry measurements for the coherent and the incoherent DVCS channels are presented and compared to the measurements of free-proton DVCS, and to GPD models.
- Finally, a conclusion will summarize this work.

Chapter 1

Nuclear structure and medium modifications

The electromagnetic probe has been the primary tool for studying the internal structure of hadrons in terms of their fundamental constituents, i.e. the quarks and the gluons. The leptons are elementary particles characterized by their structureless nature, interacting with matter via the well-known electromagnetic force and being insensitive to strong interaction. Thus, interactions between leptons and hadrons reflect information on the internal structure of the target hadrons.

The reaction of interest in this work is the so-called Deeply Virtual Compton Scattering (DVCS). It is a lepton scattering reaction that gives access to structure functions called Generalized Parton Distributions (GPDs). These distributions provide a three-dimensional imaging of the partons in a hadron, in terms of their longitudinal momentum and transverse spatial distributions.

After the observation of the European Muon Collaboration, the so-called EMC effect, more precise measurements confirmed the effect, but its origin is still not yet fully understood. In this work, we investigate the EMC effect by adding the transverse spatial coordinates to the one-dimensional parton distribution functions, that is by measuring the GPDs.

This chapter presents first the different lepton-nucleon scattering reactions with the corresponding structure functions which can be accessed. Then, a brief review of the EMC effect is presented. After this, the DVCS reaction off nucleons is detailed. Finally, the advantage of exploring the DVCS on nuclear targets is justified as a new tool to understand the EMC effect.

1.1 Structure functions in lepton scattering reactions

1.1.1 Elastic scattering

Elastic Scattering (ES) has been employed to investigate the structure of the nucleons since the 1950's. Electron-nucleon elastic scattering is

$$e(\mathbf{P}_e) + N(\mathbf{P}_N) \rightarrow e'(\mathbf{P}_{e'}) + N'(\mathbf{P}_{N'}), \tag{1.1}$$

where the symbols in the parentheses are the energy-momentum four-vectors of the initial and the final-state particles. This process gives access to the electromagnetic Form Factors (FFs) of the nucleons. The FFs contain information on the nucleon electric and magnetic spatial distributions. Figure 1.1 represents the Feynman diagram of the electron-nucleon elastic scattering in the Born approximation, i.e. the scattering occurs through the exchange of a single virtual photon.

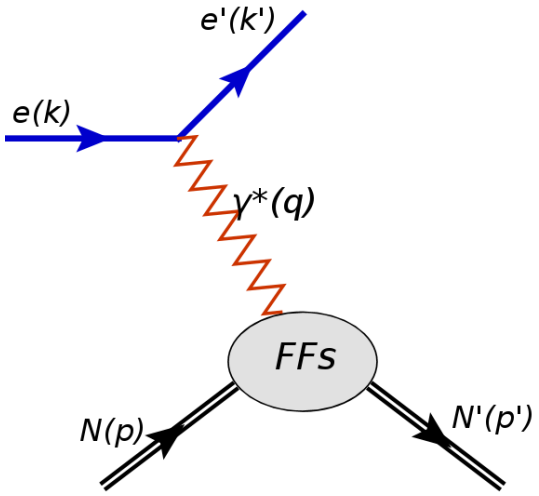

Figure 1.1: The Feynman diagram of the electron-nucleon elastic scattering in the Born approximation. The incoming lepton radiates a virtual photon (γ^*), which interacts with the nucleon, whose non-perturbative structure is parametrized by the electromagnetic FFs.

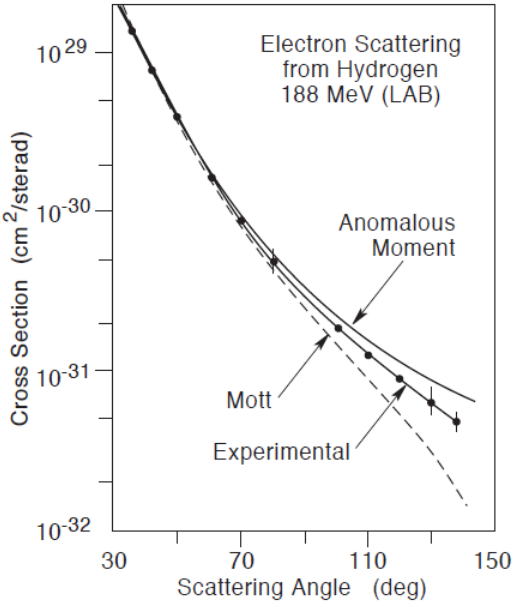

Figure 1.2: The first elastic electron-proton cross section, measured at SLAC in 1955, is compared to the Mott and anomalous moment curves. The figure is from [2].

In the lab frame, the nucleon (N) is at rest and the emitted virtual photon carries a four-momentum q. Neglecting the mass of the electron, the virtuality (Q^2) of the photon is defined as:

$$Q^2 = -q^2 \overset{lab}{=} 4\,EE'\sin^2(\theta_e/2), \tag{1.2}$$

where E (E') is the energy of the incident (scattered) electron and θ_e is the scattered electron polar angle.

The cross section of this reaction (σ) depends on the scattering amplitude ($\mathcal{M}$), which can be written as [9]:

$$\mathcal{M} = e^2\overline{u}(k',\lambda')\gamma^\mu u(k,\lambda)\,\langle N',p',h'|J^{em}_\mu(0)|N,p,h\rangle, \tag{1.3}$$

where γ^μ is the Dirac matrix, λ (λ') is the spinor helicity of the incident (scattered) lepton, h (h') is the spinor helicity of the initial (final) nucleon and $J^{em}_\mu(0)$ is the local electromagnetic current. Two equivalent parametrizations for the matrix element ($\langle N',p',h' \mid J^{em}_\mu(0)|N,p,h\rangle$) are mainly in use. The first one is the Pauli-Dirac parametrization, in which the matrix element is parametrized by the Dirac ($F_1(Q^2)$) and Pauli ($F_2(Q^2)$) FFs. The second one is the Sachs parametrization, in which the matrix element is parametrized by electric ($G_E(Q^2)$) and magnetic ($G_M(Q^2)$) FF. These two are connected to $F_{1,2}$ by:

$$G_E(Q^2) = F_1(Q^2) + \frac{Q^2}{4M^2}F_2(Q^2), \tag{1.4}$$

$$\text{and} \quad G_M(Q^2) = F_1(Q^2) + F_2(Q^2). \tag{1.5}$$

In terms of the Sachs parametrization, the unpolarized differential cross section of $ep \to ep$ elastic

scattering (Rosenbluth formula [10]) can be formulated as:

$$\left(\frac{d\sigma}{d\Omega}\right)_{exp} = \left(\frac{d\sigma}{d\Omega}\right)_{Mott} \frac{E'}{E}\left(\frac{G_E^2(Q^2)+\tau G_M^2(Q^2)}{1+\tau} + 2\tau G_M^2(Q^2)\tan^2(\frac{\theta_e}{2})\right), \tag{1.6}$$

where $\tau = \frac{Q^2}{4M_N^2}$, M_N is the mass of the nucleon and $\left(\frac{d\sigma}{d\Omega}\right)_{Mott}$ is the Mott cross section, which is the cross section for the scattering of an electron on a point-like spin 1/2 particle. It is given by:

$$\left(\frac{d\sigma}{d\Omega}\right)_{Mott} = \frac{\alpha^2}{4E^2\sin^4\frac{\theta_e}{2}}\cos^2(\frac{\theta_e}{2}), \tag{1.7}$$

where the scattered electron goes through the solid angle $d\Omega$ and $\alpha = \frac{e^2}{4\pi} \sim \frac{1}{137}$ is the electromagnetic coupling constant.

Figure 1.2 shows the first electron-proton elastic cross section measurement at the Stanford Linear Accelerator Center (SLAC) in April 1955 [2]. The experimental curve shows deviations from the calculated Mott and anomalous[1] curves at large scattering angles of the electron. This deviation has led Robert Hofstadter to conclude that the protons have an extended structure, and made him earn the Nobel prize in 1961 [1]. Figure 1.3 shows an example of the extracted electric and magnetic FFs of the proton and the neutron. The reader is referred to references [12] and [13] to find the results in terms of the $F_1(Q^2)$ and $F_2(Q^2)$ FFs.

In a frame where the nucleon goes to the speed of light, Fourier-like transforms of the FFs (G_E, G_M) provide information on the partons spatial charge and magnetic distributions inside the nucleon in the transverse plane [14] [15].

1.1.2 Deep inelastic scattering

The second lepton scattering reaction that has been widely used to unravel the nucleon structure in terms of partons is called Deep Inelastic Scattering (DIS). Figure 1.4 shows the Feynman diagram of the electron-nucleon DIS at leading order. In DIS, only the scattered electron is detected. This reaction was performed for the first time at SLAC in the 1960's [5].

The invariant mass of the final hadronic system resulting from the electron-nucleon interaction can be written as:

$$W^2 = (p+q)^2 = M^2 + 2\nu M_N - Q^2, \tag{1.8}$$

where ν ($= E - E'$) is the energy transferred by the virtual photon. In elastic scattering, $W^2 = M_N^2$, as the nucleon remains intact and no other particles are produced. At high Q^2, the nucleon has a high probability to break up, creating a complicated hadronic system. $W > 2$ GeV/c^2 and $Q^2 > 1$ GeV^2/c^2 are typical values for the DIS regime. In fact, a virtual photon with $Q^2 > 1$ GeV^2/c^2 has a wavelength ($\lambda \propto 1/\sqrt{Q^2}$) smaller than the typical size of the nucleon (~ 1 fm). Therefore, the virtual photon sees the partons of a nucleon. The condition W > 2 GeV/c^2 is applied to avoid the region where the nucleon is excited to resonant baryon states.

[1] The Rosenbluth cross section for a point-like proton with anomalous magnetic moment

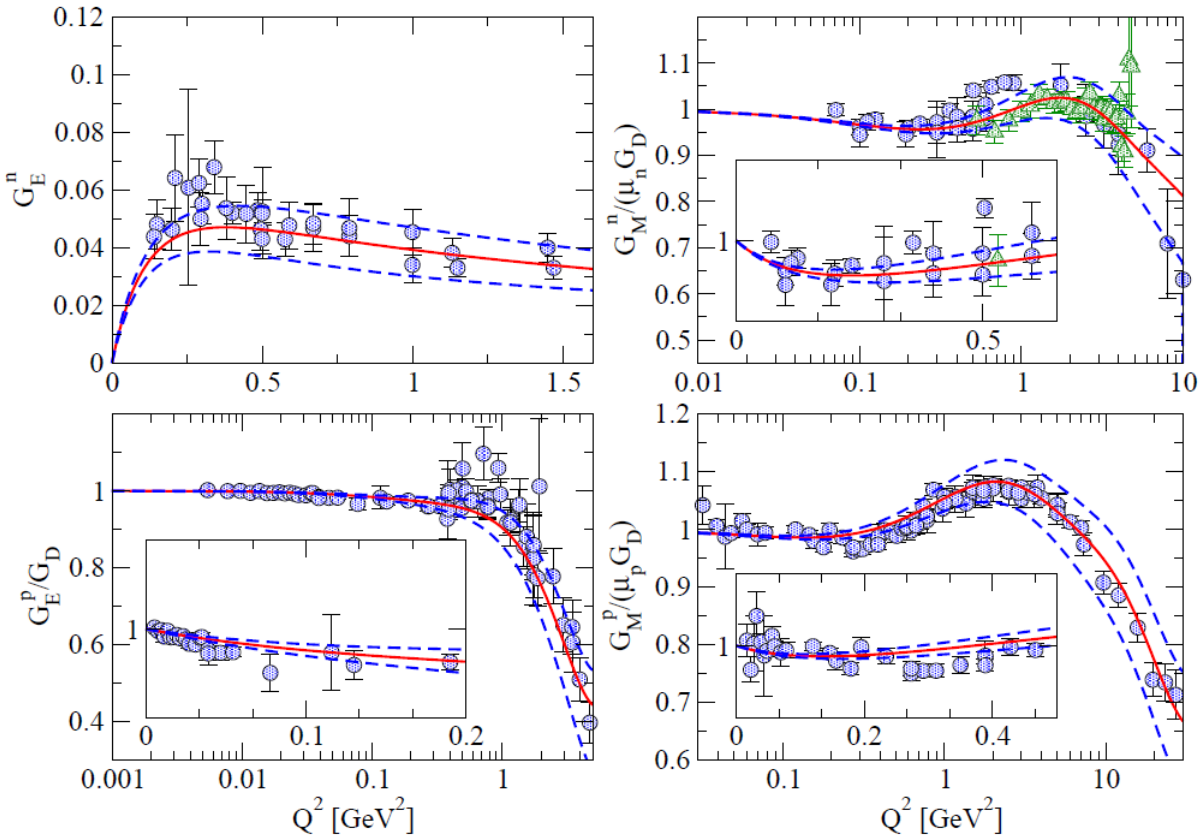

Figure 1.3: The world data for proton and neutron electromagnetic FFs (the JLab data are the green triangles). The data points are normalized to the dipole. The red curves are fits by C. F. Perdrisat and his collaborators, with the dash curves indicating the 1-σ deviation from the fit. The figure is from [11].

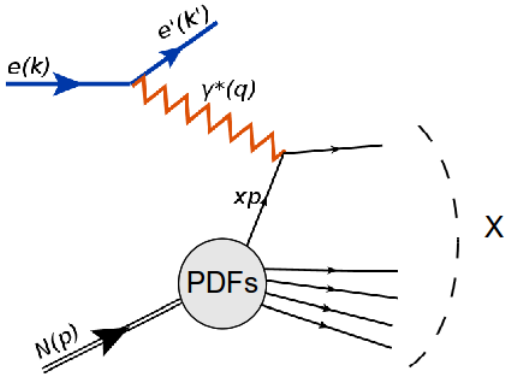

Figure 1.4: The Feynman diagram of the electron-nucleon DIS at leading order.

The impulse approximation assumes that the virtual photon in DIS interacts with a free parton of the nucleon, neglecting the interactions between the partons. Due to the the high virtuality of the photon, the electromagnetic interaction between the photon and the parton is much faster than the strong interaction between the partons. In 1964, Drell and Walecka calculated the unpolarized cross section of ep→eX [16]. They have parametrized the matrix element using two structure functions, $W_{1,2}$, that depend on the energy transferred by the photon (ν) and its virtuality (Q^2):

$$\left(\frac{d^2\sigma}{d\Omega d\nu}\right)_{lab} = \frac{\alpha^2}{4E^2\sin^4\frac{\theta_e}{2}}\left(W_2(\nu,Q^2)\cos^2\frac{\theta_e}{2} + 2W_1(\nu,Q^2)\sin^2\frac{\theta_e}{2}\right). \tag{1.9}$$

If the DIS reaction is an elastic scattering on point-like partons, the structure functions $W_{1,2}(\nu,Q^2)$ can be expressed in terms of the so-called Parton Distribution Functions (PDFs), $\mathcal{F}_{1,2}$. That is

$$W_1(\nu,Q^2) = \frac{1}{M_N}\mathcal{F}_1(x,Q^2) \text{ and } W_2(\nu,Q^2) = \frac{1}{\nu}\mathcal{F}_2(x,Q^2), \tag{1.10}$$

where x is the longitudinal momentum fraction carried by the struck quark.

Experimentalists found that the two structure functions are related to each other by the Callan-Gross relation [17], that is $\mathcal{F}_2 = 2x\mathcal{F}_1$. This relation supports the quark hypothesis, stating that the quarks are point-like spin 1/2 particles. This hypothesis implies that there is an energy region $Q^2, \nu \to \infty$ (Bjorken scaling regime), where the structure functions $\mathcal{W}_{1,2}$, and as a consequence the PDFs $\mathcal{F}_{1,2}(x)$, become independent of Q^2 and depend only on the variable x, and $x = x_B$ ($x_B = \frac{Q^2}{2M_N\nu}$), the so-called Q^2-scaling. Figure 1.5 shows the measurements of the proton's $\mathcal{F}_2$ as a function of Q^2 at fixed values of x. One sees that the measurements are compatible with the model of Bjorken with some deviations. At high Q^2, $\mathcal{F}_2$ exhibits a slight dependence on Q^2. This can be explained by the increasing probability of gluon radiation leading into more quark-antiquark density at low x values. These deviations are explained in the perturbative QCD framework by the DGLAP equations [18][2].

In the infinite-momentum frame, the PDFs $\mathcal{F}_{1,2}(x)$ describe the longitudinal momentum distributions of the constituent partons in the nucleon target. Thus $\mathcal{F}_{1,2}(x)$ can be written in terms of the quarks probability density ($f_q(x)$) as:

$$\mathcal{F}_1(x) = \frac{1}{2}\sum_q e_q^2 f_q(x) \text{ and } \mathcal{F}_2(x) = x\sum_q e_q^2 f_q(x), \tag{1.11}$$

where the sum runs over all the quark flavors and $f_q(x)$ represents the probability of finding a quark of flavor q carrying a longitudinal momentum fraction x of the initial nucleon's momentum. e_q is the quark's charge.

The momentum fraction which is carried by the valence quarks and the sea quarks has been computed firstly by the EMC collaboration [20]. This fraction was found to be 0.465(23), and implied the presence of the gluons that carry this missing momentum. Figure 1.6 shows the extracted parton densities, as a function of x, by the HERA collaboration at fixed value of Q^2. One can see that the up and down valence quarks (u_v, d_v) dominate at relatively large x, with about twice the contribution coming from the up quarks as the down quarks. This supports the quark model stating that the proton contains one down and two up valence quarks. As x decreases, the gluons and the sea quarks distributions dominate because more gluons are radiated.

[2] These equations have been derived independently by Dokshitzer, Gribov and Lipatov, Altarelli and Parisi, and are called DGLAP equations.

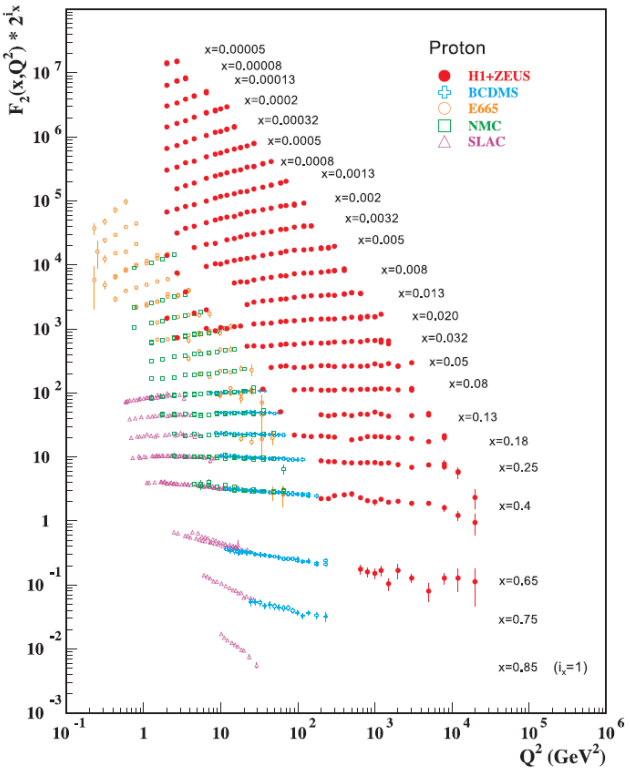

Figure 1.5: The proton's structure function $\mathcal{F}_2^p$ as a function of Q^2 at fixed values of x measured using electron and positron DIS reactions on the proton (experiments H1 and ZEUS) with the HERA collider and using electrons (SLAC) and muons (BCDMS, E665, NMC) on fixed targets. The figure is from [19].

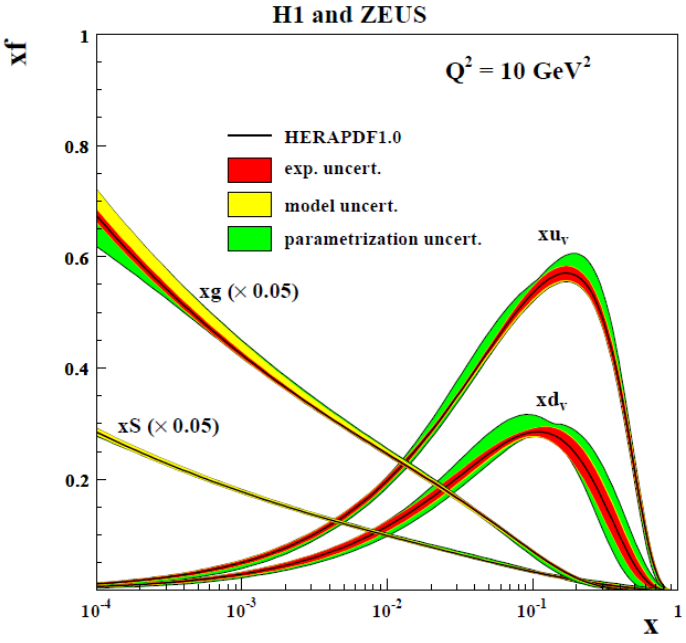

Figure 1.6: The distributions of x times the unpolarised parton function $q(x)$ from HERAPDF1.0 [21], at Q^2 = 10 GeV^2/c^2. The gluon and sea quark distributions are scaled down by a factor 20.

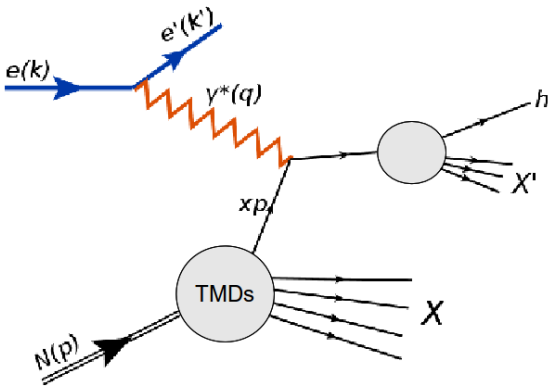

Figure 1.7: Leading order Feynman diagram for the electron-nucleon semi-inclusive deep inelastic scattering.

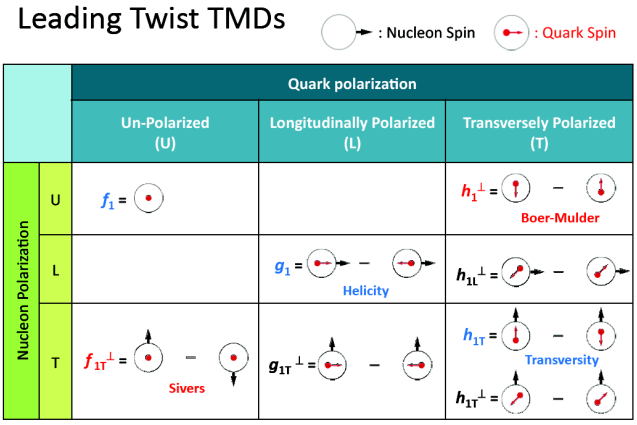

Figure 1.8: The TMDs at leading twist of the SIDIS scattering on a nucleon. These TMDs are classified according to the polarization configurations of the nucleon and the quarks. Similar TMDs exist for the gluons.

1.1.3 Semi-inclusive deep inelastic scattering

The DIS gives information on the longitudinal momentum distributions of the partons in the infinite-momentum frame of the hadron, and has no sensitivity to the partons transverse momentum distributions. The correlation between the partons' longitudinal and transverse momenta is accessible via Semi-Inclusive Deep Inelastic Scattering (SIDIS). Figure 1.7 shows the leading order Feynman diagram for SIDIS, with one final-state hadron (h) being detected. The kinematics of this hadron carries information on the original transverse motion of the target partons.

In SIDIS, the dynamics of the partons in the transverse momentum space are contained in structure functions called Transverse Momentum Dependent PDFs (TMDs). In reference [22], A. Bacchetta *et al.* derived the most general formula of the SIDIS cross section. At leading order, the electron-nucleon SIDIS cross section is parametrized by eight TMDs, see table 1.8. The TMDs are functions of two variables: x, the longitudinal momentum fraction carried by the struck quark, and k_T its transverse momentum.

Experimentally, the first SIDIS asymmetries were observed by HERMES [23, 24] and CLAS [25, 26] on an unpolarized proton target. COMPASS performed then many studies with polarized proton and deuteron targets [27, 28]. Generally speaking, the observed SIDIS signals suffer from a lack of statistics that limits our knowledge about the TMDs. The future experiments at JLab after the upgrade in both Halls, A [29] and B [30], will give better precision and larger kinematical coverage, that will enrich our knowledge about these structure functions.

1.1.4 Deeply virtual Compton scattering

More information on the hadronic structure lies in the correlation between the momentum and the spatial degrees of freedom of the constituent partons. Such correlations are accessible via the GPDs [31, 34]. The GPDs contain information on the correlation between longitudinal momenta and transverse positions of the partons. Also they contain information on the

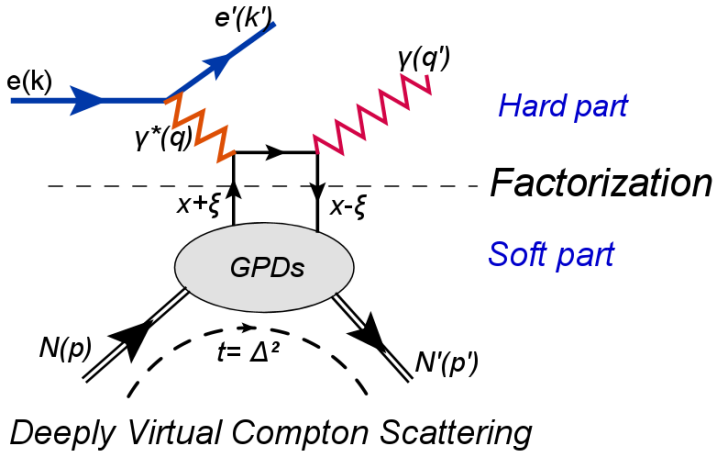

Figure 1.9: Schematic of the leading-twist handbag diagram of DVCS on a nucleon (N), at the leading order in the coupling constant (α_s).

quark-antiquark structure of the target. The GPDs are accessible via hard exclusive reactions, like Deeply Virtual Compton Scattering (DVCS) and Deeply Virtual Meson Production (DVMP). The DVCS process is the exclusive electroproduction of a real photon from a quark of the nucleon.

The twist is defined as the dimension of an operator minus its spin. The leading twist of DVCS is n = 2, and higher twists are suppressed by a power of $(M_N/Q)^{n-2}$ [35]. The DVCS reaction ($eN \rightarrow e'N'\gamma$) at leading twist (twist-2) and at leading order in the strong coupling constant of QCD (α_s), is described by the handbag diagram shown in figure 1.9. In the DVCS process, a highly virtual photon (γ^*), radiated by the incident electron (e), interacts with a quark which emits a real photon (γ) before going back to the nucleon. The final-state photon of the DVCS process is replaced by a final state meson in the case of the DVMP reaction [31].

The hard reactions are characterized by the factorization property. With this property, the handbag diagram in figure 1.9 can be factorized into two parts, a hard and a soft part. The hard part is calculable by perturbative methods, while the soft part is non-perturbative and is parametrized in terms of the GPDs. This factorization has been proven for the DVCS amplitude by two independent calculations: one by John Collins and Andreas Freund [32], and one by Xiangdong Ji and Jonathan Osborne [33].

The GPDs depend on three variables: x, ξ and t. $x+\xi$ is the nucleon's longitudinal momentum fraction carried by the struck quark, 2ξ is the longitudinal momentum fraction of the momentum transfer Δ ($= p' - p$), and t ($=\Delta^2$) is the squared momentum transfer between the initial and the final states of the nucleon. One can define a GPD (x,ξ,t) as the probability amplitude of picking up a parton with a longitudinal momentum $x+\xi$ and putting it back in the nucleon with a longitudinal momentum $x-\xi$, without breaking the nucleon, at a squared momentum transfer t. In this section we briefly introduced the DVCS process and the GPDs. More details will be presented in sections 1.3 and 1.4.

1.1.5 Parton distributions family

The most general hadronic structure functions are called Generalized Transverse Momentum Distributions (GTMDs). They are five-dimensional density distributions, correlating the longitudinal and the transverse momenta, with the transverse spatial coordinates of the partons. Figure

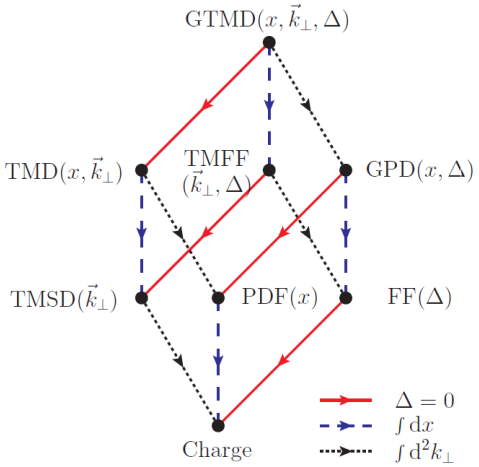

Figure 1.10: The GTMDs and their reduction to measurable structure functions such as the GPDs, the TMDs, the PDFs, and the FFs. The variables x, k_T and Δ are the parton longitudinal momentum fraction, transverse momentum fraction and the momentum transfer (t = - Δ^2), respectively. The figure is from [36].

1.10 shows the family of the parton distributions.

Although the GTMDs cannot be measured experimentally, applying symmetry arguments or integrating over certain variables of the GTMDs, reduces the number of their degrees of freedom. For instance, integrating the GTMDs over the partons' transverse momentum (k_T) leads to the GPDs, while taking the forward limit ($\Delta = 0$) of the GTMDs yields the TMDs. On the other hand, integrating the GTMDs, the GPDs, and the TMDs over the partons' longitudinal momentum x leads to the Transverse Momentum Form Factors (TMFFs), the Form Factors (FFs), and the Transverse Momentum Spin Densities (TMSDs) respectively. Furthermore, the forward limit of the GPDs (FFs) gives the ordinary PDFs (charge).

One can see that the different structure functions are correlated and these connections have to be verified in the theoretical models. For example, to constrain GPD models, one must verify the relations linking the GPDs to the FFs, and to the PDFs. See references [36], [37], [38] and the references therein for more discussions on these correlations.

1.2 The EMC effect

The European Muon Collaboration (EMC) has discovered the nuclear modifications of the parton distribution functions $\mathcal{F}_2(x)$, i.e. the ratio of a lepton-nucleus to a lepton-deuteron DIS cross section per nucleon is not unity.

During the last 3 decades, more precise measurements of the EMC effect have been carried out at CERN [20, 39], SLAC [40], HERMES [41], JLab [42], and Fermilab [43]. Figure 1.11 shows the combined measurements of the per-nucleon DIS cross section in nitrogen and carbon as a function of the longitudinal momentum fraction x. Four regions are defined based on the deviation of the DIS cross section ratio, where different nuclear effects play a role. The regions are:

- The shadowing region ($x < 0.07$): where the cross section ratio is less than 1 and decreases with decreasing x. In this region, the sea quarks are expected to be the major contributor to

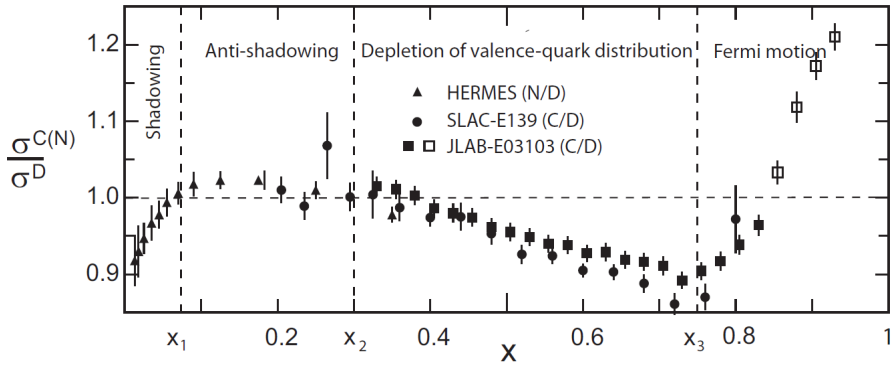

Figure 1.11: The EMC effect in carbon and nitrogen in terms of the DIS cross-section ratio $\sigma^{C(N)}/\sigma^{D}$ as a function of x. The open squares denote the results of data at W^2 below 2 GeV^2/c^4, where W is the invariant mass of the photon-nucleon system [44].

the cross section.

- The anti-shadowing region ($0.07 < x < 0.3$): where the ratio shows a small increase of a few percent above 1. There is no clear explanation of this feature, but it might be dynamically generated by the excess of pions in nuclei [45].
- The EMC effect region ($0.3 < x < 0.7$): where the ratio is suppressed almost linearly with increasing x. The main contribution to the measured cross section is expected to come from the valence quarks. Thus, the cross section ratio reflects the behaviour of the valence quark distributions.
- The Fermi motion region ($x > 0.7$): the ratio is enhanced with increasing x. Free nucleon cross section vanishes at the limit $x_B \to 1$, while it is not the case for a bound nucleon due to the Fermi motion of the nucleons.

As shown previously, the structure function $\mathcal{F}_2(x)$ shows a scaling in the Björken limit, i.e. it becomes independent on Q^2 and depends only on x (see figure 1.5). Thus it is expected that the EMC effect will be independent of Q^2 as well. This is illustrated in figure 1.12, in which the carbon to deuterium DIS cross section is plotted as a function of x at different values of Q^2. One can conclude that the EMC ratios are independent on Q^2.

1.2.1 Dependence on nuclear properties

The EMC effect appears to depend on the nuclear characteristics, such as the nuclear density and the atomic number. In the EMC region, one can investigate the EMC dependence on the nuclear characteristics by looking at the EMC ratios at certain values of x, but this approach suffers limiting factors, such as the precision in the normalizations. However, if we assume that the EMC effect exhibits a universal linear dependence on x, and only its magnitude varies for different nuclei, then the slope of this x-dependence is the best observable. Figure 1.13 shows the extracted slope for several nuclei as a function of A$^{-1/3}$, and as a function of the nuclear density.

The variation of the EMC effect as a function of A$^{-1/3}$ is close to be linear for heavy nuclei, while it is not the case for the light nuclei. Regarding the density-dependence, except for the ^9Be, the EMC slope appears to be correlated to the average nuclear density. One explanation

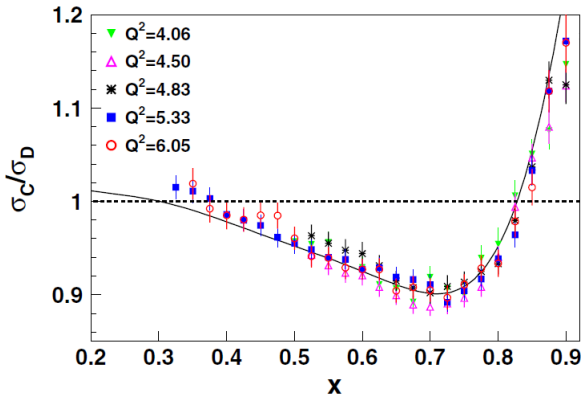

Figure 1.12: Carbon EMC ratios at five Q^2 values (Q^2 quoted at $x = 0.75$). The solid curve is the SLAC fit to the carbon EMC ratio. The figure is from [42].

for the behaviour of ^9Be is that this nucleus can be described by two dense core alphas plus a neutron, which orbits in the whole volume resulting in a smaller average density than the density experienced by the nucleons, that are in the alpha clusters. This supports the idea that the EMC effect depends on the local nuclear environment, and it is not straightforwardly scaled by the nuclear average density nor by the atomic number.

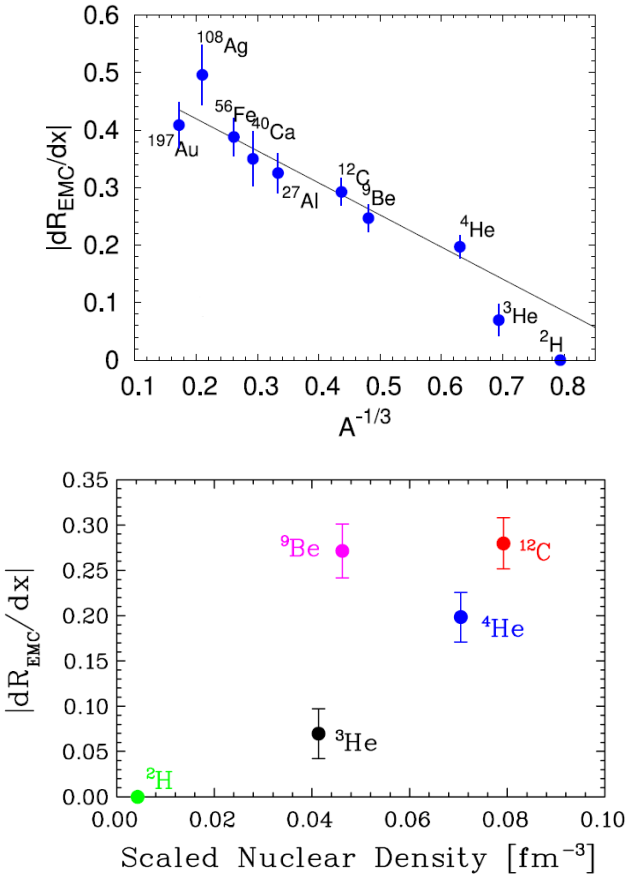

Figure 1.13: On the top: the slope of the EMC ratio for $0.35 < x < 0.7$ as a function of $A^{-1/3}$, where A is the atomic number of the different nuclei [46]. On the bottom: the slope is plotted as a function of the nuclear density [42].

1.2.2 Links with short range correlations

As shown in section 1.1.2, $W > 2$ GeV/c^2 and $Q^2 > 1$ GeV^2/c^2 are the typical values for DIS on a nucleon. These cuts usually limit x to be smaller than 1, but in an inclusive electron scattering of a nucleus A, the data can in principle cover x ranges from 0 to A. A study was performed, at JLab, to investigate the nucleon-nucleon short-range correlations, by measuring the per-nucleon inclusive cross sections at x greater than 1. The results are shown in figure 1.14.

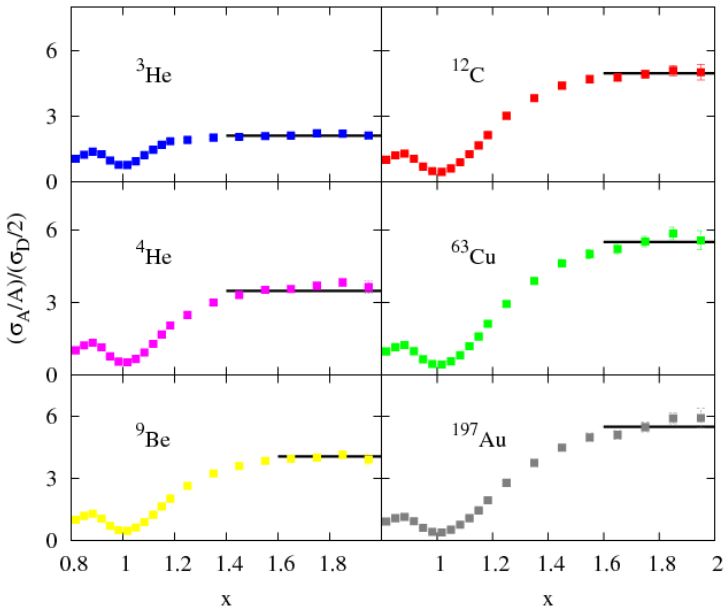

Figure 1.14: The inclusive cross section ratio σ^A/σ^D as a function of x for various nuclei in the region $0.8 < x < 2$ measured at Hall C, JLab [47].

The inclusive cross section ratio σ^A/σ^D shows a plateau pattern for $x \in$ [1.4: 2.0]. This behaviour can be interpreted as the result of Short Range nucleon-nucleon Correlations (SRC). One can see that the height of the plateau differs from a nucleus to another, which is direclty related to the number of SRC pairs in the nuclei. This observation led to another very interesting observation when compared to the slope of the EMC effect. The results can be seen in figure 1.15, where the slope of the EMC ratios and the height of the plateaus were measured independently. This correlation supports the idea that the EMC effect might be connected to the nucleon-nucleon SRCs.

1.2.3 Theoretical models

The EMC effect has been precisely measured for various nuclei as briefly shown in the previous sections, and the references therein. Dependences and correlations on the nuclear properties, and with the SRCs were established. However, there is no universally accepted explanation for the origin of this effect. Here is a list of some models used to explain the EMC effect:

Pion excess in nuclei: the mesons, specially pions, are responsible for the long-range nucleon-nucleon interactions in a nucleus. This implies that one has to take into account the pions degrees of freedom in the nuclear spectral function calculations [49]. This hypothesis was one of the first EMC models. However, with these extra pions, one has to see enhancement for the sea quarks in

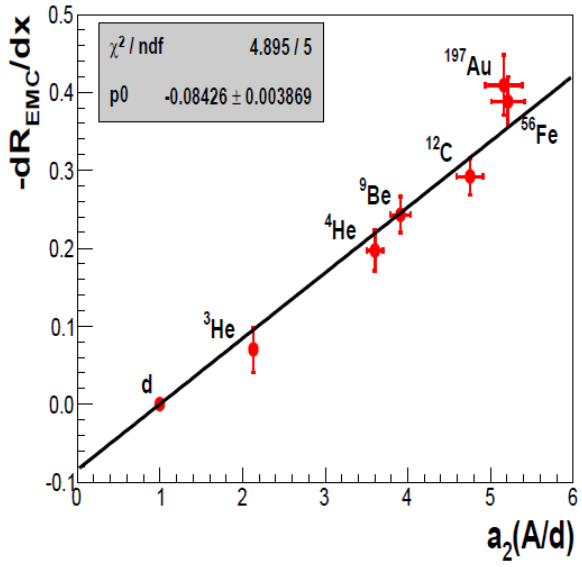

Figure 1.15: The slope of the EMC effect ($0.35 < x < 0.7$) is plotted versus height of the inclusive cross section plateau ($a2(A/d)$) shown in figure 1.14. The figure is from [48].

a nucleus compared to a free nucleon. Latter on, a series of experiments were performed, and no enhancement was observed [50].

Nuclear binding: in these models, the spectral function of the nucleus is the incoherent sum over all the hadronic constituents, such as nucleons and pions. Then, the quarks distributions of the hadrons are convoluted with the nuclear binding and the Fermi-motion effects [51, 52, 53].

Medium modification: the bound nucleons are assumed to have additional effects, such as quark exchange and quarks coupling between nearby nucleons, due to their wave functions overlapping in the nuclear medium. For instance, this overlapping leads to change the confinement radius of the quarks inside the bound nucleons, and as a consequence their momentum distributions [54, 55, 56, 57, 58].

It turns out that we cannot fully identify the origin of the EMC phenomenon from the one-dimensional parton distribution functions as measured in DIS. However, we might get additional insights on the EMC effect by measuring bound nucleon momentum and the effects of transverse degrees of freedom.

1.3 Nucleonic DVCS

In the infinite-momentum frame, where the initial and the final nucleons go at the speed of light along the positive z-axis, the partons have relatively small transverse momenta compared to their longitudinal momenta. Referring to figure 1.9, the struck parton carries a longitudinal momentum fraction $x+\xi$ and it goes back into the nucleon with a momentum fraction $x-\xi$. The GPDs are defined in the interval where x and $\xi \in$ [-1,1], which can be separated into three regions as can be seen in figure 1.16. The regions are:

- $x \in [\xi,1]$: both momentum fractions $x+\xi$ and $x-\xi$ are positive and the process describes the emission and reabsorption of a quark.
- $x \in [-\xi,\xi]$: $x+\xi$ is positive reflecting the emission of a quark, while $x-\xi$ is negative and is interpreted as an antiquark being emitted from the initial proton.
- $x \in [-1,-\xi]$: both fractions are negative, and $x+\xi$ and $x-\xi$ represent the emission and reabsorption of antiquarks.

  The GPDs in the first and in the third regions represent the probability amplitude of finding a quark or an antiquark in the nucleon, while in the second region they represent the probability amplitude of finding a quark-antiquark pair in the nucleon [59].

Following the definition of reference [60], the differential DVCS cross section is obtained from the DVCS scattering amplitude ($\mathcal{T}_{DVCS}$) as:

$$\frac{d^5\sigma}{dQ^2\,dx_B\,dt\,d\phi\,d\phi_e} = \frac{1}{(2\pi^4)32}\frac{x_B\,y^2}{Q^4}\left(1+\frac{4M^2x_B^2}{Q^2}\right)^{-1/2}|\mathcal{T}_{DVCS}|^2, \tag{1.12}$$

where ϕ_e is the azimuthal angle of the scattered lepton, $y = \frac{E-E'}{E}$ and Q^2, x_B, t, ϕ are the four kinematic variables that describe the process. The variable ϕ is the angle between the leptonic and the hadronic planes, as can be seen in figure 1.17.

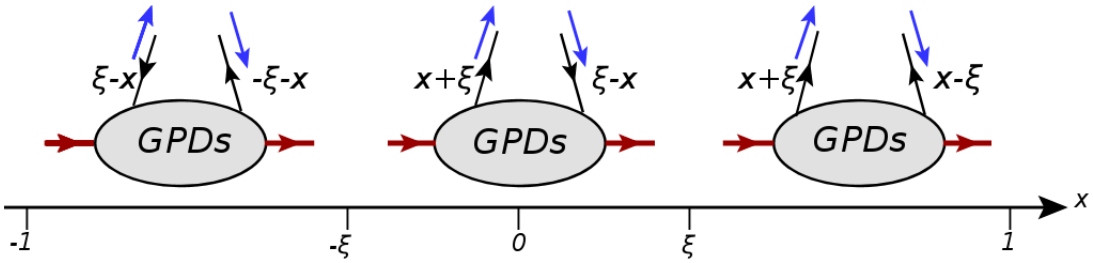

Figure 1.16: The parton interpretations of the GPDs in three x-intervals [-1,-ξ], [-ξ,ξ] and [ξ,1]. The red arrows indicate the initial and the final-state of the proton, while the blue (black) arrows represent helicity (momentum) of the struck quark.

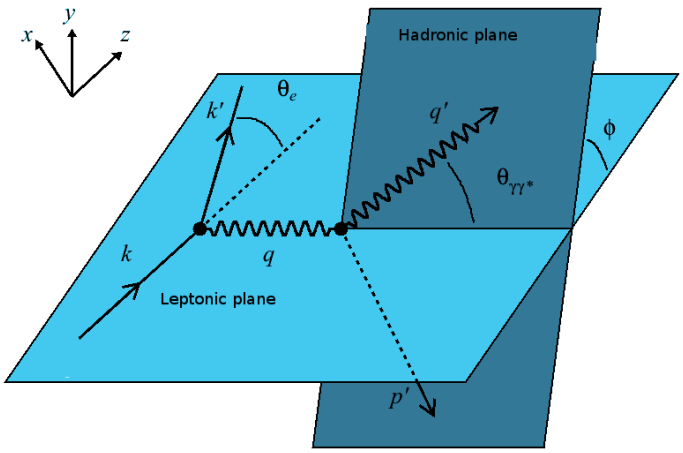

Figure 1.17: The definition of the azimuthal angle ϕ between the leptonic and the hadronic planes.

By neglecting the mass of the quark with respect to the energies of γ^* and γ, the DVCS scattering amplitude can be parametrized by four quark helicity conserving (chiral-even) GPDs: H, E, $\widetilde{H}$ and $\widetilde{E}$ as:

$$\begin{aligned}\mathcal{T}_{DVCS} = \sum_q (|e|Q_q)^2 \varepsilon^*_\mu \varepsilon_\nu \Bigg\{ & \\ g_\perp^{\mu\nu} \int_{-1}^{1} dx \left[\frac{1}{x-\xi+i\varepsilon} + \frac{1}{x+\xi-i\varepsilon}\right] \times \frac{1}{2}\bar{u}(p') \left[H^q\gamma^+ + E^q i\sigma^{+\alpha}\frac{\Delta_\alpha}{2m_N}\right] u(p) & \\ + i\varepsilon^{\mu\nu+-} \int_{-1}^{1} dx \left[\frac{1}{x+\xi-i\varepsilon} - \frac{1}{x-\xi+i\varepsilon}\right] \times \frac{1}{2}\bar{u}(p') \left[\tilde{H}^q\gamma^+\gamma_5 + \tilde{E}^q\gamma_5\frac{\Delta^+}{2m_N}\right] u(p) \Bigg\}, & \end{aligned} \tag{1.13}$$

where $\bar{u}(p')$ and $u(p)$ are the spinors of the nucleon.

The GPDs H, E, $\widetilde{H}$ and $\widetilde{E}$ are defined for each quark flavor (q = u, d, s, ...). Analogous GPDs exist for the gluons, see references [31, 60, 61] for details. In this work, we are mostly concerned by the valence quark region, in which the sea quarks and the gluons contributions do not dominate the DVCS scattering amplitude.

The GPDs H, E, $\widetilde{H}$ and $\widetilde{E}$ are called chiral-even GPDs because they conserve the helicity of the struck quark. The GPDs H and $\widetilde{H}$ conserve the spin of the nucleon, while E and $\widetilde{E}$ flip it. The H and E GPDs are called the unpolarized GPDs as they represent the sum over the different configurations of the quarks' helicities, whereas $\widetilde{H}$ and $\widetilde{E}$ are called the polarized GPDs because they are made up of the difference between the orientations of the quarks' helicities.

If one keeps the quark mass, another set of GPDs gives contribution to the DVCS amplitude. They are called chiral-odd GPDs. They give information about the quarks helicity-flip transitions. At leading twist, there are four chiral-odd GPDs that parametrize the helicity-flip structure of the partons in a nucleon: H_T, E_T, $\widetilde{H}_T$ and $\widetilde{E}_T$ [62]. Analogous set of chiral-odd GPDs exist for the gluon sector (see [62, 63]). The chiral-even GPDs contribute mostly in the regions where $\xi<x$ and $x<-\xi$, while the chiral-odd GPDs have larger contribution in the $x<|\xi|$ region [60].

1.3.1 Basic properties of GPDs

Links to the ordinary FFs and PDFs

Links between GPDs and the FFs are constructed by integrating the GPDs over the momentum fraction x at given momentum transfer (t). Because of Lorentz invariance, integrating over x removes all the references to the particular light-cone frame, in which ξ is defined. Therefore, the result must be ξ-independent as can be see in equation 1.14:

$$\begin{aligned} \int_{-1}^{1} dx\, H^q(x,\xi,t) &= F_1^q(t), \qquad \int_{-1}^{1} dx\, E^q(x,\xi,t) = F_2^q(t), \\ \int_{-1}^{1} dx\, \widetilde{H}^q(x,\xi,t) &= G_A^q(t), \qquad \int_{-1}^{1} dx\, \widetilde{E}^q(x,\xi,t) = G_P^q(t), \end{aligned} \tag{1.14}$$

where $F_1^q(t)$ and $F_2^q(t)$ are the previously introduced Dirac and Pauli FFs, $G_A^q(t)$ and $G_P^q(t)$ are the axial and pseudoscalar electroweak FFs. The latter two can be measured in electroweak interactions; see reference [64] for more details about the electroweak FFs.

From the optical theorem, the DIS cross section is proportional to the imaginary part of the forward amplitude of the doubly virtual Compton scattering (production of a spacelike ($Q^2 < 0$) virtual photon in the final state instead of a real photon) [65, 66]. In the limit $\xi \to 0$ and t $\to 0$, the GPDs are reduced to the ordinary PDFs, such that for the quark sector:

$$H^q(x,0,0) = q(x), \qquad \widetilde{H}^q(x,0,0) = \Delta q(x), \tag{1.15}$$

where $q(x)$ is the unpolarized PDF, defined for each quark flavor, that was introduced in section 1.1.2. The polarized PDFs $\Delta q(x)$ are accessible from polarized-beam and polarized-target DIS experiments. There are no similar relations for the GPDs E and $\widetilde{E}$, as in the scattering amplitude, equation 1.13, they are multiplied by factors proportional to t ($= \Delta^2$), which vanish in the forward limit. Figure 1.18 summarizes the physics interpretations of the GPDs, the FFs, the PDFs, and the links between them.

Polynomiality of GPDs

The GPDs have a key property which is the polynomiality. This property comes from the Lorentz invariance of the nucleon matrix elements. It states that the x^n moment of the GPDs must be a polynomial in ξ with a maximum order of n+1 [60, 68].

$$\int_{-1}^{1} dx\, x^n H^q(x,\xi,t) = \sum_{(even)i=0}^{n} (2\xi)^i A_{n+1,i}^q(t) + mod(n,2)(2\xi)^{n+1} C_{n+1}^q(t), \tag{1.16}$$

$$\int_{-1}^{1} dx\, x^n E^q(x,\xi,t) = \sum_{(even)i=0}^{n} (2\xi)^i B_{n+1,i}^q(t) - mod(n,2)(2\xi)^{n+1} C_{n+1}^q(t), \tag{1.17}$$

$$\int_{-1}^{1} dx\, x^n \widetilde{H}^q(x,\xi,t) = \sum_{(even)i=0}^{n} (2\xi)^i \widetilde{A}_{n+1,i}^q(t), \tag{1.18}$$

$$\int_{-1}^{1} dx\, x^n \widetilde{E}^q(x,\xi,t) = \sum_{(even)i=0}^{n} (2\xi)^i \widetilde{B}_{n+1,i}^q(t). \tag{1.19}$$

where $mod(n,2)$ is 1 for odd n and 0 for even n. Thus, the corresponding polynomials contain

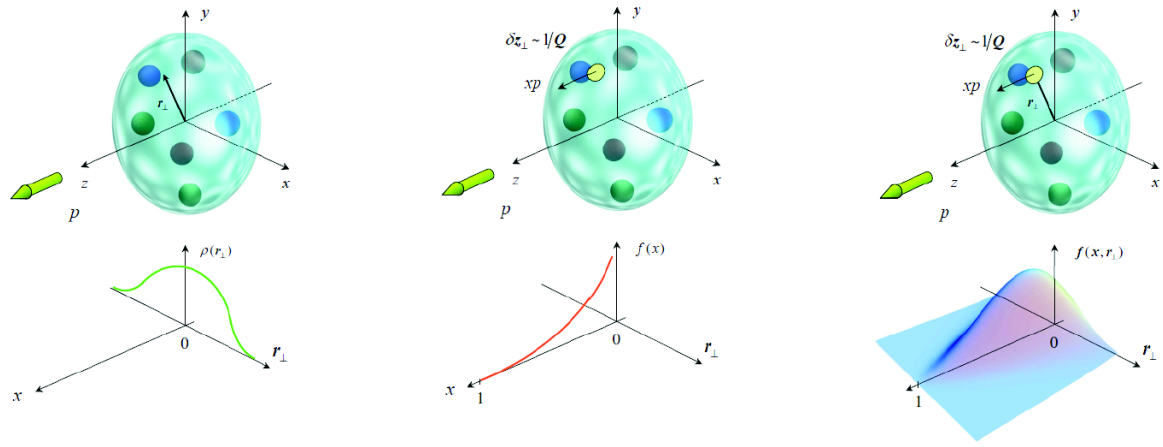

Figure 1.18: The links between the GPDs and the ordinary FFs and PDFs. From left to right: the FFs reflect, via a Fourier transform, the two-dimensional spatial distributions of the quarks in the transverse plane; the PDFs give information about the longitudinal momentum distributions of the partons; finally, the GPDs provide a three-dimensional imaging of the partons in terms of both their longitudinal momenta and their position in the transverse space plane. The figure is from [67].

only even powers of the skewedness parameter ξ. This follows from time-reversal invariance, i.e. $GPD(x,\xi,t) = GPD(x,-\xi,t)$ [69]. This implies that the highest power of ξ is $n+1$ for odd n (singlet GPDs) and of highest power n in case of even n (non-singlet GPDs). Due to the fact that the nucleon has spin $1/2$, the coefficients in front of the highest power of ξ for the singlet functions H^q and E^q are equal and have opposite signs. This sum rule is the same for the gluons [61, 63].

As a consequence of the polynomiality of the GPDs, the first moments of GPDs lead to the ordinary form factors, as shown previously in this section. X. Ji derived a sum rule [68] that links the second moments of the quark GPDs H^q and E^q, in the forward limit ($t = 0$), to the total angular momentum ($J_{quarks} = \frac{1}{2}\Delta\Sigma + L_{quarks}$), where $\Delta\Sigma$ is the contribution of the quark spin to the nucleon spin and L_{quarks} is the quarks orbital angular momentum contribution, as:

$$J_{quarks} = \frac{1}{2}\int_{-1}^{1} dx\; x\,[H^q(x,\xi,t=0) + E^q(x,\xi,t=0)] \tag{1.20}$$

A similar expression exists for the gluons contribution (J_{gluons}).

The spin of a nucleon is built from the sum of the quarks' and the gluons' total angular momenta, $\frac{1}{2} = J_{quarks} + J_{gluons}$. Regarding the experimental measurements, the EMC collaboration [70] has measured the contribution of the spins of the quarks ($\Delta\Sigma$) to the nucleon spin to be around 30%. Therefore, measuring the second moments of the GPDs H and E will give access to the quarks orbital momentum (L_{quarks}) which will complete the sector of the quarks in understanding the nucleon spin. For the gluon total angular momentum (J_{gluons}), it is still an open question how to decompose J_{gluons} into orbital (L_{gluons}) and spin (Δg) components and to access them experimentally, see reference [71] for more discussions on this subject.

1.3.2 Compton form factors

The GPDs are real functions of two experimentally measurable variables, ξ and t, and one unmeasurable variable, x, in the DVCS reaction. Therefore, the GPDs are not directly measurable. In DVCS what we measure are the Compton Form Factors (CFFs) that are linked to the GPDs. As shown in equation 1.13, the DVCS scattering amplitude, at leading order in α_s and leading twist, contains x-integrals of the form, $\int_{-1}^{+1} dx \frac{GPD^q(x,\xi,t)}{x\pm\xi\mp i\varepsilon}$, where $\frac{1}{x\pm\xi+i\varepsilon}$ is the propagator of the quark between the two photons. The integrals can be written as:

$$\int_{-1}^{+1} dx \frac{GPD^q(x,\xi,t)}{x\pm\xi\mp i\varepsilon} = \mathcal{P}\int_{-1}^{1} dx \frac{GPD^q(x,\xi,t)}{x\pm\xi} \pm i\pi GPD^q(x=\mp\xi,\xi,t), \tag{1.21}$$

where $\mathcal{P}$ stands for the Cauchy principal value integral. The DVCS amplitude can be decomposed into four complex CFFs, such that for each GPD there is a corresponding CFF. For instance, for the GPD $H^q(x,\xi,t)$, the real and imaginary parts of its CFF ($\mathcal{H}(\xi,t)$) at leading order in α_s can be expressed as:

$$\mathcal{H}(\xi,t) = \Re e(\mathcal{H})(\xi,t) - i\pi \Im m(\mathcal{H})(\xi,t) \tag{1.22a}$$

$$\text{with} \qquad \Re e(\mathcal{H})(\xi,t) = \mathcal{P}\int_0^1 dx [H(x,\xi,t) - H(-x,\xi,t)]\, C^+(x,\xi) \tag{1.22b}$$

$$\text{and} \qquad \Im m(\mathcal{H})(\xi,t) = H(\xi,\xi,t) - H(-\xi,\xi,t), \tag{1.22c}$$

where the term corresponding to the real part is weighted by $C^+(x,\xi)$ $(= \frac{1}{x-\xi} + \frac{1}{x+\xi})$, which appears also in an analogous expression for the GPD $E^q(x,\xi,t)$. The real parts of the CFFs that are associated with the GPDs $\widetilde{H}^q(x,\xi,t)$ and $\widetilde{E}^q(x,\xi,t)$, are weighted by $C^-(x,\xi)$ $(= \frac{1}{x-\xi} - \frac{1}{x+\xi})$. See reference [66] for the full expressions.

1.3.3 Bethe-Heitler

Experimentally, the DVCS is indistinguishable from the Bethe-Heitler (BH) process, which is the reaction where the final photon is emitted either from the incoming or the outgoing leptons, as shown in figure 1.19. The BH process is not sensitive to GPDs and does not carry information about the partonic structure of the hadronic target. The BH cross section is calculable from the well-known electromagnetic FFs.

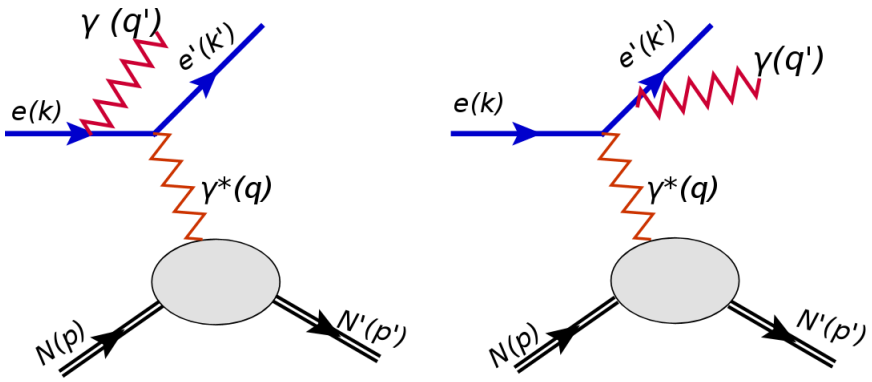

Figure 1.19: Schematic for the Bethe-Heitler process. The final real photon can be emitted from the incoming electron (left plot) or from the scattered electron (right plot).

The $ep \to ep\gamma$ differential cross section of a longitudinally-polarized electron beam on an unpolarized proton target can be written as [34, 72]:

$$\frac{d^5\sigma^\lambda}{dQ^2 dx_B dt d\phi d\phi_e} = \frac{\alpha^3}{16\pi^2} \frac{x_B\, y^2}{Q^2\sqrt{1+(2x_b M_N/Q)^2}} \frac{|\mathcal{T}_{BH}|^2 + |\mathcal{T}^\lambda_{DVCS}|^2 + \mathcal{I}^\lambda_{BH*DVCS}}{e^6} \tag{1.23}$$

where λ is the beam helicity, $\mathcal{T}_{DVCS}$ is the pure DVCS scattering amplitude, $\mathcal{T}_{BH}$ is the pure BH amplitude and $\mathcal{I}^\lambda_{BH*DVCS}$ represents the interference amplitude. At leading twist, A. V. Belitsky, D. Mueller and A. Kirchner have shown that these amplitudes can be decomposed into a finite sum of Fourier harmonics, the so-called BMK formalism [34], as:

$$|\mathcal{T}_{BH}|^2 = \frac{e^6(1+\varepsilon^2)^{-2}}{x_B^2 y^2 t \mathcal{P}_1(\phi)\mathcal{P}_2(\phi)} \left[c_0^{BH} + \sum_{n=1}^{2} \left(c_n^{BH}\cos(n\phi) + s_n^{BH}\sin(\phi) \right) \right] \tag{1.24}$$

$$|\mathcal{T}_{DVCS}|^2 = \frac{e^6}{y^2 Q^2} \left[c_0^{DVCS} + \sum_{n=1}^{2} \left(c_n^{DVCS}\cos(n\phi) + \lambda s_n^{DVCS}\sin(n\phi) \right) \right] \tag{1.25}$$

$$\mathcal{I}_{BH*DVCS} = \frac{\pm e^6}{x_B y^3 t\, \mathcal{P}_1(\phi)\mathcal{P}_2(\phi)} \left[c_0^{I} + \sum_{n=0}^{3} \left(c_n^{I}\cos(n\phi) + \lambda s_n^{I}\sin(n\phi) \right) \right] \tag{1.26}$$

where $\mathcal{P}_1(\phi)$ and $\mathcal{P}_2(\phi)$ are the BH propagators. The leading twist expressions of the DVCS, BH and interference Fourier coefficients on a proton target can be found in reference [34]. The $+(-)$ sign in the interference term stands for the negatively (positively) charged lepton beam. In the case of an unpolarized proton target, the coefficients of the $\sin(\phi)$ in the BH amplitude are zeros.

1.3.4 Observables and recent measurements

Experimentally, one can measure the CFFs via fitting experimental observables such as, cross sections and spin asymmetries, and finding the magnitudes of the Fourier coefficients shown in equations 1.24-1.26. In the kinematical domain of JLab, the measured total photon-leptoproduction cross section is dominated by the BH in most of the phase space. Nevertheless, the DVCS signal is enhanced by the interference with the BH. Therefore, extracting the CFFs from the measured total cross section is possible but not a trivial task. The cross section difference and spin asymmetries are sensitive to the interference term, and can provide access to DVCS and GPDs in an almost linear way. In particular, the spin asymmetries are easier to measure than the cross sections because most of the normalization and the acceptance issues of the cross section cancel in the asymmetry ratios.

Figures 1.20 and 1.21 show the measured beam-polarized cross section difference ($\Delta d^4\sigma$ in figure 1.20, $d^4\Sigma$ in figure 1.21) and the total cross section ($d^4\sigma$) on a proton from the Hall B (CLAS) and Hall A of JLab, respectively. The cross section difference is mostly sensitive to the imaginary part of the CFF $\mathcal{H}$, while the total cross section is mostly sensitive to the real part of the CFF $\mathcal{H}$ for a proton target.

Three spin asymmetries can be measured depending on the polarization of the lepton beam and the target: the beam [73], the target [74], and the double-spin asymmetry [75].

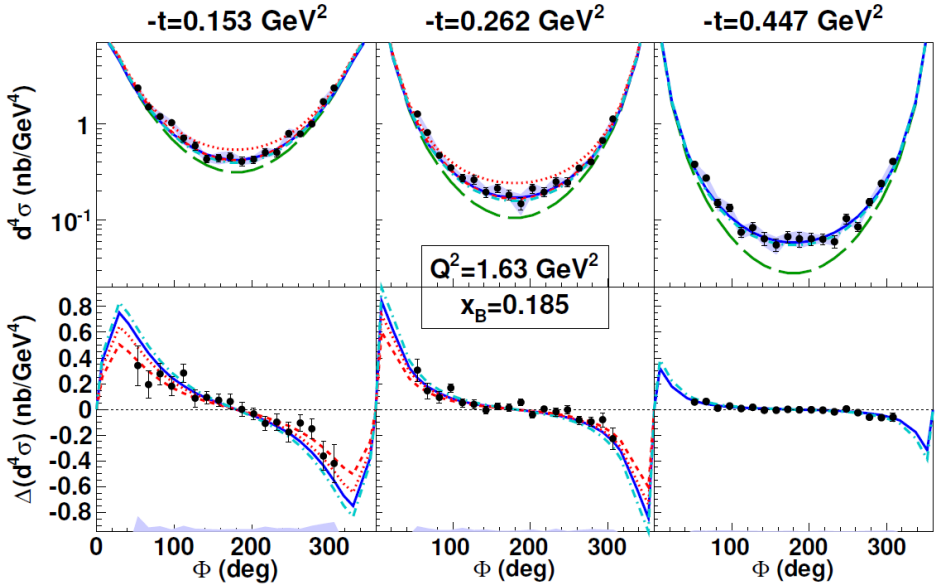

Figure 1.20: The total cross section (top row) and polarized cross section difference (bottom row) for the $ep \to e'p'\gamma$ reaction measured at Hall B, JLab, as a function of ϕ for 3 bins in $-t$ in a particular bin in (Q^2, x_B)=(1.63 GeV^2/c^2, 0.185). The green long-dashed curves show the BH contribution only. The other curves correspond to theoretical predictions including the DVCS contribution. The figure is from [76].

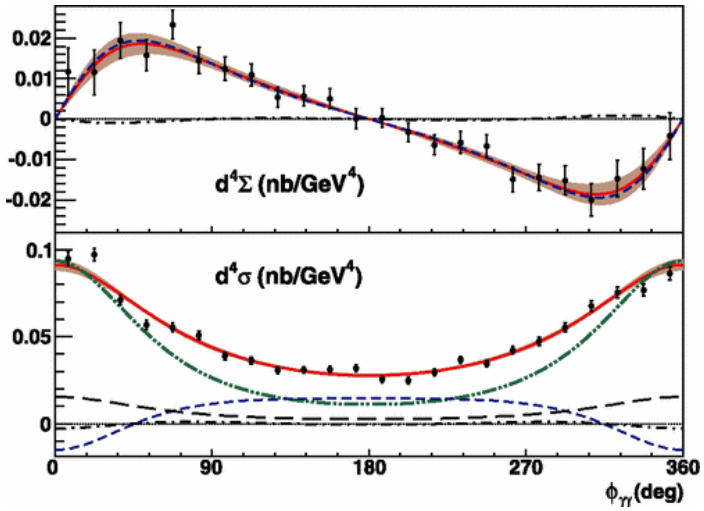

Figure 1.21: The total cross section (top panel) and polarized cross section difference (bottom panel) for the $ep \to e'p'\gamma$ reaction measured at Hall A, JLab, as a function of ϕ in a particular bin (Q^2, x_B, t) = (2.3 GeV^2/c^2, 0.36, -0.28 GeV^2/c^2). In both plots, the red curves are fits to the data. The short-dashed (blue) and the long-dashed lines are the fitted imaginary and real parts respectively of the leading twist CFF. On the bottom panel: the dot-dot-dashed (green) line represents the pure BH contribution. The dot-dashed curves are the fitted twist-3 contribution. The figure is from [77].

1.4 DVCS off Helium-4

Nuclear targets provide access to the measurement of two DVCS channels: the coherent and the incoherent one. In the coherent channel, the target nucleus remains intact and recoils as a whole while emitting a real photon ($eA \rightarrow e'A'\gamma$, where A represents the nucleus target). This process allows to measure the nuclear GPDs of the target nucleus, which contain information on the partons correlations and the nuclear forces in the target [78, 79]. In the incoherent channel, the nucleus breaks up and the DVCS takes place on a bound nucleon that emits the final photon ($eA \rightarrow e'N'\gamma$ X). This latter allows to measure the GPDs of the bound nucleons and study the medium modifications of the nucleons in the nuclear medium. Figure 1.22 shows the twist-2 handbag diagrams of the two DVCS channels.

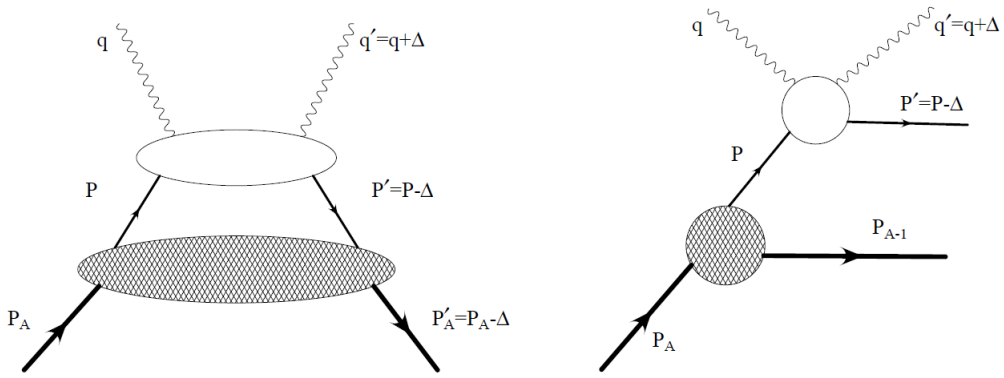

Figure 1.22: The leading twist handbag diagrams of the two DVCS channels from a nuclear target, coherent channel (on the left) and incoherent channel (on the right).

As for the nucleons, the number of the different GPDs needed to parametrize the partonic structure of a nucleus depends on the different configurations between the spin of the nucleus and the helicity direction of the struck quark. In principle, for a target of spin s, the number of the chiral-even GPDs is equal to $(2s+1)^2$ for each quark flavor. For instance, at leading twist level, nine chiral-even GPDs are required to parametrize the partonic structure of the deuteron, because it has a spin one [80, 81, 82, 83]. This makes studying this nucleus a non-trivial task. The DVCS off spinless nuclear targets, such as ^{4}He, ^{12}C and ^{16}O, is simpler to study as only one chiral-even GPD ($H_A(x,\xi,t)$) arises at leading twist to parametrize their partonic structure. Also, at leading twist the quarks helicity-flip structure in these spinless nuclei is parametrized by a unique chiral-odd GPD.

Nuclear DVCS provides a quantitative information on the nuclear medium effects, such as the confinement size of the bound nucleons [84], see figure 1.23. The Fourier transform of the nucleon GPDs over the momentum transfer Δ gives the transverse separation (b') between quarks in the nucleon, while the Fourier transform of the nuclear GPD ($H_A(x,\xi,t)$) gives the transverse separation (b) between the quarks in the nucleus. Knowing these two separations, one can in principle access the transverse separation ($\beta = b - b'$) between the nucleons in a nucleus [79].

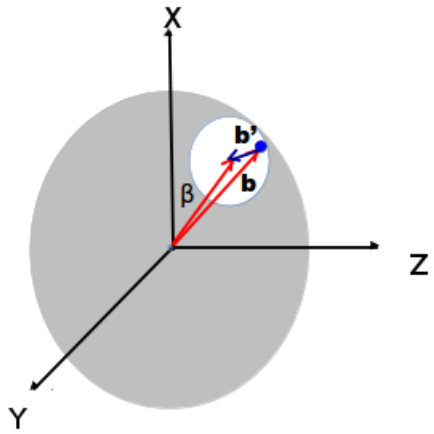

Figure 1.23: The spatial coordinates of quarks in a nucleus. See main text for definition of the variables. The figure is from [85].

As shown in figure 1.13, the ^{4}He nucleus shows a clear EMC effect. This nucleus is characterized by its spin-zero, a high density and it is a well-known few-body system. These aspects make the ^{4}He nucleus an ideal target to be considered for the understanding of the nuclear effects at the partonic level.

In principle, the ^{4}He GPD $H_A(x,\xi,t)$ follows the same properties than the nucleonic GPDs, that were introduced in section 1.3.1. These are:

- The universality of H_A: the H_A describes the partonic structure of ^{4}He in a DVCS reaction the same way as in a DVMP reaction.
- In the forward limit ($t \to 0$), H_A is reduced to the usual PDF of ^{4}He that is accessible via DIS.
- H_A can be decomposed into a polynomial in ξ.
- The first moment of H_A is the ^{4}He elastic electromagnetic form factor $F_A(t)$, such as:

$$\sum_q \int_{-1}^{1} dx\ H_A^q(x,\xi,t) = F_A(t), \tag{1.27}$$

  where the sum runs over all the quark flavors.

- The second moment of $H_A^q(x,\xi,t)$ reads

$$\int_{-1}^{1} dx\ x H_A^q(x,\xi,t) = M_2^{q/A}(t) + \frac{4}{5}\xi^2 d_2^{q/A}(t) \tag{1.28}$$

  where the first term of the right-hand side represents the momentum fraction carried by each quark flavor q, and the second term is encoding information about the forces experienced by partons inside the nucleus [78].

- H_A is not directly measured from experiment, but we measure its corresponding Compton form factor $\mathcal{H}_A$.

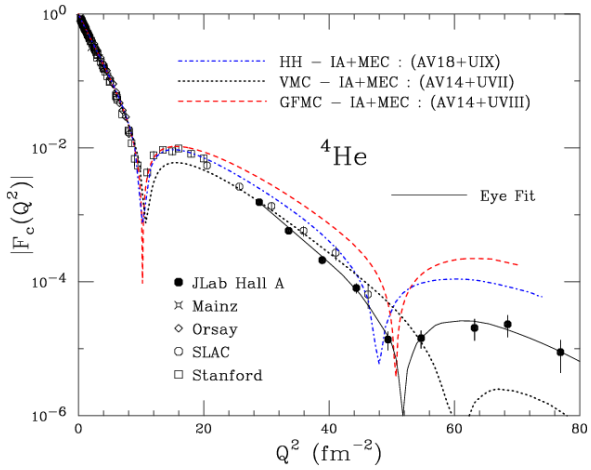

Figure 1.24: ^{4}He charge form factor measurements at Stanford, SLAC, Orsay, Mainz and JLab Hall A compared with theoretical calculations. The figure is from [87].

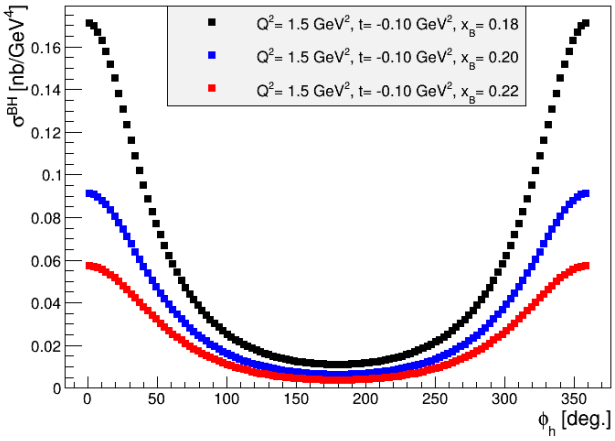

Figure 1.25: The calculated BH cross section as a function of ϕ on a ^{4}He target at three values of x_B and fixed values of Q^2 and t. (t = -0.1 GeV^2/c^2 corresponds to $Q^2 \approx 2.57$ fm^{-2} on figure 1.24).

As for the nucleon (see equation 1.13), the ^{4}He DVCS amplitude can be expressed as [63]:

$$\mathcal{T}_{DVCS} \propto \sum_q e_q^2 \mathcal{P} \int_{-1}^{1} dx \left(\frac{1}{x-\xi} + \frac{1}{x+\xi} \right) H_A^q(x,\xi,t) - i\pi \sum_q \left(e_q^2 \left[H_A^q(\xi,\xi,t) - H_A^q(-\xi,\xi,t) \right] \right), \tag{1.29}$$

where the first term on the right-hand side stands for the real part of the CFF $\mathcal{H}_A$, while the second term for the imaginary part of $\mathcal{H}_A$.

The coherent DVCS amplitude is enhanced through the interference with the BH process, that is calculable from the well-known elastic FF. Figure 1.24 shows the world measurements of the ^{4}He $F_A(t)$ along with theoretical calculations. Following the $F_A(t)$ parametrization by R. Frosch and his collaborators [86] (valid at the small values of $-t$ which are of interest in this work), figure 1.25 shows the calculated BH as a function of the azimuthal angle between the leptonic and the hadronic planes (ϕ), using a 6 GeV electron beam on a ^{4}He target.

The experimentally measured $e\ ^4He \rightarrow e\ ^4He\gamma$ cross section can be decomposed into BH, DVCS, and interference terms. The differential cross section can be written like in equation 1.23, where the Björken variable x_B should be replaced by $x_A = \frac{x_B M_N}{M_A}$ and M_A is the mass of the ^{4}He. By generalizing the BMK model, the nuclear BH, DVCS and interference scattering amplitudes can be decomposed into a finite series of Fourier harmonics as in equations 1.24, 1.25 and 1.26 by introduting the nuclear x_A and the ^{4}He FF instead of the nucleon ones [82]. The detailed expressions of these amplitudes can be found in Appendix A.

1.4.1 Beam-spin asymmetry

As mentioned in section 1.3.4, most of the experimental normalization and acceptance issues cancel out in an asymmetry ratio. The beam-spin asymmetry is measured using a polarized

lepton beam on an unpolarized target (U). JLab provides a longitudinally (L) polarized electron beam, $P_B \approx 85$ %. It is defined as:

$$A_{LU} = \frac{d^5\sigma^+ - d^5\sigma^-}{d^5\sigma^+ + d^5\sigma^-}. \tag{1.30}$$

where $d^5\sigma^+(d^5\sigma^-)$ is the photon electroproduction differential cross section for a positive (negative) beam helicity.

At leading twist, the beam-spin asymmetry (A_{LU}) with the two opposite helicities of a longitudinally-polarized electron beam (L) on a spin-zero target (U) can be written as:

$$\begin{aligned} A_{LU} \;=\; & \frac{x_A(1+\varepsilon^2)^2}{y}\, s_1^{INT}\sin(\phi) \Bigg/ \Bigg[\sum_{n=0}^{n=2} c_n^{BH}\cos(n\phi) + \\ & \frac{x_A^2 t(1+\varepsilon^2)^2}{Q^2} P_1(\phi)P_2(\phi)\, c_0^{DVCS} + \frac{x_A(1+\varepsilon^2)^2}{y}\sum_{n=0}^{n=1} c_n^{INT}\cos(n\phi)\Bigg], \end{aligned} \tag{1.31}$$

where $c^{BH}_{n=0,1,2}$, c_0^{DVCS}, $c^{INT}_{n=0,1}$ and s_1^{INT} are the Fourier coefficients of the BH, the DVCS and the interference amplitudes, respectively, for a spin-zero target [82]. $\mathcal{P}_1(\phi)$ and $\mathcal{P}_2(\phi)$ are the BH propagators. The full expressions of these factors can be found in Appendix A.

A_{LU} can be rearranged as [88]:

$$A_{LU}(\phi) = \frac{\alpha_0(\phi)\,\Im m(\mathcal{H}_A)}{\alpha_1(\phi) + \alpha_2(\phi)\,\Re e(\mathcal{H}_A) + \alpha_3(\phi)\left(\Re e(\mathcal{H}_A)^2 + \Im m(\mathcal{H}_A)^2\right)} \tag{1.32}$$

where $\Im m(\mathcal{H}_A)$ and $\Re e(\mathcal{H}_A)$ are the imaginary and real parts of the CFF $\mathcal{H}_A$ associated to the GPD H_A. The α_i's are ϕ-dependent kinematical factors that depend on the nuclear form factor F_A and the independent variables Q^2, x_B and t. The exact expressions of the α_i's can be found in Appendix A. Using these factors, one can find in a model-independent way $\Im m(\mathcal{H}_A)$ and $\Re e(\mathcal{H}_A)$ from fitting the experimental A_{LU} as a function of ϕ for given values of Q^2, x_B and t.

1.4.2 Theoretical predictions

On-shell calculations

In the model based on the impulse approximation of V. Guzey *et al.* [89, 90], a nucleus is assumed to consist of non-relativistic non-interacting nucleons, and these nucleons interact independently with the probe. Therefore, the nuclear GPD H_A can be described as the sum of the individual nucleons' GPDs. Assuming that the nucleon GPDs H and E are the dominant GPDs in the unpolarized target scattering case, the nuclear GPD H_A for each quark flavor q can be written as:

$$\begin{aligned} H_A^q(x_A,\xi_A,t) = \frac{dx_N}{dx_A}\Bigg[& Z\left(H_p^q(x_N,\xi_N,t) + \frac{t}{4M^2}E_p^q(x_N,\xi_N,t)\right) \\ & + (A-Z)\left(H_n^q(x_N,\xi_N,t) + \frac{t}{4M^2}E_n^q(x_N,\xi_N,t)\right)\Bigg] F_A(t), \end{aligned} \tag{1.33}$$

where the factor dx_N/dx_A is the Jacobian for the transformation of x from the nucleonic x_N to the nuclear x_A. It is equal to $A(2-x_A)/(2-x_B)$ with $x_A = x_B/A$. For the free nucleons, the GPDs are constructed using the double distributions ansatz [91]. In this approximation, the GPD H with its evolution in Q^2, can be written as:

$$H^q(x,\xi,t,Q^2) = \int_0^1 d\beta \int_{-1+|\beta|}^{1+|\beta|} d\alpha \delta(\beta+\alpha\xi-x)\pi(\beta,\alpha)\beta^{-\alpha'(1-\beta)t} q_v(\beta,Q^2), \tag{1.34}$$

where the parameters α and β are new variables that link x and ξ linearly as $x = \beta + \alpha\xi$, q_v is the valence unpolarized PDF and the profile function $\pi(\beta,\alpha)$ takes the form

$$\pi(\beta,\alpha) = \frac{3}{4}\frac{(1-\beta)^2-\alpha^2}{(1-\beta)^3}. \tag{1.35}$$

The t-dependence of the GPD is introduced through Regge ansatz [66], with the slope α' equal to 1.105 GeV^{-2} that allows to recover the ordinary form factors of the nucleons.

This model enables to link the nuclear CFFs to the ones of the nucleons. However, it neglects the medium modifications and the binding effects between the nucleons in a nucleus. To take into account the nuclear modifications, the bound nucleons can be assumed to be modified in proportion to the corresponding bound nucleon elastic form factors [92]. That is, the GPD H of the bound proton ($H^{q/p*}$) can be written as:

$$H^{q/p*}(x,\xi,t,Q^2) = \frac{F_1^{p*}}{F_1^p} H^{q/p}(x,\xi,t,Q^2), \tag{1.36}$$

where F_1^p (F_1^{p*}) is the Dirac form factor of the free (bound) proton. The bound nucleon form factor is calculated using the Quark-Meson Coupling (QMC) model [93], which predicts a suppression of the bound nucleon electromagnetic form factors (relative to those in free nucleon) as the nuclear density increases. As a result of these calculations, figure 1.26 shows the ratio of the bound (incoherent DVCS channel off ^{4}He) to free proton beam-spin asymmetry (A_{LU}), at ϕ = 90°, as a function of x_B, using a 6-GeV longitudinally-polarized electron beam at Q^2= 2 GeV^2/c^2 and two values of the transfer momentum t. This ratio represents a generalization of the EMC effect, for t greater than zero. This model predicts an enhancement of the bound-proton beam-spin asymmetry, which increases with t.

Off-shell calculations

Another model for nuclear GPDs in the impulse approximation uses the nuclear spectral function. For a spin-zero nucleus, the GPD H^A can be written as [79]:

$$H^A(x,\xi,t) = \sum_N \int \frac{d^2P_\perp dY}{2(2\pi)^3} \frac{1}{A-Y} \mathcal{A}\rho^A(P^2,P'^2) \times \sqrt{\frac{Y-\xi}{Y}} \left[H^N_{OFF}(\frac{x}{Y},\frac{\xi}{Y},P^2,t) - \frac{1}{4}\frac{(\xi/Y)^2}{1-\xi/Y} E^N_{OFF}(\frac{x}{Y},\frac{\xi}{Y},P^2,t) \right] \tag{1.37}$$

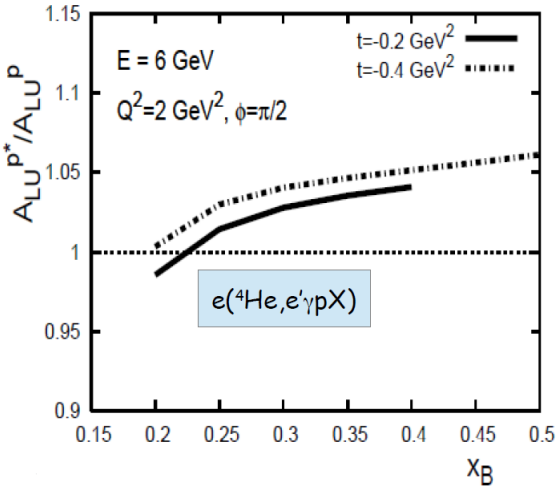

Figure 1.26: The theoretical predictions by V. Guzey [92] for the "generalized" EMC effect in terms of the beam-spin asymmetry ratio between the bound proton in ^{4}He and the free proton as a function of Björken variable x_B. The calculations are performed at two values of $-t$, 0.2 and 0.4 2 GeV^2/c^2, with a 6 GeV electron beam and Q^2 = 2 GeV^2/c^2.

where P and P' are the incoming and outgoing nucleons three-momenta, Y is a dynamical variable defined as $\frac{y+A\xi}{1+\xi}$, $\mathcal{A} = (Y-\xi/2)(\sqrt{Y(Y-\xi)})$ is a normalization factor, $\rho^A(P^2, P'^2)$ is the off-forward nuclear spectral function accounting for all configurations of the final nuclear system and the binding effects between the nucleons. In a non-relativistic approximation, ρ^A is defined as [94]:

$$\rho^A(P^2, P'^2) = 2\pi M_A \int dP\, P\, \Phi(P)\, \Phi(P') \tag{1.38}$$

with Φ is the (Fourier transformed) overlap integral between the initial and final nuclear wave functions. The off-forward nucleon GPDs, H^N_{OFF} and E^N_{OFF}, are characterized by the off-shellness which is linked to P^2. One recovers the free nucleon GPDs by disregarding this off-shellness.

The nuclear effects can be expressed with the ratio between the nuclear and the nucleon GPDs. This ratio becomes equal to the ordinary EMC ratio in the forward limit ($t = 0$). As the nuclear form factor of the ^{4}He has a steeper drop in t than the nucleonic one, it is more convenient to define the ratio between normalized GPDs as:

$$R_A(x, \xi, t) = \frac{H^A(x, \xi, t)/F^A(t)}{H^p(x, \xi, t)/F^1_p(t)} \tag{1.39}$$

where $F^1_p(t)$ is the Dirac form factor of the proton. Figure 1.27 shows the EMC ratios measured via DIS on ^{4}He compared to theoretical calculations. One can see that the latter calculations by S. Liuti and K. Taneja describe the EMC effect differently than the first scenario due to the off-shell effects of the nucleons associated in their calculation.

The nuclear effects can be also viewed as the beam-spin asymmetry ratio ($\frac{A^{Incoh}_{LU}}{A^p_{LU}}$) between the incoherent proton and the free proton. Figure 1.28 shows the predicted EMC effect in ^{4}He in terms of $\frac{A^{Incoh}_{LU}}{A^p_{LU}}$ as a function of x_B. The calculated ratio appears to be very sensitive on t, which encodes the information on the transverse degrees of freedom of the partons in the nucleon.

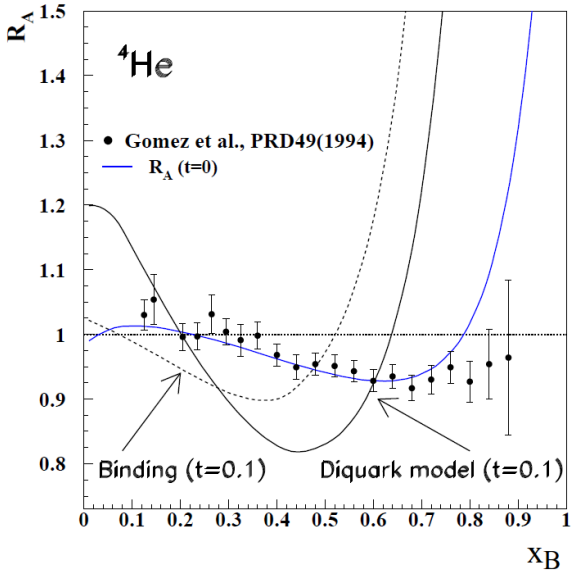

Figure 1.27: The EMC effect in ^{4}He. The data points are the ^{4}He EMC ratios [95]. The black dotted and solid curves are theoretical calculations based on a binding and a diquark model respectively, at $-t$= 0.1 GeV^2/c^2. The blue curve shows the theoretical calculation at the forward limit by Liuti and Taneja [79].

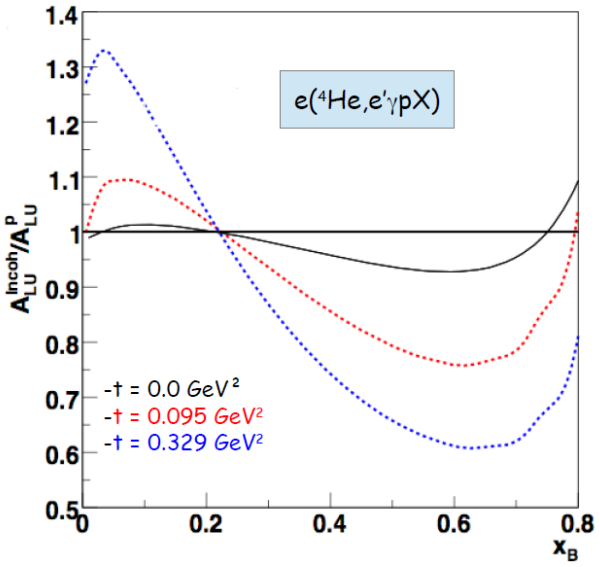

Figure 1.28: The theoretical calculations by S. Liuti and K. Taneja [79] of the beam-spin asymmetry ratio between the bound proton, in ^{4}He, and the free proton. The ratio is plotted as a function of x at three different values of $-t$: 0, 0.095, and 0.329 GeV^2/c^2.

We conclude that nuclear DVCS is a promising field that can give more details about the nature of the nuclear forces through the study of the nuclear GPDs, and through the study of the modifications of the nucleons' GPDs in nuclei.

1.4.3 Nuclear DVCS measurements

The first nuclear DVCS experiments were carried out by the HERMES collaboration [96]. In these measurements, longitudinally-polarized electron and positron beams at energies equal to 27.6 GeV were scattered onto fixed nuclear targets (hydrogen, helium-4, nitrogen, neon, krypton and xenon) to study the DVCS reaction. The HERMES spectrometer did not detect the nuclear recoils. However, the exclusivity of the selected DVCS event were ensured by a cut on the missing mass of the final state configuration $e\gamma X$. The separation between the coherent and the incoherent DVCS channels was made with a cut on t: the coherent channel is assumed to dominate the low t-region, while the higher t-region is assumed to be dominated by the incoherent channel on the protons and the neutrons. Figure 1.29 shows the $\sin(\phi)$ amplitude of the beam-spin asymmetries off the different targets in t-bins measured by HERMES. These asymmetries are further separated into coherent and incoherent asymmetries. Figure 1.30 shows the mass dependence of the $\sin(\phi)$ amplitude of the coherent and the incoherent beam-spin asymmetries integrated over all the data sample for each target type.

The HERMES inclusive measurements of the nuclear beam-spin asymmetries clearly suffer from a lack of statistics for a precise investigation of their physics content. Within the given uncertainties, their nuclear beam-spin asymmetries have shown neither enhancement, nor a nuclear-mass dependence.

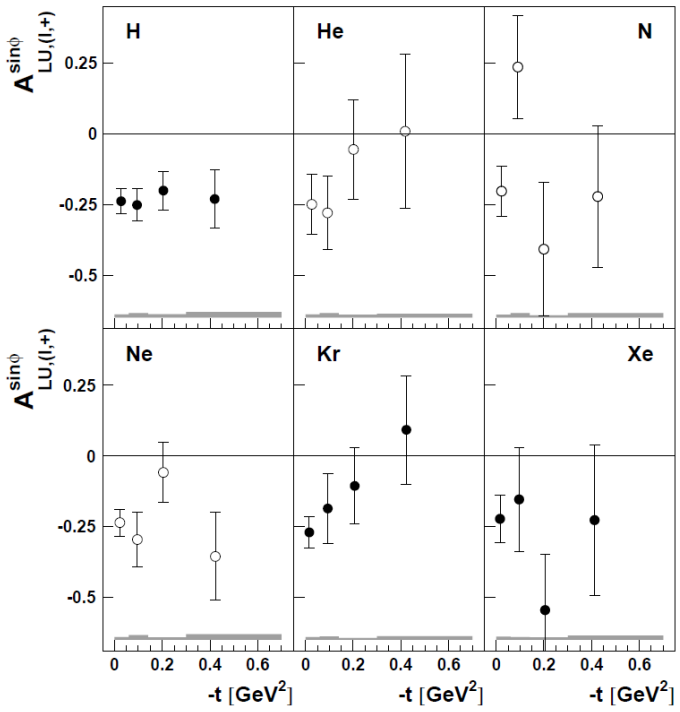

Figure 1.29: The t-dependence of the $\sin(\phi)$ amplitude of the beam-spin asymmetries measured by HERMES on different nuclear targets. The error bars show only the statistical uncertainties, while the systematic uncertainties are indicated by the bands on each plot. [96].

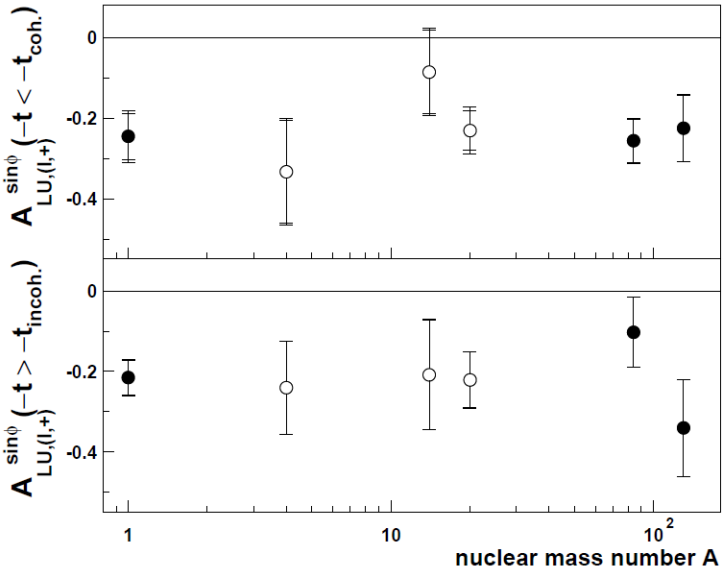

Figure 1.30: The nuclear-mass dependence of the $\sin(\phi)$ amplitude of the beam-spin asymmetries for the coherent (upper panel) and the incoherent (lower panel) data samples. The values of t_{coh} and t_{incoh} for each nuclear target were determined from Monte-Carlo simulations [96].

Chapter 2

Experimental setup

The experiment described in this thesis has been carried out in the Hall B of the Thomas Jefferson National Accelerator Facility (JLab), Virginia, USA. JLab, founded in 1984, was initially named Continuous Electron Beam Accelerator Facility (CEBAF). This research facility is dedicated to study the fundamental structure of nuclear matter. It provides electron beams, with energies up to 6 GeV and 100% duty cycle, to three experimental Halls (A, B and C) simultaneously. The Hall B houses the CEBAF Large Acceptance Spectrometer (CLAS) which is run by a collaboration of 44 universities and research institutes from 11 countries. Our experiment was performed in 2009 with a longitudinally-polarized electron beam of 6.064 GeV scattering onto a gaseous ^4He target to study the nuclear medium modifications of parton distributions using the DVCS off the ^4He target. To ensure the exclusivity of our reaction, the basic setup of CLAS was upgraded with a Radial Time Projection Chamber (RTPC) to detect the low-energy recoil nuclei, an additional calorimeter (IC) to detect the energetic forward-emitted real photons, and a solenoid magnet to minimize the effects of Møller electrons. In this chapter, the experimental apparatus and the working principle of each sub-detector will be presented.

2.1 CEBAF

CEBAF (shown in figure 2.1) consists of a polarized-electrons injector, two linear accelerators (linacs) connected by circulating arcs. The beam can be delivered to three experimental Halls, A, B and C. The injector produces 67 MeV polarized electrons using a polarized photocathode gun. Then, these electrons are injected into the north linac to be accelerated. Each linac contains 20 cryomodules with an accelerating gradient that varies from 5 MeV/m to 7 MeV/m depending on the desired beam energy. After five successive orbits, the initially injected electrons reach energies up to 6 GeV and polarizations up to 85%. The linacs' radio-frequency system chops the 1497 MHz beam into 2 ns intervals. Thus, each experimental Hall receives electron bunches at a frequency of 499 MHz.

Each experimental Hall of JLab has its own characteristics. Hall A was designed to achieve a luminosity of several $10^{38} cm^{-2} s^{-1}$ using two identical High-Resolution Spectrometers (HRS). Each HRS covers 120 mrad vertically and rotates horizontally from 12.5° to 150° with respect to the beam line. So in principle, one can cover a large horizontal acceptance, but only 60 mrad at a time [97]. Hall C is achieving the same luminosity as Hall A using two spectrometers. One is optimized to detect high-momentum particles and the other one detects relatively lower energy particles. Each spectrometer covers ±75 mrad (±35 mrad) in term of the vertical (horizontal) angular acceptance at each position. Each spectrometer can rotate on rails around the target extending the horizontal acceptance from 12.5° to 90° with respect to the beam line [98]. Hall B can reach a luminosity of the order of $10^{34} cm^{-2} s^{-1}$ with its 4π CLAS detector [99]. In the following, we present the basic apparatus of CLAS and the upgrades made for the DVCS experiment, which is the subject of this thesis.

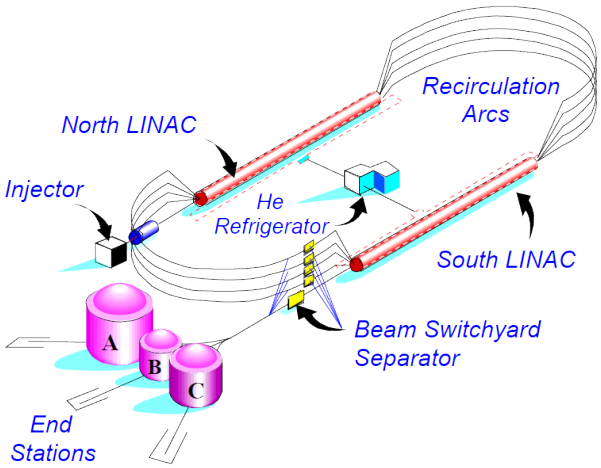

Figure 2.1: Schematic layout of CEBAF with the three experimental halls (A, B and C).

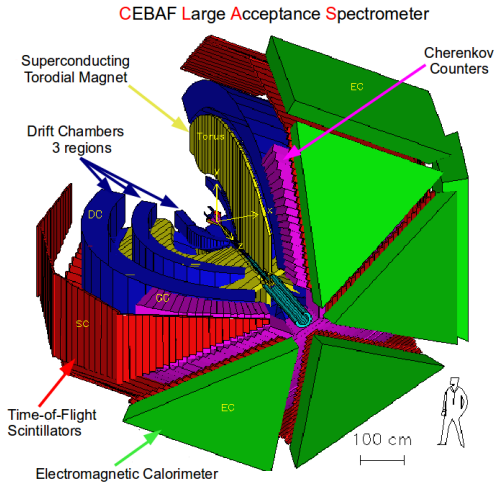

Figure 2.2: Three dimensional representation of the basic apparatus of CLAS detector in the Hall B. The subdetectors are indicated.

2.2 CLAS detector

CLAS was designed to use electron and tagged-photon beams scattering onto fixed targets. It was initially designed to achieve a continuous recording rate up to 2 kHz. The continuous development of the CLAS's data acquisition system has resulted in the recording of rates up to 4 kHz by the beginning of the year 2000 [99]. The basic setup of CLAS is shown in figure 2.2. It is composed of three regions of Drift Chambers (DCs) for the tracking of charged particles, of a superconducting torus magnet which provides a tracking by bending the particle trajectories, of Cherenkov Counters (CCs) to separate electrons from negative pions, of Scintillation Counters (SCs) to identify charged hadrons by measuring their Time Of Flight (TOF) and of forward Electromagnetic Calorimeters (ECs) to measure the energies of electrons and photons, and to detect neutrons. In the following subsections, the design and working principle of each sub-detector are presented.

2.2.1 Superconducting torus magnet

The heart of the CLAS tracking system is a toroidal magnetic field that enables the detection of charged particles with momenta greater than 250 MeV/c. The toroidal field is generated by six superconducting coils, each is about 10 m in perimeter and 5 m in length, surrounding the beam-line. The magnetic field has mainly azimuthal components, therefore the trajectories are bent towards or away from the beam direction leaving the azimuth unchanged. Figure 2.3 shows a schematic view of the torus, and figure 2.4 shows the contours of the value of the magnetic field in the mid-plane between two adjacent coils. The structure of the torus divides the whole CLAS detector into six independent sectors containing the same sub-detectors (DCs, CCs, SCs and ECs).

2.2.2 Drift chambers

The tracking of charged particles in CLAS is dealt with Drift Chambers (DCs). The DCs cover polar angles from 8° to 154° with ∼80% coverage of the azimuth (polar-angle dependent). As mentioned in the previous section, the torus structure divides CLAS into six azimuthal sectors. In each sector, the DCs are divided radially into three regions (R1, R2 and R3), as can be seen in

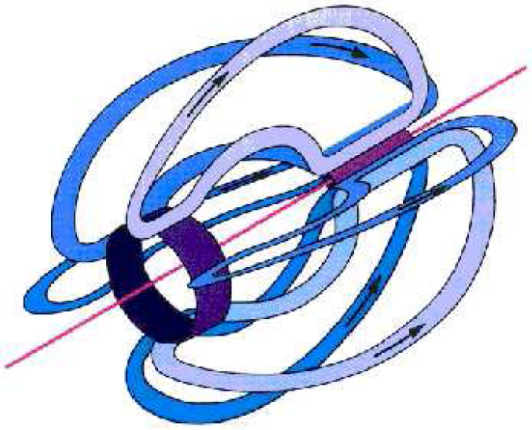

Figure 2.3: A schematic drawing of CLAS's torus magnet.

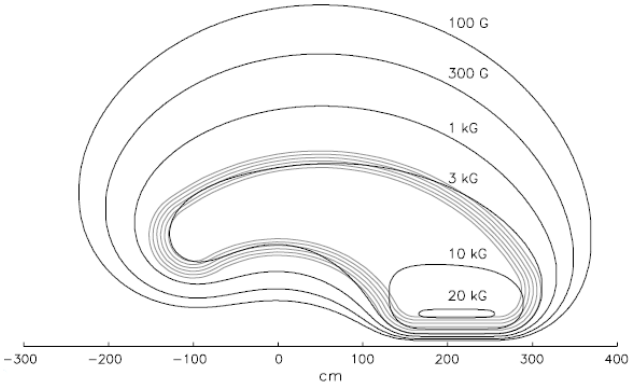

Figure 2.4: The contours of constant magnetic field in the mid-plane between each adjacent two coils.

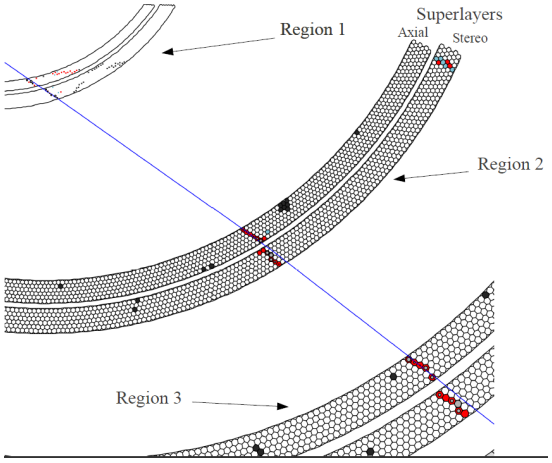

Figure 2.5: A schematic view of the three DCs regions of CLAS. The wire layers in each region are grouped into two super-layers; one is axial to the magnetic field and the other is tilted at a 6° stereo angle.

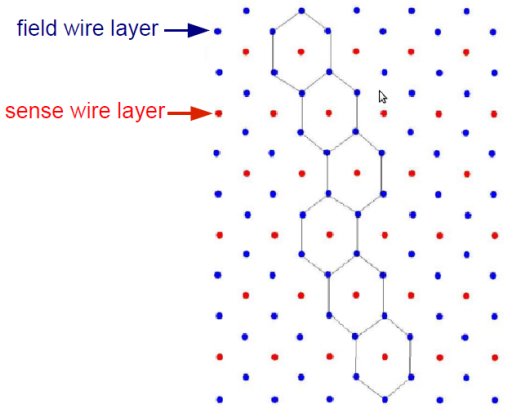

Figure 2.6: The hexagonal drift cells of the DCs. The perimeters of the hexagons are drawn to outline each cell. In this scheme, the highlighted cells are representing fired cells when a charged particle is passing though this portion of the drift chambers.

figure 2.2 and figure 2.5. The three regions share the same material and wedge-like shapes, but they are subject to different strengths of magnetic field, and their sizes increase radially. The R1 chambers surround the target in a low-field region, the R2 chambers are located between the coils of the torus, with the highest field, and the R3 chambers are placed in a relatively low-field region.

The DCs are constructed from two types of wires: sense and field wires. The sense wires are 20-μm-diameter gold-plated tungsten, and are brought to a positive potential, while the field wires are 140-μm-diameter gold-plated aluminium, and are connected to a negative potential. These wires are arranged to form layers of hexagonal drift cells, as can be seen in figure 2.6. The layers are grouped to form two super-layers in each region (R1, R2 and R3): one is co-axial with the magnetic field and the other is tilted at a 6° stereo angle providing azimuthal information. The number and the size of the cells in each drift region increase uniformly with increasing radial distance from the beam line. All the layers are placed in a 90% argon-10% CO_2 gas

mixture, providing a good tracking efficiency (>95%), adequate resolutions and reasonably short collection times, in order to reduce the random signals coming from target-generated Møller electrons and X-rays.

The tracking procedure within the DCs is performed in two steps: Hit-Based Tracking (HBT) and Time-Based Tracking (TBT). In the HBT, groups of continuous hits in each super-layer are recognized and a track segment from each group is constructed. Then, the segments from the individual super-layers are linked using a look-up table to obtain an initial estimation of the track by taking into account the magnetic field. Within the TBT step, the Distances Of Closest Approach (DOCA) are calculated from the measured drift times of the hits, and compared to the initial track. Finally, a minimization procedure (χ^2 minimization) between the DOCA and the initial track gives the final parametrization of the track to be refitted.

Regarding the tracking resolution, the DCs' design keeps small tracking uncertainties. However, some sources increase the uncertainties, such as, non-ideal knowledge of the true magnetic field and slight geometric misalignments of the chambers. Even with these challenges, the DCs have a fractional momentum resolution between 1% and 1.5% at 1 GeV/c momenta. Regarding the angular resolutions, a 1 mrad (4 mrad) resolution has been achieved in the measured polar (azimuthal) angles. For detailed design and efficiency studies, the reader can refer to [100].

2.2.3 Cherenkov counters

The CLAS detector has 6 gas Cherenkov Counters (CCs), corresponding to the six sectors. These detectors serve a dual function: triggering on electrons for electron-scattering experiments, and separating electrons from negative pions. Their work principle is based on the emission of Cherenkov light when a charged particle moves with a speed greater than the speed of light. This is achieved when high-energy particles move in a medium having refraction index greater than one. The C_4F_{10} (perfluorobutane) was chosen as the radiator gas for its high index of refraction (n = 1.00153). This gas provides a high photon yield and a pion momentum threshold of 2.5 GeV/c.

In CLAS, the CCs are placed behind the third region of the drift chambers, as can be seen in figure 2.2. They cover polar angles up to 45°, and 80% of the azimuthal angles. Figure 2.7 shows a schematic view of the CCs for one sector of CLAS. Due to the size variation of each

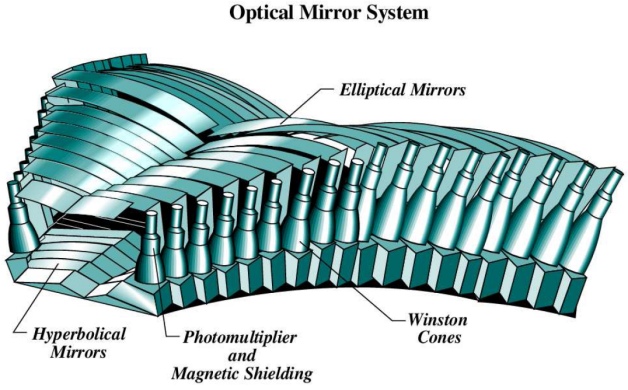

Figure 2.7: A schematic view of the CCs in one sector of CLAS.

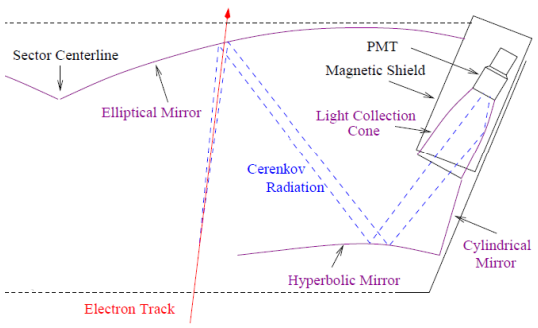

Figure 2.8: One Cherenkov counter with a typical electron track crossing the radiator gas producing photo-electrons.

sector in θ, each CCs system is divided into 18 regions in θ, with two light collecting modules in each region. In this configuration, CLAS has 216 modules (6 (sectors) $\times$ 18 (regions in θ) $\times$ 2 (modules in ϕ)). Figure 2.8 shows the structure of one CC. It is made up of a mirror system which focuses the emitted light onto Photo-Multiplier Tubes (PMTs). The PMTs are located in the fringe field region of the toroidal coils. They are surrounded with high permeability magnetic shields. Figure 2.8 shows a schematic drawing of a typical electron track crossing the medium. It emits photons which are focused by the mirrors before being collected by the PMT.

In Reference [101], the efficiency of the CCs is studied through the measured photoelectrons yield. In the fiducial regions of the the CCs, which are defined by the edges of the mirrors, the efficiency is greater than 98%. Outside the fiducial regions, such as the sector's center-line region where the gap between the mirrors is large, the efficiency has very strong variation. Thus the events with electrons outside the fiducial regions have to be excluded from the analysis.

2.2.4 Time-of-flight scintillation counters

The DCs track the charged particles, allowing to measure their momenta. In order to separate hadrons (pions, kaons and protons) experimentally, one needs to determine their masses. This can be achieved by measuring their velocities with a time resolution better than 300 ps, to distinguish between hadrons with momenta up to 2.5 GeV/c. CLAS is supplied with six identical Time-Of-Flight (TOF) scintillation systems. Figure 2.9 shows a schematic view of the TOF system in a sector of CLAS. The TOF systems are placed after the CCs, as shown in figure 2.2, and cover polar angles from 8° to 145°.

Each TOF system consists of 57 Bicron BC-408 scintillator strips. They share the same thickness of 5.08 cm, but they have different lengths and widths depending on their positions. The length of the strips varies from 30 cm to 450 cm and the width of the first 23 and the last four is 15 cm, while the remaining ones are 22 cm wide. At the ends of each scintillator strip, two light guides with two PMTs are attached, to read signals. The PMTs are shielded from the magnetic field of CLAS. The configuration with two PMTs per strip enables position reconstruction via the time difference between the two signals. The reconstructed position is required to associate a TOF hit to the proper track as measured by the DCs.

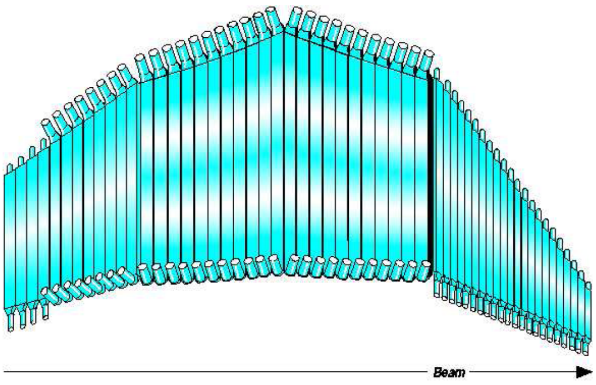

Figure 2.9: A schematic drawing of the Time-of-flight system in one sector of CLAS. Each sector has 57 scintillator strips with two light guides and two PMTs at the ends of each strip.

The average distance of flight from the target to the TOF scintillators is 474 cm. Thus, the time of flight difference between pions and kaons at 1 GeV/c is 1.67 ns, while the difference between pions and protons at the same momenta is 5.72 ns. The CLAS TOF systems provide an adequate timing resolution that varies from 120 ps (in the forward scintillator strips) to 250 ps (in the strips at polar angles greater than 90°). More details about the structure of the strips, light guides, PMTs, readout system and resolution studies can be found in [102].

2.2.5 Electromagnetic calorimeters

The outermost sub-detectors of CLAS are six independent forward Electromagnetic Calorimeters (ECs), drawn in green in figure 2.2. They have the same triangular shape, 16 radiation lengths of thickness, basic structure elements (lead-scintillator strips), and they cover polar angles from 8° to 45°. The ECs serve the goal of detecting electrons at momenta above 500 MeV (and rejecting pions via their total deposited energy), detecting photons, at energies above 200 MeV (which enables π^0 and η reconstruction through their two-photons decay), and detecting the neutrons by measuring their time-of-flight [99]. Under these requirements, the ECs were designed to achieve the following criteria:

- Good electrons and photons fractional energy resolution ($\Delta E/E < 10\%$ at 1-GeV energy).
- Position resolution δr of about 2 cm at 1-GeV energy.
- Time-of-flight resolution around 1 ns, required to distinguish neutrons from photons at energies below 2.5 GeV.
- Reconstructed mass resolution of two-photons decays ($\Delta m/m$) less than 15%, which is needed to provide adequate π^0/η separation.
- Neutron detection efficiency greater than 50% at momenta greater than 1.5 GeV/c.

Each EC is made of 39 combined triangular layers divided into three oriented planes, each parallel to a side of the triangle (U, V and W), as shown in figure 2.10, to determine the hit position. Moreover, each module is divided into two independent regions (inner and outer) with a thickness ratio of 5:8 in order to give more detailed information on the total deposited energy, which is needed to perform the electron-pion discrimination. Each combined layer consists of a 10-mm-thick Bicron (BC412) scintillator followed by a 2.2-mm-thick lead sheet. Furthermore, each layer has 36 strips parallel to the orientation of each containing plane. All the facing strips of each oriented plane in each region (inner or outer) of each sector are connected via a fiber-optic light-readout system to transmit the light from the strip to a PMT. In this configuration, the six EC modules have 6 (number of EC modules) $\times$ 36 (number of strips/layer) $\times$ 3 (number of orientation planes) $\times$ 2 (number of regions per EC module) $=$ 1296 PMTs [103]. The area of the layers is increasing with the radial distance from the target in order to minimize the shower leakage at the edges.

The sampling fraction of the calorimeter is the ratio of the deposited energy in the scintillators (measured by the PMTs) to the real energy of the particle. With our layers combination, the sampling fraction has been estimated to be around one third. Thus the actual energies of the electrons and the photons are the measured ones divided by this fraction. Showering particles deposit energies proportionally to their momenta. On the other hand, the Minimum Ionizing Particles (MIPs), such as the pions, deposit a constant rate of energy per layer while crossing the EC. In our configuration, this rate has been estimated to be 2 MeV/layer. It was shown [103] that a 60-MeV cut on the measured deposited energy in the inner region of the EC removes a large

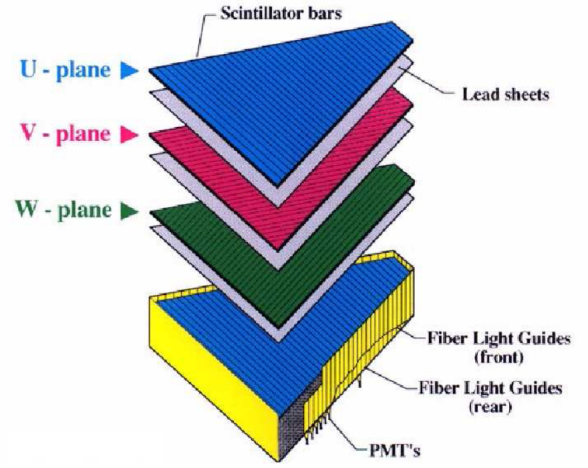

Figure 2.10: An illustrative view of one EC, showing the three planes U, V and W.

part of the negative pions which contaminate the electrons sample. This will be empathized in section 4.1.1.

Neutron detection in the EC primarily consists on the discrimination between photons and neutrons using the time-of-flight measurements for momenta up to 2.5 GeV/c. With the setup of CLAS, an efficiency of 50% neutron detection, at neutron-momentum greater than 1.5 GeV/c, was measured in the p(e,e$'\pi^+$)n reaction [104].

2.3 Inner calorimeter

In the basic setup of CLAS, the photons are detected by the forward electromagnetic calorimeters which cover polar angles from 8° to 45°. With a 6 GeV electron beam, a large part of the DVCS photons are produced at polar angles below 8°. In the CLAS-E1DVCS experiment (2005) [105], CLAS was upgraded with the addition of an Inner Calorimeter (IC). This calorimeter covers polar angles between 5° and 15°. Figure 2.11 shows a schematic plot of our experimental setup, CLAS-EG6 experiment. The front face of the IC is facing the downstream side of the Radial TPC (RTPC) and placed at 16 cm from the center of CLAS.

The IC is constructed from 424 lead-tungstate ($PbWO_4$) crystals. Each crystal is 16 cm long (corresponding to 17 radiation lengths) with a 1.33 $\times$ 1.33 cm^2 front surface and a 1.6 $\times$ 1.6 cm^2 back surface. The energy resolution is around 3% for photon energies between 2 GeV and 5 GeV and the angular resolution is between 3 to 5 mrad for the same energy range [106].

2.4 Solenoid

At occupancies greater than 4%, the efficiency of the drift chambers starts to drop and the resolution gets worse. The first region of the DCs (R1) has a higher occupancy than the other two regions (R2 and R3), mostly due to noise. This noise mainly comes from the Møller electrons, which are low-energy electrons produced in the scattering of the electron beam on the target's electrons. To reduce the effect of the noise, CLAS was upgraded by adding a solenoid that surrounds the target [105]. The magnet provides a nominal filed of 4.5 T at the center of the

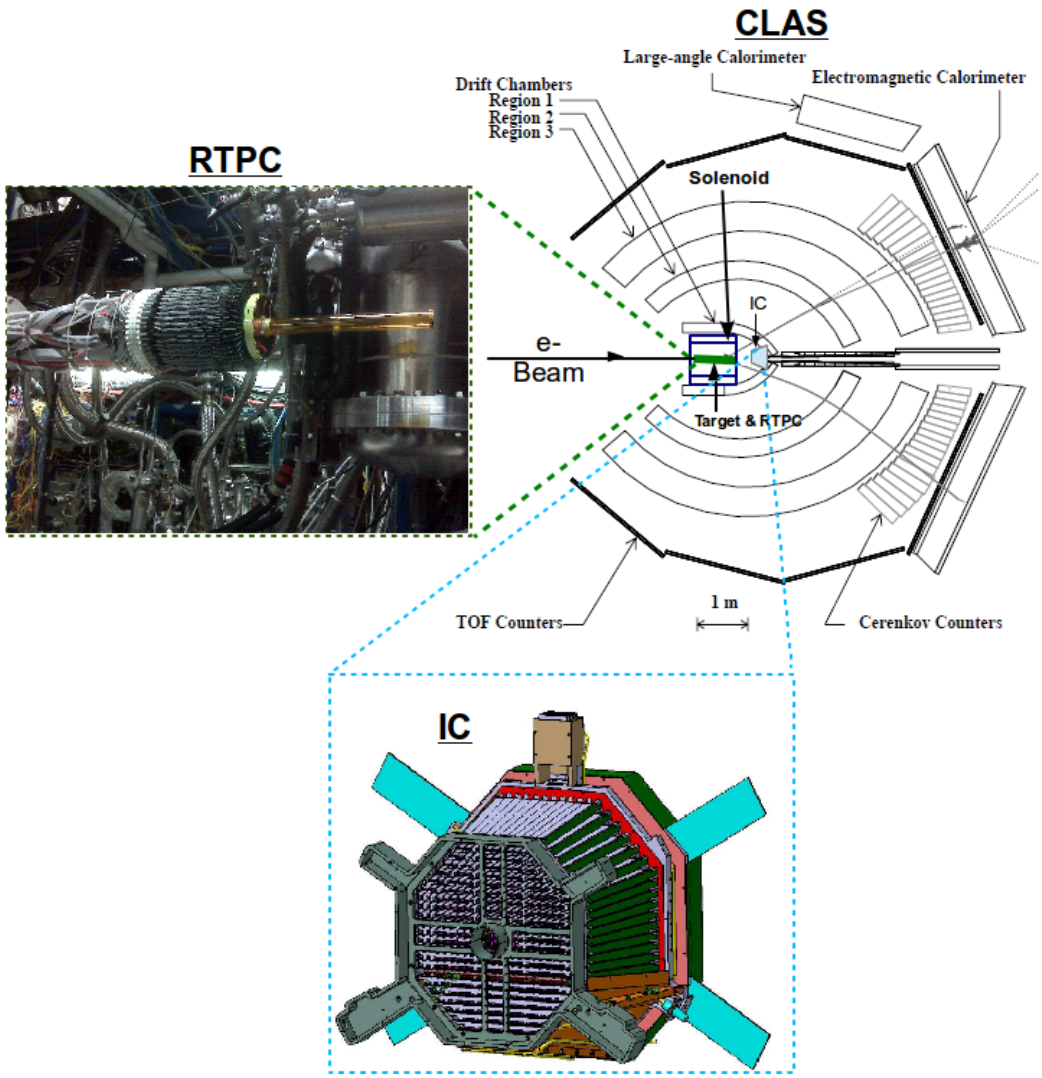

Figure 2.11: The CLAS-EG6 experimental setup in the y-z plane. The basic apparatus of CLAS is shown in the right top plot, a zoom on the IC is shown on the bottom plot, and a photo of the RTPC and the target are shown in the left top plot. The RTPC is surrounded by a solenoid (in blue). The grey lines indicate tracks of particles inside CLAS.

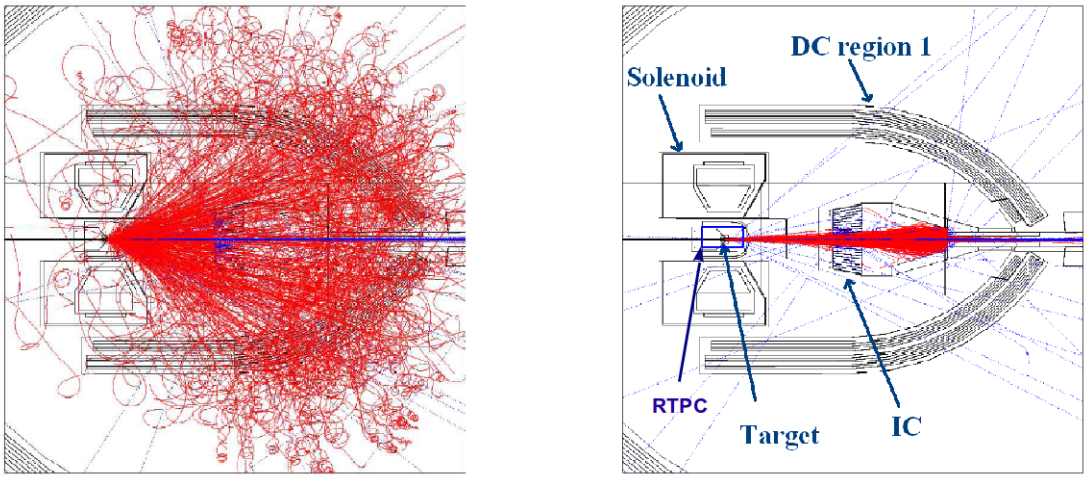

Figure 2.12: The tracks of the produced Møller electrons (in red) without applying the solenoid field (on the left) and with applying it (on the right) [106].

target. This solenoid deflects the produced Møller electrons to very forward angles preventing them from arriving to the first drift region. It also serves the purpose of shielding the IC from the Møller electrons. Figure 2.12 shows a GEANT3 simulation of the Møller electrons tracks without applying the solenoid field (left), and how these electrons are bent to small polar angles, less than 4°, when the solenoid field is applied (right).

2.5 Conclusion

CLAS detects charged particles with p/q greater than 250 MeV/c. With a 6-GeV electron beam, the momenta (over charge) of the recoiling ^4He nuclei range between 50 MeV/c and 300 MeV/c, which are undetectable with CLAS. To detect these low-energy recoils, the RTPC was added. The top-left plot of figure 2.11 shows a picture of the RTPC. The next chapter is dedicated to describe the structure, working principle, and calibration procedures of the RTPC.

Chapter 3

Radial time projection chamber

3.1 Introduction

The Time Projection Chambers (TPCs) were first introduced in 1976 by D.R. Nygren. They provide precise three-dimensional tracking of charged particles. Nowadays, the TPCs are widely used in physics experiments, such as high-energy physics (ALEPH, DELPHI, ...), heavy-ion physics (STAR, ALICE, ...) and rare-event searches (XENON, NEXT, ...) experiments. In the CLAS-EG6 experiment, a radial TPC has been built and used to detect low-energy nuclear recoils. This chapter presents the details of the structure, working principle and the calibration techniques of the RTPC.

3.2 The EG6 RTPC

The target of the CLAS-EG6 experiment is a 6-atm-pressure ^4He gas. At 6 GeV incident electron beam energy, the recoil ^4He nuclei, from the coherent DVCS channel, have an average momentum (per charge) around 100 MeV/c, while the "standard" CLAS detects charged particles with a threshold of 250 MeV/c. For detecting such low-energy recoils, a Radial TPC (RTPC) was added to CLAS.

In 2009, the CLAS-EG6 group [88] has built the RTPC with a design inspired from a previous experiment of CLAS, called BoNuS [107]. Figure 3.1 shows a close photo of the RTPC, while figure 3.2 shows a schematic drawing of its internal structure, taken on a plane perpendicular to the beam line. It is a 200 mm-long and 150 mm-diameter TPC, composed of two electronically separated modules, each covering about 150° of the azimuthal angle. Contrary to the BoNus detector, the detection volumes of the two modules of our RTPC are not separated. The RTPC tracks charged particles through the ionizations that they leave while traversing a gas-filled detection volume. The ionized electrons drift under the effect of an electric field, they are amplified by a gas electron multiplier system, and they are detected on a collection system.

3.2.1 Design

The RTPC has the following substructure, from the beam axis to the exterior:

- The target extends along the RTPC's central z-axis, with a diameter of 6 mm. It is enclosed in a 27-μm-thick Kapton wall.
- The first gas gap extends from 3 mm to 20 mm radial distances. It is filled with ^4He gas at one atmospheric pressure. This region is swarmed with Møller electrons induced by the beam, but filling this region with a light gas like ^4He at low pressure minimizes their secondary interactions, while the magnetic field of the solenoid keeps them away from the sensitive drift region. This gap is surrounded by a potentially grounded window made of 4-μm-thick aluminized mylar.

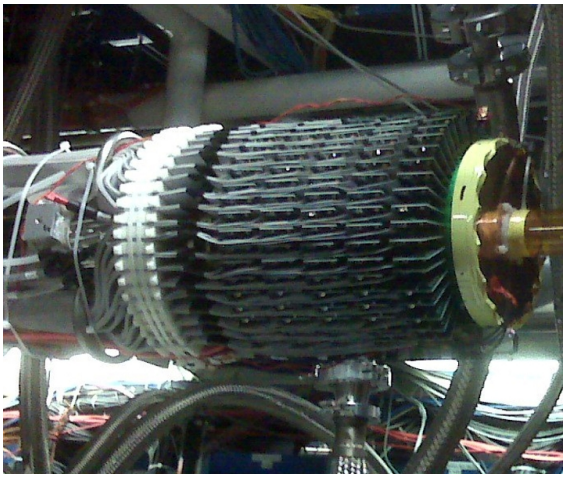

Figure 3.1: A view of the RTPC before insertion into the solenoid. The incident electron beam comes from the left.

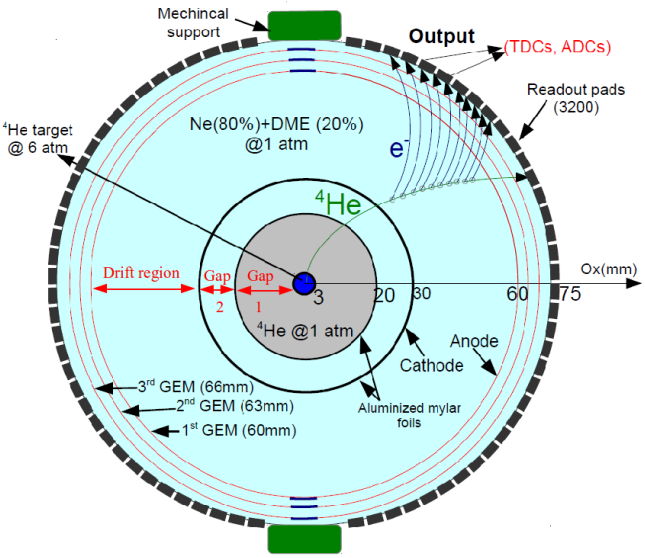

Figure 3.2: A cross section of the RTPC taken on a plane perpendicular to the beam line, with a typical ^4He track crossing the drift volume.

- The second gas gap extends from 20 mm to 30 mm radial distances and is filled with a gas mixture of 80% Neon(Ne) and 20% Dimethyl Ether(DME: C_2H_6O). This drift gas fills all the regions, starting from the inner side of this gap to the external shell.
- The cathode foil, which is made of 4-μm-thick aluminized mylar, surrounds the second gas gap. It is connected to a voltage of 4.3 kV to generate an electric field in the drift region.
- The drift region is filled with the Ne-DME gas mixture. It extends from the cathode, 30 mm from the beam line, to the first gas electron multiplier layer, 60 mm from the beam line.
- The amplification system is composed of three Gas Electron Multiplier (GEM) layers located at radii of 60 mm, 63 mm, and 66 mm. In this configuration, the first GEM layer represents the anode.
- The electron collection system has an internal radius of 69 mm and collects the charges. The data are then pre-amplified and transmitted to the data acquisition system.

The Ne-DME gas mixture has been chosen as the drift gas because of its low-diffusion characteristics and small Lorentz angles (the angles between the drift direction of electrons under the influence of magnetic field and the direction of the electric field). These characteristics minimize the changes in the drift velocity of the ionization electrons [108].

The GEMs amplify the ionized electrons to produce measurable signals. Figure 3.3 shows a microscopic photo of a GEM. It is made from an insulator (Kapton) sandwiched between two copper layers. The mesh of each GEM layer is chemically etched with 50-μm-diameter holes in double-conical cross section shapes, as can be seen from the schematic plot on the right.

The electrons amplification is achieved through the holes via the strong electric field, that is generated by a 400-V potential difference between the two copper layers. Such a strong

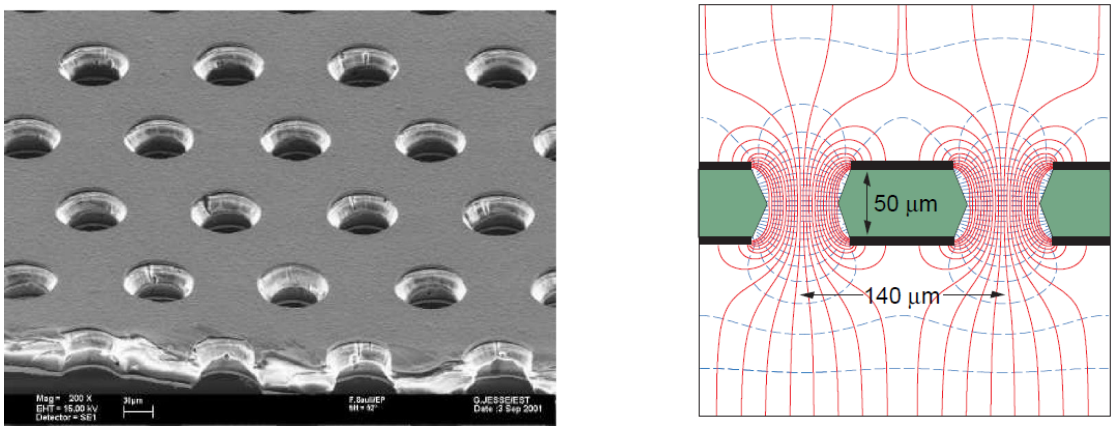

Figure 3.3: On the left: A microscopic image of a GEM shows the amplification holes, and the two copper layers, separated by a Kapton insulator. This figure is from [109]. On the right: Schematic of the hole structure in the GEMs with the electric field lines (solid red) and the equipotentials (dashed blue). This figure is from [110].

field leads to high ionization by the initial electrons and therefore amplification of the signals. Furthermore, an additional potential difference of 150 V is set between each two successive GEM layers to push the amplified electrons towards the readout board. In this configuration, the three GEM layers have an overall gain of the order of 10^6.

The RTPC electron collection system has 3200 readout pads. Each module of the RTPC has 40 rows and 40 columns of readout pads, each is 5 mm long and 4.45 mm wide. Each group of 16 pads is connected to a pre-amplifier that carries the recorded signals' information to the acquisition electronics. There are 20 rows and 5 columns of pre-amplifiers per module. This readout system records the charge information in time bins. The charge is measured in Analog-to-Digital-Converter (ADC) units, while the time bins are in Time-to-Digital-Converter (TDC) units, each TDC is equal to 114 ns, and indicates the time taken by the electron to drift from the ionization point along a particle's trajectory to the readout board.

3.2.2 Working principle

When a charged particle traverses a gas, it ionizes the gas-atoms along its trajectory. In a TPC, the electrons released in the ionization drift towards the readout board under the effect of an applied electric field. The drift velocity depends on the gas mixture, and on the electric ($\vec{E}$) and magnetic ($\vec{B}$) fields. The recorded time of the electrons provides information on how far the initial ionizations happened in the drift region, leading to reconstruct the original points of ionization, while the recorded ADCs give the deposited energy.

In our TPC the cathode and the anode are two cylinders. Thus, the generated $\vec{E}$ field in the drift region has a purely radial components, perpendicular to the beam line, with a magnitude around 500 V/cm. However, the two-cylinders configuration produces small gradient components at the sides of the RTPC. This issue was solved by installing field cages at the ends of the RTPC to keep a regular $\vec{E}$ field.

The $\vec{B}$ field is generated by the solenoid. Figure 3.4 shows the magnetic field vectors in

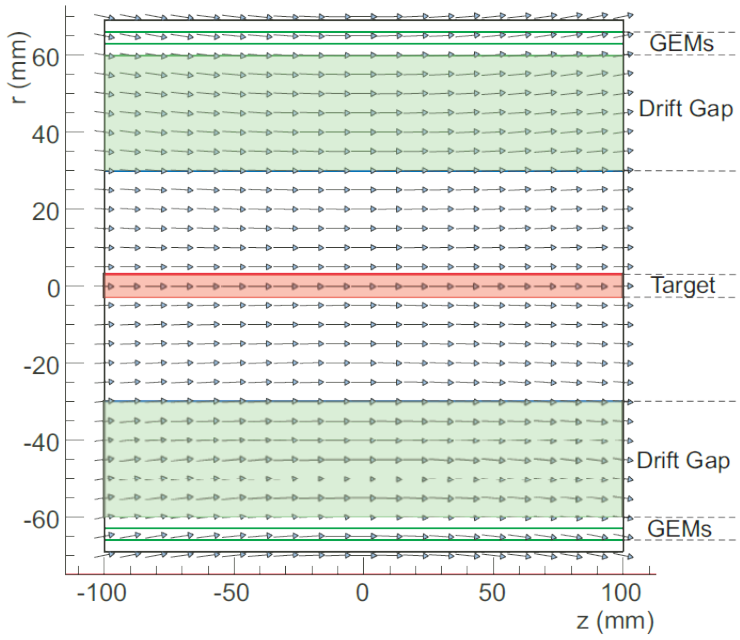

Figure 3.4: The solenoid magnetic field vectors in the RTPC, shown in the $r-z$ plane, where r is the radial distance from the central axis and z represents the longitudinal distance along the RTPC.

the different regions of the RTPC. The presence of the magnetic field enables us to deduce the momentum of a charged particle from the curvature of its track and the known magnetic field.

3.2.3 Track reconstruction

In order to reconstruct tracks we must first select the good hits. The first step is the rejection of out-of-time hits and the noise reduction, as will be explained in section 3.3.5. The second step is the spatial reconstructing of the hits, using the extracted drift speed and drift paths. For each registered hit, the position of the initial ionization is obtained from the recorded time (TDC) and from the position of its pad. In the third step, the reconstructed nearby hits are linked together in chains. The maximum distance between two adjacent hits must be less than 10.5 mm to chain them. Then, the number of hits per chain is required to be greater than 10 hits in order to proceed to the fitting step.

A fit to a chain of hits is performed in two iterations. In the first iteration, the hits of the chain are fitted with a helix. The helix fit is based on a circle fit in the $x-y$ plane followed by a linear fit in the $s-z$ plane for the hits of the chain, where $s=\sqrt{x^2+y^2}$. In the second iteration, the residual between the fit and each hit is calculated. If the hit's residual is greater than 5 mm, the hit is excluded from the chain. Then the hits are re-fitted with the same previous helix fit giving five final parameters for each track's chain. From these five parameters, one can reconstruct all the parameters of a track. For example, one can calculate the momentum (per charge) from the longitudinal component of the magnetic field ($\vec{B_z}$), the radius of curvature of the track (r_0) and

the polar angle (θ), like:

$$p_{tot} = \sqrt{p_{\parallel}^2 + p_{\perp}^2}, \quad \text{with } p_{\perp} = 0.3 \cdot B_z \cdot |r_0| \text{and } p_{\parallel} = p_{\perp}/tan(\theta), \tag{3.1}$$

where the unit of p is GeV/c, B_z is Tesla (T) and r_0 is meters (m). For example, In a magnetic field of 4.5 T, the recoil ^{4}He nuclei from DVCS (elastic) reaction have kinetic energies in the range [10, 25] ([17, 35]) MeV, from momenta of [260, 450] ([360, 550]) MeV and r_0 [20, 45] ([40,60]) mm.

3.3 RTPC calibration

Reconstructing a trajectory from the recorded time information of the electrons requires a good knowledge of their drift speed and drift paths. Also, the gains of the readout pads are required, to calculate $\frac{dE}{dx}$ from the recorded ADCs. In our experiment, the drift speed is parametrized using the good tracks detected in the RTPC during the experimental run period. The drift paths and the gain calibration of the RTPC require well identified events, and for this we use elastic scattering ($e^4He \rightarrow e^4He$). We use data from calibration runs with beam energies of 1.024 and 1.269 GeV. These runs were taken to enhance the cross section of the elastic process, which is highly suppressed at higher beam energy.

A GEANT4 simulation for the RTPC has been developed to help in extracting the drift paths and the gains. Their extractions are based on comparing the experimentally identified ^4He elastic tracks to the GEANT4 simulated ones. Indeed, the kinematics of each elastic ^4He is calculated from the electron measured in CLAS, and then it is simulated in GEANT4. The output of the simulation is finally compared with the actually measured signals. In the following subsections, we first present the selection of the RTPC tracks and the elastic events, then we detail the techniques of the calibrations.

3.3.1 Event selection

Figure 3.5 shows a drawing of a segment of the RTPC, in a plane perpendicular to the beam line. On this drawing, a ^4He track (in green) crosses the volume of the RTPC, producing a chain of ionization points within the drift gas. The released electrons follow the drift paths (in black) towards the readout board under the effect of the electromagnetic field between the anode and the cathode. The electrons released close to the cathode take the maximum drift time (TDC_{max}) to reach the readout pads, while the electrons released close to the anode take the minimum time (TDC_{min}), which is the trigger time (15 TDCs). In our convention, the distance between the first ionization point in the chain and the cathode is labelled as *sdist*, while the distance between the last point and the anode is labelled as *edist*.

Different levels of performances are observed between the two modules of the RTPC. This can be expected since they are electronically separated. For this reason, we will show their distributions separately. The right module of the RTPC covers the azimuthal angles between 90° and 270°, while the left-side module covers the rest of the azimuthal angles.

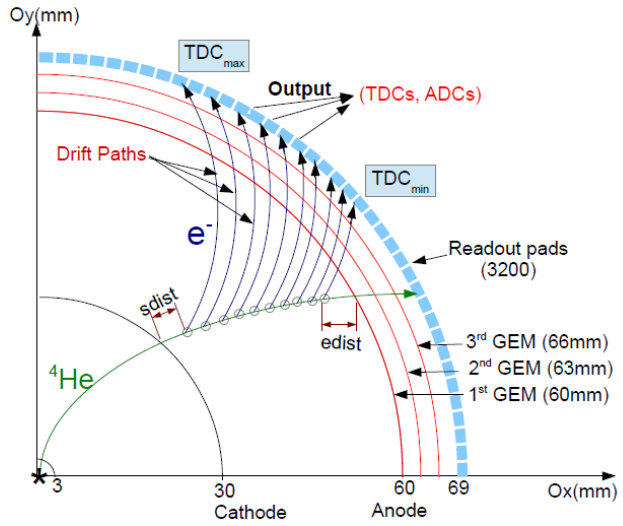

Figure 3.5: Schematic of a segment of the RTPC in a plane perpendicular to the beam line, with a ^4He track (in green) crossing the volume. See the text for description of the various elements and notations.

3.3.1.1 RTPC good track requirements

A good RTPC track passes the following requirements:

- The number of active pads is greater than 3: each track must have recorded hits from at least four different readout pads in order to be considered.

- Z-vertex cut (z $\in$ [-80,80] mm): we apply a cut on z-vertex of the reconstructed tracks to be within the RTPC, figure 3.6.

- Positive curvature ($r_0 > 0$): the ^4He is a positively charged nucleus and the reconstructed track in the RTPC must have positive curvature. In other words, it travels in a clockwise direction if one looks in the direction of the electron beam. The curvature distribution of the collected RTPC tracks is shown in figure 3.7.

- Helix-fit quality ($\chi^2 < 3.5$): each track in the RTPC is constructed from helix fitting an ionization chain. The quality of the fit (χ^2) is defined as:

$$\chi^2 = \frac{\sum_{i=1}^{N_{pts}} \frac{(r_i^{pt} - r_i^{helix})^2}{\sigma_r^2} + \frac{(\phi_i^{pt} - \phi_i^{helix})^2}{\sigma_\phi^2} + \frac{(z_i^{pt} - z_i^{helix})^2}{\sigma_z^2}}{N_{pts} - 4} \tag{3.2}$$

  where r_i^{pt}, ϕ_i^{pt}, z_i^{pt} are the radial, azimuthal, longitudinal coordinates of each hit "i". The coordinates of the closest point on the helix fit to the point i are r_i^{helix}, ϕ_i^{helix} and z_i^{helix}. σ_r, σ_ϕ, σ_z are the experimental observed resolutions, which are equal to 0.53 mm, 2° and 6 mm respectively. N_{pts} is the total number of the hits in the chain. Figure 3.8 shows the χ^2 distributions for the positive tracks which originate within the RTPC.

- *sdist* ($\in$ [-2.0,2.0] mm) and *edist* ($\in$ [-1,5] mm) cuts: the cuts are applied to ensure that a track is on time, i.e. that the first ionization point is close to the cathode and the last point is close to the anode. The *sdist* and *edist* distributions are shown in figures 3.9 and 3.10 respectively.

- Vertex correspondence: the track reconstructed in the RTPC has to originate from the same place as the electron that triggered the event. We define Δz as the difference between the electron z-vertex and the z-vertex of the RTPC track. Due to variations in the electric and the magnetic fields along the 200 cm of length of the RTPC, Δz shows a dependence on the longitudinal position along the RTPC (z_{RTPC}). This can be seen in figure 3.11. These distributions are fitted to extract the mean and the width of Δz as a function of z_{RTPC}. We will then apply a 2σ cut around the mean to select the RTPC good tracks. The parametrizations of the mean (μ) and the width (σ) of Δz can be found in Appendix B.

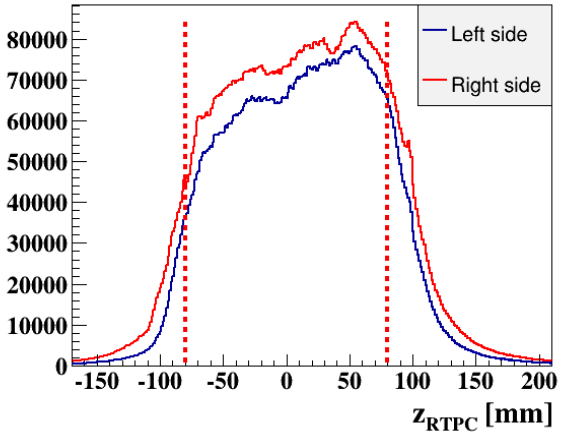

Figure 3.6: The z-vertex distributions for the reconstructed tracks in the RTPC.

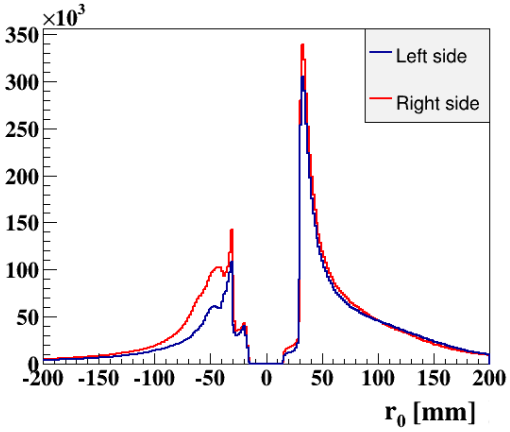

Figure 3.7: The radius of curvature of the reconstructed tracks in the RTPC.

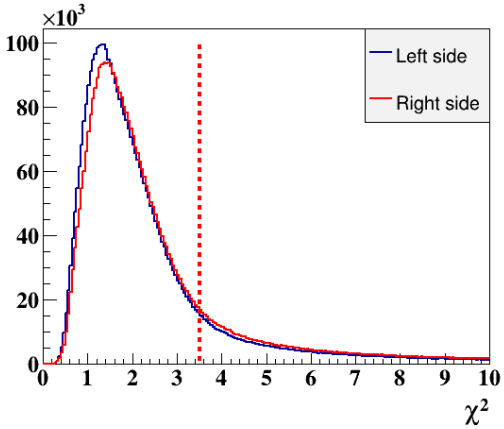

Figure 3.8: The χ^2 distribution for the positive tracks in the RTPC. The red line represents cut we apply to select good tracks.

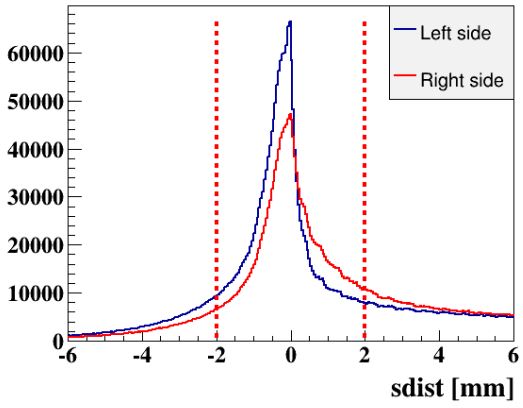

Figure 3.9: *sdist* distribution for the positive tracks in the RTPC. We set $|sdist| < 2.0$ mm to select good tracks.

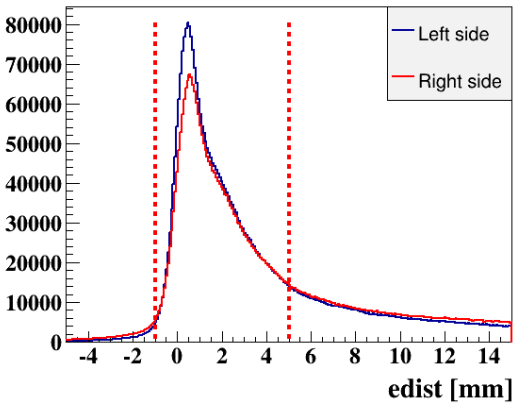

Figure 3.10: *edist* distribution for the positive tracks in the RTPC. We require -1.0 mm < *edist* < 5.0 mm to select the good tracks.

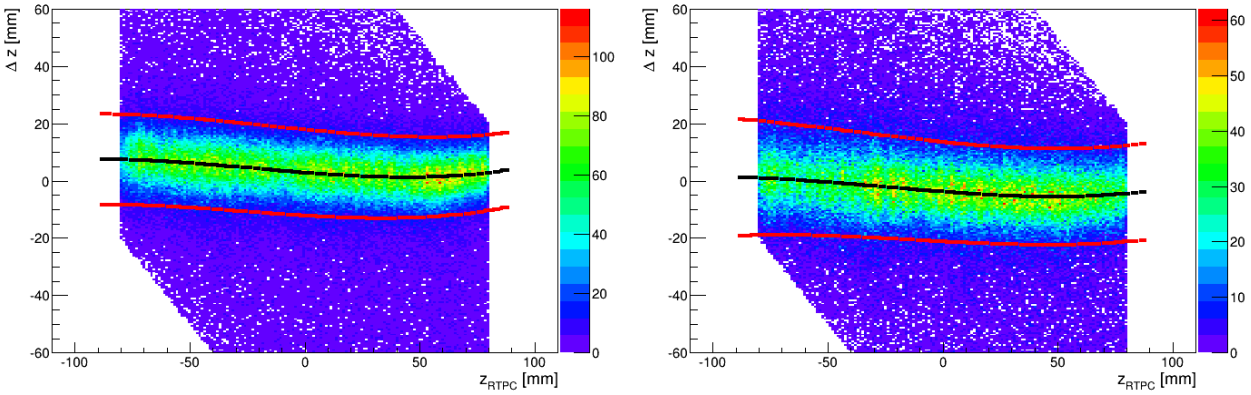

Figure 3.11: The Δz distribution versus the RTPC longitudinal position (z_{RTPC}) for the left and the right modules of the RTPC, respectively. The black lines represent the mean value of Δz as a function of z_{RTPC}, while the red lines are 2σ cuts around the mean.

3.3.1.2 Elastic selection

The elastic process on ^4He is defined as:

$$e(k) + ^4He(p) \rightarrow e(k') + ^4He(p') \tag{3.3}$$

with the symbols in parenthesis representing the four-momenta of the particles.

In addition to the previously good-track requirements, in order to select the elastic events we impose further constraints. The co-planarity between the scattered electron and the recoil ^4He is ensured using $\Delta\phi$ ($=\phi_e - \phi_{^4He}$) as shown in Figure 3.12. Like Δz, $\Delta\phi$ shows a dependence on z, so the same procedures adapted for Δz (finding the mean and the width as functions of z) are carried out for $\Delta\phi$. The resulting parametrizations can be found in Appendix B as well. We apply 2σ cuts (red lines) around the mean (black lines) of $\Delta\phi$ to select the elastic events.

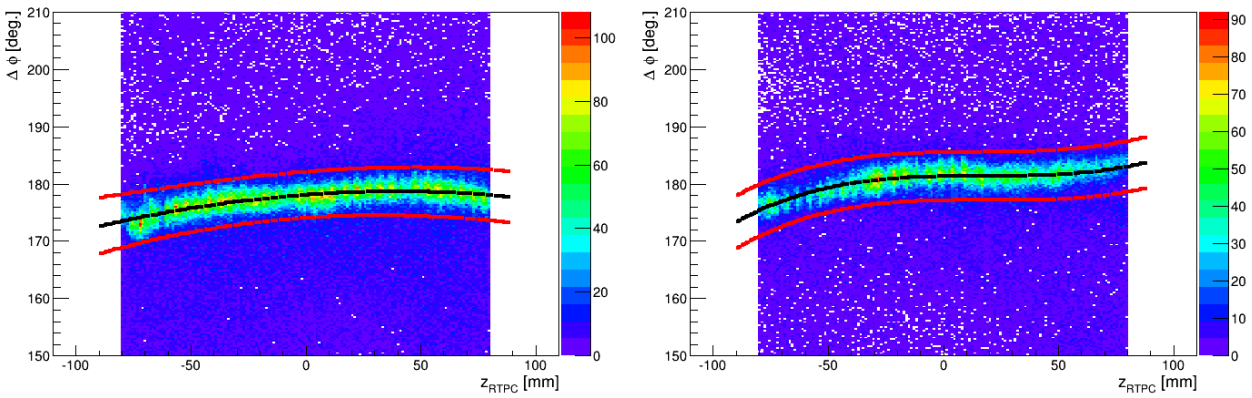

Figure 3.12: The distributions of $\Delta\phi$ as a function of z along the RTPC for the selected good tracks in the RTPC, for the two halves of the RTPC respectively. In each plot, the black line is the mean of $\Delta\phi$ and the red lines are 2σ cuts to select the elastic events.

An additional elastic cut is performed by comparing the measured ^4He polar angle to the calculated one, based on the measured electron in CLAS. Indeed, from momentum conservation the ^4He polar angle can be calculated as:

$$\theta_{cal}^{^4He} = sin^{-1}\left(\frac{p_{e'}}{p_{cal}^{^4He}} \cdot \sqrt{1 - cos^2\theta_{e'}}\right) \tag{3.4}$$

$$\text{with } p_{cal}^{^4He} = \sqrt{(E_b + M_{^4He} - p_{e'})^2 - M_{^4He}^2} \tag{3.5}$$

where $p_{e'}$ and $\theta_{e'}$ are the electron's measured momentum and polar angle, E_b is the beam energy and $M_{^4He}$ is the helium mass (3.727 GeV/c^2). Figure 3.13 shows the $\Delta\theta$ ($\theta_{cal}^{^4He}$ - $\theta_{meas}^{^4He}$) distribution versus the ^4He z-vertex. No significant difference was observed between the two modules regarding this quantity. The obtained parametrization of the mean and the width of the $\Delta\theta$ distribution can be found in Appendix B.

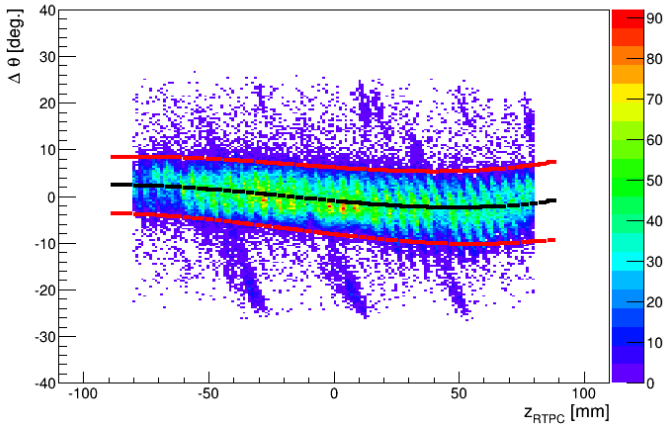

Figure 3.13: The $\Delta\theta$ distribution, for the selected events after the $\Delta\phi$ cut, as a function of z along the RTPC. The black line represents the mean, while the red lines are 2σ cuts around the mean to select the elastic ^4He events.

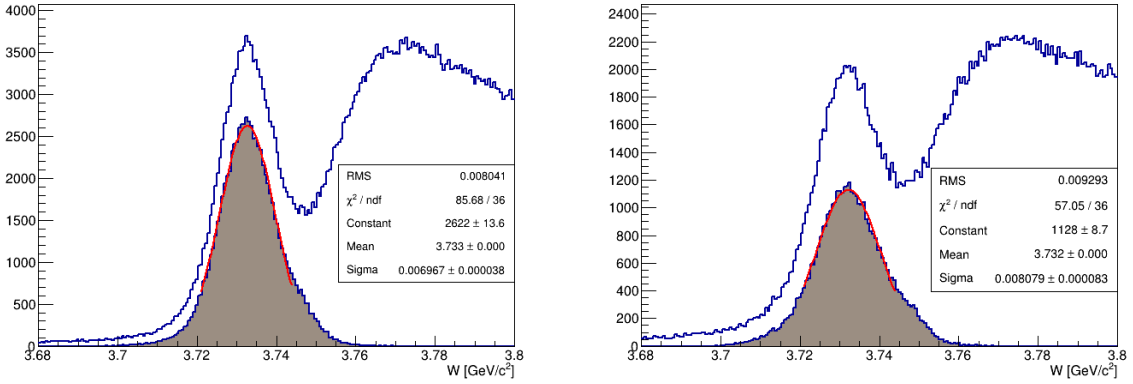

Figure 3.14: The invariant mass distributions for identified good events (in blue) and the clean elastic ones (in shaded) for each of the two modules of the RTPC, respectively.

Constructing the invariant mass is one way to verify the efficiency of the previously described selection procedures. Using the kinematics of the incident electron, the detected scattered electron and the rest ^4He target, the invariant mass (W) can be defined as:

$$W = \sqrt{-2E_b p_{e'}(1 - cos(\theta_{e'})) + M_{^4He}^2 + 2(E_b - p_{e'})M_{^4He}}. \tag{3.6}$$

with the conventions for the variables as in equation 3.5. Figure 3.14 shows the W distribution of the events that have good tracks in the RTPC, and the identified elastic events. One can see the good agreement between the helium-4 real mass and the mean value of the identified elastic events.

3.3.2 Drift speed parametrization

The electrons follow their drift paths with a certain speed, named drift speed. This speed is affected by the experimental conditions, such as the variations in the magnetic field or in the gas composition. We can measure this speed using the tracks detected in the RTPC, as it is explained in this section.

In our TPC, the electrons released close to the cathode take the maximum drift time (TDC_{max}) to reach the readout pads while the geometrical symmetry along the RTPC ensures that these electrons always travel the same distance. Therefore, by identifying the TDC_{max}, the drift speed can be deduced. Figure 3.15 shows the time profile of the collected hits for the detected good tracks. The experimental drift time ranges between the trigger time (TDC_{min} = 15 TDCs) to 75 TDCs. The time profile shows an expected dropping edge at high TDCs due to the geometrical constraints. In order to avoid the statistical effects in determining the TDC_{max}, we define a value named as $TDC_{max/2}$ at which the dropping edge passes to half of the maximum number of hits in each hits-time profile. $TDC_{max/2}$ is inversely proportional to the drift speed.

We measure the $TDC_{max/2}$ along the length of the RTPC to take into account the variations in the electric and magnetic fields. The results can be seen in figure 3.16, where a clear variation of the drift speed along the RTPC was observed.

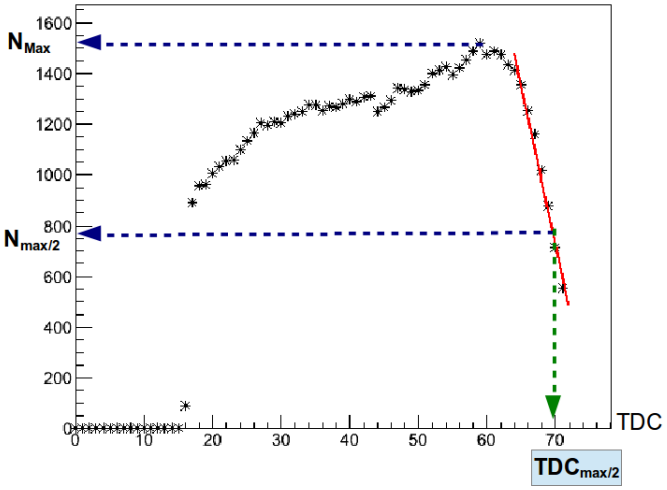

Figure 3.15: Time profile of the collected hits for the RTPC good tracks in one experimental run, run 61511. The $TDC_{max/2}$ is the time at which the dropping edge passes half the maximum number of hits.

We also have monitored the $TDC_{max/2}$ during the time of the experiment, to take into account possible variations. The EG6 experiment has recorded data with different electron-beam energies: 1.204, 5.7, 6.064 and 1.269 GeV. The 5.7 and 6.064 data sets suffer from low elastic cross sections compared to the 1.206 and 1.269 data sets. For this reason, we use all the RTPC good tracks and not only the elastic ones. Before checking the stability of $TDC_{max/2}$ over the experimental running period, we want to check the feasibility of using all good tracks for the purpose of parametrizing the drift speed. In this check, the $TDC_{max/2}$ identified using the good tracks of the 1.206-GeV data set is compared to the one identified from the elastic events of the same data sets. The result is shown in figure 3.17, in which the ratio between the two $TDC_{max/2}$ is plotted as a function of the longitudinal position along the RTPC. This ratio is consistent with 1, within 1%. Thus we can conclude that using the hits of the collected good tracks is a good approximation.

As far as the variation with time is concerned, figure 3.18 shows the identified $TDC_{max/2}$ values in the individual runs, in which each run is two hours of data taking. One can see a non-negligible variation over the three months of data taking due to the changes in the experimental conditions, probably because the proportions of the drift gas were not perfectly under control.

We notice that the $TDC_{max/2}$ ($= \frac{Drift\ path\ length}{Drift\ speed}$) varies with both run number (time) and the geometry of the RTPC (z along the RTPC). To extract the $TDC_{max/2}$ parametrization, we construct the dependence on z for each run in the form:

$$TDC_{max/2}(z) = p_0 + p_1 * e^{p_2*(z-p_3)^2}. \tag{3.7}$$

The parameters: p_0, p_1, p_2, and p_3 are extracted for all the runs. The results can be found in Appendix B. Final fits are performed for these parameters as functions of the run number, and so the drift speed parametrization depends on the run and z along the RTPC. The numerical parametrizations of p_0, p_1, p_2, and p_3 can be found in Appendix B, table B.1.

These functions are implemented in our reconstruction codes, and, as a result of adapting the

drift speed with these functions, more good tracks and elastic events were identified comparing to the previous calibration set. Figure 3.18 shows the gain percentages of the good tracks (GT) and the elastic events (El) in few runs. One can see a gradual improvement with time because of giving the right drift speed, which together with the drift paths gives more precise reconstructed hits chain. Therefore, the parameters of the reconstructed tracks (*sdist*, *edist* ... etc) pass the selection requirements and so more tracks are considered good.

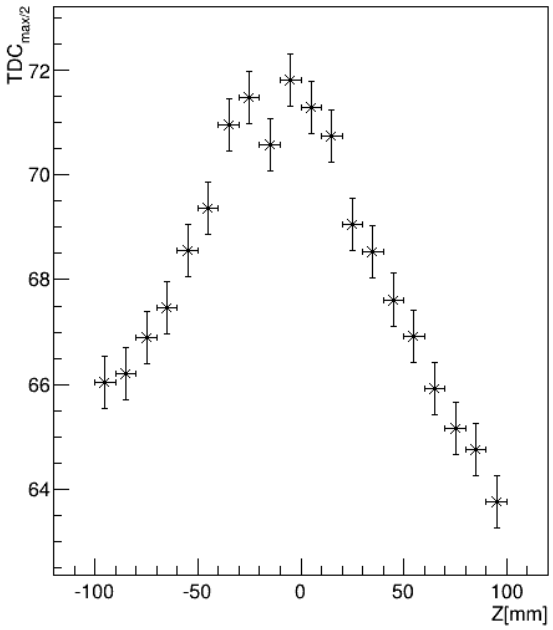

Figure 3.16: $TDC_{max/2}$ variation as a function of the longitudinal position along the RTPC in one experimental run, 61510.

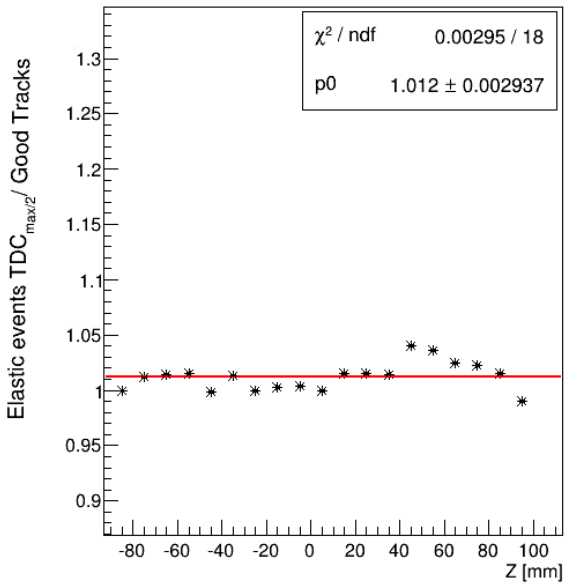

Figure 3.17: Ratio between $TDC_{max/2}$ extracted using the RTPC good tracks and the one extracted using the clean elastic events, both from the 1.204-GeV dataset.

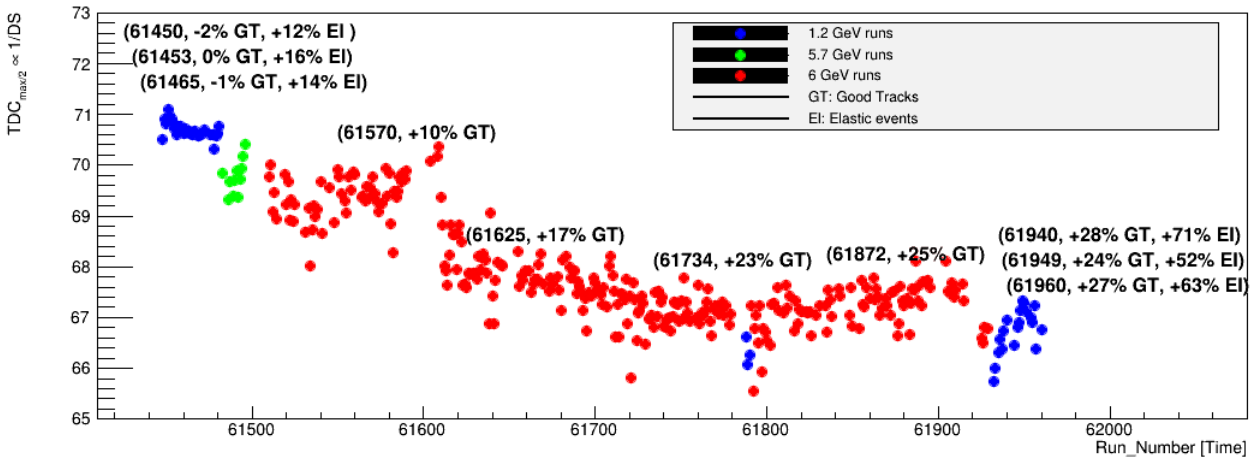

Figure 3.18: $TDC_{max/2}$ as a function of run number. The gain after calibration in the collected good tracks (GT) and elastic events (El) is shown for a sample of runs.

3.3.3 Drift paths parametrization

A drift path is the trajectory that an electron follows after being released in the drift region. The standard software to calculate these paths is the MAGBOLTZ program [111]. This program requires precise knowledge of the experimental conditions, such as the detector's geometry, the exact composition of the drift gas and the applied electric and magnetic fields. Thus any variation in these conditions would give inaccurate calculated drift paths. In the EG6 experiment, MAGBOLTZ has been used to calculate a first set of drift paths, but it was observed for the drift speed that we do not have a perfect knowledge of the RTPC's conditions. Therefore, the first set of the drift paths is not accurate. For this reason, we chose to calculate the drift paths in a way that does not require an exact knowledge of the conditions in the chamber, based on our experimental data.

In our alternative method, we use the identified elastic ($e\ ^4He \rightarrow e\ ^4He$) events to extract the drift paths. For these events, the kinematics of the recoil ^4He are calculated from the scattered electron. Then the electrons' drift paths can be extracted from comparing the experimentally measured hits in the chamber to the hits of the simulated-GEANT4 ^4He. In this technique, the drift paths are obtained independently of our knowledge of the exact conditions in the RTPC, such as the electric field and the geometry. However, this technique and the MAGBOLTZ program are similar in the sensitivity to the variations in the magnetic field.

Due to the magnetic field, the drift paths are not linear. This is handled by the following procedures, in which we perform the drift paths' extraction in two passes. In the first pass, we assume a linear correlation between the radius of emission R (the hit's radial distance from the beam line) and the drift time, to link the GEANT4 hits to realistic hits. Thus, we obtain an initial set of drift paths. In the second pass, we refine the initial correlation between the radius and the time using the initial drift paths, and we extract final drift paths. To take into account the effect of the magnetic field variations, the extracted parametrization will depend on the z position along the RTPC. The following extraction procedures are performed in a polar coordinate system (R, ϕ), with ϕ being the azimuthal angle of the hit. We define $\Delta\phi$ the difference between the simulated ϕ of the hit and the ϕ of the pad measuring the hit.

The procedure steps are:

- Initial linear correlation between R and TDC, to link the GEANT4 hits to the measured ones. In our TPC, the maximum R equals 60 mm (close to the anode) at the trigger time (TDC_{min} = 15 TDCs), and the minimum R equals 30 mm (close to the cathode) at maximum TDC, which is equal to 75 TDCs. Then, the linear correlations can be written as:

$$R(TDC) = \frac{60-30}{15-75}(TDC-15)+60. \tag{3.8}$$

  We apply 3 TDCs-wide windows around the linear R-TDC correlation to select the GEANT4 simulated hits. Figure 3.19 shows the distribution of R versus TDC for the selected simulated hits in a single z bin.

- From these selected hits, we construct the drift paths $\Delta\phi$ (= $\phi_{sim.}$ - ϕ_{hit_pad}) versus TDC. The results can be seen in figure 3.20. The $\Delta\phi$ changes as a function of TDC, showing the electrons drift in ϕ due to the Lorentz angle.

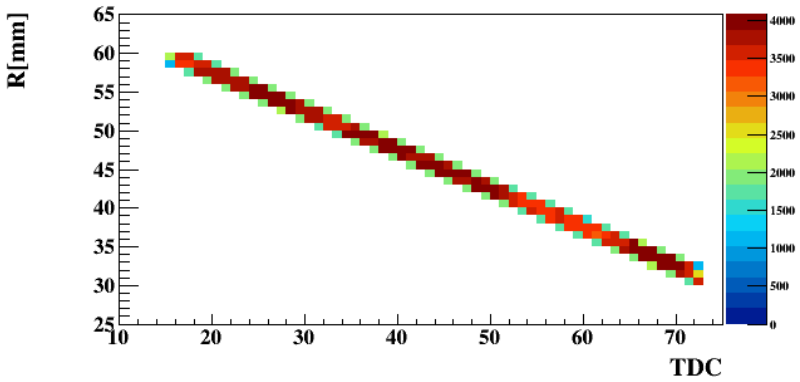

Figure 3.19: (First pass). Distribution of R as a function of TDC for the simulated hits located in one z bin. The width of the bin is 10 mm, with the center at z = 5 mm.

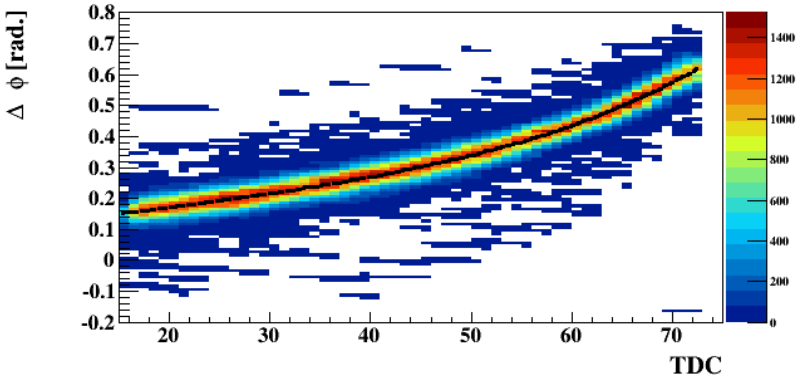

Figure 3.20: (First pass). Distribution of $\Delta\phi$ as a function of TDC for the simulated hits located in the same z bin shown in figure 3.19. The black line represents a fit for $\Delta\phi$.

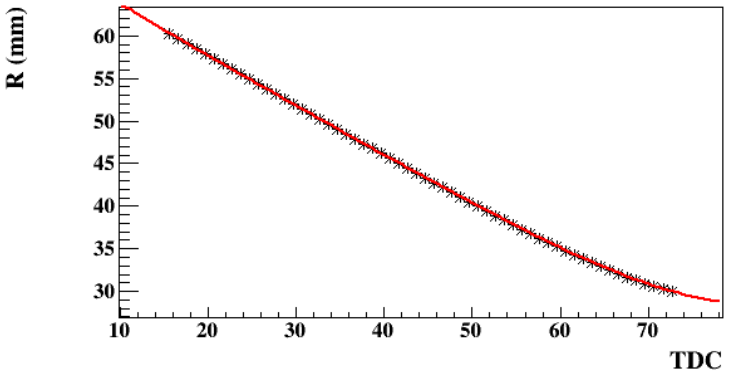

Figure 3.21: (Second pass). The calculated R as a function of TDC is corrected by the $\Delta\phi$ relation extracted from the first pass.

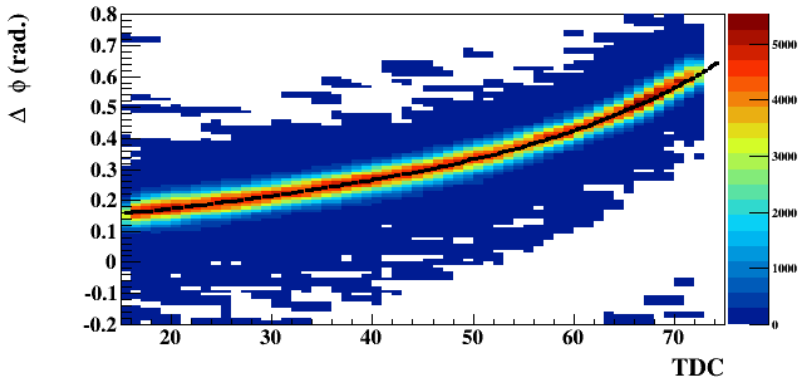

Figure 3.22: (Second pass). Distribution of $\Delta\phi$ as a function of TDC for the simulated hits located in the same z bin shown in figure 3.19. The black line represents the final drift paths.

- The correlation between R and TDC is refined using the extracted initial $\Delta\phi$ as a function of TDC as:

$$R(TDC) = R_{min} + \sum_{i=TDC_{Max}}^{TDC} \sqrt{DS^2 - R^2(i) \cdot \left(\frac{\partial\Delta\phi}{\partial TDC}(i)\right)^2}, \tag{3.9}$$

  where DS is the average drift speed, equal to 0.7 mm/TDC (6.14 μm/ns), R_{min} equals to 30 mm, $R(i)$ is the linear correlation defined in equation 3.8 and $\Delta\phi(i)$ is the fit in figure 3.20. The calculated R, figure 3.21, is very close to straight line, confirming our initial assumption.

- In the second pass, we use the newly found R(TDC) relation to construct new $\Delta\phi$ distributions, see figure 3.22. The black line represents the final drift paths.

As a further check, we performed a third pass in which the R(TDC) correlation is refined using the drift paths from the second pass and new drift paths were extracted. As a result, we observed no difference between the drift paths of the second and the third passes. In other words, extracting the drift paths from two iterations gives us stable drift paths.

The first drift paths were extracted using the elastic events from the early 1.204 GeV dataset. In order to ensure the consistency of these drift paths over the experimental running period, we extracted another set of drift paths using the elastic events of the 1.269 GeV runs. We observed no difference between the two sets of the drift paths, ensuring their stability over the experimental period and leaving the dependence on the TDC and z. The final drift paths are extracted using both datasets, 1.204 and 1.269 GeV. They take the form:

$$\Delta\phi(TDC, z) = \sum_{i=0}^{4} p_i(z) * TDC^i, \tag{3.10}$$

where the parameters, p_0, p_1, p_2, p_3 and p_4 are functions of z, as can be seen in Appendix B, table B.2. The final drift paths are implemented in our reconstruction codes such that the reconstructed position of each hit becomes:

$$\phi_{exp}(z, TDC) = \phi_{hit\_pad} - \Delta\phi(z, TDC). \tag{3.11}$$

It is important to note that the drift paths have shown strong sensitivity to the other RTPC calibrations. Therefore, we performed iterative extractions of the drift paths, and, as results more

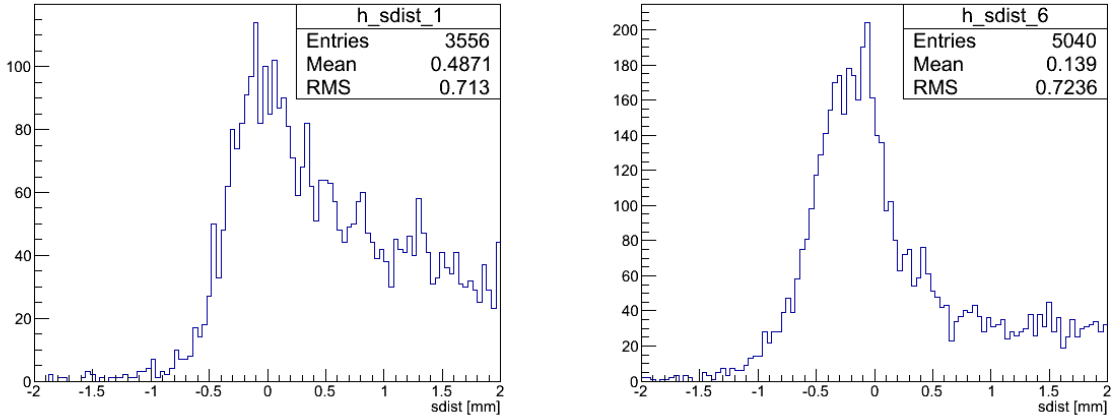

Figure 3.23: The *sdist* distribution for the collected tracks in the RTPC using the same initial collected data with an old set of drift paths, on the left, and a newer set, on the right.

good tracks were reconstructed, and the signal to background ratio was improved. Figure 3.23 shows an illustration of the improvements in terms of the *sdist* parameter, using the same initial collected data with an old drift paths (on the left) and a newer set (on the right).

3.3.4 Gain calibration

The previous parametrizations of the drift speed and the drift paths were carried out using the time information of the recorded electrons, which, together with the known magnetic field, results in momentum measurement. The second important information is the amplitude of the signal provided in ADC units. Since each charged particle deposits a certain amount of energy ($\frac{dE}{dX}$) when crossing a material, we can identify particles based on this variable. The ($\frac{dE}{dX}$) depends on the characteristics of the particle, such as its energy, mass and charge, and the nature of the medium as well.

$\frac{dE}{dX}$ can be calculated using the Bethe-Bloch formula [114]:

$$\left\langle \frac{dE}{dX} \right\rangle = \rho K z^2 \frac{Z}{A} \frac{1}{\beta^2} \left[\frac{1}{2} ln \left(\frac{2 m_e c^2 \beta^2 \gamma^2 T_{max}}{I_{max}} \right) - \beta^2 - \frac{\delta \beta \gamma}{2} \right] \tag{3.12}$$

$$\text{with } T_{max} = \frac{2 m_e c^2 \beta^2 \gamma^2}{1 + 2\gamma m_e / M + (m_e/M)^2} \tag{3.13}$$

where T_{max} is the maximum kinetic energy of a free electron in a single collision, and z, M, β are the charge, mass and speed ($=p/\sqrt{M^2+p^2}$, where p is the momentum) of the particle, respectively. m_e is the electron mass and the constant K is equal to $4\pi N_A r_e^2 m_e c^2$ = 0.307075 MeV mol^{-1} cm^2. Z, A, I, ρ are the effective charge, atomic number, mean excitation energy and mass density of the medium. In the RTPC, these constants are equal to 66, 126.79 mg mol^{-1}, 99.79 eV and 1.03 mg/cm^3, respectively.

Experimentally, $\frac{dE}{dX}$ can be calculated from the collected ADCs as:

$$\left\langle \frac{dE}{dX} \right\rangle = \frac{\sum_i \frac{ADC_i}{Gi}}{vtl}, \tag{3.14}$$

where the sum runs over all the pads contributing to a track. ADC_i is the recorded amplitude in each pad i, and G_i is its gain. The vtl is the total visible length of the track in the active drift volume.

The electron collection system of the RTPC has 3200 readout pads. The gain of each pad is the ratio between the deposited energy and the output recorded value. Predominantly, these gains can be extracted by two techniques. The first one is by comparing the experimental recorded $\frac{dE}{dX}$ to the expected values calculated from the Bethe-Bloch formula. This method involves a series of equations to be solved for the gains. The second technique is based on comparing the experimental ADCs to the GEANT4 simulated ones, track by track. Then, the ADCs of each pad is compared to the ADCs of the other pads in the same track.

The second method requires improvements in the simulation, in order to match the real experiment. In summary, these improvements are:

- Update the simulation including the previously extracted parametrizations of the drift speed and the drift paths.
- Global ADC normalization to give reasonable simulated values. In the left module, 1 ADC is equal to 17 eV, while it is equal to 21 eV in the right module. These normalizations were extracted from the comparison of the data to the GEANT4 simulation.
- Rejection of the signals from bad pads. During the experiment, the readout system of the RTPC suffered from 555 dead or noisy pads. These pads are marked by the dotted squares in figure 3.26.
- Smearing the position of the simulated hits. Experimentally, the average number of hits per track is around 80 while the initially reconstructed mean value from the simulation is around 50. We apply a Gaussian smearing on the position of the simulated hits to make the simulation more realistic, see figure 3.24.
- Application of the TPC's DAQ cut on the simulated data. Experimentally, each pad must have at least 3 consecutive time bins, with ADC values above the threshold, 35 ADCs, in order to be recorded. Then, the hits of 3 neighboring bins on each side of the above threshold bins are also recorded, while the other hits are not.

Figure 3.25 shows the simulated ADCs (upper plot) and the experimental ones (lower plot) as a function of the TDCs for the same track. The same color in the two plots refers to hits recorded by the same readout pad. In this step, the gain of each pad is defined as the ratio of the mean experimental ADCs to the mean simulated ADCs for the same track. Then, for each pad, these gain ratios were collected from the elastic events and fitted by a Landau function to give their overall calibration as a basis. Next, we apply the extracted gains on the experimental data and we find the ratio between the mean ADC value of each pad to the mean ADC of the whole track. This ratio is collected from all the elastic events and a gain correction factor is extracted for each pad. The final gains of the second method are then corrected by the fraction from the last step.

The two extraction techniques of the gains were investigated for the EG6 experiment using the elastic events from the 1.206 GeV data set. As the two modules of the RTPC are electronically separated, we look at their calibrations separately. Figure 3.27 shows the ratio between the calculated $\frac{dE}{dX}$, using the gains of both methods, and the GEANT4 simulated $\frac{dE}{dX}$ for the elastic events in the two modules of the RTPC. We conclude that extracting the gains from comparing

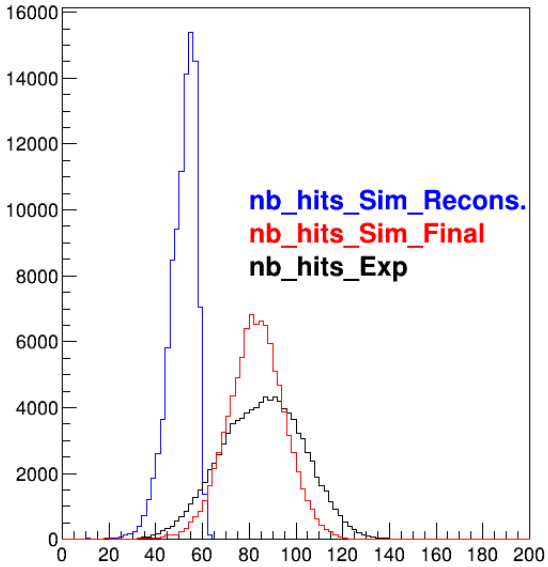

Figure 3.24: The distributions of the number of hits per track. The black, the blue and the red distributions are the number of hits per track for respectively, the experimental data, initial simulation, and the final simulation.

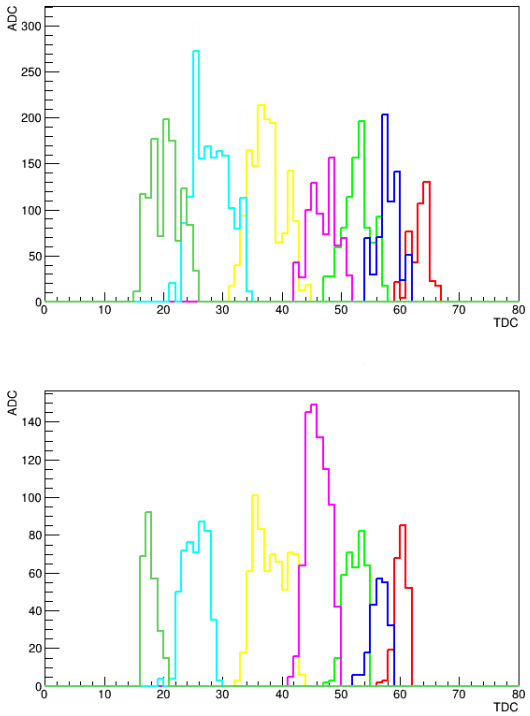

Figure 3.25: The simulated (top) and the experimental (bottom) ADCs versus TDC distributions for the same track. The same colors indicate hits that were registered in the same pad for the simulation and the experiment.

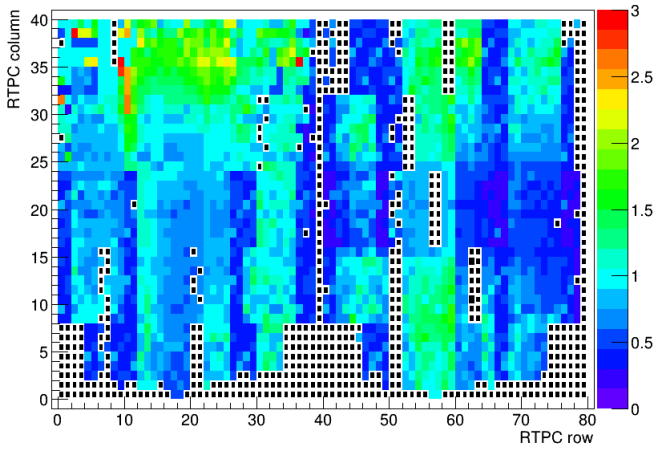

Figure 3.26: The extracted gains from the second method. The dotted squares refer to the position of the excluded pads.

data to simulation in terms of the ADCs of the individual tracks gives more precise gains than solving the series of equations. Figure 3.26 shows the gains from the second method, where the dotted squares refer to the dead or noisy pads. These are the ones that are implemented in the EG6 reconstruction codes.

In the left module of the RTPC, figure 3.27, one notices an additional unexpected lower peak ($dEdx_{exp}/dEdx_{sim} \sim 0.3$). These events pass all the elastic requirements but for some reasons they have lower ADC values. They make 7% of all the elastic events. After extended studies, the nature of these particles is not identified yet. We note that this is a global phenomenon in the left module as 94% of the left module's pads recorded hits for events in both regions (the low-region at $dEdx_{exp}/dEdx_{sim} \sim 0.3$, and the region where the peak is around 1). For instance, figure 3.28 shows the average ADC versus TDC distributions for the recorded hits in one of these pads in the left module. For the moment, the events in the low-region will be excluded from the analysis.

To check the validity of the extracted gains, we show in figure 3.29 $\frac{dE}{dX}$ versus the momentum (per charge unit) measured in the RTPC for all the collected tracks of the 1.206 GeV data set. In the plots, we add the theoretical lines derived from the Bethe-Bloch formula for possible detected particles: ^4He, ^3He, ^3H, Deuterium (d) and the protons. One sees different bands corresponding to the different detected particles. Even though the bands are very large, the $\frac{dE}{dX}$ can be used to perform particles identification for large data set.

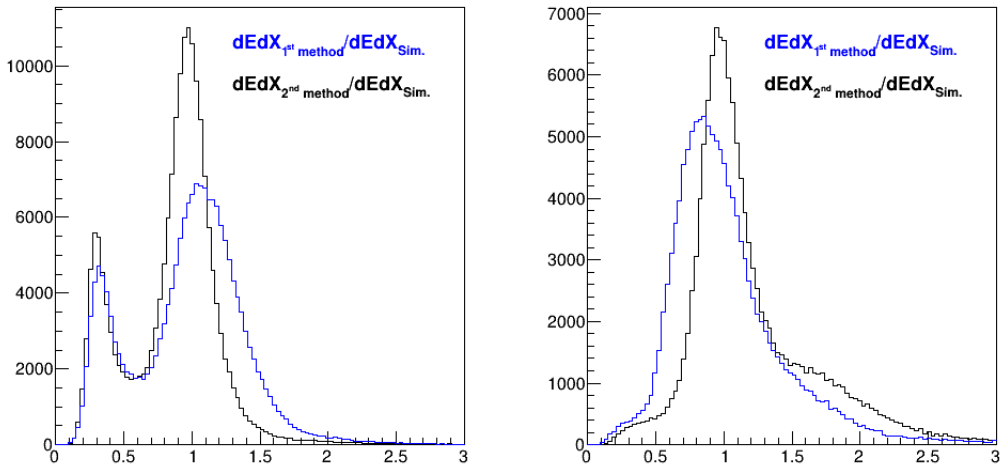

Figure 3.27: The ratio between the experimental dE/dx, using the gains obtained with the two methods (1^{st} in blue, and 2^{nd} in black), to the GEANT4 simulated dE/dx, plotted for the two modules of the RTPC, respectively left and right.

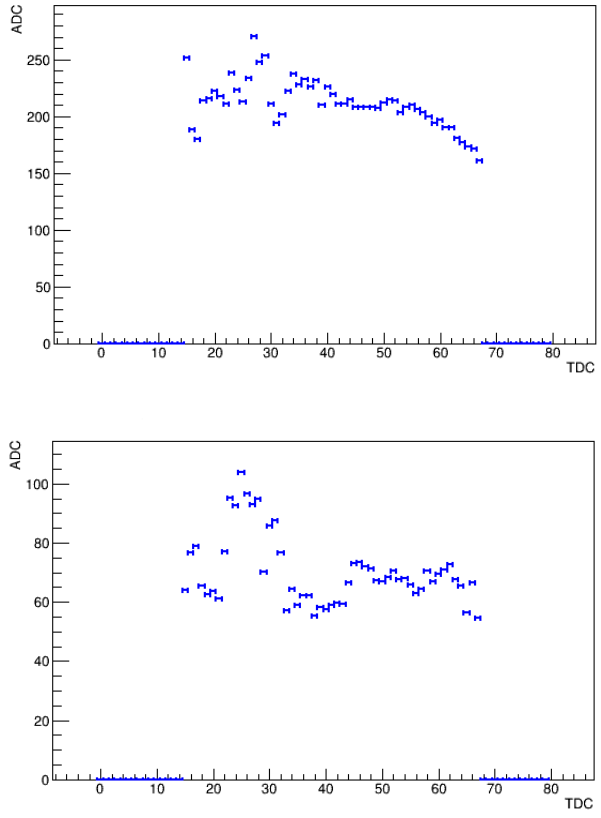

Figure 3.28: The average ADC vs. TDC distributions of the experimental hits recorded for the elastic events in one pad of the left module, pad number 706. On the top: the distribution for the elastic tracks in the region where $\mathrm{dEdx}_{exp}/\mathrm{dEdx}_{sim} \sim 1$. On the bottom: the distribution for the elastic tracks that exhibit $\mathrm{dEdx}_{exp}/\mathrm{dEdx}_{sim} \sim 0.3$.

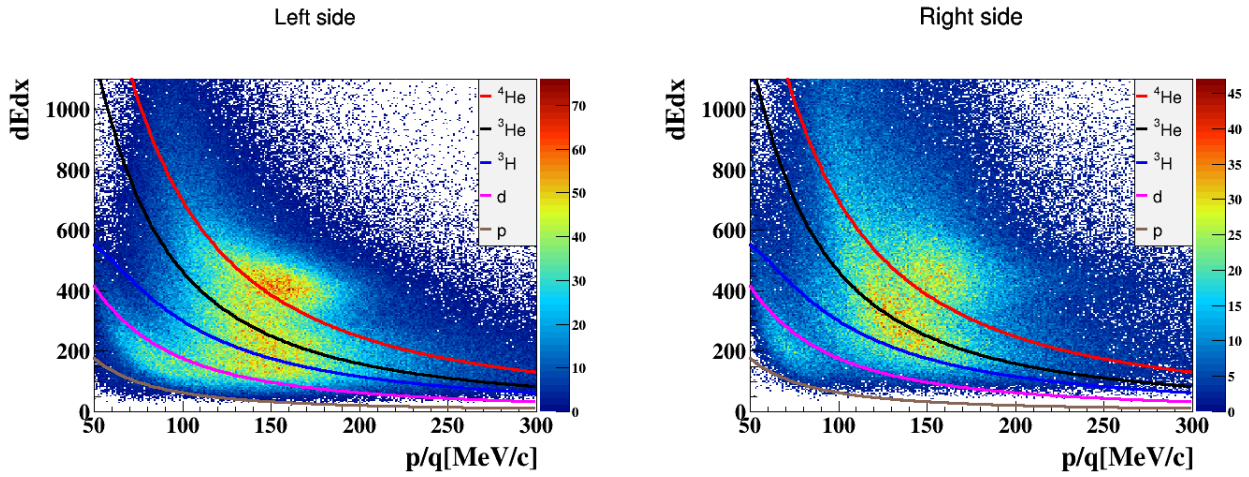

Figure 3.29: The experimental $\frac{dE}{dX}$ calculated using the second method gains versus p/q of all the collected good tracks in the RTPC in the early 1.204 GeV dataset.

3.3.5 Noise rejection

The RTPC was designed to reduce the noise and the Møller electrons via the first and the second gas gaps. Nevertheless, at 1.204-GeV of electron beam energy, the recoiled elastic ^4He nuclei have a relatively low kinetic energy, around 20 MeV. This forced us to lower the RTPC threshold, which yielded to the recording of more noise compared to putting a higher threshold. We investigated the noise presence in the data using the RTPC good tracks after all the calibrations. This investigation has been carried out by plotting the ADC versus TDC for the recorded hits in each readout pad. About 18% of the active pads have shown an oscillatory noise shape at low TDC values, as can be seen in figure 3.30, which mostly comes from the electronics. An algorithm was developed by the EG6 group to remove hits corresponding to this noise without suppressing good hits. First, the ADC vs TDC noise curve was parameterized. Next, for every event and channel independently, the number of hits falling on this curve is counted. If a significant number of hits lie far above or below the noise curve, no rejection is performed. If most of the hits below TDC=30 fall on the noise curve, all hits below TDC=30 are rejected for that channel. Figure 3.30 shows the effect of this noise rejection for one very noisy pad.

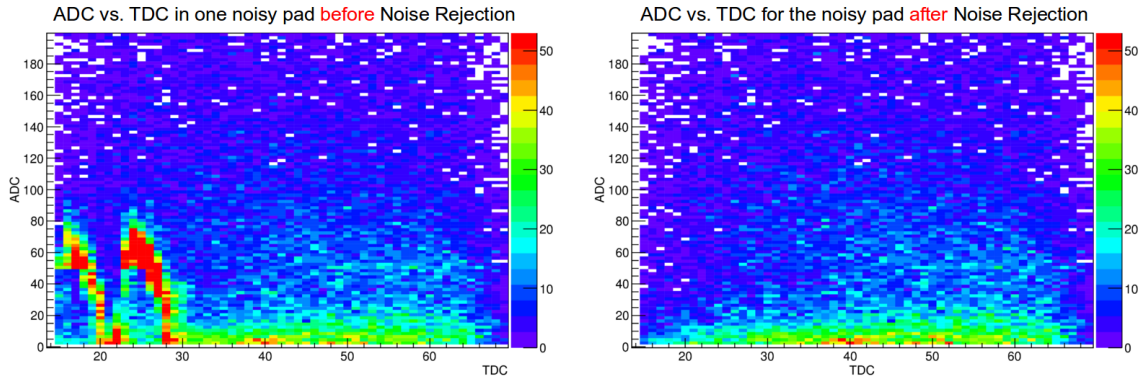

Figure 3.30: The integrated ADC vs. TDC of the hits for the good tracks before (left) and after (right) the noise reduction, for a given pad that shows strong noise shape. The color scales are identical in both plots.

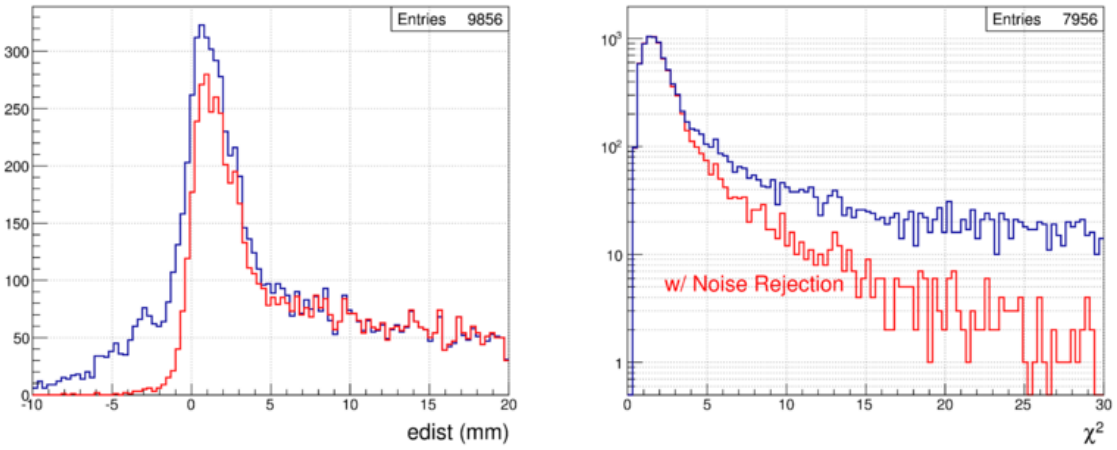

Figure 3.31: The *edist* (left) and the χ^2 (right) distributions for all the tracks collected in the RTPC before (blue) and after (red) the noise rejection, for a small data sample.

As a result of the noise reduction, 5% more good tracks were collected, and the signal to background ratio improved, as can be seen in figure 3.31.

3.4 Tracking resolution

The RTPC tracking resolution is defined as the spread of the reconstructed track vertex, angles and momentum with respect to their true values. In the EG6 experiment, we use the cleanly identified elastic events to estimate the RTPC resolutions. The CLAS detector provides electron detection with an angular resolution around 1 and 4 mrad in θ and ϕ respectively, a z-vertex resolution of about 1 mm, and a momentum resolution ($\frac{\Delta p}{p}$) around 0.5% [99]. With such electron resolutions, one can extract the RTPC resolutions by comparing the calculated kinematics of the recoil elastic ^4He nuclei with the measured experimental values, as shown in figures 3.32, 3.33, 3.34, 3.35 for the two halves of the RTPC separately. The distributions are fitted with a Gaussian and the extracted widths are listed in table 3.1. One can see that for the resolution, the two modules of the RTPC show almost the same performance. These resolutions will be used to match the simulated data to the experimental ones, as will be shown in the following chapter.

One notices slight shifts in Δz (figure 3.32), $\Delta\phi$ (figure 3.33), and $\Delta\theta$ (figure 3.34) distributions. The reason of the shifts may rise from our non-perfect knowledge of the exact conditions in the chamber, such as the magnetic field, that affect the reconstructed parameters of the tracks. The reconstructed momenta show 10-15% systematic shifts compared to the calculated values. dedicated studies were carried out to understand these shifts, such as energy loss corrections and possible correlations other variables. The reason is not fully understood yet, and further work is needed on this side.

RTPC's module	σ_z	σ_ϕ	σ_θ	σ_p
Left module	6.03 mm	1.93°	3.78°	9%
Right module	7.40 mm	1.94°	4.02°	8 %

Table 3.1: The resolutions of the two modules of the RTPC.

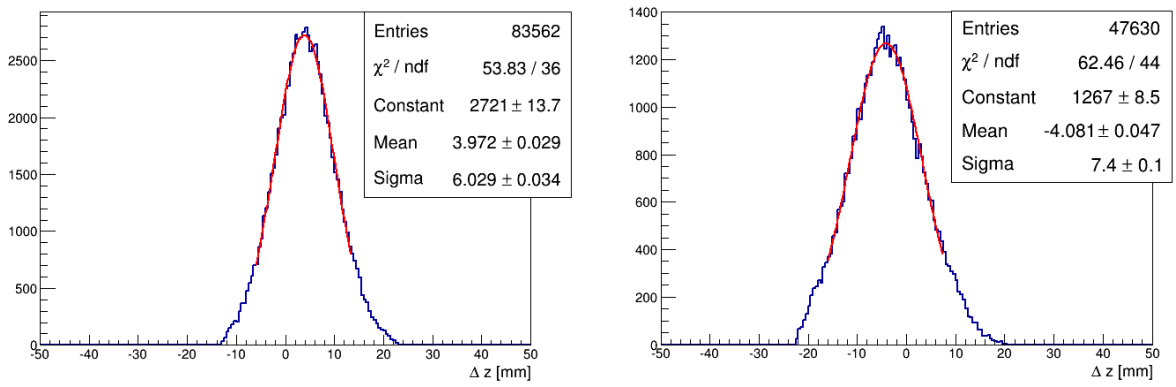

Figure 3.32: The z-vertex resolution of the two modules of the RTPC, respectively.

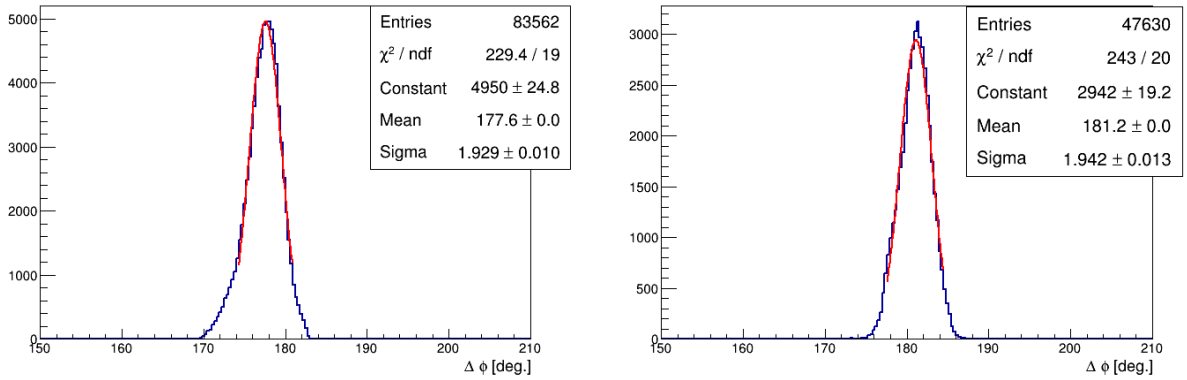

Figure 3.33: The azimuthal angle resolution of the two modules of the RTPC, respectively.

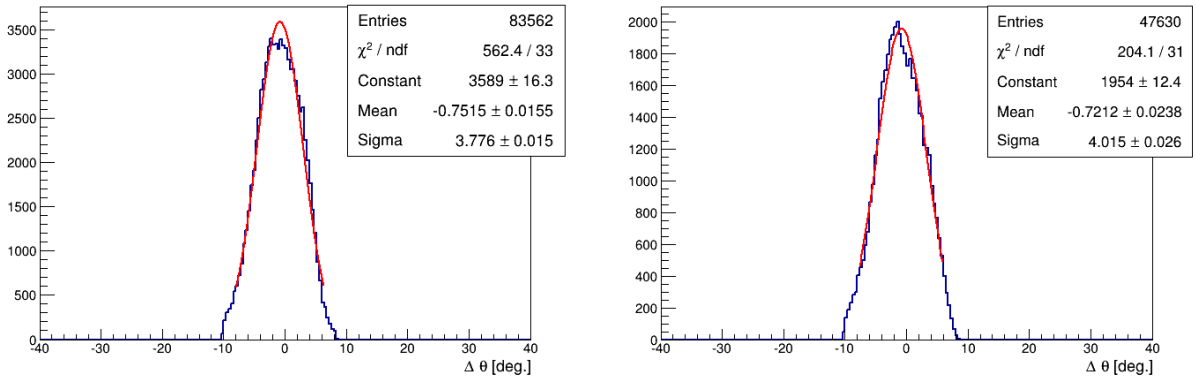

Figure 3.34: The polar angle resolution of the two modules of the RTPC, respectively.

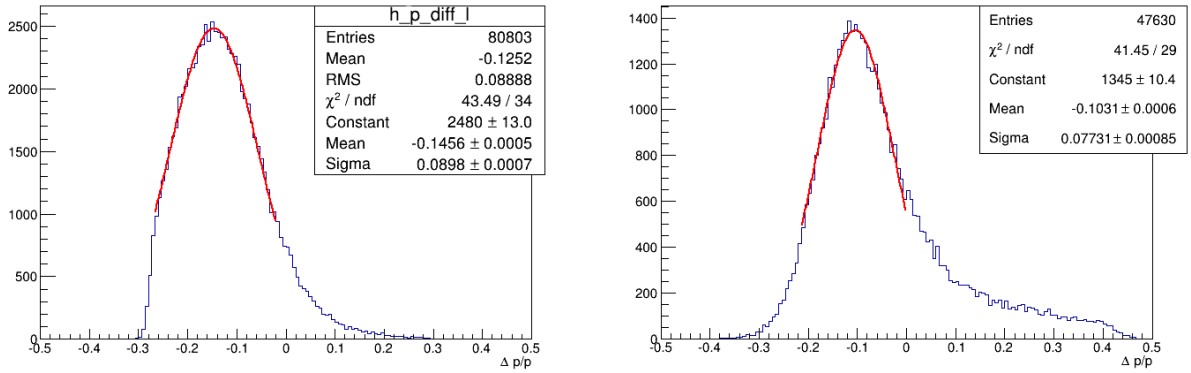

Figure 3.35: The momentum resolution of the two modules of the RTPC, respectively.

Chapter 4

Particles reconstruction and simulation

The final state of a coherent (incoherent) DVCS event consists of three particles: an electron, a ^{4}He (a proton), and a real photon. To identify the DVCS events, we first identify, individually, the different particles of interest. Then, events with three detected final-state particles will be further filtered by imposing the energy-momentum conservation laws, as will be presented in the following chapter.

Even after imposing the conservation laws and the kinematical cuts, the DVCS sample will not have 100% truly DVCS events. In our kinematical region, the main contamination to our DVCS channels comes from the electroproduction of neutral pions. For instance, in the coherent π^0-electroproduction, when one of the two-photons coming from the π^0-decay passes the DVCS requirements, it will be counted as a DVCS event. Thus, these events have to be subtracted. For this purpose, we perform a technique in which we combine the measured exclusive π^0-electroproduction data sample with a Monte-Carlo simulation to evaluate the background in the selected DVCS sample. For this technique, we need to identify the experimental π^0s that come in the coherent and the incoherent π^0-electroproduction channels.

In this chapter, we presents the procedures carried out to identify the final-state particles of interest, the Monte-Carlo simulation we used, and the applied kinematic corrections.

4.1 Particles identification

4.1.1 Electron identification

The electron detection triggers the data acquisition system to record data from all the sub-detectors of CLAS. In this analysis, a particle which passes the following set of criteria is assumed to be a good electron.

Initial requirements

- Negative charge: the torus magnet generates a field which has mainly azimuthal components. Hence, the trajectory of a negative particle will be bent towards the beam line direction without changing azimuth. Consequently, information on its charge is accessible from the curvature of its trajectory.
- $(DC_{stat}, EC_{stat}, SC_{stat}, CC_{stat}) > 0$: these status variables are linked to the number of hits and the thresholds in the different sub-detectors of CLAS. Thus, we select the electrons which have positive status in the different sub-detectors as a first step to reduce the noise in the data sample.
- $stat > 0$: this variable is positive if the trajectory of a particle passes the two steps of the tracking in the DCs, Hit-Based Tracking (HBT) and Time-Based Tracking (TBT).

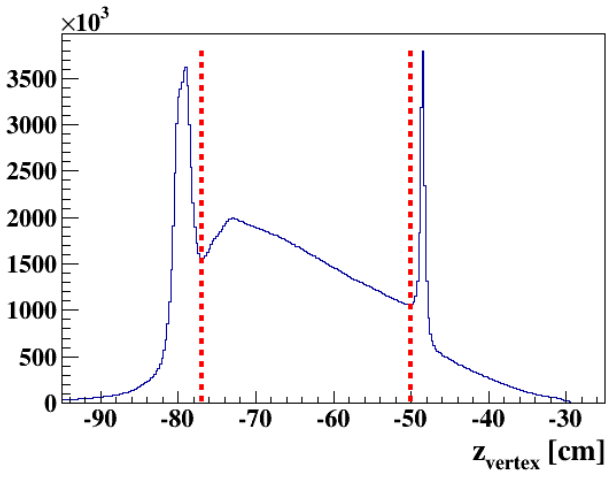

Figure 4.1: The reconstructed longitudinal vertex of the collected negative particles. The two dashed red lines represent the chosen cut, -77 cm < z_{vertex} < -50 cm, to eliminate the particles which originate from the windows and outside the target.

- Momentum cut (p_{e^-} > 0.8 GeV/c): we apply this cut to select electrons inducing small radiative effects as they are inversely proportional to the energy of the particle.

- Vertex cut: the target is centered at -64 cm with respect to the center of CLAS. Figure 4.1 shows the reconstructed z-vertices for the collected negative particles. One sees two sharp peaks corresponding to the two aluminum windows at the ends of the target. These particles have to be rejected as they originate from outside the target. As will be emphasized later, we need an accurate determination of the electron's vertex to ensure the correspondence between the final-state particles, which all have to originate from the same point.

Fiducial cuts

Some regions of CLAS have to be excluded from the analysis to ensure an accurate detection of the different particles. For instance, an electron that hits the edge of the EC will have only part of its electromagnetic shower contained within the detector. Also, the structure of the torus magnet divides CLAS into six separate sectors, which makes edge effects non-negligible. For this reason, the following set of fiducial cuts is applied:

  - EC fiducial cut: each EC has a triangular shape with its three sides labelled as U,V and W. We apply a set of cuts (60 cm < U, V < 360 cm, W < 390 cm) to reject the electrons which hit the EC close to the edges, as shown in figure 4.2.

  - CC fiducial cut: in reference [101], G. Adams *et al.* have studied the efficiency of the CCs. They found that within the fiducial regions, which are defined by the edges of the CCs mirrors, the detection efficiency is stable and is around 98%. Outside the fiducial regions, the efficiency shows strong variations. In reference [113], M. Osipenko *et al.* have developed a coordinate system to represent the CC hits with respect to the center of each sector in CLAS. In this frame, the CCs mirror edges can be defined as:

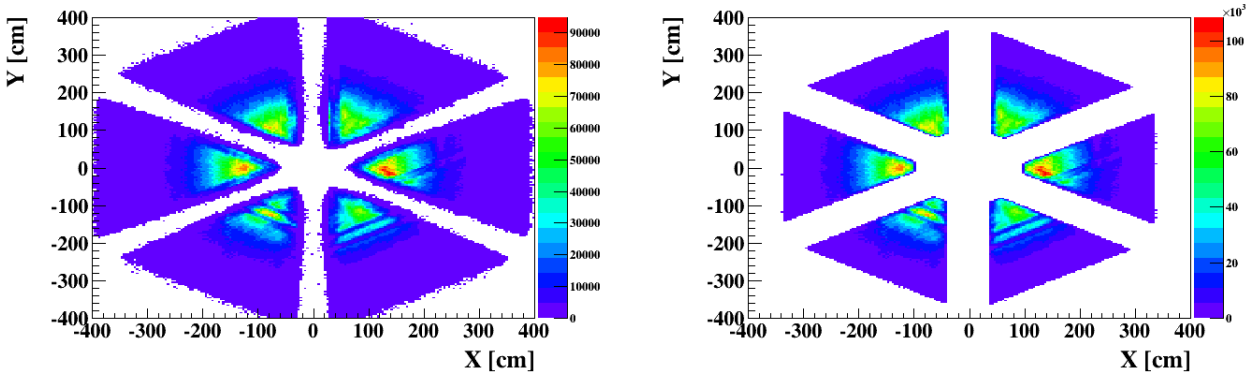

Figure 4.2: On the left: XY distribution for the negative particles in the EC before the U, V and W cuts. On the right: the same distribution is plotted after the cuts. X and Y are the coordinates in the EC with respect to the center of CLAS.

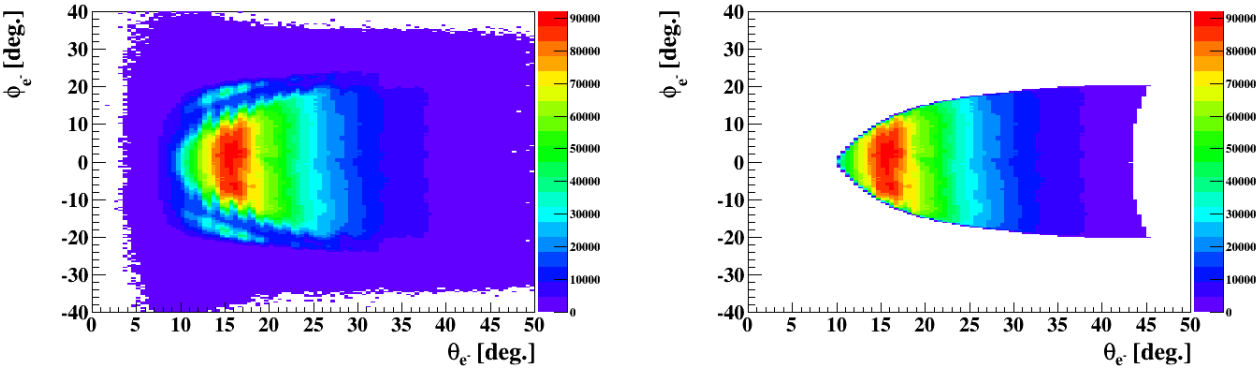

Figure 4.3: Azimuthal angle as a function of polar angle for the negative particles before (left) and after (right) applying the CC fiducial cut. The angles are calculated with respect to the center of each sector in CLAS.

$$\phi_e = -63.32792 + 11.05609 \cdot \theta_e - 0.6344957 \cdot \theta_e^2 + 1.873895 * 10^{-2} \cdot \theta_e^3 - 2.762131 * 10^{-2} \cdot \theta_e^4 + 1.604035 * 10^{-2} \cdot \theta_e^5. \quad (4.1)$$

Based on these works, we reject all the hits located outside the mirror edges. Figure 4.3 shows an illustration of this cut.

– IC shadow cut: this cut originates from the location of the IC in front of the innermost part of the DCs. The electrons which are produced at polar angles lower than 14° will hit the IC. The left plot of figure 4.4 illustrates this effect, and the right plot shows the effect of this cut.

– DC fiducial cut: the DCs have low detection efficiency at the edges because only part of the tracks are detected [100]. Therefore, we apply a fiducial cut to reject the particles at the edges. The left plot of figure 4.4 shows the XY distribution of all the negative particles in DC1. The result of applying the DC fiducial cut can be seen in figure 4.5.

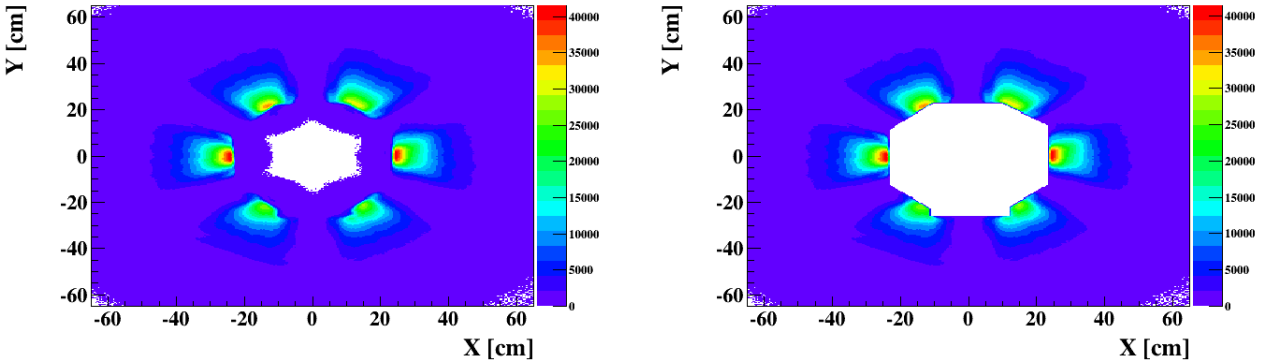

Figure 4.4: On the left: XY distribution for all the negative particles in the first region of the DC before applying the IC shadow cut. On the right: the same distribution after the cut.

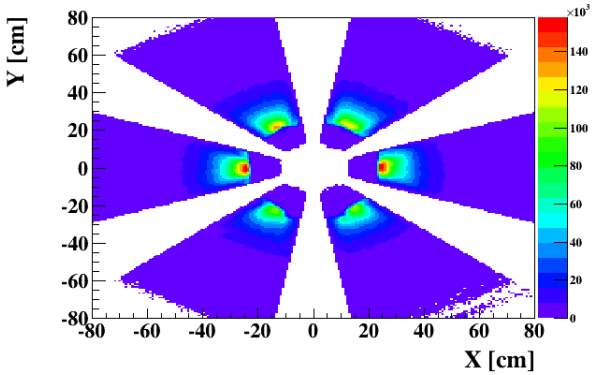

Figure 4.5: XY distribution for all the negative particles in DC1 after applying the DC fiducial cut.

EC energy cuts

Referring to the discussion in section 2.2.5, the Minimum Ionizing particles (MIPs), such as pions, deposit constant amounts of energy per distance while traversing the EC. In contrast, the showering particles, such as electrons and photons, deposit energies proportional to their momenta. We use two energy cuts to clean the electrons from the main contamination, i.e. π^-s.

- Minimum deposited energy: the inner and the outer parts of the EC have thicknesses 15 cm and 24 cm, respectively. The simulations show that pions deposit a constant energy amount of 2 MeV/cm, independently of their momenta. Figure 4.6 shows the deposited energy in the outer part of the EC (EC_{out}) as a function of the energy deposited in the inner part (EC_{in}), after the fiducial cuts. On the x-axis, one can see a clear region, around 30 MeV, that comes mainly from the negative pions, which deposit 2 MeV/cm along the 15 cm thickness of the inner EC. We use a cut of 60 MeV on EC_{in} to reject these particles.
- An additional cut, correlating the measured deposited energy and the momentum, is applied. Figure 4.7 shows the ratio of the total deposited energy in the ECs (EC_{tot} =

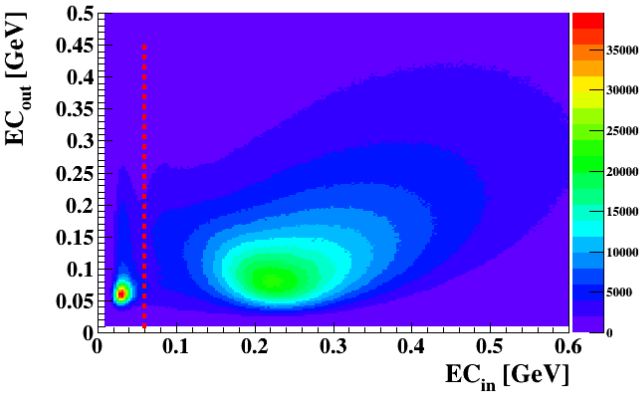

Figure 4.6: Deposited energies in the EC: E_{out} as a function of E_{in}. The dashed red line represents a 60 MeV cut on EC_{in} to reject the π^-s.

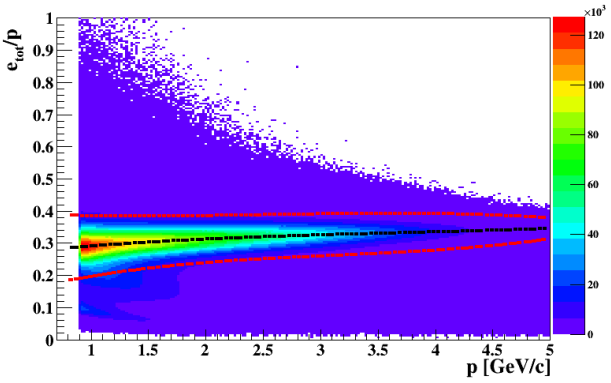

Figure 4.7: E_{tot}/p as a function of p. The black dashed line represents the mean value of E_{tot}/p as a function of p. The red dashed lines represent the 2.5σ cuts.

EC_{in} + EC_{out}) to the momentum (p) as a function of p. One notices that EC_{tot}/p varies slightly with the momentum due to variations in the efficiencies of the DC and EC. We apply 2.5σ cuts around the mean (μ) to select the good electrons, using to the following parametrizations of the mean (μ) and the width (σ):

$$\mu(p) = 0.256084 + 0.0432374 \cdot p - 0.00914180 \cdot p^2 + 0.00081589 \cdot p^3 \quad (4.2)$$

$$\sigma(p) = 0.0572976 - 0.0272689 \cdot p + 0.008576 \cdot p^2 - 0.00097998 \cdot p^3 \quad (4.3)$$

CC cut

The Cherenkov counters have been designed to separate electrons from pions below 2.5 GeV/c momentum. In this region, the pions are not supposed to produce photoelectrons. However, low momentum δ-electrons can be produced from the diffusion of the pions in the Cherenkov gas. These δ-electrons produce a small number of photoelectrons. Figure 4.8 shows the distributions of the number of photoelectrons ($nphe$) produced by the negative particles in three different stages of selecting the electrons.

One sees from figure 4.8 that the single-photoelectron peak is strongly reduced after applying the energy cuts. We conclude that the particles causing the single-photoelectrons peak are linked to particles with low deposited energy in the EC_{in}, figure 4.6. We apply a final cut on the red distribution in figure 4.8 ($nphe > 2$), and we assume that the negative particles which pass all the previous requirements and produce more than 2 photoelectrons in the CC are good electrons. Figure 4.9 shows the azimuthal angle as a function of the polar angle for the good electrons.

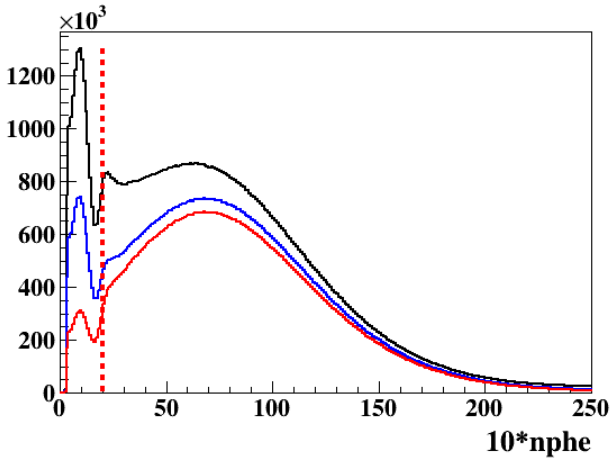

Figure 4.8: Distribution of number of photoelectrons emitted by negative particles in the CC ($nphe$·10). The black curve represents the distribution after the initial cuts, the blue curve is after the geometrical cuts and the green curve is after applying all the cuts including the EC energy cuts. The dashed red line represents the cut we apply ($nphe > 2$) to select the good electrons.

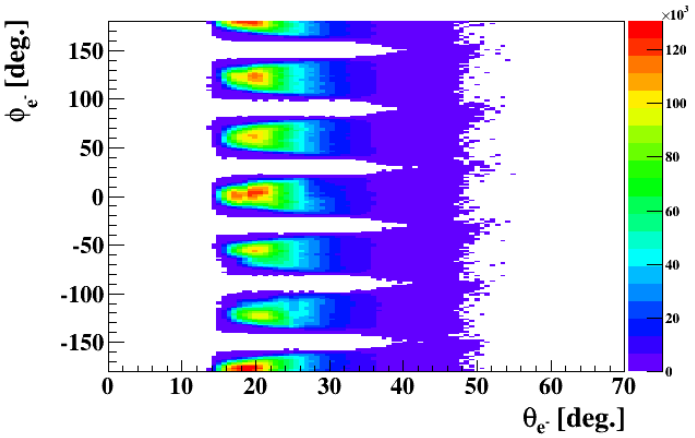

Figure 4.9: ϕ vs. θ distribution of the selected electrons.

4.1.2 Proton identification

Similar to the electrons, the protons are affected by the geometrical and the efficiency effects of the different sub-detectors of CLAS. The following conditions are required to select the good protons.

- Coincidence with one and only one good electron.
- Initial track requirements: the positive charge of the proton results in bending its trajectory away from the beam line direction. Thus, a positive charge is required from the curvature of the track. Like for the electrons, the proton candidates must pass the two steps of the tracking in the DCs, have signal above the threshold in the SCs ($SC_{stat} > 0$) and originate from a vertex within the target (-77 cm < z_{vertex} < -50 cm).

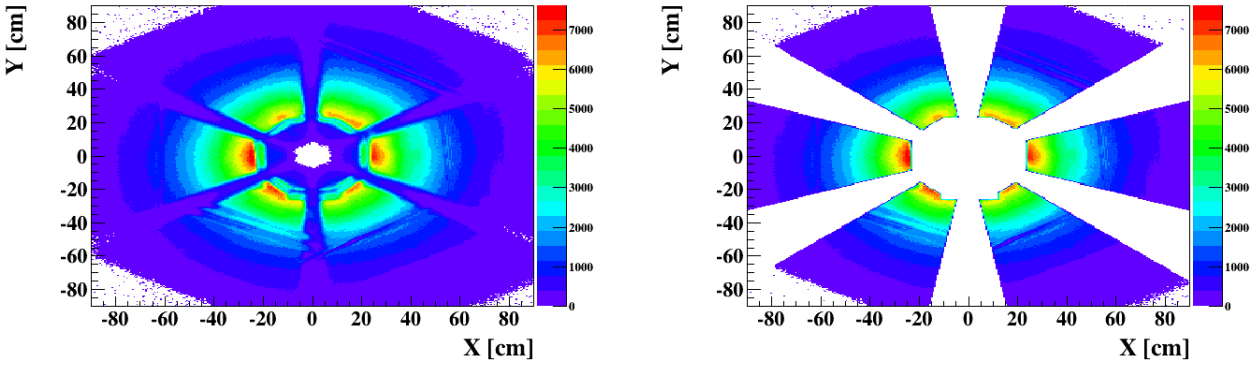

Figure 4.10: XY plane projection in DC1 for the positive particles before (left) and after (right) IC shadow and DC fiducial cuts.

- Fiducial cuts: the tracks of the protons detected close to the edges of the DC can only be partially reconstructed. As for the electrons, the protons which are recoiled at polar angles smaller than 14° hit the IC. We apply the previously presented (in section 4.1.1) DC and IC shadow fiducial cuts to avoid these effects. Figure 4.10 shows the XY projection in the DC1 for the collected positive particles which passed the initial track requirements, before and after these two fiducial cuts.

- Velocity ($\Delta\beta$) cut: the previous cuts do not separate the protons from other positive particles, such as positive pions and kaons. A very clear separation can be obtained by associating the information from the SCs and the DCs. The velocity of a charged particle can be calculated by using the momentum (p) reconstructed in the DCs and the Time-Of-Flight (t_{TOF}) measured by the SCs. We define:

$$\Delta\beta = \beta_{SC} - \beta_{DC} = \frac{l_{track}}{c \cdot t_{TOF}} - \frac{p}{\sqrt{p^2 + m_p^2}} , \tag{4.4}$$

  where l_{track} is the measured track length and m_p is the proton mass. On the left plot of figure 4.11, $\Delta\beta$ is plotted as function of momentum. One can see two main trends in this plot: the region around zero corresponds to the protons, while the one above corresponds to the positive pions (π^+). The right plot shows a one-dimensional distribution of $\Delta\beta$ zoomed in the region of the protons.

- Vertex matching: the last cut is the correspondence between the longitudinal vertices of the detected electron and proton. Figure 4.12 shows the difference $\Delta z = z_e - z_p$ and the chosen cuts (red dashed lines).

Finally, figure 4.13 shows the azimuthal angle as a function of the polar angle distribution for the identified protons after all the selection cuts. One notices that the population of the protons is different from one sector to another, which comes from the dead regions in some sectors.

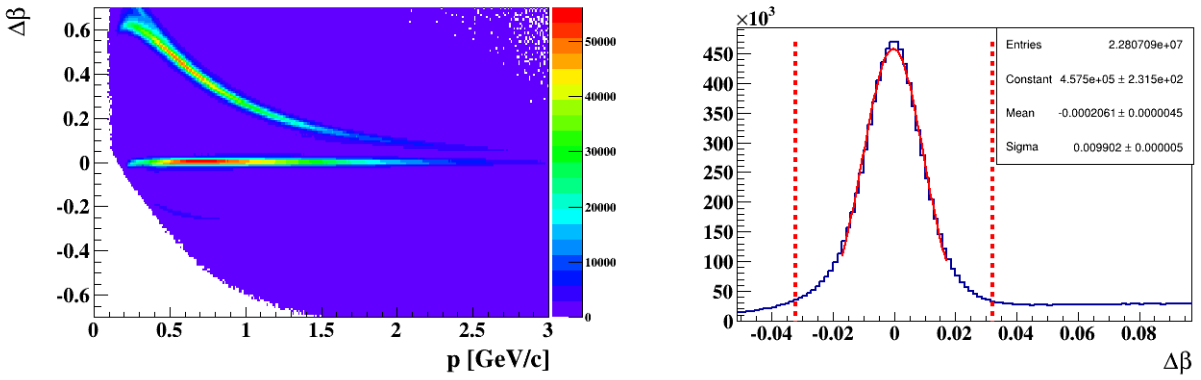

Figure 4.11: On the left: $\Delta\beta$ as a function of p for the detected positive particles after the fiducial cuts. On the right: one-dimensional distribution of $\Delta\beta$ zoomed in the region of the protons. The red dashed lines represent $\pm 3\sigma$ cuts around the mean to select good reconstructed protons.

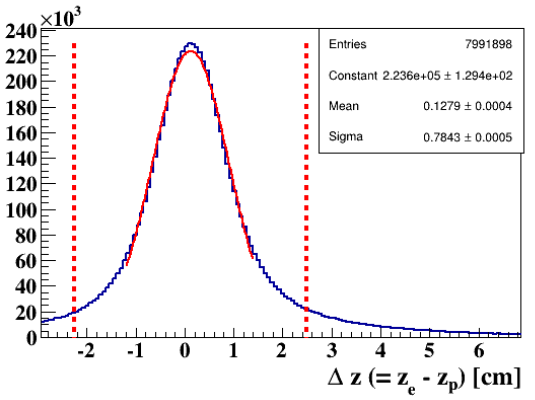

Figure 4.12: Δz distribution. The red dashed lines indicate $\pm 3\sigma$ cuts around the mean.

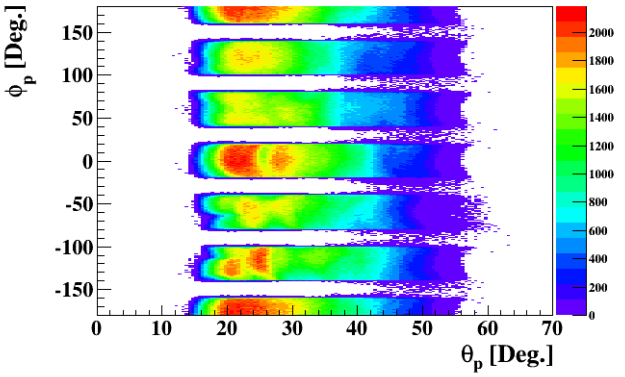

Figure 4.13: ϕ vs. θ for the selected protons.

4.1.3 Photon identification

CLAS is equipped with two calorimeters that can detect photons: the IC, covering polar angles from 4° to 14°, and the EC, covering polar angles from 8° to 45°. Like for the other particles, in addition to the coincidence with one good electron, we require a set of criteria to ensure the quality of the detected photons. Due to the efficiency constraints in both calorimeters, we restrict the energy of the selected photons to be greater than 300 MeV. Further requirements are applied depending on each detector.

EC photons

A particle has to fulfill the following conditions in order to be considered a good photon:

- Neutral charge: this condition is achievable via the information from the drift chambers. A photon candidate in the EC must not be associated with a track in the DCs.
- EC fiducial cut: like for the electrons, this requirement is made to reject the photons which

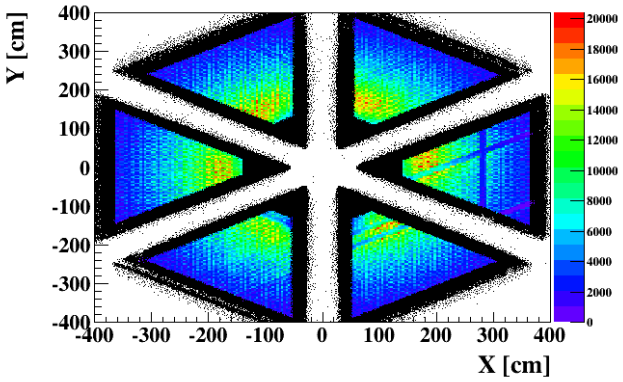

Figure 4.14: XY projection of the neutral particles in the EC. The coloured regions represent photons which passed the EC fiducial cuts, while the black regions are out of the fiducial cuts.

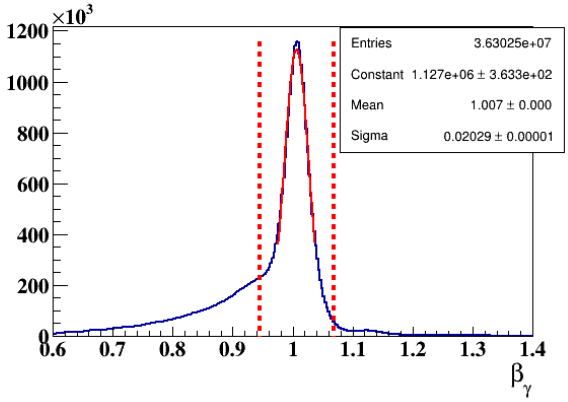

Figure 4.15: β distribution of neutral particles in the EC. The two vertical lines represent $\pm 3\sigma$ cuts around $\beta = 1$ to select photons.

are detected at the edges of the EC. Figure 4.14 shows the XY plane distribution of EC neutral particles. We use the cuts: 100 cm < U, V < 360 cm, and W < 390 cm, to select the EC photons.

- Velocity (β) cut: the scattered electron and its associated photon originate from the same vertex. Knowing the electron vertex ($\overrightarrow{V_e}$) and the photon hit position in the EC ($\overrightarrow{R_\gamma}$), one can calculate the photon velocity β as:

$$\beta_\gamma = \frac{l}{ct} = \frac{|\overrightarrow{R_\gamma} - \overrightarrow{V_e}|}{c(t_{EC} - t_{trg})} \tag{4.5}$$

where l is the traveled distance from the vertex to the hit point in the EC. The traveling time (t) is calculable from the relative difference between the trigger time (t_{trg}) and the EC timing (t_{EC}). Figure 4.15 shows the β distribution of the neutral particles in the EC.

IC photons

For IC photons, we use the following cuts:

- IC fiducial cuts: the photons which hit the edges of the IC deposit only part of their energies within the calorimeter. For this reason, we reject the photons which hit the innermost or the outermost rings of the IC [115]. Figure 4.16 illustrates this cut.
- Møller electrons reduction: a two-dimensional plot of photon polar angles as a function of the energy shows an overcrowded region at low θ and low energy. This can be seen in figure 4.17. This region is mostly populated by the Møller electrons and must be excluded from the analysis. We optimized a linear cut for this region, shown by the black dashed line. The vertical extension of this line shows the minimum energy cut (E_γ > 300 MeV).

To summarize the photon selection, the two-dimensional distribution of azimuthal angle as a function of polar angle for IC and EC photons is shown in figure 4.18.

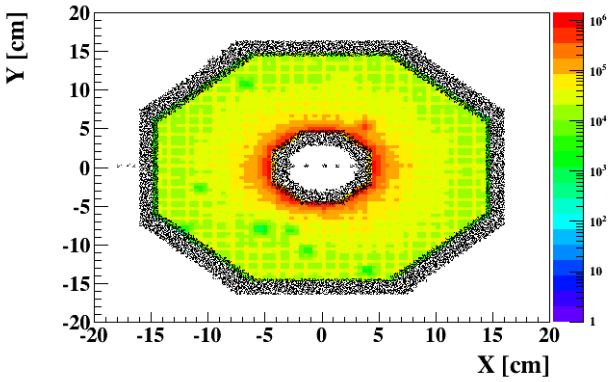

Figure 4.16: XY distribution for the IC photons. The photons which hit the black innermost and outer regions are excluded from this analysis.

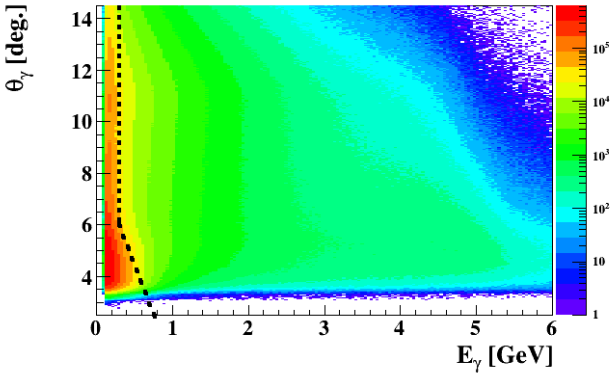

Figure 4.17: θ versus E for the IC photons which passed the fiducial cuts. The black dashed line represents the cut to reject the Møller electrons.

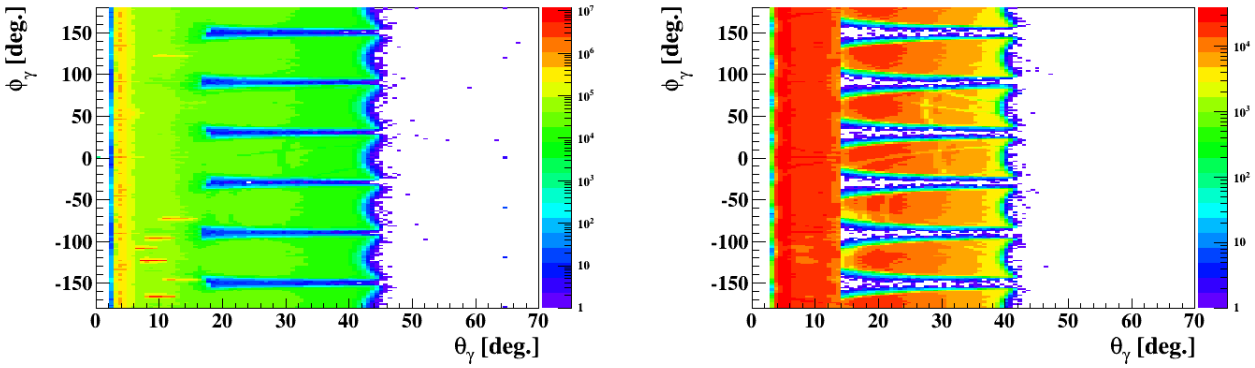

Figure 4.18: On the left: ϕ versus θ for all the neutral particles before the cuts. On the right: ϕ vs. θ for the the selected photons.

4.1.4 Helium-4 identification

Details on the RTPC's structure and the definition of the different variables were given in chapter 3, section 3. In the following, we show the cuts to select the RTPC good tracks with a 6-GeV beam energy. The distributions will be shown for the two independent modules of the RTPC separately, labelled as left and right sides. The cuts are:

- Coincidence with one and only one good electron.
- Number of active pads greater than 3: the track has to have recorded hits from at least four different readout pads.
- Positive track curvature.
- Vertex cut: figure 4.19 shows the z-vertices of the positive-curvature tracks. The difference between the heights of the two distributions indicate that the two modules of the RTPC have different performances.

- Track helix-fit quality: figure 4.20 shows the χ^2 distributions for the positive tracks originating within the RTPC. We apply $\chi^2 < 3.5$ to select good ^{4}He tracks.
- *sdist* and *edist* cuts: figures 4.21 and 4.22 show the *sdist* and *edist* distributions, for the positive tracks, originated within the RTPC, and having good χ^2 values.
- Z-vertex cut: like for the protons, the RTPC's reconstructed track has to originate from the same electron vertex. Figure 4.23 shows the difference between the z of the reconstructed vertices of the electron and the associated RTPC tracks.
- Fiducial cuts: to remove the tracks which hit the mechanical supports between the two model of the RTPC, and which hit the upstream of the targets holder. Figure 4.24 illustrates the effect of the fiducial cuts in addition to the previous cut, in which azimuthal angle is plotted as a function of polar angle for the tracks in the RTPC before, and after all the cuts.

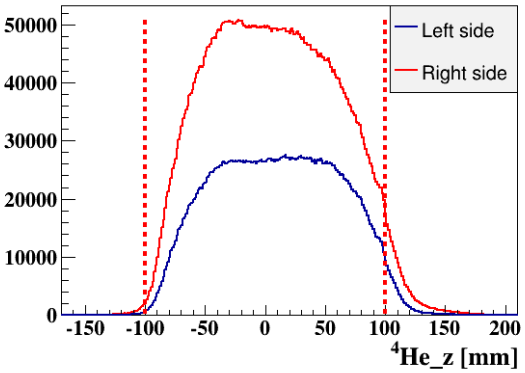

Figure 4.19: z-vertices for the reconstructed positive tracks with respect to the RTPC center (-64 cm with respect to the CLAS center), in the two modules of the RTPC. We chose the cut -100 mm < z < 100 mm to select good tracks.

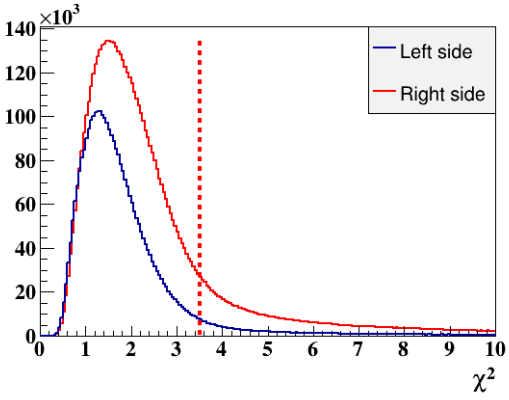

Figure 4.20: χ^2 distribution for the tracks in the two modules of the RTPC, with the cut we require to select good tracks: $\chi^2 < 3.5$.

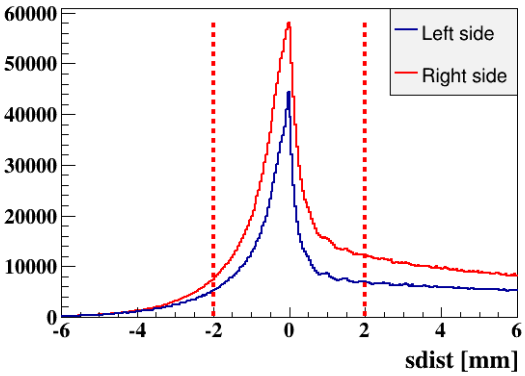

Figure 4.21: *sdist* distribution for the positive tracks in the RTPC. $|sdist| < 2.0$ mm cut is applied to select good tracks.

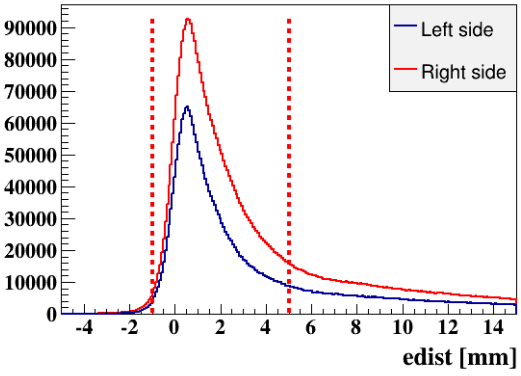

Figure 4.22: *edist* distribution for the positive tracks in the RTPC. We require -1.0 mm < *edist* < 5.0 mm to select good tracks.

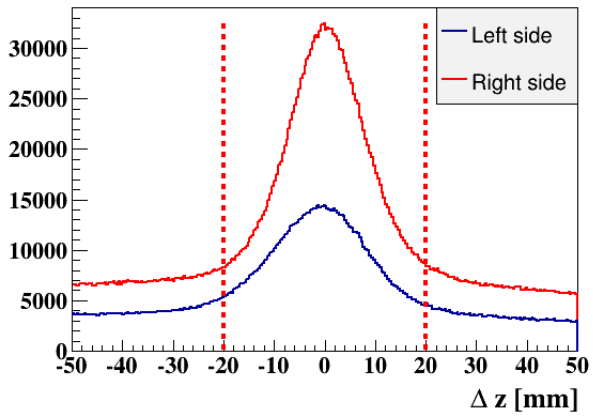

Figure 4.23: Difference between the z-vertices of the detected electron and the good track in the RTPC. We require the absolute value of Δz to be less than 20 mm.

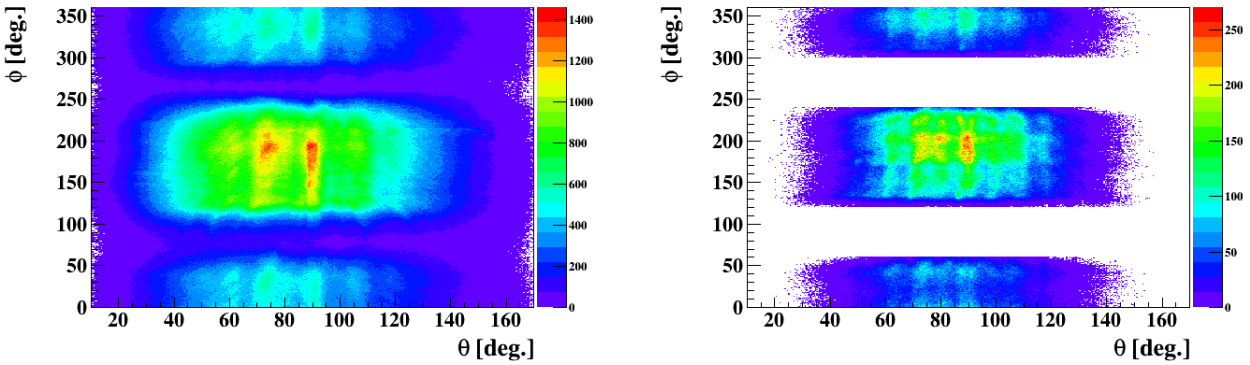

Figure 4.24: On the left: ϕ vs. θ for the positive-curvature tacks in the RTPC before the cuts. On the right: the same distribution after all the cuts.

4.1.5 π^0 identification

In this analysis, we identify the π^0s with the goal of DVCS background subtraction as will be addressed in section 5.5. The π^0 identification is based on its two real photons decay mode ($\pi^0 \rightarrow \gamma\gamma$), with a branching ratio around 98.8%. In our experimental configuration, the reconstructed neutral pions can be categorized into three topologies: ICIC (the two photons are detected in the IC), ICEC (one photon in the IC and the second in the EC), and ECEC (the two photons are detected in the EC). The nominal mass of the π^0 is 0.135 GeV/c^2. The reconstructed invariant mass of the detected pair of photons can be seen in figure 4.25, for the three topologies. One can see clear peaks corresponding to the neutral pions in the three distributions.

One can conclude from the mean and sigma values of the distributions in figure 4.25 that the IC has a better energy resolution than the EC. About 97% of the simulated DVCS events, as can be seen in the bottom-right plot, have the real photon emitted at very forward angles covered by IC. For these reasons, we chose to exclude the DVCS events which have their photons in the EC.

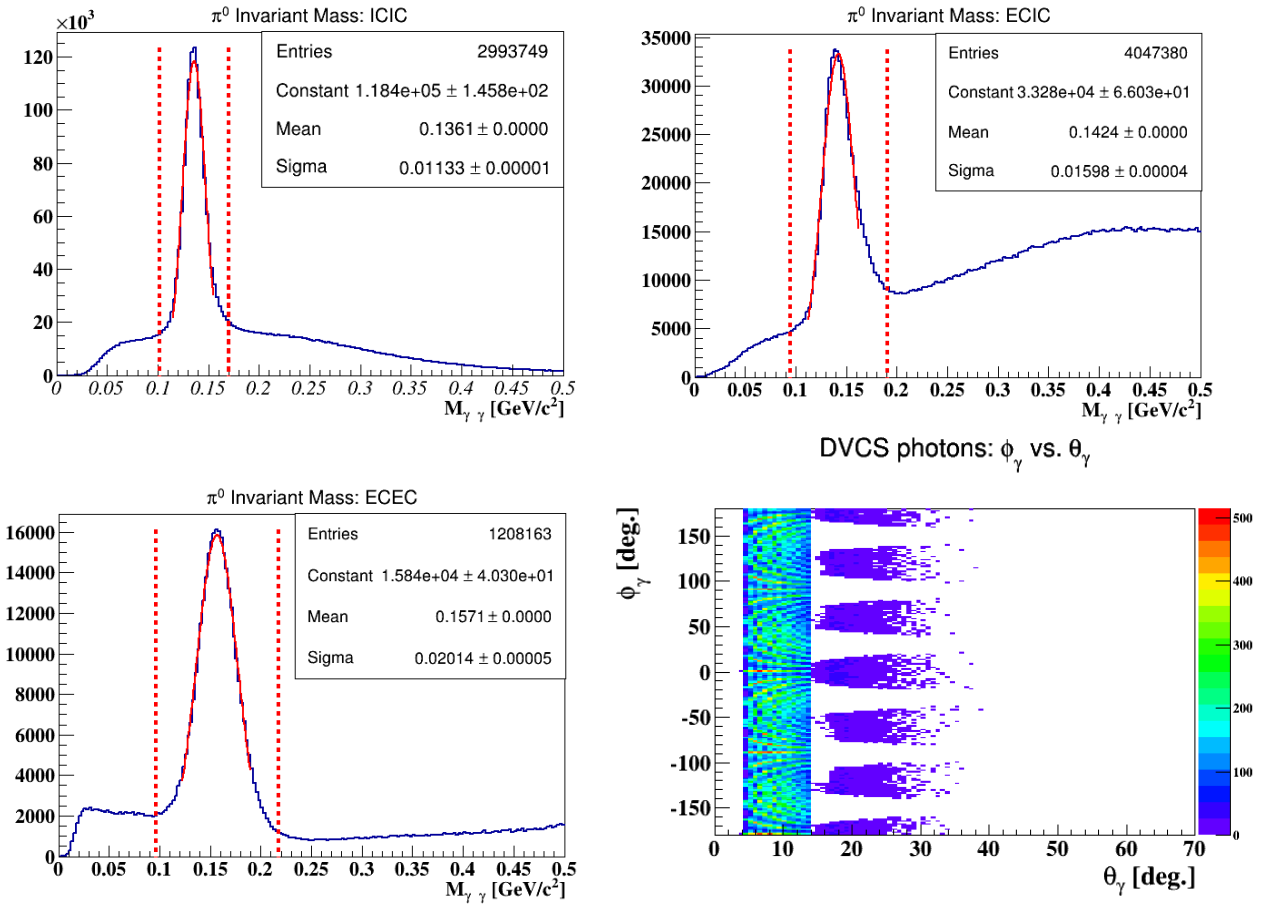

Figure 4.25: The reconstructed invariant mass of the photon pairs in the three topologies: ICIC, ECIC and ECEC. On the bottom-right: ϕ vs. θ distribution for the simulated DVCS photons, shown that most of the DVCS photons are located in the IC.

Hence we are left with the two π^0 topologies, ICIC and ICEC, for the background subtraction as will be addressed later in this chapter.

4.2 Simulation

The Monte-Carlo simulation is used in this analysis for two goals: understanding the behaviour of the particles of interest in the detectors, and computing the acceptance for the DVCS background subtraction. The key stages of the simulation are summarized in figure 4.26: Monte-Carlo generated events pass in a GEANT3 simulation (GSIM) for the CLAS detector, then are processed with a package called GPP to add resolution and efficiency effects, and finally are reconstructed by a package named RECSIS, from which we obtain the physical quantities of each particle, like it is done for real data. In the following, each simulation stage will be briefly presented.

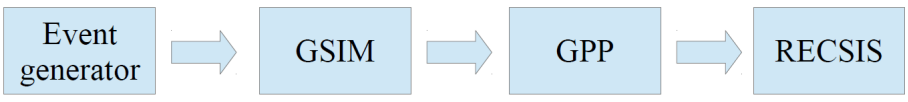

Figure 4.26: The scheme shows the main simulation steps.

4.2.1 Event generator

Events are generated randomly in the measured ranges of Q^2, x_B, t, and ϕ . Then, they are weighted with a parametrization of the cross section which roughly reproduces the DVCS and exclusive π^0 electroproduction data [115]:

$$\frac{d^4\sigma}{dQ^2 dx_B dt d\phi} \propto \left(\frac{Q_0^2}{Q^2}\right)^{\alpha} * \frac{1}{1+(\frac{x_B-x_c}{c})^2} * \frac{1}{(1+bt)^{\beta}} * (1-d(1-cos(\phi))). \tag{4.6}$$

This parametrization is the product of four factors which reproduce the DVCS and π^0, characteristics as follows:

- the Q^2-dependent term accounts for the depth of the interaction: Q_0^2 is the minimum allowed value and the α is a parameter which controls the shape of the distribution.
- the x_B term accounts for the dependence of the cross section on the parton distribution functions, with x_c the mean value of the Bjorken variable x_B.
- the t term accounts for the t-dependence of the elastic form factors of the helium and of the proton, via the parameters b and β.
- the ϕ term accounts for the cross section dependence on this angle, via the parameter d. The DVCS and the BH have a different behaviour than the π^0 exclusive events.

Table 4.1 shows the values of the parameters used for the cross section parametrization of the four channels of interest: $e^4He\gamma$, $e^4He\pi^0$, $ep\gamma$, and $ep\pi^0$.

Parameter	$e^4He\gamma$	$e^4He\pi^0$	$ep\gamma$	$ep\pi^0$
Q_0^2	1.0 GeV^2/c^2	1.0 GeV^2/c^2	1.0 GeV^2/c^2	1.0 GeV^2/c^2
α	2.5	3.0	1.5	1.5
b	-11.0 GeV^2/c^2	-8.8 GeV^2/c^2	-1.408 GeV^2/c^2	-1.408 GeV^2/c^2
β	12.0	7.3	4.0	1.5
x_c	0.2	0.3	0.2	0.5
c	0.2	0.3	0.2	0.5
d	0.4	0	0.4	0

Table 4.1: Values of the parameters adapted in our event generator.

4.2.2 GSIM

GSIM is a GEANT3-based simulation of the CLAS detector, developed by the CLAS collaboration [116]. This simulation takes into account all the experimental environment, such as the target's position, materials, and geometry, and also the various sub-detectors' materials and geometries, to reproduce the behaviour of particles traversing the detector.

4.2.3 GPP

For the purpose of making the simulation more realistic, the output of GSIM is fed to the GSIM Post-Processing (GPP) package. This package applies resolution effects on the different measured quantities, and also reads efficiency maps to match the simulation to the real experiment. The resolutions are categorized into three groups, time, position, and energy resolution. In

the following, we present the techniques used in this work to extract the smearing factors for the simulation.

SC time smearing

The GPP takes a single factor to smear the time in a Gaussian form. Figure 4.27 shows an illustration of the time smearing effects, in which $\Delta\beta$ for the protons ($\Delta\beta = \beta_{measured} - \beta_{calculated}$) is compared for data and simulation. The chosen SC smearing factor is 2.1.

DCs position smearing

The GPP uses three factors to smear the positions of the hits in the DCs, in a Gaussian form. These smearing factors are extracted from comparing simulation to data in terms of the Time-Based Tracking (TBT) residual distributions, i.e. the deviation of the hits in the DCs from the fitted track. Figure 4.28 shows the experimental, initial simulated, and smeared simulated residual distributions for the collected good electrons and protons. The extracted smearing factors are: (a, b, c) = (1.1, 0.85, 1.1), where the factor a stands for smearing of DC1, b for DC2, and c for DC3. One can see the smearing effects by looking to the values of σ from the fit in each Super-Layer (SL). We conclude that these factors match the simulation to the data.

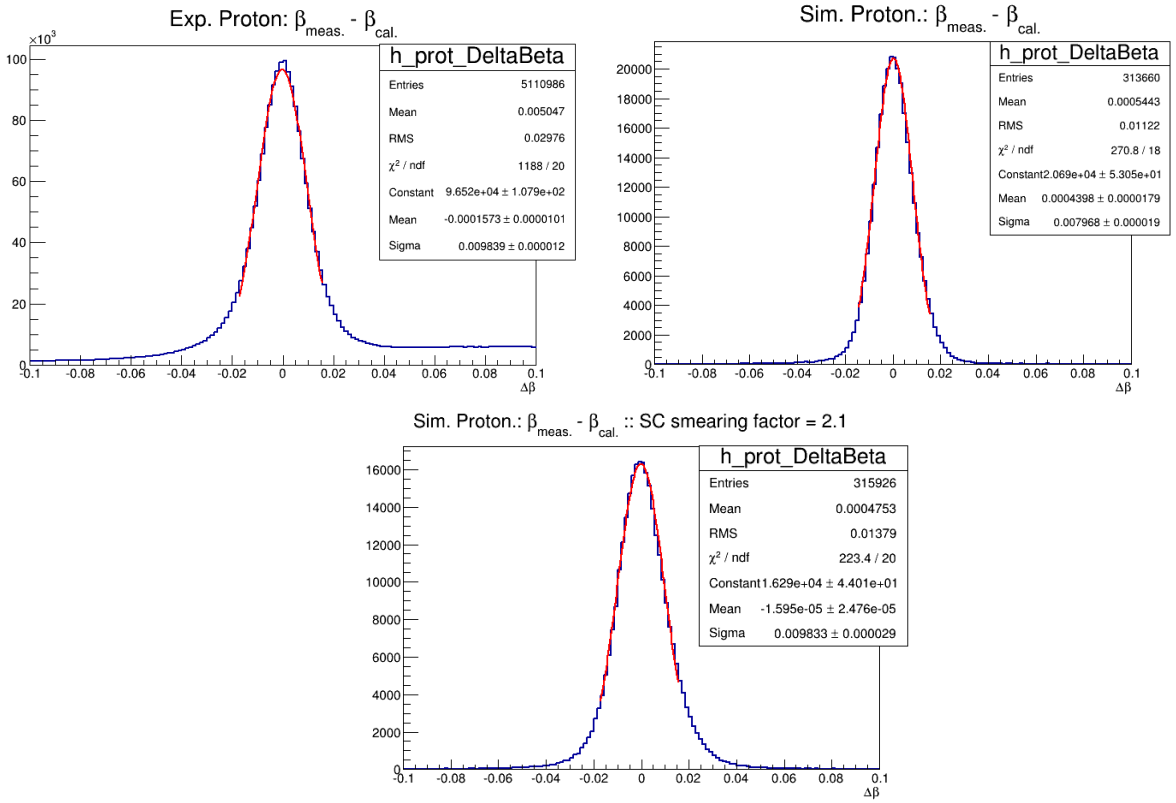

Figure 4.27: Illustration of the SC time smearing via the $\Delta\beta$ distributions for the protons. On the top left: $\Delta\beta$ distribution of the experimental data. On the top right: the simulated data without smearing. On the bottom: the simulated data after SC time smearing with a factor equal to 2.1.

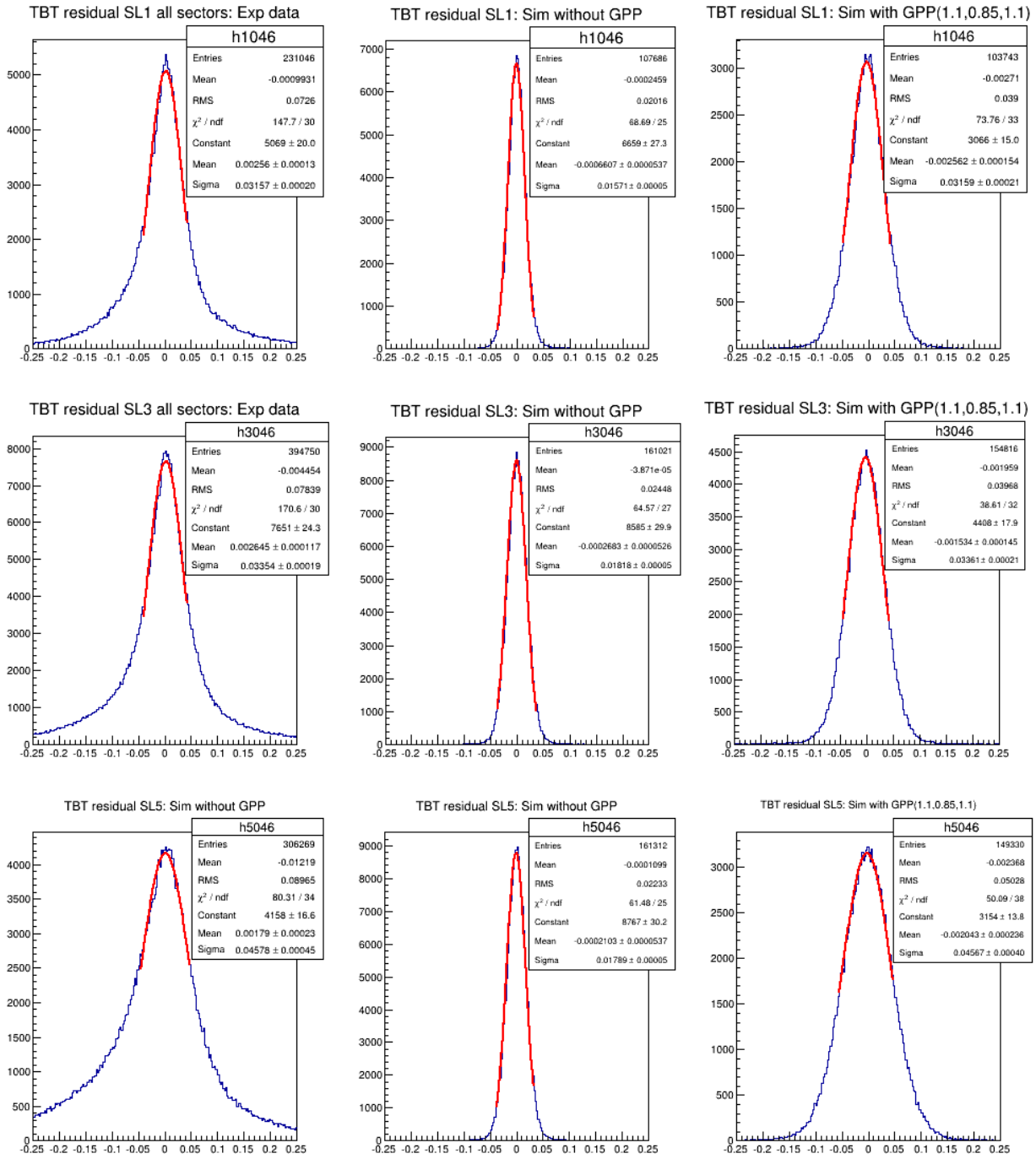

Figure 4.28: Time-Based Tracking (TBT) residual distributions for the electrons and the protons in the first super-layer (top panel), the second super-layer (middle panel) and the third super-layer (bottom panel) of the experimental data (first column), of the simulation without GPP (second column), and the simulation with GPP DC-position smearing factors: 1.1, 0.85, and 1.1 for a, b, and c respectively.

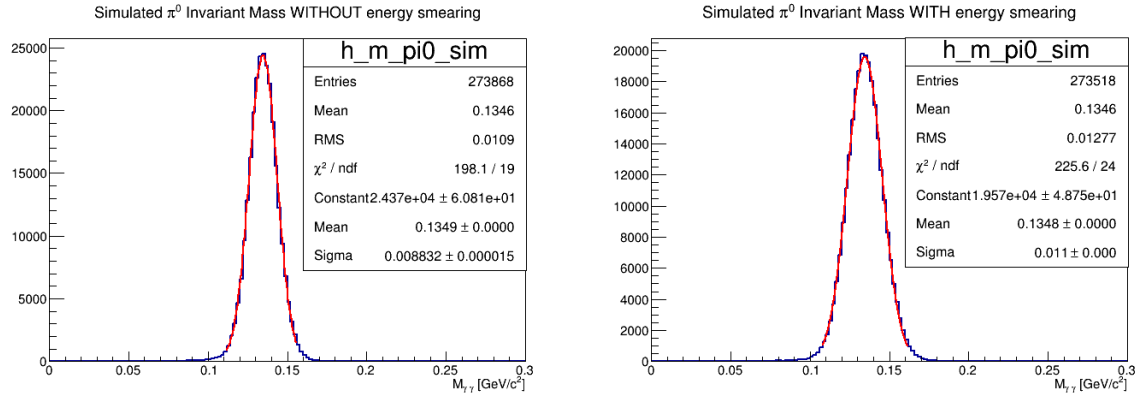

Figure 4.29: The invariant mass of the Monte-Carlo simulated π^0 without IC energy smearing, on the left, and with smearing, on the right.

IC energy smearing

An energy smearing for the IC photons is also needed. The GPP software uses three factors to perform this smearing: *ic_a*, *ic_b*, and *ic_c*, where *ic_a* accounts for the smearing of the width of the noise around zero using a Gaussian, while *ic_b* and *ic_c* are the smearing factors for the ADC values, using Gaussians as well. Our parameters are: 0.008, 0.036, and 0.024 respectively. Figure 4.29 shows the effect of these smearing factors on the simulated invariant mass of the π^0. The associated experimental distribution can be seen on the top left plot of figure 4.25. One notices that the smeared width of the simulated distribution matches the measured experimental one.

4.2.4 RECSIS

RECSIS is the reconstruction package of CLAS which is used for both data and simulation. The detector responses, in terms of ADCs and TDCs, are converted by RECSIS into physical meaningful physical quantities, such as momentum, using lookup tables. In this process, the thresholds on the different detectors (DCs, CCs, ECs, SCs, IC, and RTPC) are applied to filter the signals before the reconstruction procedures. After this reconstruction, the outputs of RECSIS for the experimental and the simulated events can be compared directly, as will be presented in the next section.

4.2.5 RTPC fastmc

All the sub-detectors of CLAS are implemented in the GSIM GEANT3 simulation except for the RTPC, for which a GEANT4 simulation has been developed. As a first step, we replace the RTPC's simulation by a fast Monte-Carlo (fastmc) package at the level of the event generator to make the simulated ^4He more realistic and matching the data. This fastmc smears the ^4He kinematics and applies the RTPC's acceptance. Regarding the smearing, the momentum, polar angle, azimuthal angle and z-vertex of the ^4He are smeared with Gaussians using the observed tracking resolutions of the RTPC (see chapter 3, section 5). For the acceptance, the fastmc:

- ensures that the ^4He track intersects the cathode and the GEMs of the RTPC.

- removes the tracks which hit the mechanical supports between the two modules of the RTPC.
- removes the track if it goes to the upstream end of the target's holder.
- applies the RTPC's thresholds on the momentum and the polar angle.

The fastmc does these functions on the Monte-Carlo generated ^4He for the channels $e^4He\gamma$ and $e^4He\pi^0$. The other particles are fed to GSIM through the previously mentioned simulation-reconstruction chain procedures.

4.3 Kinematic corrections

The simulation enables us to extract kinematic corrections for the different particles, by comparing the reconstructed physical quantities from the simulation to the initially generated ones. In general, the reconstructed azimuthal angles of all the particles are consistent with the generated ones, while the reconstructed polar angles and momenta show some deviations. Therefore, corrections are required. In the following, the electron and the proton corrections are applied on both data and simulation, while the simulated photons are corrected differently from the experimental ones, as will be explained and justified.

4.3.1 Electron corrections

The reconstructed kinematics of the simulated electrons are roughly consistent with the generated quantities, as can be seen in figure 4.30. Nevertheless, we extracted and applied corrections on the electrons to achieve a higher precision. The corrected polar angles and momenta take the form:

$$\theta_{corr.} = \frac{\theta_{rec.}}{f(\theta_{rec.})} \qquad p_{corr.} = \frac{p_{rec.}}{f(p_{rec.})} \tag{4.7}$$

where $f(\theta_{Rec.})$ and $f(p_{Rec.})$ are the functions shown, respectively, on the left and right plots of figure 4.30.

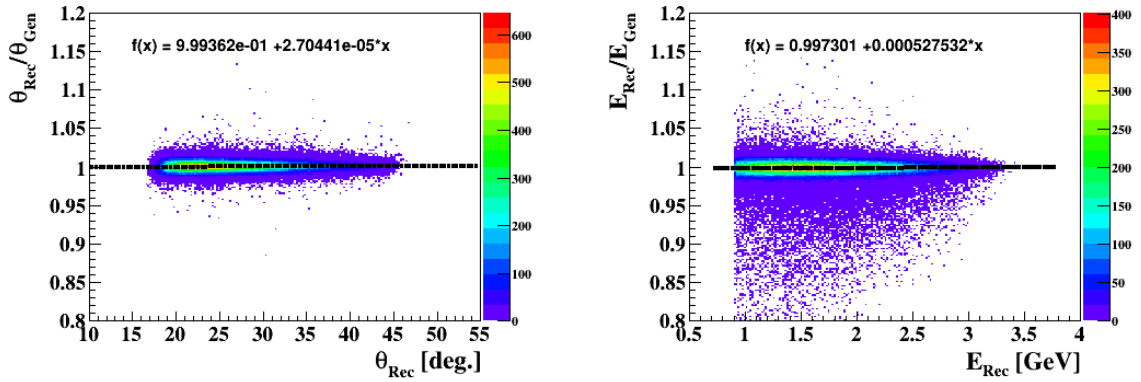

Figure 4.30: Electron corrections. On the left: The ratio of the reconstructed to the generated electron polar angles is plotted as a function of the reconstructed polar angle. The mean of the distribution is parametrized by the black curve. On the right: the momentum ratio (Rec/Gen) is plotted as a function of the reconstructed momentum and parametrized by the black curve .

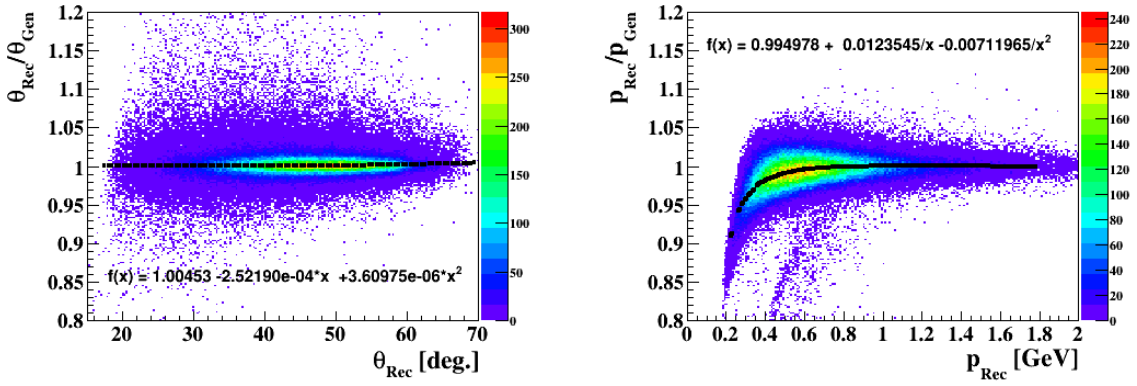

Figure 4.31: Proton corrections. On the left: the reconstructed-generated polar angle ratio is plotted as a function of the reconstructed angle and fitted with the black curve. On the right: the momentum ratio is plotted as a function of the reconstructed momentum.

4.3.2 Proton corrections

The same procedures for the extraction of the kinematic corrections of the electrons have been carried out for the protons. The results can be seen in figure 4.31. The corrected polar angles and momenta are obtained using equations 4.7 and the functions shown on each plot of figure 4.31.

4.3.3 IC photon corrections

The IC calibration shows variations over the running period due to changes in the setting, such as shifts in the beam position. Corrections of the IC simulated photons are extracted from comparing them to the generated photons, while, on the experimental side, further corrections are extracted by comparing the reconstructed invariant mass of π^0 to its theoretical mass.

4.3.3.1 Simulated IC photons

The simulated IC photons shows non-negligible polar angle and energy deviations from the expected kinematics. This can be seen in figure 4.32. These deviations are almost systematic shifts, in which the polar angle deviation might be coming from badly defined geometrical values within GSIM. For these photons, we followed the same techniques of comparing the reconstructed quantities to the generated ones in order to extract the correction functions.

As an illustration of the corrections, figure 4.33 shows the squared $e\gamma X$ missing mass distribution for the simulated $ep\gamma$ DVCS events before the corrections, on the left, and after the corrections, on the right. In this configuration, the missing particle is the proton, such that the expected mean value should be the mass squared of the proton ($0.938^2 = 0.8798$). The right value is obtained after the corrections.

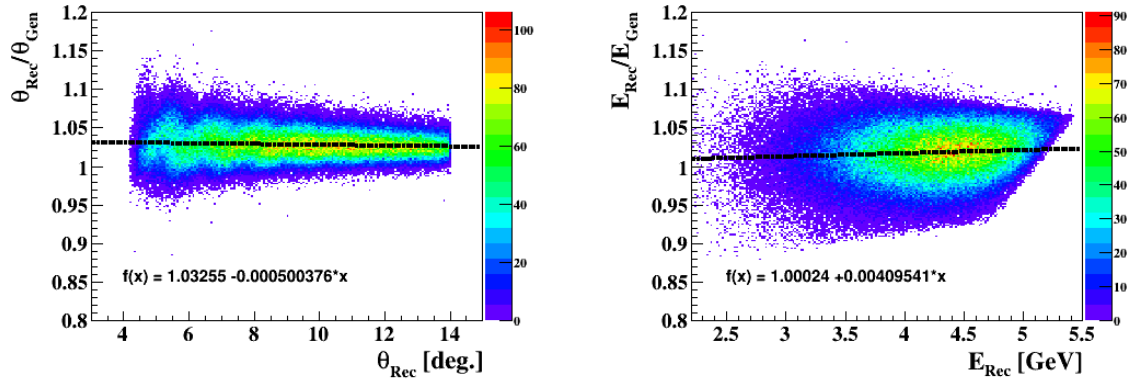

Figure 4.32: Corrections for the simulated IC photons. On the left: the reconstructed-generated polar angle's ratio is plotted as a function of the reconstructed polar angles. On the right: the energy ratio is plotted.

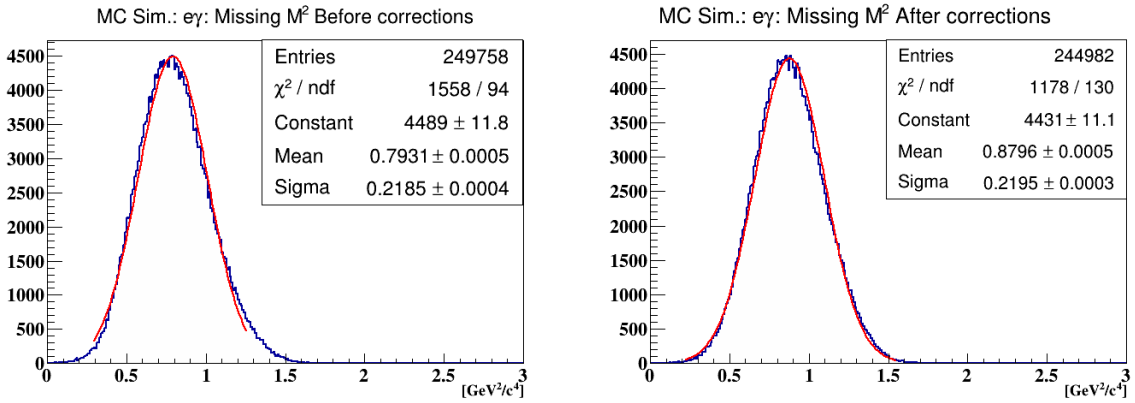

Figure 4.33: An illustration of the corrections in terms of the squared $e\gamma X$ missing mass distribution for the $ep\gamma$ simulated DVCS events.

4.3.3.2 Experimental IC photons

For the experimental IC photons, we used the reconstructed invariant mass of the π^0 in the ICIC topology to ensure the consistency of the IC calibration over the experimental running time. In this investigation, we require each π^0 photon to have a minimum energy of 500 MeV in order to avoid low efficiency effects of the IC at low energies. Moreover, the energy difference between the two photons of the π^0 has to be less than 500 MeV for the purpose of extracting corrections, as will be explained later in this section.

In the CLAS-EG6 experiment, the reconstructed π^0 displays a linear dependence on the energy, as can be seen in figure 4.34. In order to ensure the consistency of the calibration over time, we constructed this mass-energy dependence for the individual runs. Figure 4.35 shows the extracted slope (α) and offset (β), from the linear fits of the mass versus the energy of π^0, as a function of run number. One notices a non-negligible variation over the experimental running period due to changes in the experimental conditions, such as changes in the triggers and the beam position.

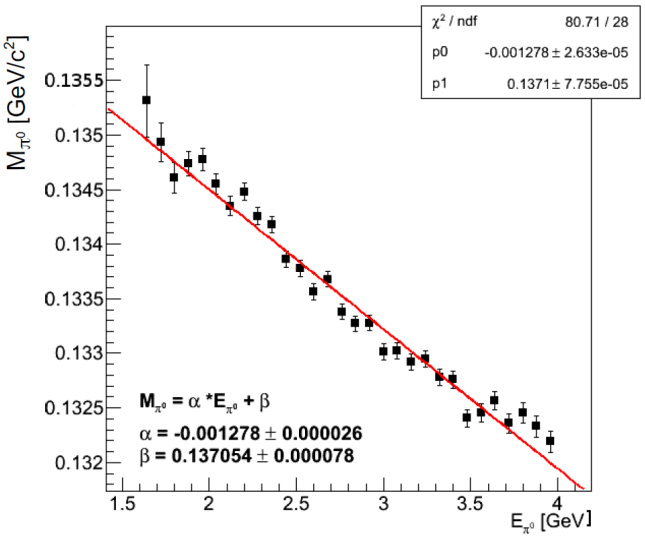

Figure 4.34: The invariant mass of the reconstructed π^0 as a function of its energy. The red line represents a linear fit.

To extract energy corrections for IC photons, the two distributions of figure 4.35 have been parametrized by functions of the form:

$$\alpha(x) = c_0 + c_2\left[e^{-c_3(x-c_1)} - e^{-c_4(x-c_1)}\right], \tag{4.8}$$

$$\beta(x) = p_0 + p_2\left[e^{-p_3(x-p_1)} - e^{-p_4(x-p_1)}\right], \tag{4.9}$$

where x is the run number, the values of the parameters of α and β can be found in Appendix C (tables C.1 and C.2 respectively). The requirement of a 500 MeV maximum difference between the two photons allows to assume that the two photons have approximately the same energy ($E_{\pi^0} = 2E_\gamma$). Then, the correction take the form:

$$\frac{E^{\pi^0}_{corr}}{M^{\pi^0}_{Theoretical} = 0.135GeV} = \frac{E^{\pi^0}_{uncorr}}{M^{\pi^0}_{uncorr}} \tag{4.10}$$

$$\Longrightarrow E^{\gamma}_{corr} = \frac{0.135 * E^{\gamma}_{uncorr}}{\alpha(run) * 2 * E^{\gamma}_{uncorr} + \beta(run)} \tag{4.11}$$

which takes as input the measured uncorrected photon energy (E^{γ}_{uncorr}), and the α and β parameters, which depend on the run number. It then returns the corrected energy (E^{γ}_{corr}).

After these corrections, our collaborators at Argonne National Laboratory, C. Moody and N. Baltzell, have observed a mass-radial dependence of the reconstructed π^0's [118], in the ICIC topology. Their observation can be seen on the top left plot of figure 4.36. To correct for this unexpected behaviour, additional corrections are required. In this correction, the π^0's are selected such that the difference between the two photons radial distances is less than 1 cm. After that, the fractional invariant mass of the π^0's, i.e. the ratio between the theoretical mass of π^0 to the experimentally reconstructed mass, is constructed as a function of the average energy of the two photons, at different radial distances. It is then linearly fitted. The results can be seen in figure 4.36.

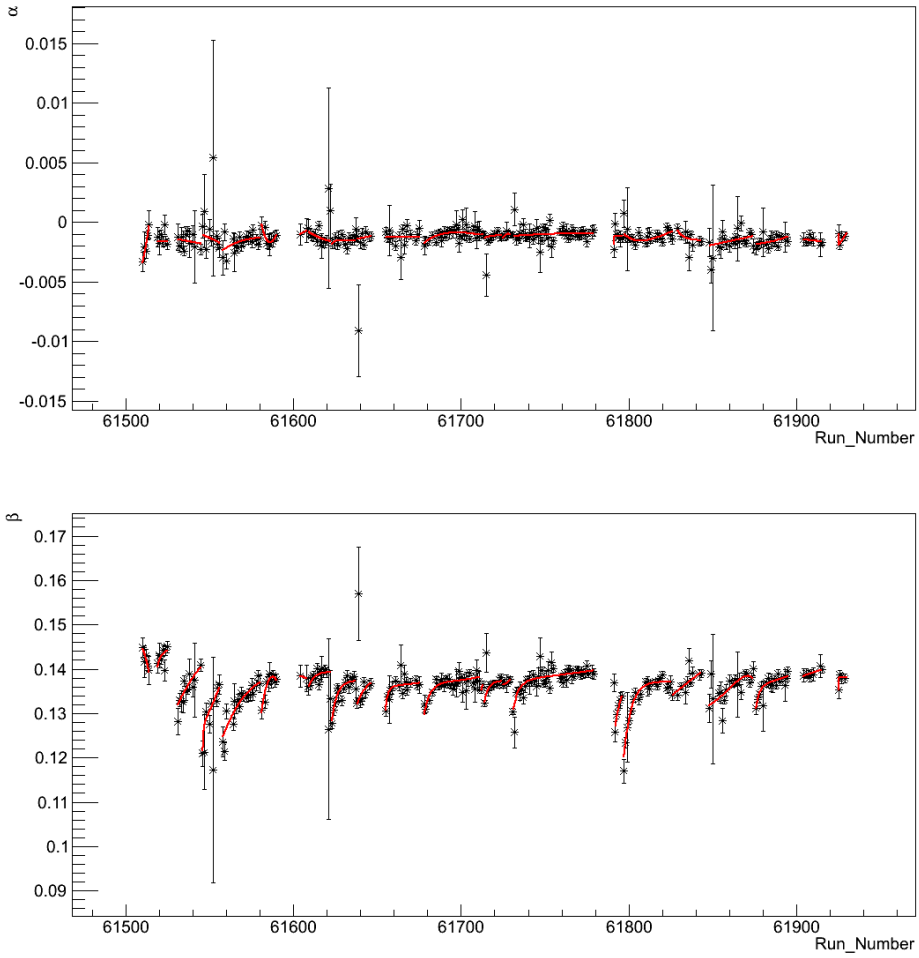

Figure 4.35: The slope (α) and the offset (β) from linear fits of M^0_π vs. E^0_π, as a function of run number. The red lines represent the fitting functions.

Assuming that the energy correction returns a corrected energy labelled as E^γ_{corr}, the final corrected energy (E^γ_{final}) can be written as:

$$E^\gamma_{final} = \frac{E^\gamma_{corr}}{2 * S(r) * E^\gamma_{corr} + O(r)} \tag{4.12}$$

where S(r) and O(r) are the slope and the offset fitted as a function of the radial distance "r". These functions are polynomials and their parameters can be seen in figure 4.36.

As results of the latter corrections, figure 4.37 shows the fractional invariant mass distributions for the neutral pions as a function of the electron z-vertex, before the corrections, on the left, and after the corrections, on the right. One can see the linear dependence before the corrections, and how this issue was resolved via the radial corrections.

The biggest improvements have been observed for the DVCS events in both channels, coherent and incoherent. Figure 4.38 shows the missing energy distribution of the coherent DVCS events, on the left, and of the incoherent channel, on the right. Regarding the coherent channel, one sees

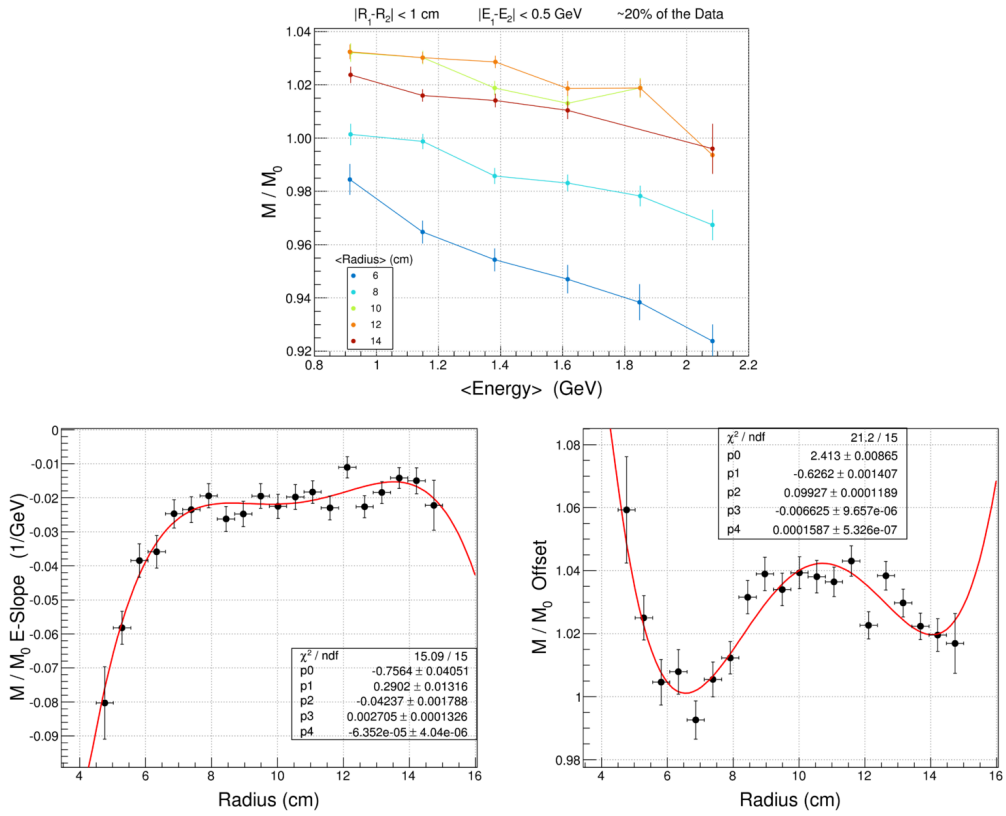

Figure 4.36: The IC energy corrections are applied before the radial corrections. On the top: the fractional mass is plotted for different radial distances (different colors) as a function of the two photons average energy. On the bottom: the slope (on the left) and the offset (on the right) resulting from the linear fits of the top distributions. These figures are from [118].

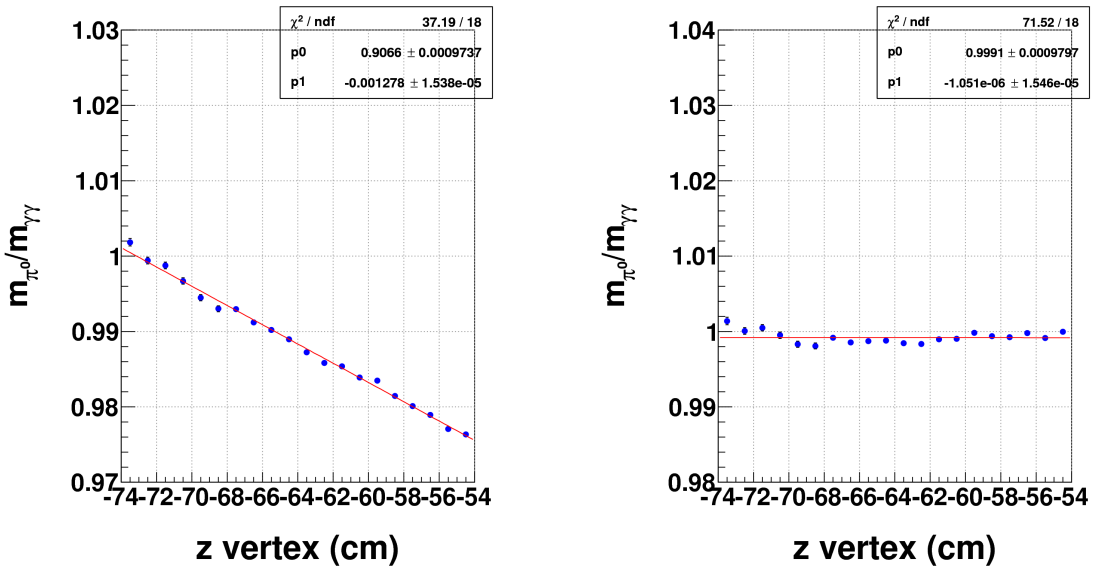

Figure 4.37: On the left: the fractional invariant mass of ICIC π^0 as a function of the electron z-vertex after the energy corrections, and before the radial corrections. On the right: the same fractional mass distributions after both corrections, energy and radial.

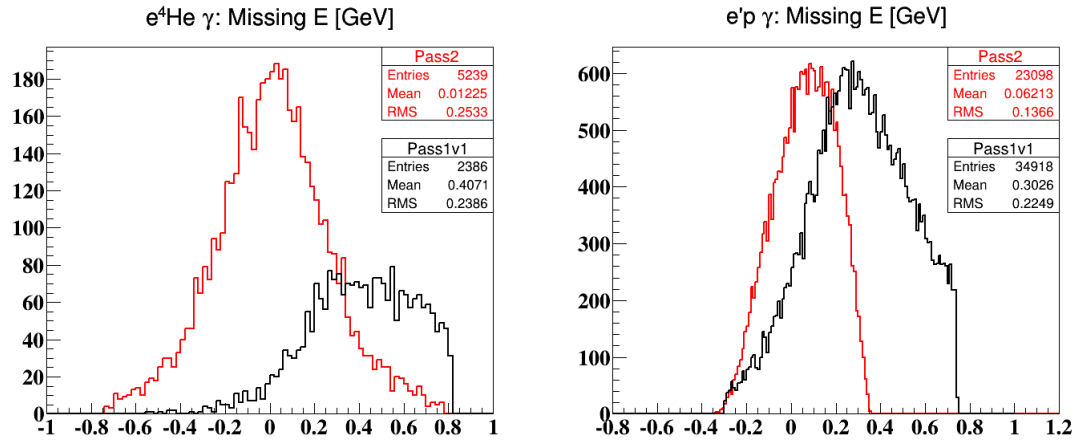

Figure 4.38: The distributions in black are without the IC photon corrections and in red with the corrections. On the left: the missing energy distribution of $e^4He\gamma$ DVCS events for data. On the right: the missing energy distribution of $ep\gamma$ DVCS events for data.

that these corrections shift the peak to the nominal value (zero value) and thus more DVCS events are collected. For the incoherent channel, these corrections clean most of the background when one combines the different exclusivity cuts, as will be shown later in this chapter.

CHAPTER 5

DVCS beam-spin asymmetry extraction

In the previous chapter, the events were filtered to select the ones which have one and only one good electron, and other good particles in coincidence with the electron. This chapter explains the procedure we used to extract the beam-spin asymmetry observable following this order: clean the DVCS data sample by choosing good run list, ensure the exclusivity of the selected events by imposing the kinematical cuts, subtract the background by combining data with simulation, and binning the identified DVCS events. This chapter contains also an estimation of the systematic uncertainty contribution from each source on the measured beam-spin asymmetry.

In the following, the selection procedures of the coherent DVCS events is detailed and generalized to the cases of incoherent DVCS, the coherent π^0, and the incoherent π^0 channels.

5.1 Coherent channel

5.1.1 Good run list

In principle, with constant beam luminosity, target density and pressure, the event rate has to be constant over the experimental time. Due to the changes in the experimental conditions, such as changing a trigger in a detector, a slight shift in the beam position or a system failure somewhere, this rate changes. We minimize the effects of these changes on the reconstructed events by selecting the good runs. To this aim, we monitor the ratio of the number of the good tracks reconstructed in the RTPC to number of the detected good electrons in CLAS (<tpc/e>) as a function of run number. Furthermore, we also look at this ratio in the six sectors of CLAS, as they are independent of each other and their performances might be different.

After the PID procedures, a run is considered good if:

- The integrated $< tpc/e >$ rate over the six sectors of CLAS is consistent with the neighboring runs.
- The six sectors show small fluctuations for each run.

Figure 5.1 shows the integrated and the sector-dependence of <tpc/e> for the individual runs. One notices a universal variation of this ratio over the three months of data taking. This can be attributed to changes in the RTPC, in particular the changes in the RTPC's trigger configuration and the drift gas proportions.

5.1.2 Coherent DVCS event selection

Events with one and only one good electron, one and only one good RTPC track and at least one good photon are considered good coherent DVCS candidates. Even though the DVCS reaction has only one real photon in the final state, events with more than one good photon are not discarded at this stage. This is motivated by the fact that some photons correspond to random

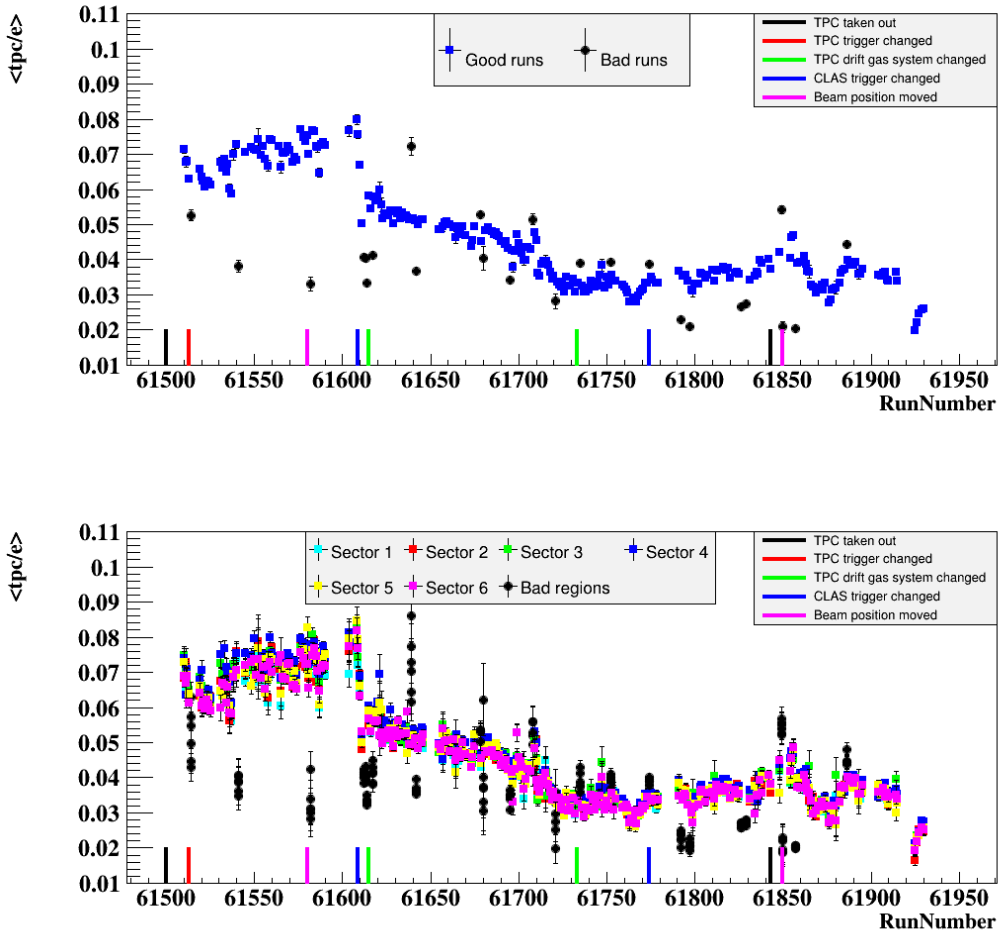

Figure 5.1: On the top: The integrated $< tpc/e >$ ratio (over the six sectors of CLAS) for the individual runs. The blue points refer to the good runs, while the black ones are the rejected ones. On the bottom: the $< tpc/e >$ ratio is shown for each sector of CLAS. The colored points indicate the different sectors of each good run, while the black ones are the sectors of the rejected runs without color difference between the sectors. In both plots, the experimental setting changes that might cause a change in the event rate are indicated with vertical colored lines.

coincidences and discarding these events results in losing good events. Then, events with one or more π^0 are removed from the coherent DVCS sample. After that, the most energetic photon in each remaining event is chosen as the DVCS photon. Next, to consider an event as a clean ^4He DVCS, it has to pass respectively two sets of requirements: DVCS characteristic cuts and exclusivity cuts.

DVCS characteristics

- $Q^2 > 1$ GeV^2: to ensure that the interaction occurs at the partonic level and the applicability of the factorization in the DVCS handbag diagram.

- The invariant mass of the system of the virtual photon and the target proton is greater than 2 GeV/c^2 to avoid the resonance region.

- $-t > -t_{min}$: the transferred momentum squared to the recoil ^4He has to be greater than a minimum value defined by the kinematics of the beam and the scattered electron as:

$$t_{min} = \frac{-Q^2 \cdot 2(1-x_A)(1+\varepsilon^2-\sqrt{1+\varepsilon^2})}{4x_A(1-x_A)+\varepsilon^2}, \tag{5.1}$$

where $\varepsilon^2 = \frac{4M^2_{^4He}x^2_A}{Q^2}$, $x_A = \frac{M_p \cdot x_B}{M_{^4He}}$ and M_p ($M_{^4He}$) is the proton (^4He) mass.

In the case of the proton DVCS, the variable x_A is replaced by the Bjorken x_B in the formula for t_{min}.

- $E_\gamma > 2$ GeV. This is a cleaning cut applied on the blue distributions in figure 5.2 to reduce the background in the DVCS sample before all the following exclusivity cuts.

Exclusivity cuts

The coherent DVCS reaction is:

$$e(\mathbf{P}_e) + \ ^4He(\mathbf{P}_{^4He}) \rightarrow e'(\mathbf{P}_{\mathbf{e'}}) + \ ^4He'(\mathbf{P}_{^4He'}) + \gamma(\mathbf{P}_\gamma) \tag{5.2}$$

where the symbols in the parentheses are the energy-momentum four-vectors. We define the additional four-vectors:

$$\begin{aligned}
\text{virtual photon vector } (\mathbf{P}_{\gamma^*}) &= \mathbf{P}_e - \mathbf{P}_{e'} && (5.3)\\
\mathbf{P}_X^{e^4He\gamma} &= \mathbf{P}_{\gamma^*} + \mathbf{P}_{^4He} - (\mathbf{P}_\gamma + \mathbf{P}_{^4He'}) && (5.4)\\
\mathbf{P}_X^{e^4He} &= \mathbf{P}_{\gamma^*} + \mathbf{P}_{^4He} - \mathbf{P}_{^4He'} && (5.5)\\
\mathbf{P}_X^{e\gamma} &= \mathbf{P}_{\gamma^*} + \mathbf{P}_{^4He} - \ \mathbf{P}_\gamma && (5.6)
\end{aligned}$$

The exclusivity of the coherent DVCS reaction is ensured by imposing the following conservation laws:

- Co-planarity cut ($\Delta\phi$). In principle, the virtual photon, the emitted real photon and the recoil helium lie in the same plane, which is called the hadronic plane. Thus the DVCS events must have $\Delta\phi$ values around zero. The hadronic plane can be defined in three ways:

$$\begin{aligned}
\overrightarrow{HP}_1 &= \overrightarrow{\mathbf{P}}_{^4He'} \times \overrightarrow{\mathbf{P}}_{\gamma^*} && (5.7)\\
\overrightarrow{HP}_2 &= \overrightarrow{\mathbf{P}}_{^4He'} \times \overrightarrow{\mathbf{P}}_{\gamma} && (5.8)\\
\overrightarrow{HP}_3 &= \overrightarrow{\mathbf{P}}_{\gamma^*} \times \overrightarrow{\mathbf{P}}_{\gamma} && (5.9)
\end{aligned}$$

$\Delta\phi$ is defined to be the ϕ difference between these planes and is calculable from three combinations: ($\overrightarrow{HP}_1$, $\overrightarrow{HP}_2$), ($\overrightarrow{HP}_1$, $\overrightarrow{HP}_3$) and ($\overrightarrow{HP}_2$, $\overrightarrow{HP}_3$). We investigated the three combinations and we decided to use the second one as $\Delta\phi$ has better resolution.

- Missing energy, mass and transverse momentum ($p_X^T = \sqrt{(p_X^x)^2 + (p_X^y)^2}$) cuts on $\mathbf{P}_X^{e^4He\gamma}$.

- Missing mass cuts on the e^4HeX and $e\gamma X$ systems, which are defined as $(P_X^{e^4He})^2$ and $(P_X^{e\gamma})^2$ respectively.

- Cone angle cut between the measured real photon and the missing particle in the e^4HeX configuration. It is defined as:

$$\theta(\gamma, e^4HeX) = cos^{-1}\left(\frac{\overrightarrow{\mathbf{P}}_{\gamma} \cdot \overrightarrow{\mathbf{P}}_{X}^{e^4He}}{|\overrightarrow{\mathbf{P}}_{\gamma}||\overrightarrow{\mathbf{P}}_{X}^{e^4He}|}\right). \tag{5.10}$$

Figure 5.2 summarizes all the exclusivity cuts. In these plots, the blue distributions represent the coherent events after the DVCS characteristic cuts and before all the exclusivity cuts. The shaded distributions stand for the events which passed all the exclusivity cuts except the one on the quantity plotted. We fitted each shaded distribution by a Gaussian and then we applied 3σ cuts around the mean value of each distribution. The events which pass these cuts are assumed to be good ^4He DVCS events.

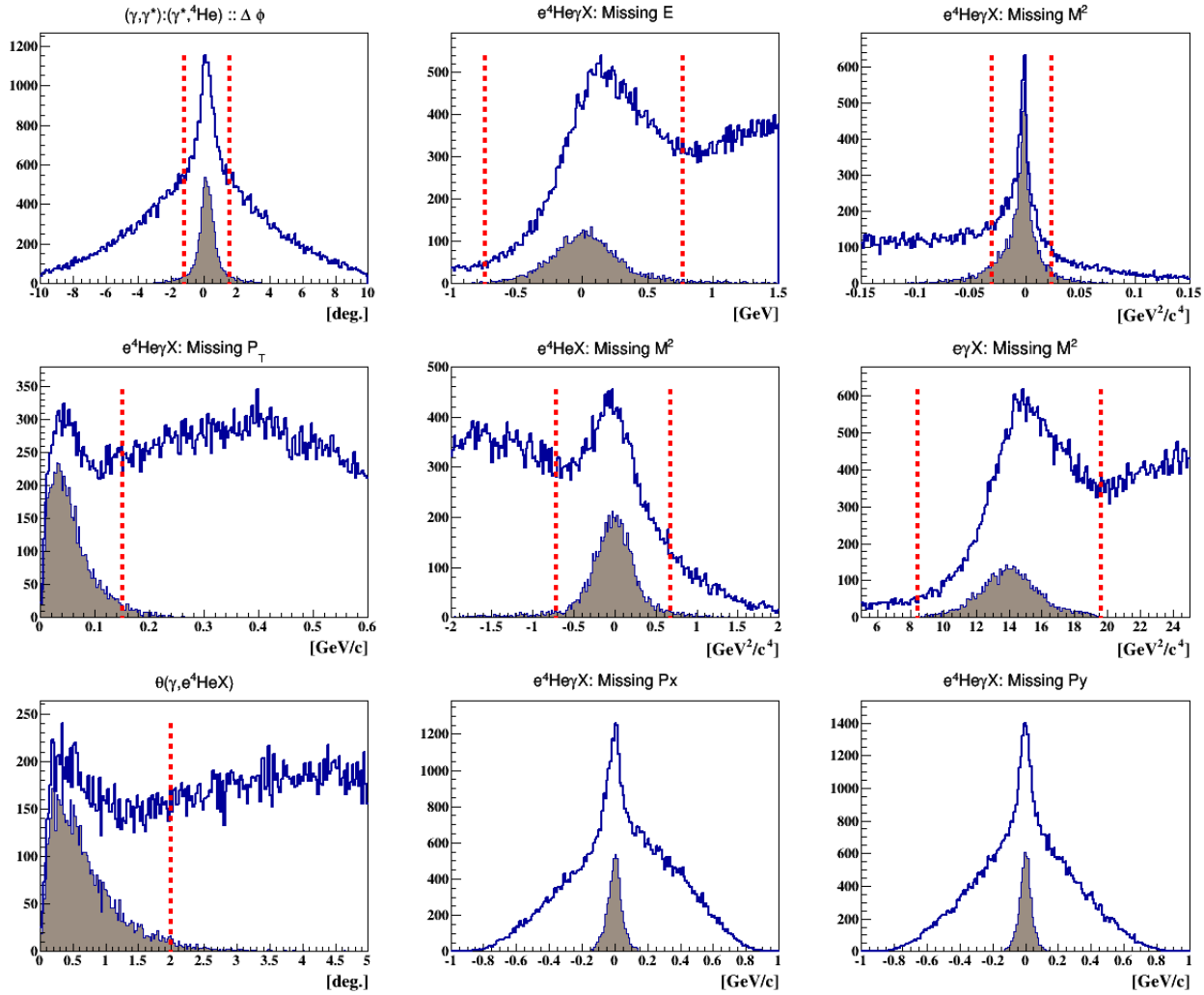

Figure 5.2: The coherent DVCS exclusivity cuts. The blue distributions represent the coherent DVCS events candidate. The shaded distributions represent the events which passed all the exclusivity cuts except the quantity plotted. The vertical red lines represent 3σ cuts. The missing momentum in x and y directions in the configuration $e^4He\gamma X$, are shown for information. The mean and the sigma values of each quantity can be found in Appendix E, table E.1.

5.1.3 Comparison with simulation

Coherent DVCS events were simulated according to the procedures described in section 4.2.1. Then, events are selected following the same identification criteria as for the experimental data. Finally, an equivalent set of DVCS exclusivity cuts are applied as for the coherent data.

Figure 5.3 shows the comparison between the experimental and the simulated DVCS events as a function of the kinematic variables: Q^2, x_B, $-t$, and ϕ. Figure 5.4 shows the comparison as a function of the quantities used for the exclusivity cuts.

The distributions in figures 5.3 and 5.4 show a satisfying match between the experimental and the simulated data. Moreover, the black vertical lines in 5.4, which represent the nominal values that come from the conservation laws, are in agreement with both datasets.

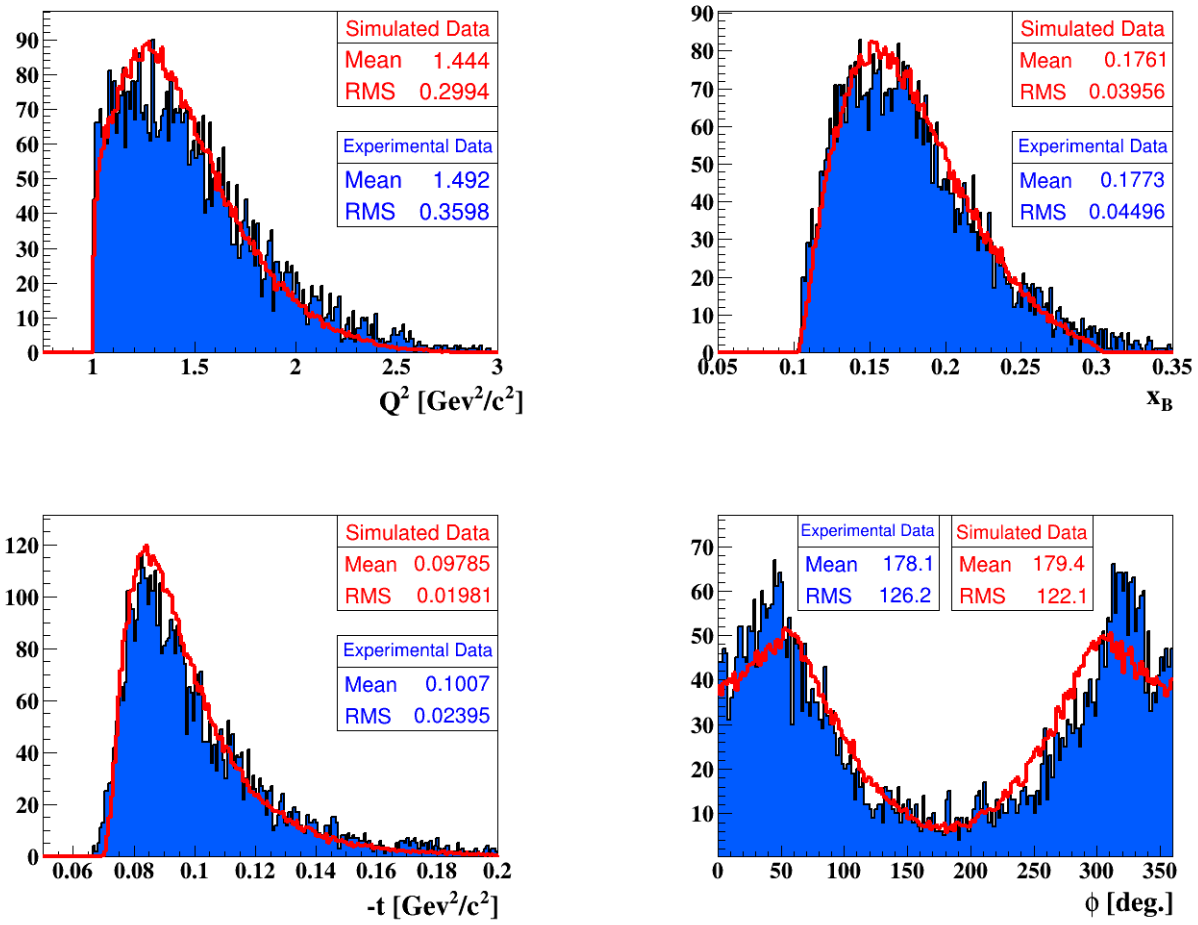

Figure 5.3: Comparison between the simulated $e^4He\gamma$ DVCS events (in red lines) and the experimental DVCS events (in shaded blue) as a function of the kinematic variables: Q^2, x_B, $-t$, and ϕ.

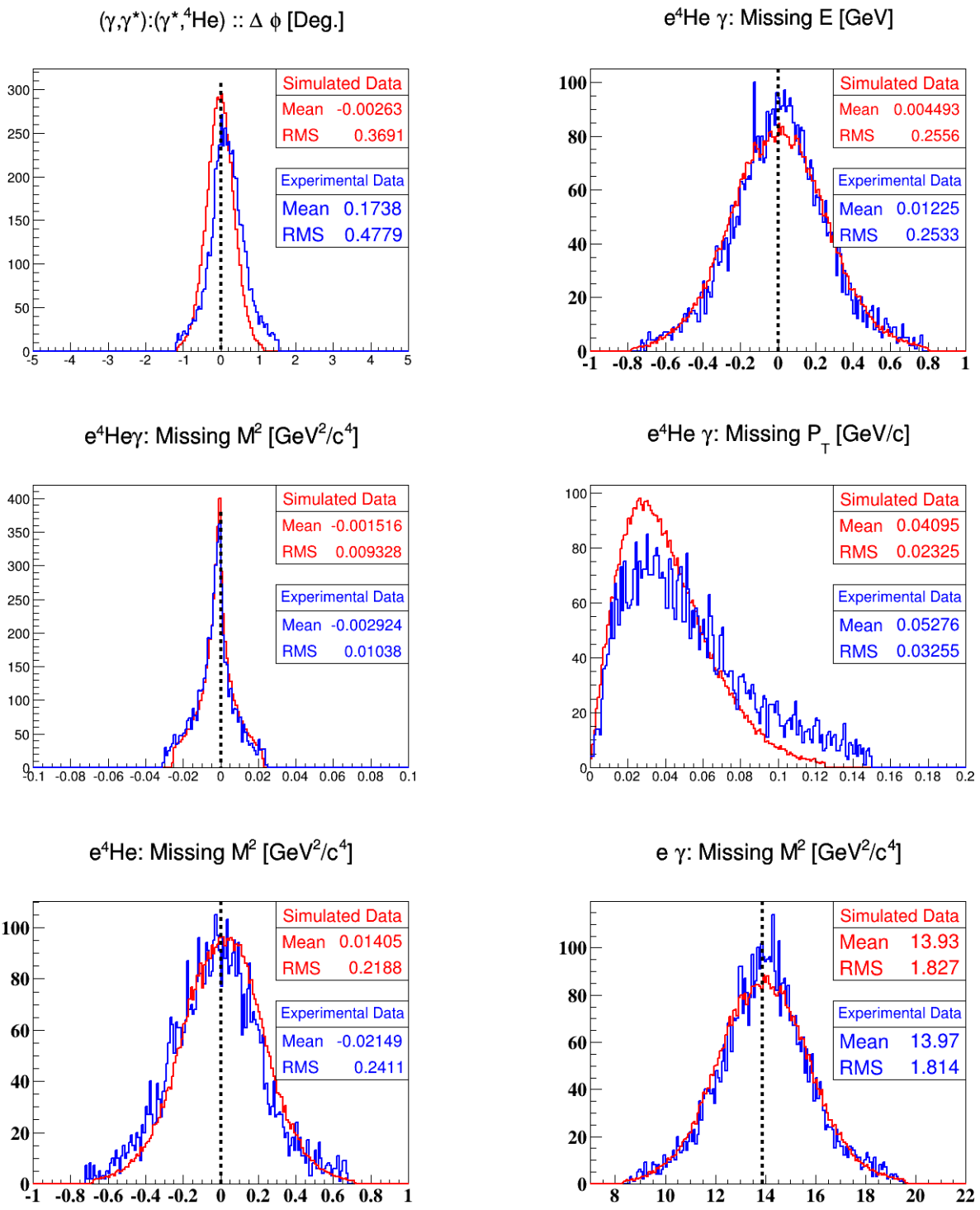

Figure 5.4: Comparison between simulated and experimental $e^4He\gamma$ DVCS events. The distributions from left to right and from top to bottom are: Co-planarity cut, missing energy, missing mass squared and missing transverse momentum in the configuration of detecting all the three final-state particles, missing mass squared in the e^4HeX and $e\gamma X$ configurations respectively. The vertical black lines indicate the theoretically expected value for each quantity.

5.2 Incoherent channel

In this channel, the DVCS process happens on a bound proton. Thus, the final state has a recoil proton instead of the helium nucleus. Therefore, events with one good electron, one recoil proton, and at least one real photon are the good candidates here. For the rest, we follow the same steps that were introduced for the coherent DVCS selection.

5.2.1 Good run list

The events rate stability is verified by looking at the rate of the detected number of protons to the detected electrons (<p/e>). Like for the coherent channel, the same technique for the determination of the good run list is followed herein. The results are presented in figure 5.5.

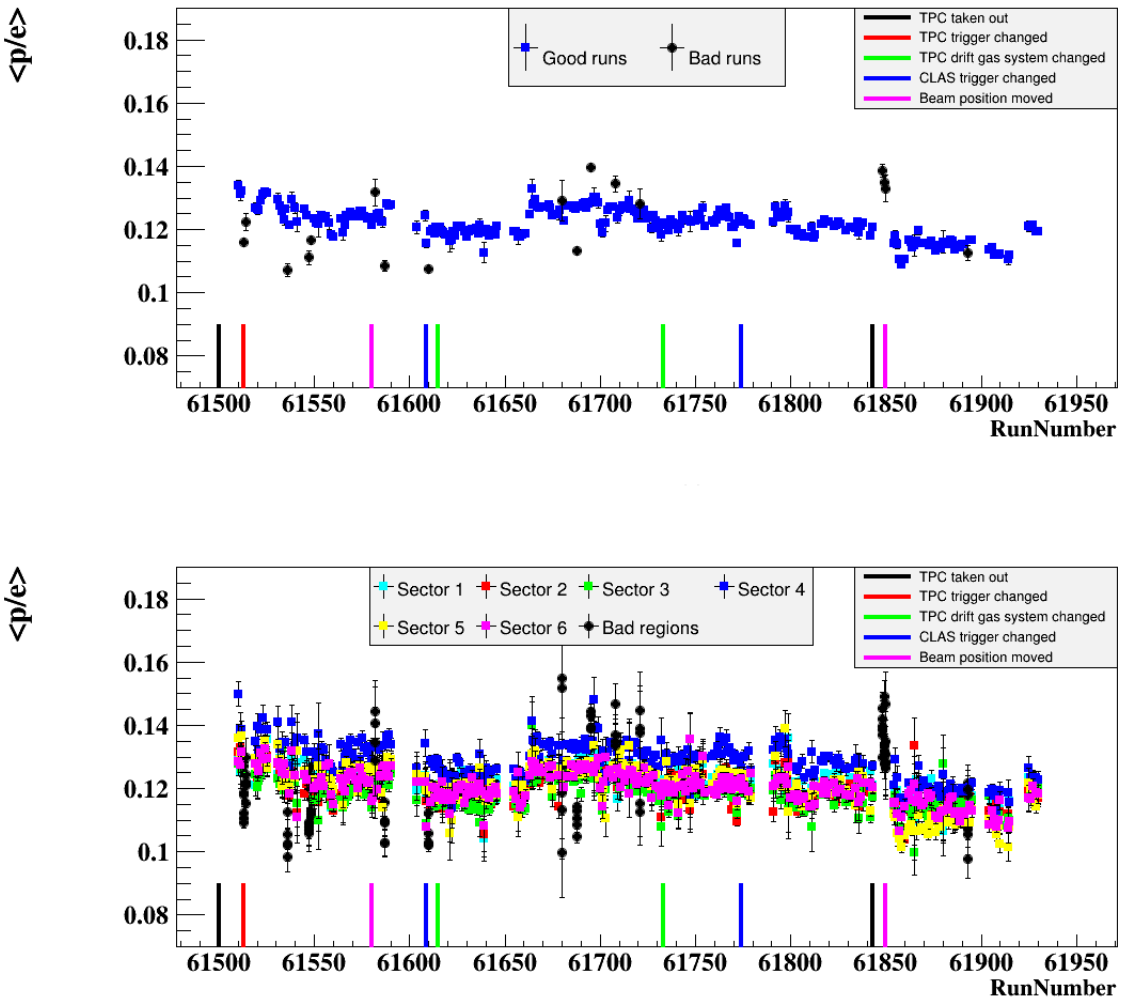

Figure 5.5: On the top: the integrated $<p/e>$ ratio as a function of run number. The blue points refer to the good runs, while the black points are the rejected ones. On the bottom: the same ratio for each run, is shown for each sector of CLAS. The colored points indicate the six sectors, while the black points are the sectors of the rejected runs.

5.2.2 Proton DVCS event selection

To certify that an event is a proton DVCS one, we require the same DVCS kinematic cuts as those presented for the coherent DVCS selection. Then, the exclusivity of the DVCS reaction is ensured by applying an equivalent set of exclusivity with taking a proton at rest as the target, instead of ^4He. Figure 5.6 summarizes these exclusivity cuts.

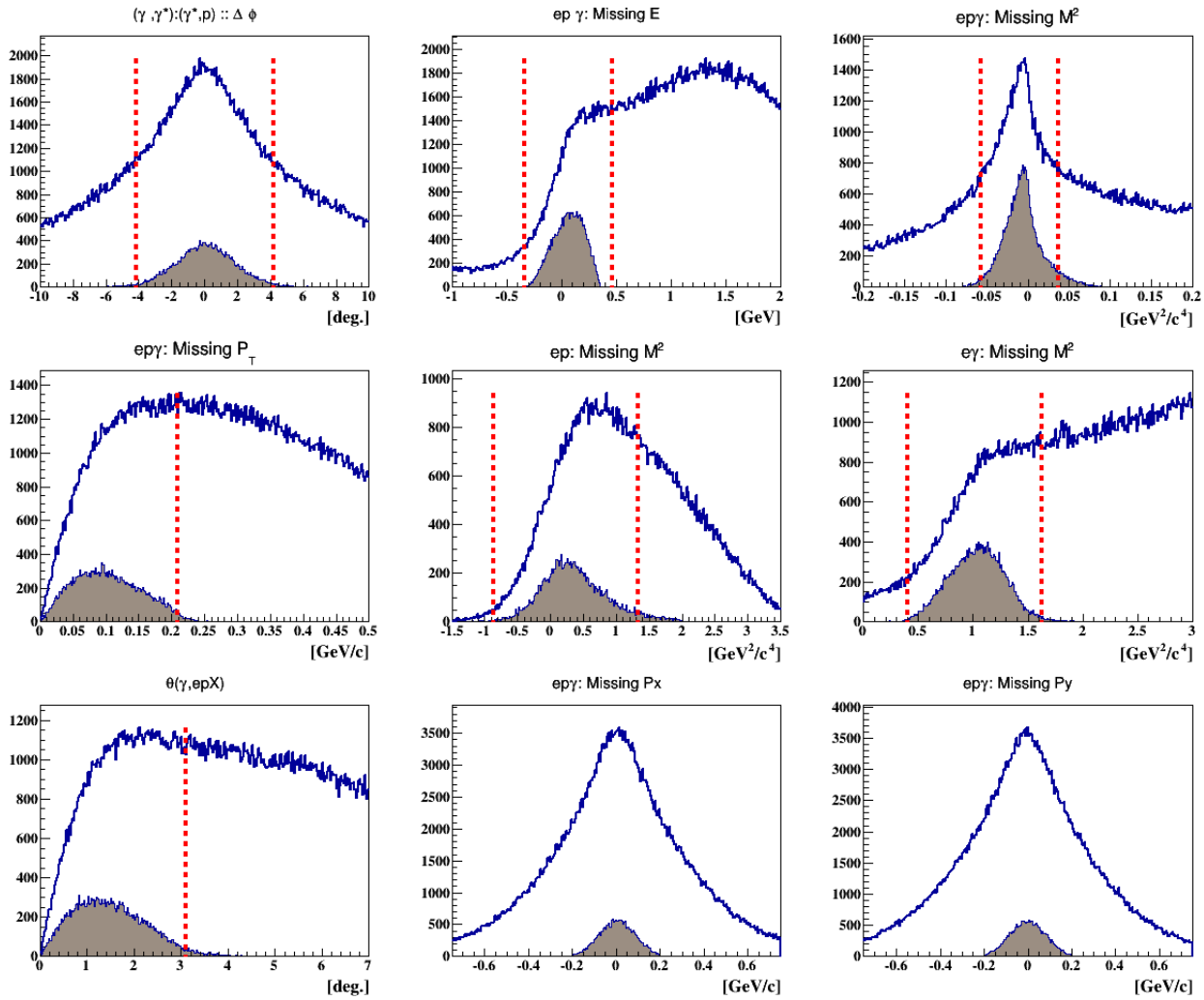

Figure 5.6: The incoherent DVCS exclusivity cuts. The blue distributions represent all the events with one good electron, one good proton, and at least one photon in the IC. The shaded brown distributions show the incoherent DVCS events which passed all the exclusivity cuts except the one on the quantity drawn. The distributions from left to right and from top to bottom are: the proton-photon coplanarity, the missing energy, missing mass squared, missing transverse momentum from $ep\gamma X$, the missing mass squared epX and the missing mass squared $e\gamma X$, the angle between the missing particle in epX and the measured photon, the missing P_x and P_y in $ep\gamma X$. The vertical red lines represent 3σ cuts. The mean and sigma values of each shaded distribution are listed in table E.3.

5.2.3 Comparison with simulation

The three particles of the simulated $ep\gamma$ DVCS events are selected applying the previously described identification requirements. The events with three identified particles (e, p, γ) are required to pass a set of exclusivity cuts such as the ones of the experimental incoherent DVCS events. In this section, a comparison between the experimental and the simulated data is carried out.

Figure 5.7 shows the comparison between the simulated (red lines) and the experimental (shaded blue) incoherent DVCS events as a function of the four kinematic variables: Q^2, x_B, $-t$, and ϕ. Figure 5.8 shows the comparison as a function of the variables used to select exclusive DVCS events.

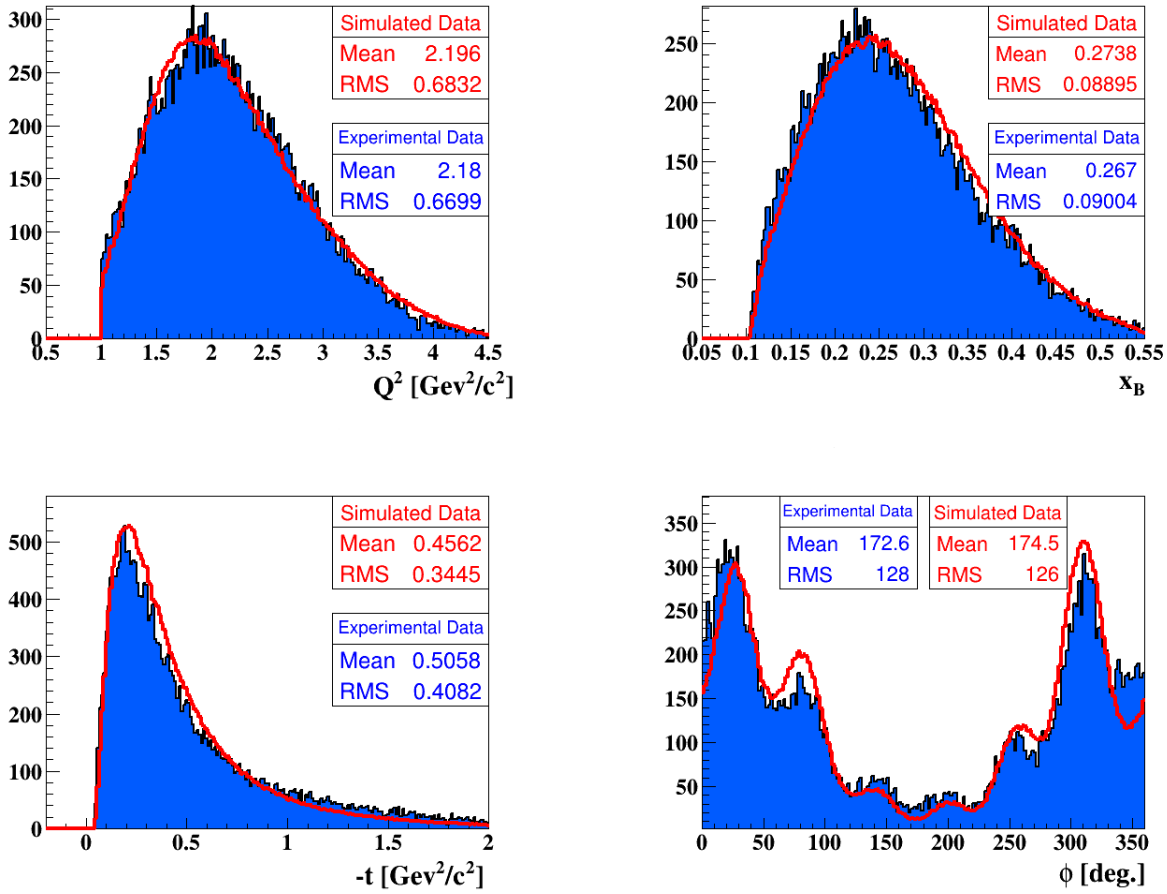

Figure 5.7: Comparison between the Monte-Carlo simulated $ep\gamma$ DVCS events (red lines) and the experimental ones (blue shaded distributions) in terms of the kinematics: Q^2, x_B, $-t$, and ϕ, respectively from left to right and from top to bottom.

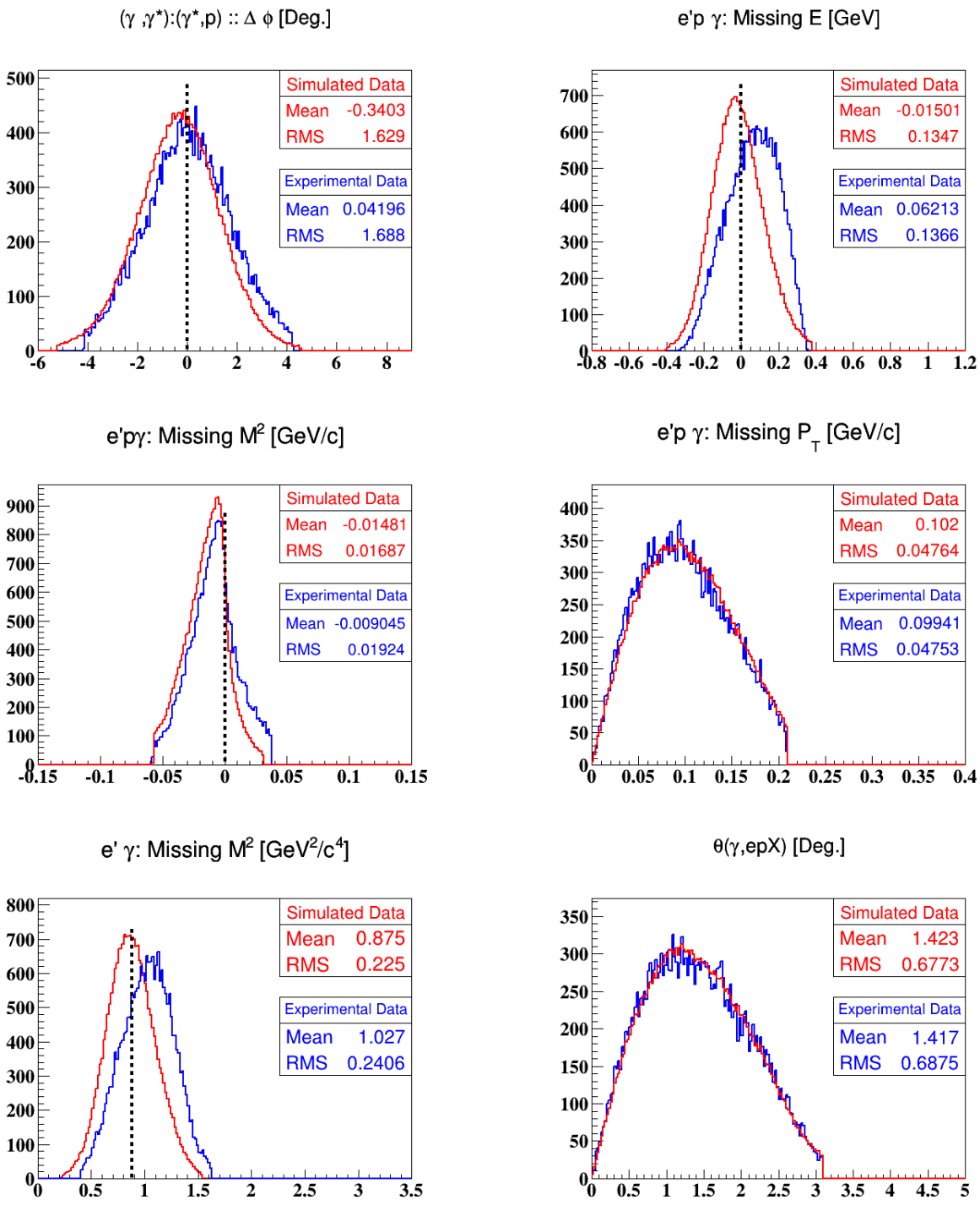

Figure 5.8: Comparison between simulated and experimental $ep\gamma$ DVCS events in terms of the variables used for exclusivity cuts. The vertical black lines indicate the theoretically expected values for each exclusive quantity.

5.3 Kinematic coverages

The one-dimensional distributions of explored kinematical regions can be seen in figure 5.3 for the coherent, and in figure **??** for the incoherent DVCS channels. In figure 5.9, we show two-dimensional distributions of these variables to display the correlations between them.

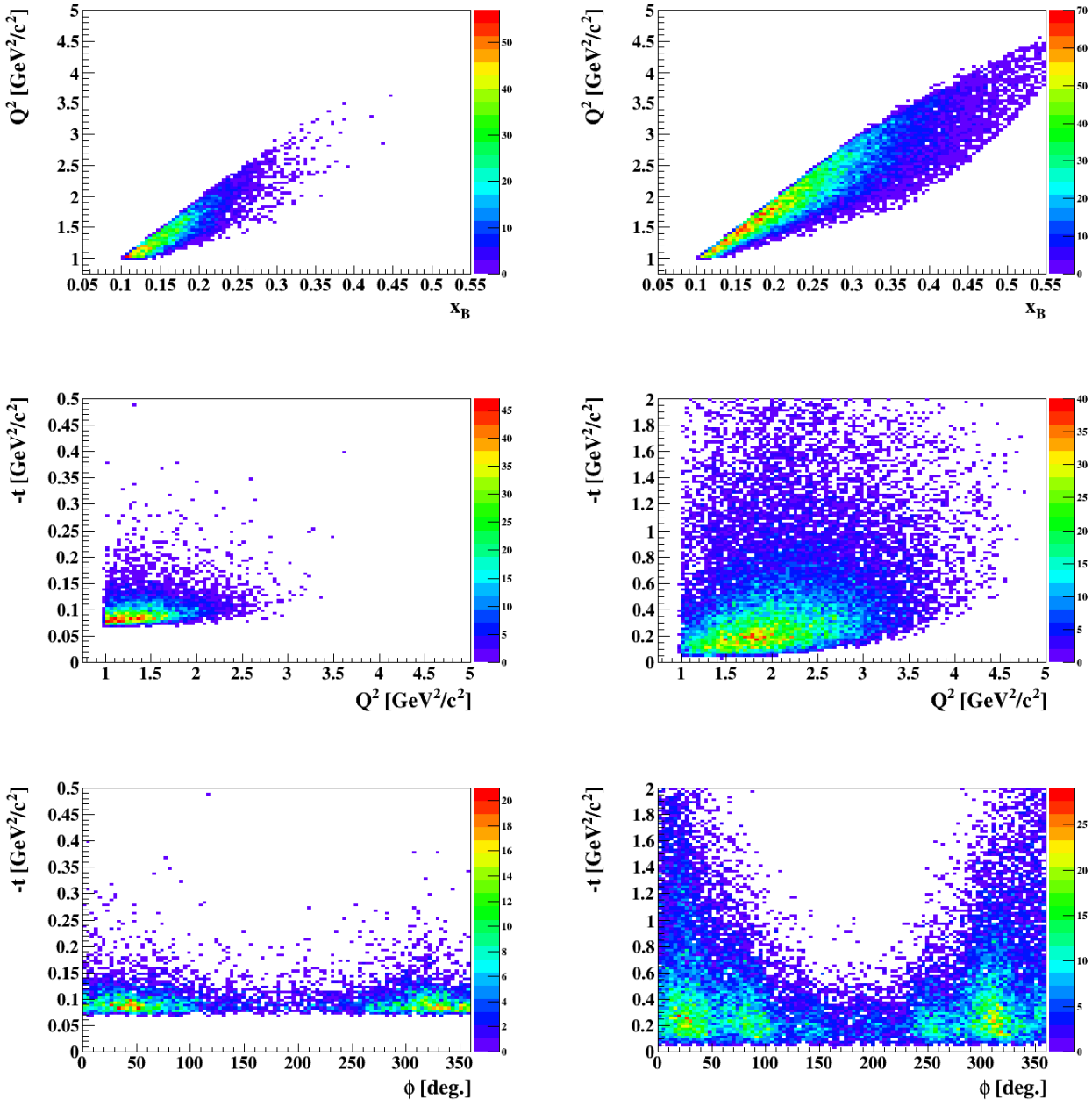

Figure 5.9: The coherent DVCS distributions are on the left panel, and on the right the incoherent ones, while the top panel: Q^2 as a function of x_B. On the middle panel: $-t$ as a function of Q^2. On the bottom panel: $-t$ as a function of ϕ.

5.4 Data binning

The DVCS cross section, as expressed in equation 1.12, and the A_{LU}, equation 1.30, depend on the four kinematic variables: Q^2, x_B, t, and ϕ. The number of identified coherent (incoherent) DVCS events is about 5000 (30k). Due to our limited statistics only, a two-dimensional binning is carried out in this analysis. The strongest dependence of A_{LU} is on the azimuthal angle between the leptonic and the hadronic planes (ϕ). Thus, we construct the two-dimensional bins as follows: the coherent (incoherent) measured ranges of Q^2, x_B and $-t$ are binned statistically into three (four) bins. Then, the identified DVCS events in each Q^2, x_B and $-t$ bin, are binned into nine bins in ϕ. Therefore, we are left with Q^2-ϕ bins integrated over the full ranges of x_B and $-t$, x_B-ϕ bins integrated over Q^2 and $-t$, and $-t$-ϕ bins integrated over Q^2 and x_B. For instance, figure 5.10 shows the one-dimensional bins in Q^2 and the associated bins in ϕ.

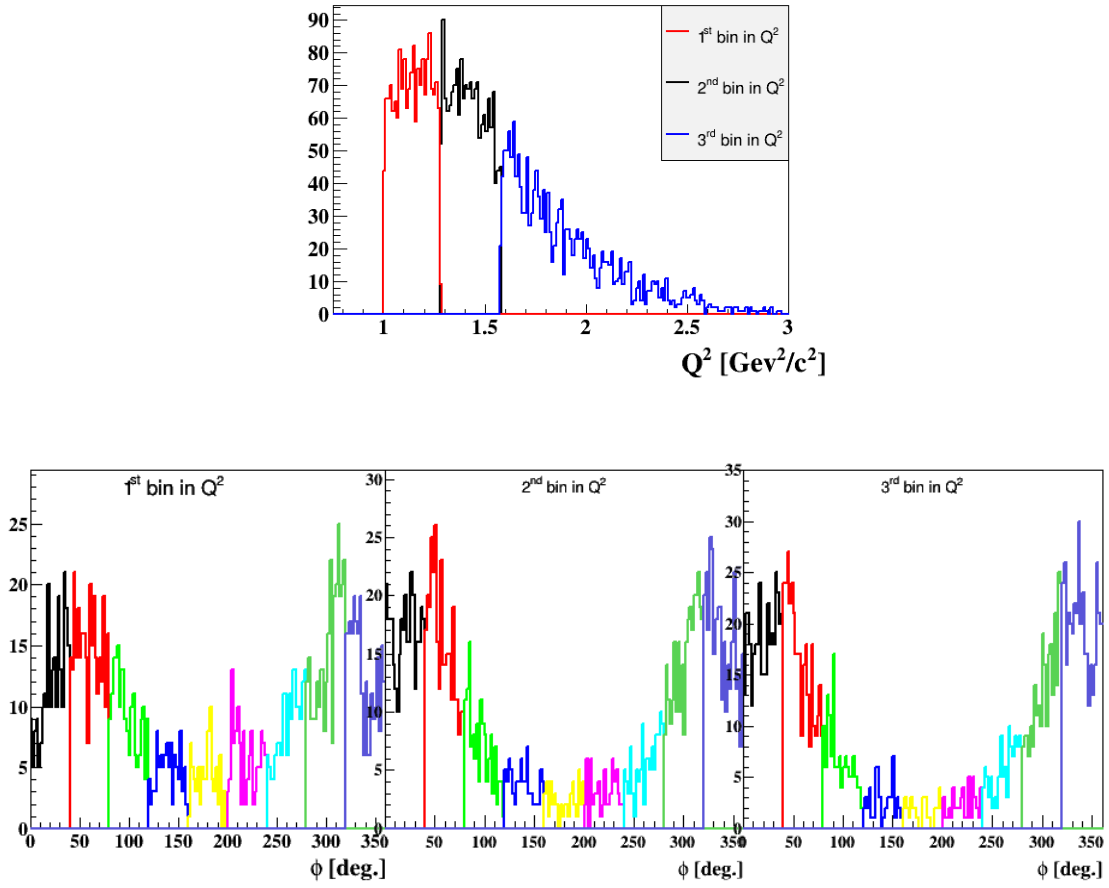

Figure 5.10: On the top: the Q^2 distribution of the collected coherent DVCS events. The different colors indicate the different bins in Q^2 integrated over the full ranges of $-t$ and x_B. On the bottom: the ϕ distributions of the coherent DVCS events for the bins in Q^2, which are shown in the top plot. The different colors in each ϕ distribution represent the nine bins in ϕ.

5.5 Background subtraction

Even with all cuts applied to select DVCS events, the events are not all DVCS events. In our kinematic region, the main contamination comes from the exclusive electroproduction of π^0

($e^4He \rightarrow e^4He\pi^0 \rightarrow e^4He\gamma\gamma$, $ep \rightarrow ep\pi^0 \rightarrow ep\gamma\gamma$) channels, in which one the two photons of the π^0 decay passes the requirements of the DVCS. Thus, the event is counted as a DVCS event. These events contaminate the DVCS sample and have to be subtracted to obtain the true number of DVCS events. In the case of the coherent channel, this can be formulated as:

$$N^{True}_{e^4He\gamma} = N^{Exp.}_{e^4He\gamma} - N^{Exp.}_{e^4He\pi^0(\gamma)}, \tag{5.11}$$

where $N^{True}_{e^4He\gamma}$, $N^{Exp.}_{e^4He\gamma}$ and $N^{Exp.}_{e^4He\pi^0(\gamma)}$ are the true number of coherent DVCS events, the experimentally measured number of $e^4He\gamma$ events and the contamination number, respectively. The contamination can be calculated by using real data and simulation. We define, for each kinematic bin and for each beam helicity state

$$N^{Exp.}_{e^4He\pi^0(\gamma)} = \frac{N^{Sim.}_{e^4He\pi^0(\gamma)}}{N^{Sim.}_{e^4He\pi^0(\gamma\gamma)}} * N^{Exp.}_{e^4He\pi^0(\gamma\gamma)}, \tag{5.12}$$

where $N^{Exp.}_{e^4He\pi^0(\gamma\gamma)}$ is the number of measured $e^4He\pi^0$ events, for which both photons of the π^0 have been detected. The quantity $\frac{N^{Sim.}_{e^4He\pi^0(\gamma)}}{N^{Sim.}_{e^4He\pi^0(\gamma\gamma)}}$ is the acceptance ratio for detecting a $e^4He\gamma$ event that originates from an $e^4He\pi^0$ event. It can be derived from Monte-Carlo simulations by generating and simulating $e^4He\pi^0$. $N^{Sim.}_{e^4He\pi^0(\gamma)}$ is the number of such events passing the DVCS requirements, while $N^{Sim.}_{e^4He\pi^0(\gamma\gamma)}$ is the number of simulated $e^4He\pi^0$ events passing the exclusivity cuts for $e^4He\pi^0$ events.

The previous formulas apply to the case of the coherent DVCS. The same procedures hold for the incoherent case by replacing the ^4He with the proton.

The selection of the exclusive $e^4He\pi^0$ and $ep\pi^0$ events requires the detection of one good electron, one good π^0 in the topology ICIC or ICEC, and one good ^4He track in the coherent case, or one good proton in the incoherent case. In order to ensure that this is a deep process, we apply the same kinematic cuts as DVCS. These cuts and the comparisons with simulation can be found in Appendix D.

Figure 5.11 shows the coherent acceptance ratio as a function of each of the four kinematic variables (Q^2, x_B, $-t$, ϕ_h). These distributions are one-dimensional, i.e. the data are integrated over all kinematical ranges except for the quantity which is binned (along the x-axis). The results for the incoherent channel can be found in figure 5.12. The mean value of the acceptance ratio for the coherent channel is around 25%, with some dependence on x_B and ϕ, and almost no dependence on Q^2 and $-t$. For the incoherent channel, the mean acceptance ratio is around 20% with some dependence on the four kinematic variables.

As presented in the previous section, we construct two-dimensional bins: Q^2-ϕ, x_B-ϕ and -t-ϕ. Thus, for each bin in Q^2, x_B and $-t$, we assume that the acceptance ratio does not change a lot within the bin range and we construct the one-dimensional acceptance ratio as a function of ϕ. The latter is used to perform the background subtraction as shown in equations 5.11 and 5.12.

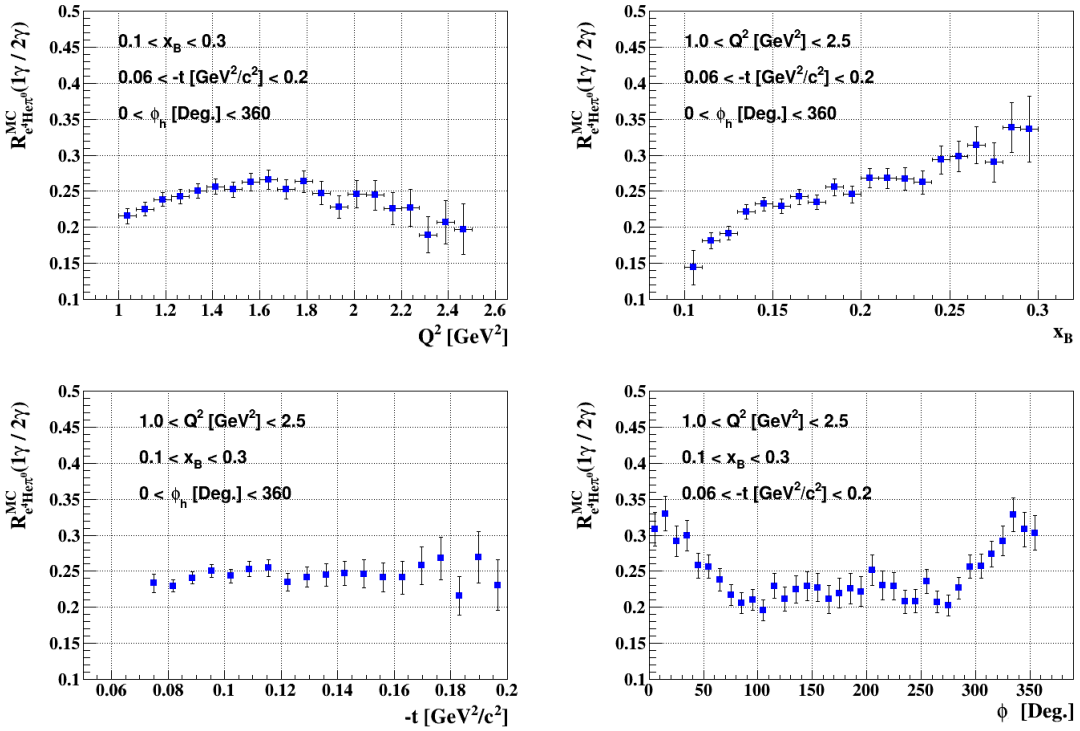

Figure 5.11: The coherent channel acceptance ratios as a function of the kinematic variables: Q^2 (top left), x_B (top right), $-t$ (bottom left), and ϕ (bottom right).

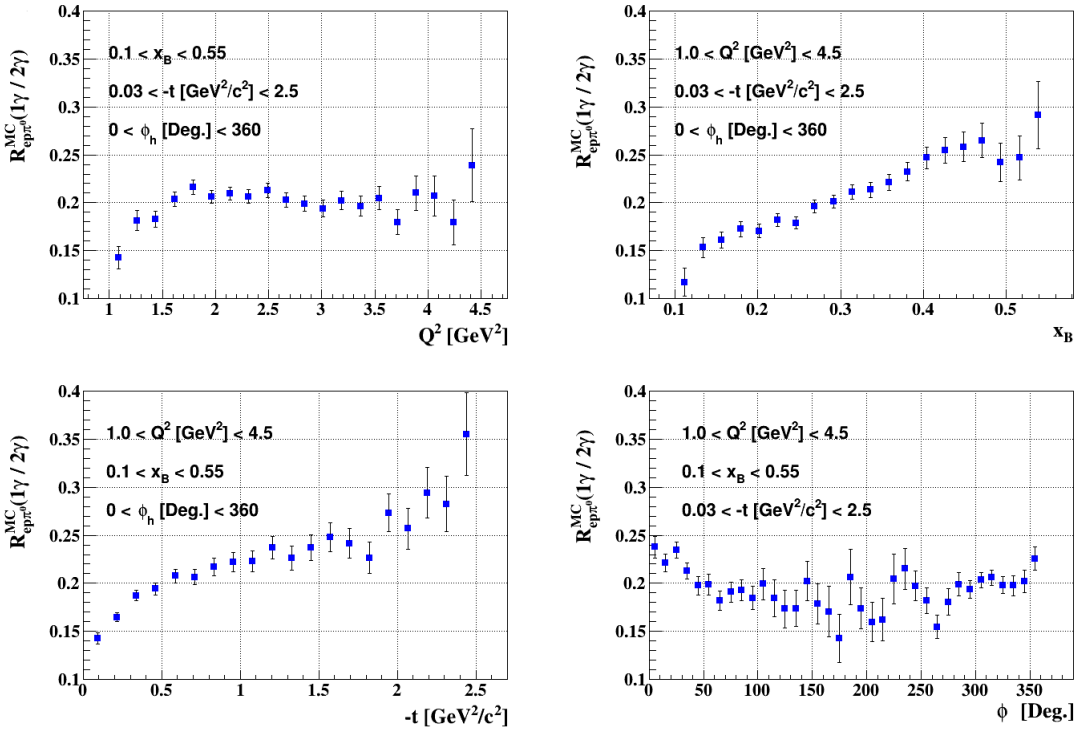

Figure 5.12: The incoherent channel acceptance ratios as a function of the kinematic variables: Q^2 (top left), x_B (top right), $-t$ (bottom left), and ϕ (bottom right).

5.6 Statistical uncertainties

In terms of the collected number of events in each beam-helicity state (N^+, N^-), A_{LU} can be expressed as:

$$A_{LU} = \frac{1}{P_B}\frac{N^+ - N^-}{N^+ + N^-}. \tag{5.13}$$

where P_B is the beam polarization, N^+ and N^- are the background-subtracted yields of DVCS events. The statistical uncertainties on the measured A_{LU} can be derived as:

$$\Delta A = \frac{1}{P_B}\sqrt{\left(\frac{\partial A}{\partial N^+}\right)^2(\Delta N^+)^2 + \left(\frac{\partial A}{\partial N^-}\right)^2(\Delta N^-)^2} = \frac{1}{P_B}\sqrt{\frac{(2N^-\Delta N^+)^2 + (2N^-\Delta N^+)^2}{(N^+ + N^-)^4}}, \tag{5.14}$$

where N^+ and N^- are

$$N^\pm = N^\pm_{e^4He\gamma} - R\ N^\pm_{e^4He\pi^0}, \tag{5.15}$$

and R is the calculated background acceptance ratio from the simulation. The statistical uncertainty on the counts ($N^\pm$) is

$$(\Delta N^\pm)^2 = (\Delta N^\pm_{e^4He\gamma})^2 + (R\ \Delta N^\pm_{e^4He\pi^0})^2 = N^\pm_{e^4He\gamma} + R^2 N^\pm_{e^4He\pi^0}. \tag{5.16}$$

The errors on P_B and R are not considered statistical errors. They contribute in the systematic uncertainties, as will be discussed in the following section. This derivation is valid for the coherent and the incoherent DVCS channels.

5.7 Systematic uncertainties

It is particularly convenient to use the A_{LU} as a DVCS observable, because most of the experimental systematic uncertainties, such as normalization and efficiencies that appear in the cross sections cancel out in the asymmetry ratio. However, some sources still affect this asymmetry and contribute in the systematic uncertainties on the measured A_{LU}. The main known sources of systematic errors are: the DVCS selection cuts, the beam polarization, the background acceptance ratio and the radiative corrections. In the following, we present an estimation of the contribution from each source.

DVCS selection cuts

In order to evaluate the systematic uncertainties stemming from the DVCS selection cuts, the analysis was repeated changing cuts. As it can be seen in figure 5.2, the 3σ cuts cover up to 97% of the events in all the distributions except the $e^4He\gamma$ missing mass distribution. In order to investigate the effect of taking different cuts on the reconstructed A_{LU}, we fix the 3σ cuts on all the exclusive quantities except for the cut on $e^4He\gamma$ missing mass. For the incoherent channel, the same procedure is carried out on the $ep\gamma$ missing mass distribution. The results can be seen in figure 5.13. The maximum variation that has been observed on the A_{LU} observable between 3σ cut and the other cuts ($\frac{\Delta A^{sys.cuts}_{LU}}{A_{LU}}$) is equal to 4% for the coherent channel and to 3.7% for the incoherent channel.

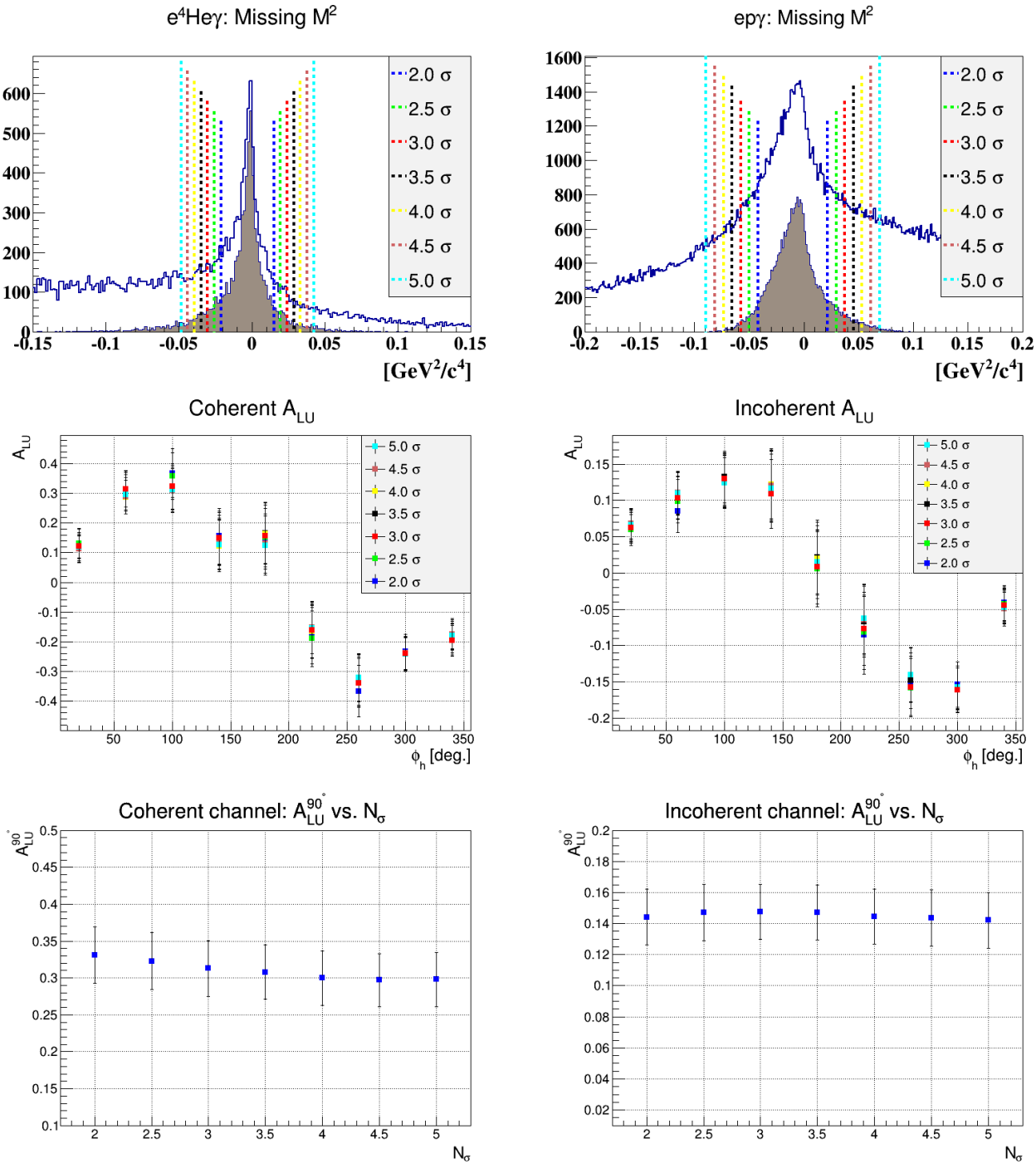

Figure 5.13: The systematic uncertainties stemming from the DVCS selection cuts in the coherent (left column) and the incoherent (right column) channels. On the top: the missing mass squared of $e^4He\gamma$ and $ep\gamma$. The different vertical coloured lines indicate the different cuts: 2.0σ, 2.5σ, ... 5σ. In the middle: the integrated coherent (incoherent) A_{LU} versus ϕ_h for the different configurations of the cuts. On the bottom: the A_{LU} at ϕ_h= 90° versus the cut widths.

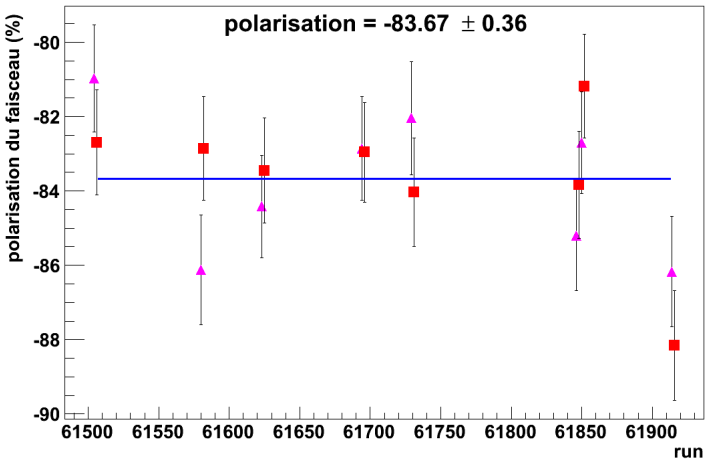

Figure 5.14: Beam polarization measurements during the CLAS-EG6 running period. The red squares are the measurements with a negative current in the Helmholtz coils of the Møller polarimeter and the purple triangles are these with a positive current. The figure is taken from [117].

Beam polarization

The beam polarization has been measured regularly during the CLAS-EG6 data taking period by using the Hall B Møller polarimeter. This polarimeter measures the angular distribution of the Møller electrons to obtain the beam polarization. Figure 5.14 shows the Møller measurements taken during the EG6 experiment. A linear fit to these measurements yields a mean polarization value of 83.67%. The precision of the Hall B Møller polarimeter ($\frac{\Delta P}{P}$) was measured to be around 3.5% [121]. We assume therefore a 3.5% systematic uncertainty on the measured asymmetries ($\frac{\Delta A_{LU}^{sys.P}}{A_{LU}} = \frac{\Delta P}{P}$).

Acceptance ratio

Predominantly, two techniques are used to estimate the systematic uncertainty associated with the calculated acceptance ratio (R) for detecting a photon originating from π^0 decay. The first is via repeating the analysis by implementing R differently, while the second technique is by using two generating models to calculate R.

Both methods were investigated. Regarding the first method, the analysis was repeated by taking three different values for R: 0.8*R, R and 1.2*R. The beam-spin asymmetries at $\phi = 90^\circ$ were extracted and compared, see figure 5.15. A maximum variation of 2% (0.6%) has been observed on the incoherent (coherent) A_{LU} at $\phi = 90^\circ$.

For the second technique, the generated events are flat in the four kinematic variables (Q^2, $-t$, x_B, ϕ). The calculated coherent and incoherent acceptance ratios (R) with and without the cross section parametrization are shown in figure 5.16. One can see that the difference between the calculated acceptance ratios is almost constant. Thus, we can conclude that the first method of taking $\pm$20% on R is is an adequate way to obtain an estimation of the systematic uncertainty associated to the calculated acceptance ratios.

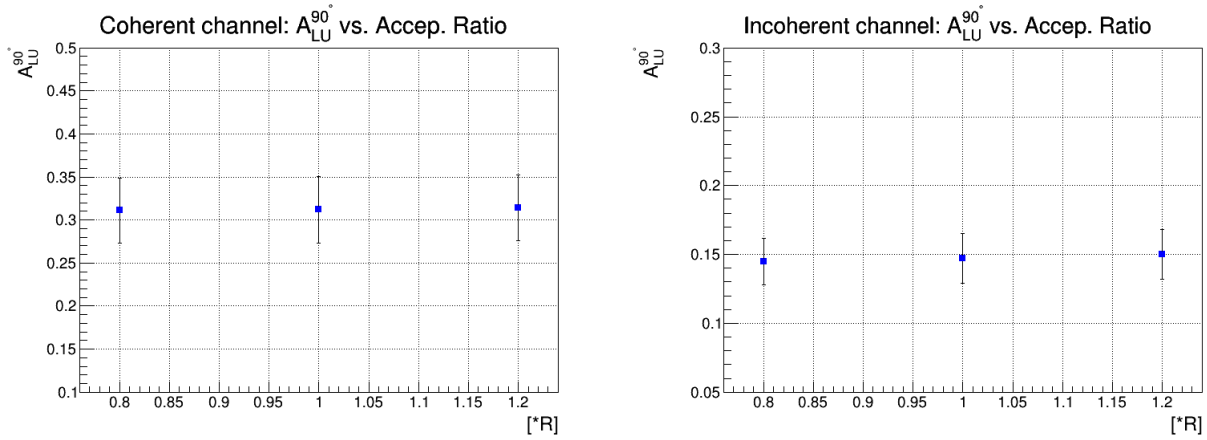

Figure 5.15: The extracted beam-spin asymmetries at $\phi = 90^\circ$ as a function of three sets of the calculated acceptance ratios: 0.8*R, 1.0*R and 1.2*R, for the coherent (on the left) and the incoherent (on the right) DVCS channels.

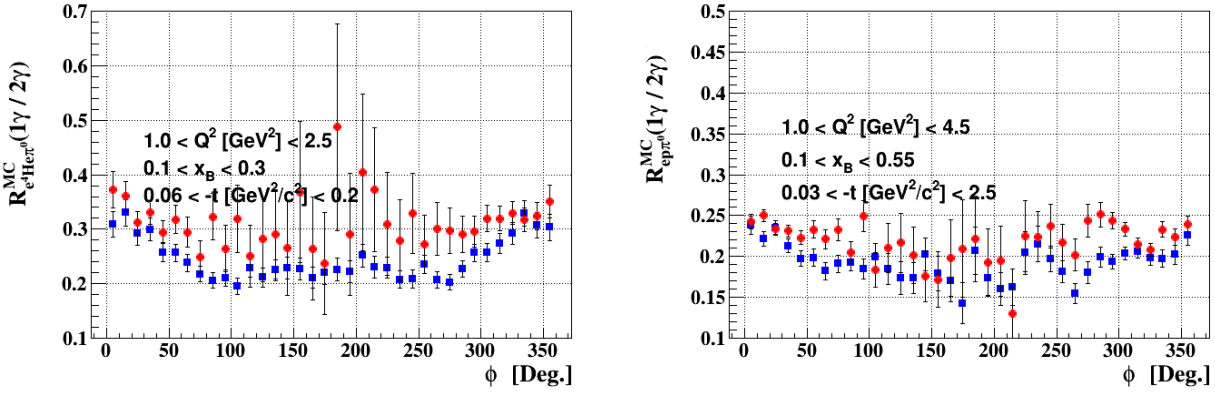

Figure 5.16: The coherent (on the top) and the incoherent (on the bottom) acceptance ratios (R) as function of the angle ϕ. In both plots, the blue (red) points are the ratios with (without) the cross section parametrization.

Radiative corrections

In this analysis, we assumed that the beam-spin asymmetry arises from the leading twist DVCS amplitude and its interference with the BH process. However, there are higher-order electromagnetic corrections which can affect the beam-spin asymmetry. Andrei V. Afanasev and his collaborators have estimated the corrections to A_{LU} which arise from such effects in a model-independent way [122]. They have performed one-loop corrections on the outgoing electron as only the radiation from it affects the A_{LU}. They found that the correction does not exceed 0.1% at a 4.25 GeV electron beam energy and Q^2=1.25 GeV^2. In our case, as the radiative emission is inversely proportional to the mass of the radiating particle, the helium and the proton contributions are negligible compared to the leptonic one. Therefore, we can still take the result of Afanasev as a good estimation for the radiative effects on our measured A_{LU}.

Systematic uncertainty summary

The total systematic uncertainty is the quadratic sum of the previously described individual uncertainties. Table 5.1 summarizes the sources of systematic uncertainty and their contributions on the measured A_{LU} at $\phi = 90^\circ$, that will be added quadratically to the statistical uncertainties on A_{LU}.

Systematic source	Coherent channel	Incoherent channel
Beam polarization	3.5%	3.5%
DVCS cuts	4 %	3.7 %
Acceptance ratio	0.6%	2.0%
Radiative corrections	0.1%	0.1%
Total	**5.3**%	**5.5**%

Table 5.1: The systematic uncertainties on the measured coherent and incoherent beam-spin asymmetries at $\phi = 90^\circ$.

Chapter 6

Results and physics interpretations

This chapter presents a proof of the function form we use to fit the beam-spin asymmetry signals. Then we present the beam-spin asymmetry measurements for both DVCS channels: the coherent and the incoherent. The data sample shown herein contains the identified DVCS events after the particle identification, the DVCS selection requirements and the background subtraction presented in the previous two chapter. The ^{4}He CFF will then be extracted from the fitted coherent beam-spin asymmetries. Finally, the EMC effect is investigated in terms of the beam-spin asymmetry ratio between our ^{4}He DVCS data and a similar analysis carried out on a free-proton data from a previous CLAS experiment (E1DVCS-2 [119] [120]).

6.1 Fitting the beam-spin asymmetry

For a spin-zero target at leading twist, the beam-spin asymmetry (A_{LU}) can be expressed as a combination of kinematical factors ($\alpha_i(\phi)$), and the real and the imaginary parts of the unique CFF $\mathcal{H}_A$. Herein we repeat equation 1.32 to show the sensitivity of A_{LU} in case of the ^{4}He DVCS.

$$A_{LU}(\phi) = \frac{\alpha_0(\phi)\,\Im m(\mathcal{H}_A)}{\alpha_1(\phi) + \alpha_2(\phi)\,\Re e(\mathcal{H}_A) + \alpha_3(\phi)\,\left(\Re e(\mathcal{H}_A)^2 + \Im m(\mathcal{H}_A)^2\right)}. \tag{6.1}$$

The factors $\alpha_{0,1,2,3}$ can be written as:

$$\begin{aligned}
\alpha_0(\phi) &= 8\,K x_A (1+\varepsilon^2)^2\,(2-y) F_A\,\sin(\phi), && (6.2)\\
\alpha_1(\phi) &= c_0^{BH} + c_1^{BH}\cos(\phi) + c_2^{BH}\cos(2\phi), && (6.3)\\
\alpha_2(\phi) &= 8\,\frac{x_A}{y}\,(1+\varepsilon^2)^2 F_A \left[K(2y - y^2 - 2)\cos(\phi)\right. && (6.4)\\
&- \left.(2-y)\frac{t}{Q^2}\left\{(2-x_A)(1-y) - (1-x_A)(2-y)^2\left(1 - \frac{t_{min}}{Q^2}\right)\right\}\right],\\
\alpha_3(\phi) &= 2\,\frac{x_A^2 t}{Q^2}\,(2 - 2y + y^2)\,(1+\varepsilon^2)^2\,\mathcal{P}_1(\phi)\mathcal{P}_2(\phi), && (6.5)
\end{aligned}$$

where $y = \frac{p\cdot q}{p\cdot k}$, $\varepsilon = \frac{2x_A M_A}{Q}$ and $x_A = \frac{Q^2}{2p\cdot q}$. The factors: $c_{0,1,2}^{BH}$ are the Fourier coefficients of the BH amplitude for a spin-zero target [82], $\mathcal{P}_1(\phi)$ and $\mathcal{P}_2(\phi)$ are the Bethe-Heitler propagators, K and t_{min} are kinematical variables. The explicit expressions of these coefficients and variables can be found in Appendix A.

In Figure 6.1, we show the $\alpha_{0,1,2,3}$ factors as functions of the azimuthal angle between the leptonic and the hadronic planes at our mean experimental values of Q^2, x_B, and t (1.5 GeV^2/c^2, 0.18, 0.1 GeV^2/c^2 respectively) using a 6 GeV electron beam. One can see that the α_3 factor is suppressed by two orders of magnitude compared to the factors α_2 and α_0. This is a consequence

of the fact that α_3 is proportional to the pure DVCS scattering amplitude that is smaller than the pure BH ($\propto \alpha_1$) and the interference ($\propto \alpha_0$ and α_2) scattering amplitudes.

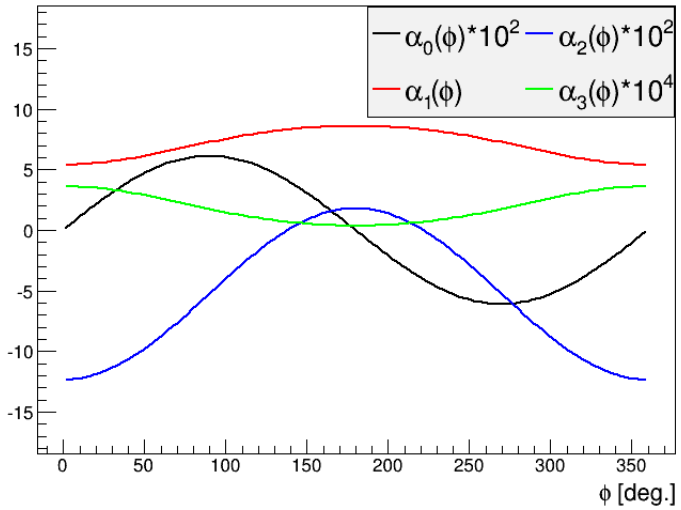

Figure 6.1: The kinematical factors: α_0, α_1, α_2 and α_3, based on the KM model [82], as functions of the angle ϕ at Q^2 = 1.5 GeV^2/c^2, x_B = 0.18, and $-t$ = 0.1 GeV^2/c^2. α_0 and α_2 are multiplied by 10^2, while α_3 is by 10^4.

One can see that α_1 is composed of a finite series of $\cos(\phi)$ terms, with the Fourier coefficients $c^{BH}_{0,1,2}$. At our mean values of Q^2, x_B and t , $c^{BH}_{0,1,2}$ are equal to 7.12702, -1.59871 and -0.120906, respectively. This quantitative comparison between $c^{BH}_{0,1,2}$ shows that the $\cos(2\phi)$ term of A_{LU} is significantly smaller than the $\cos(\phi)$ one, while the constant term (c^{BH}_0) is only a scaling factor. Therefore, we can build our A_{LU} fit function neglecting the $\alpha_3(\phi)$ term, and the $\cos(2\phi)$ term in $\alpha_1(\phi)$. Hence, A_{LU} can be parameterized with only two parameters, α and β:

$$A_{LU} = \frac{\alpha sin(\phi)}{1+\beta\cos(\phi)}, \tag{6.6}$$

$$\text{with } \alpha = \frac{\mathcal{K}s_1^{INT}}{c_0^{BH}+\mathcal{K}c_0^{INT}}, \tag{6.7}$$

$$\text{and } \beta = \frac{c_1^{BH}+\mathcal{K}c_1^{INT}}{c_0^{BH}+\mathcal{K}c_0^{INT}}, \tag{6.8}$$

where $\mathcal{K} = \frac{x_A(1+\varepsilon^2)^2}{y}$, $c^{INT}_{0,1}$ and s^{INT}_1 are the Fourier coefficients of the interference amplitude. As can be seen in equations A.15, A.16 and A.17 in Appendix A, s^{INT}_1 is linearly correlated to the imaginary part of the CFF $\mathcal{H}_A$, while c^{INT}_0 and c^{INT}_1 are linearly correlated to the real part of $\mathcal{H}_A$. Therefore, extracting the parameters α and β from fitting the experimental beam-spin asymmetry signals leads to measure the real and the imaginary parts of the CFF $\mathcal{H}_A$. Similar arguments can be made for DVCS on proton, see reference [115].

6.2 Beam-spin asymmetries

In this section, the beam-spin asymmetries will be compared to the theoretical calculations based on the two models that were presented in section 1.4.2.

6.2.1 Coherent beam-spin asymmetry

Figure 6.2 shows the coherent A_{LU} for the three sets of the two-dimensional bins. The asymmetries are fitted with the $\frac{\alpha \sin(\phi)}{1+\beta cos(\phi)}$ function form. So that $A_{LU}^{90^\circ}$ equal to α parameter of the fit.

Figure 6.3 shows the Q^2, x_B, and $-t$-dependences of the α term of A_{LU}. Within the given uncertainties, our exclusive coherent A_{LU} measurements show slight dependences on the three kinematical variables. The x_B and $-t$-dependences are compared to theoretical calculations performed by S. Liuti and K. Taneja. Their model relies on the impulse approximation and uses the spectral function of the nuclei to calculate the nuclear GPDs, and their observables as well. The calculations were carried out at slightly different kinematics than our experimental ones. The experimental results appear to be slightly enhanced compared to the calculations. These differences may arise from nuclear effects are not taken into account in the model [94]. The ^{4}He DVCS inclusive measurements of HERMES are shown on the bottom plot. Considering their uncertainties, our measurements agree with those of HERMES where overlapping. However, our limited $-t$ range does not allow us to confirm the drop at high $-t$ observed by HERMES.

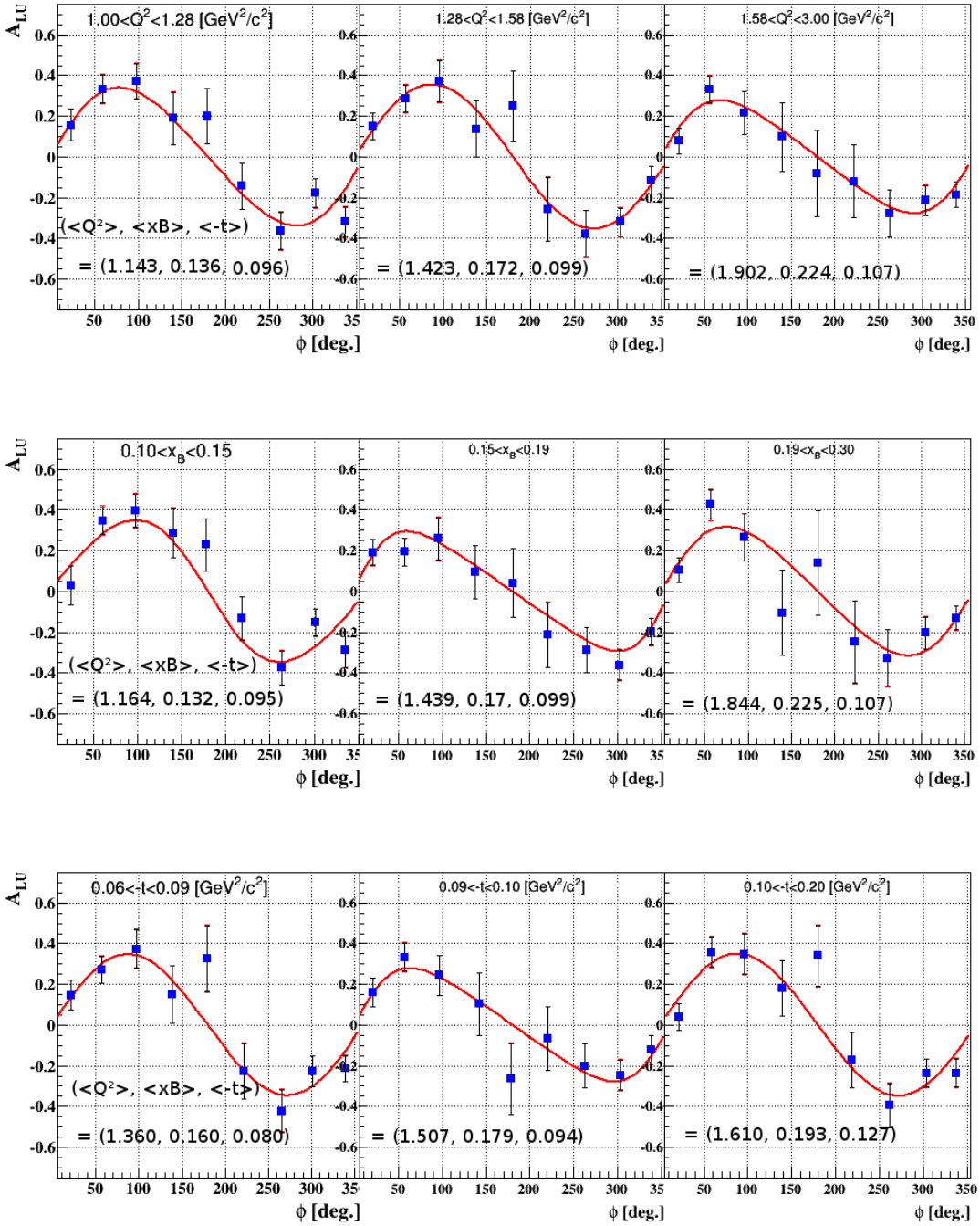

Figure 6.2: The coherent A_{LU} as a function of ϕ and Q^2 (top panel), x_B (middle panel), and $-t$ (bottom panel) bins. The blue error bars represent the statistical uncertainties shown on the top of red error bars representing quadratic sum of the systematic and the statistical uncertainties. The red curves represent fits of the form $\frac{\alpha \sin(\phi)}{1+\beta cos(\phi)}$.

6.2.2 Incoherent beam-spin asymmetry

Figure 6.4 shows the observed incoherent beam-spin asymmetries, for the three sets of the two-dimensional bins as for the coherent channel. The Q^2, x_B, and $-t$-dependences of A_{LU} at ϕ= 90° (the α parameter of the fit) are shown in figure 6.5. Our A_{LU} measurements are almost

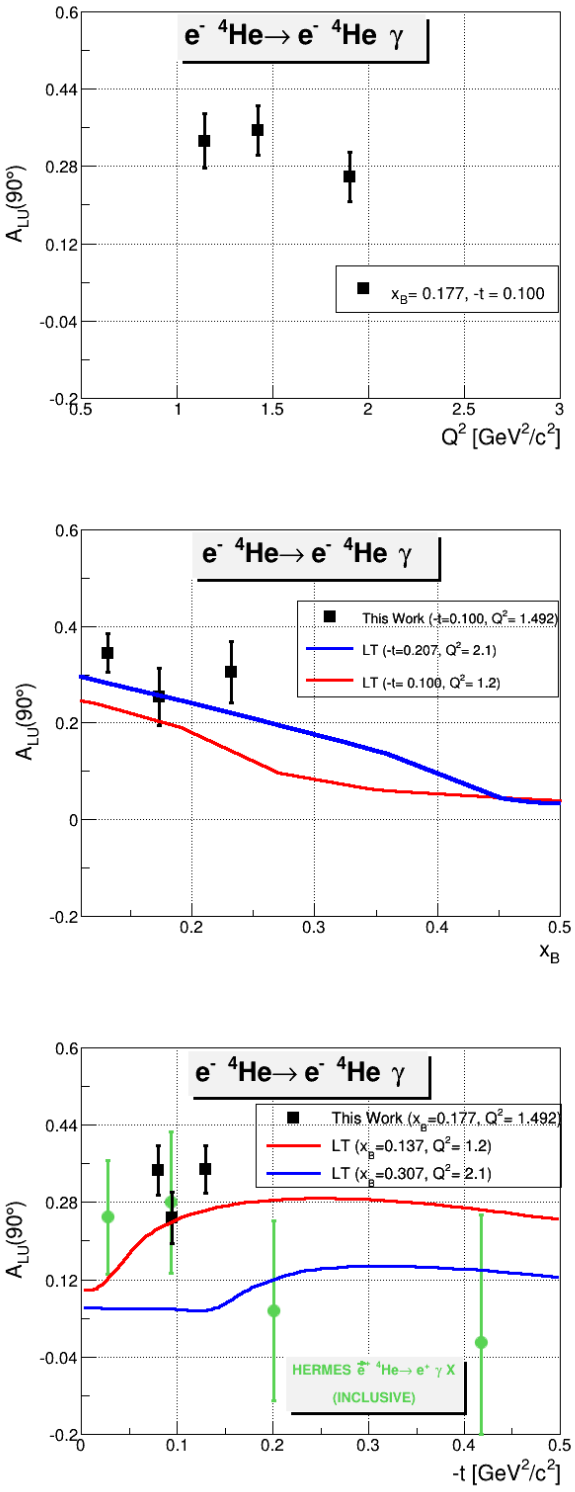

Figure 6.3: The Q^2-dependence (on the top), the x_B-dependence (on the middle), and the t-dependence (on the bottom) of the fitted coherent A_{LU} signals, at ϕ= 90°. On the middle: the red and the blue curves are theoretical predictions from [94] at two values of $-t$, 0.1 and 0.207 GeV^2/c^2. On the bottom: the black points are the extracted results from this work, the green points are the HERMES $-A_{LU}$ (positron beam was used) inclusive measurements [96], and the colored curves represent theoretical predictions from [94] at two values of x_B: 0.137 and 0.307.

flat in the three kinematical variables.

The theoretical calculations from S. Liuti and K. Taneja are carried out at slightly different kinematics than our experimental measured values. Nevertheless, one can see that our incoherent asymmetries are not well described by these calculations. For instance, in the middle plot of figure 6.5, even though our asymmetries (at $-t$ = 0.2 GeV^2/c^2) are located between the model's predictions, which are carried out at $-t$ = 0.095 and 0.329 GeV^2/c^2, they do not show the drop in $< x_B >$, as the model predicted. Similar observation can be seen as a function of $-t$ from the bottom plot.

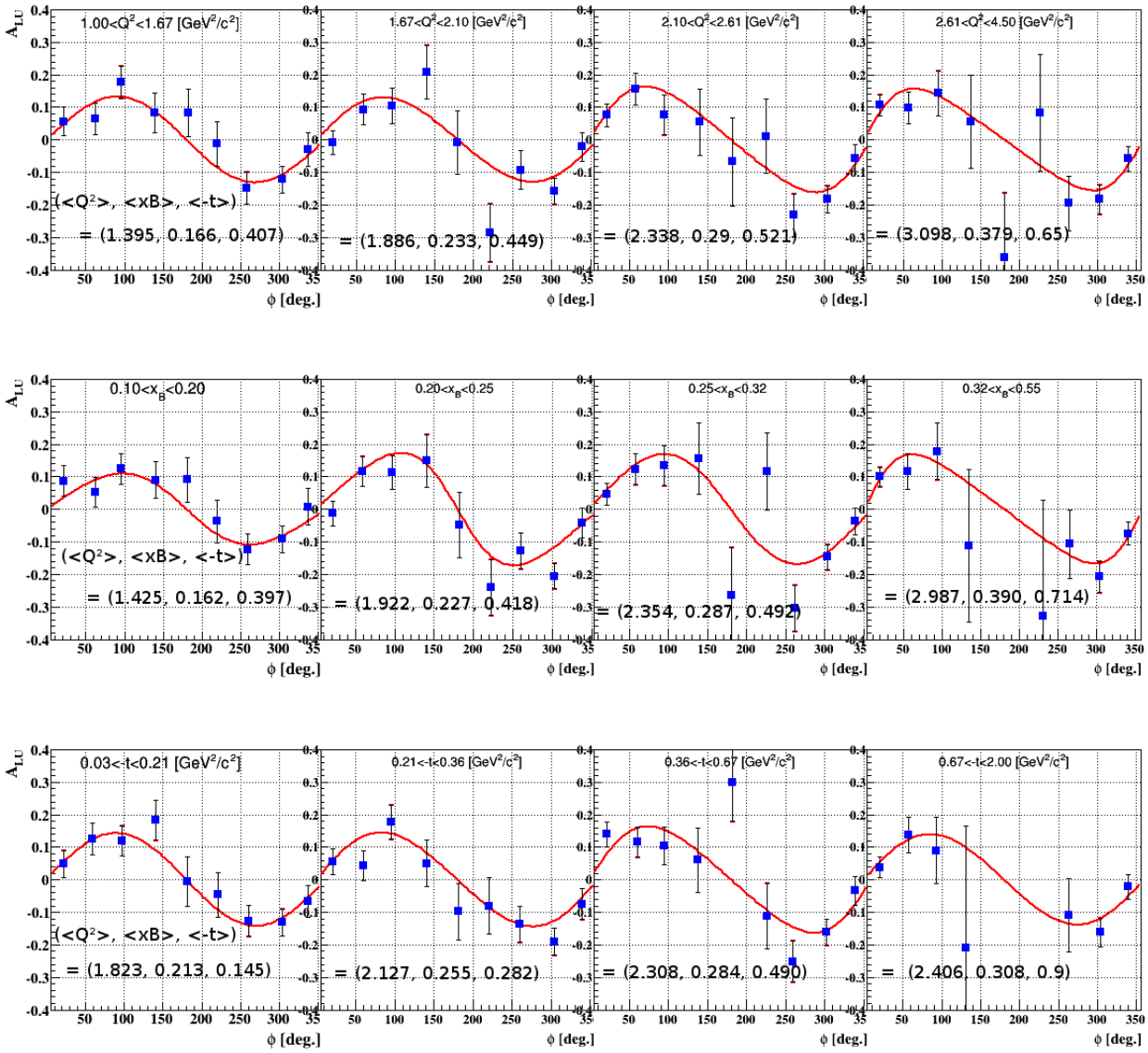

Figure 6.4: The incoherent A_{LU} as a function of the angle ϕ in Q^2, x_B, and $-t$ bins, respectively from top to bottom. The red lines represent fits to the $\frac{\alpha \sin(\phi)}{1+\beta cos(\phi)}$ function.

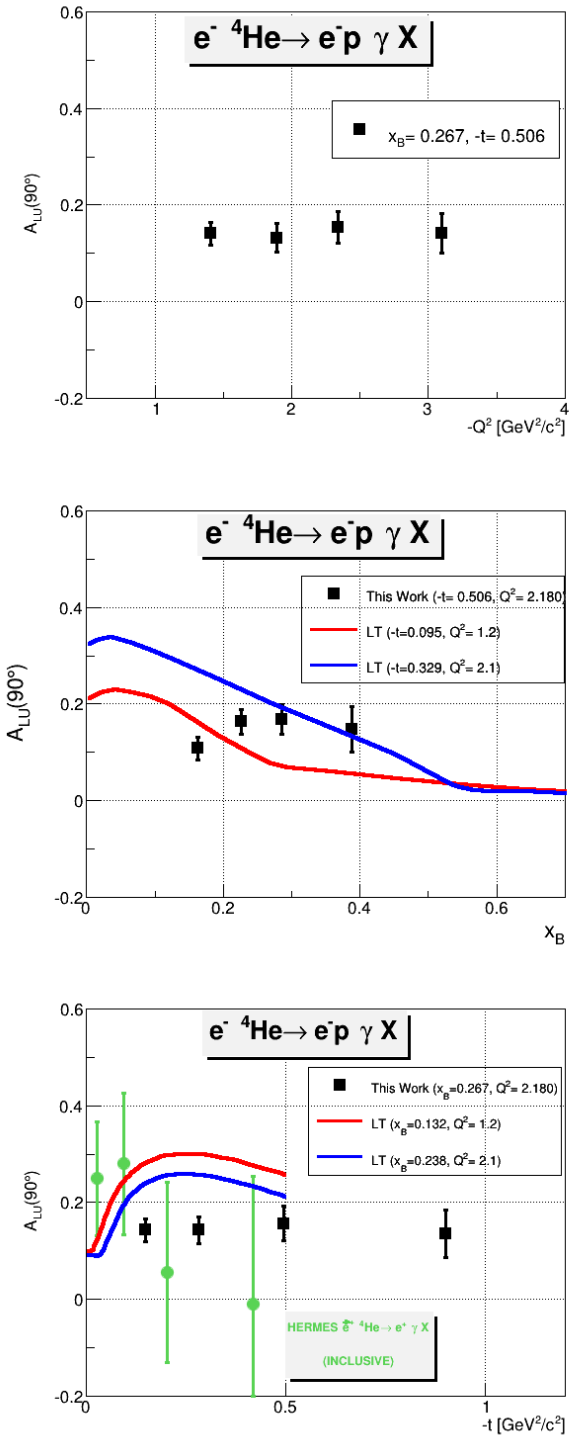

Figure 6.5: The Q^2 (on the top), x_B (on the middle), and $-t$-dependences (on the bottom) of the incoherent A_{LU}, at $\phi = 90°$. On the top left: the data have $< x_B > = 0.255$ and $< -t > = 0.2$ GeV^2/c^2. On the top right: the red and the blue curves are theoretical calculations from [94] at two values of $-t$, 0.095 and 0.329 GeV^2/c^2. On the bottom: the black points are our results at $< x_B > = 0.255$ and $< Q^2 > = 2.18$ GeV^2/c^2, the green points are the HERMES $-A_{LU}$ (positron beam was used) inclusive measurements [96], the colored curves represent theoretical calculations from [94] at two values of x_B, 0.132 and 0.238.

6.2.3 Free proton beam-spin asymmetry

Comparing our measured DVCS channels to the free-proton DVCS reaction allows us to investigate the nuclear medium effects on the GPDs. Similar analyses were performed on free-proton DVCS data sets taken by the CLAS collaboration, during the E1DVCS experiment (parts 1 and 2). The results of part 1 are already published [73, 76], but for practical reasons, we used part 2 in the following based on the work in references [119, 120]). The beam-spin asymmetries extracted in parts 1 and 2 of E1DVCS are fully compatible.

For a precise comparison between our DVCS channels and the free proton, we need to have the same binning. For this purpose, the full analysis procedure was carried out on E1DVCS (part 2) data, from the PID to the background subtraction, and binning into the same two-dimensional bins as for the coherent channel on one hand, and as for the incoherent channel on the other hand. Figure 6.6 shows the obtained free-proton A_{LU}, with the same binning in Q^2, x_B, and $-t$ as for the incoherent channel.

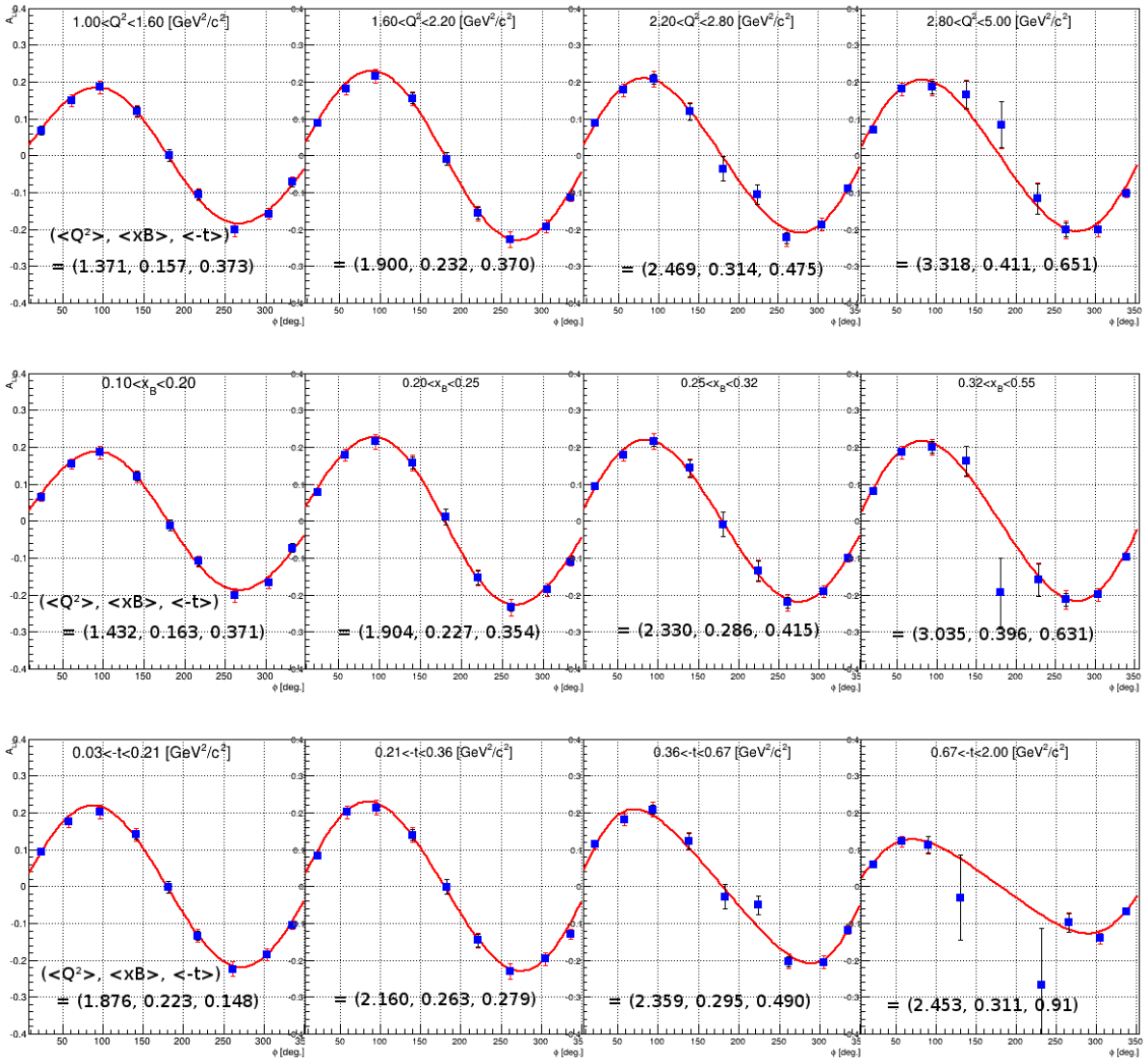

Figure 6.6: The A_{LU} of a free proton as a function of the angle ϕ in Q^2, x_B, and $-t$ bins, respectively from top to bottom. The red curves represent fits of the form $\frac{\alpha \sin(\phi)}{1+\beta cos(\phi)}$.

6.3 Helium GPD

As shown previously in the previous chapter, one can extract the real and the imaginary parts of the ^{4}He CFF $\mathcal{H}_A$ from the fitted beam-spin asymmetry signals. From the expressions of α and β (see equation 6.8), and using their experimentally extracted values (from the fits shown in figure 6.2), we perform the first experimental extraction of $\mathcal{H}_A$. The results for the imaginary and the real parts of $\mathcal{H}_A$, are presented in figure 6.7 as function of Q^2, x_B, and $-t$.

The results show significant trends on Q^2, x_B, and $-t$. More work is needed on the theoretical models to give predictions for $\mathcal{H}_A$. One can see a difference between the precision of the extracted real and imaginary parts, indicating the fact that the beam-spin asymmetry is mostly sensitive to the imaginary part of the CFF $\mathcal{H}_A$, as was anticipated in section 6.1.

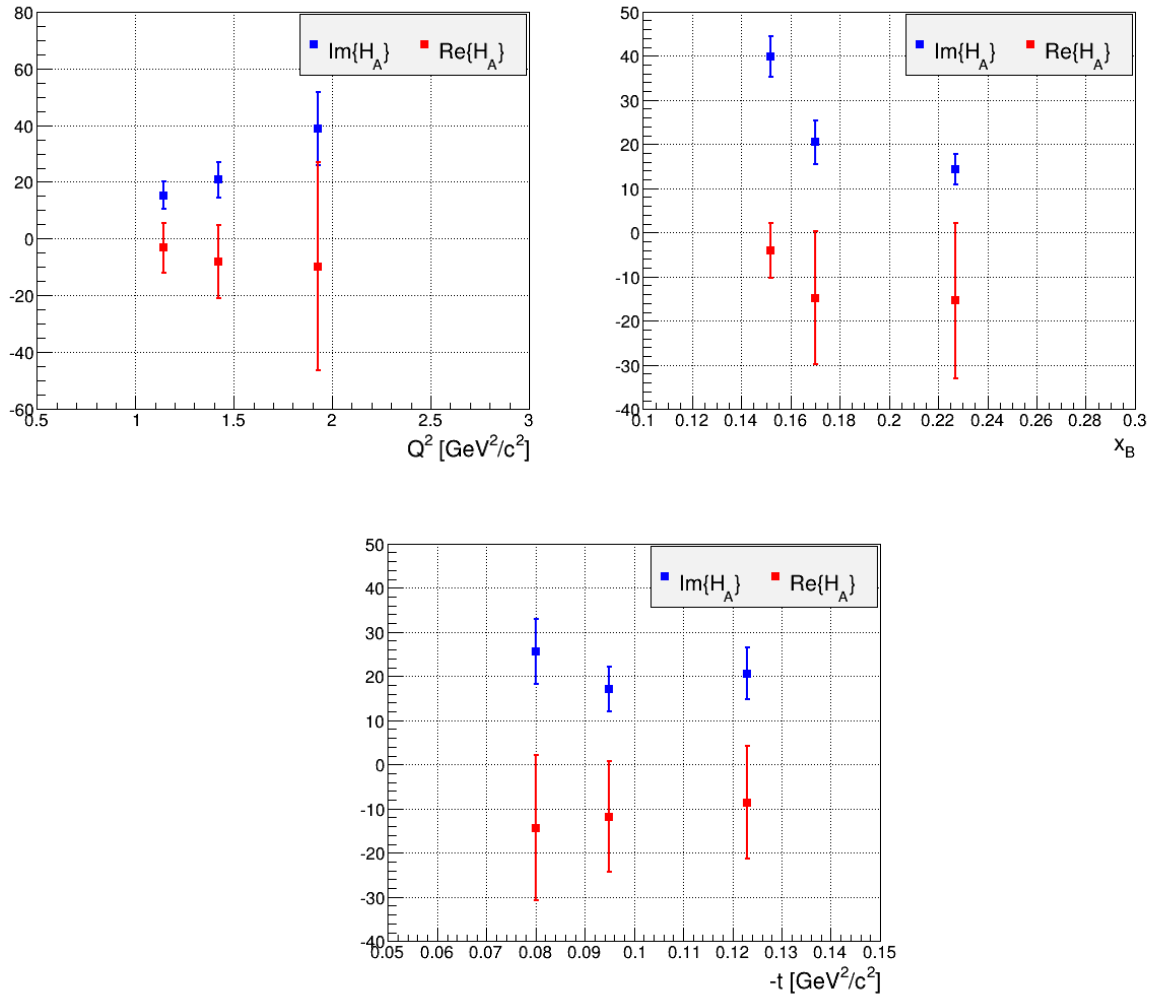

Figure 6.7: The model-independent extraction of the imaginary (blue points) and real (red points) parts of the ^{4}He CFF $\mathcal{H}_A$, as functions of Q^2 (on the top right), x_B (on the top left), and t (on the bottom).

6.4 Generalized EMC ratios

It was shown in the first chapter that beam spin asymmetry ratio between a bound nucleon and the free one reflects the effects of the nuclear medium. Additional information lies on the ratio between the nucleus beam-spin asymmetry and the one of the free nucleon.

The explored kinematical ranges of Q^2, x_B and $-t$ of the free-proton data are similar to the ones of the incoherent channel, and the two datasets were recorded using similar electron-beam energies and experimental setup. Therefore, we extracted the A_{LU} in the same two-dimensional bins on both datasets to make the A_{LU} ratio. The incoherent A_{LU} ratios at $\phi = 90^\circ$ are shown in figure 6.8 as functions of Q^2, x_B, and $-t$, along with the two theoretical predictions at similar kinematical values of Q^2, x_B and $-t$, and the data point from HERMES [96].

Within the given uncertainties, our incoherent A_{LU} ratio shows almost no dependence on Q^2. This ensures the scaling that was observed on the inclusive measurements, and as a consequence on the ordinary EMC effect, is exhibited by the generalized EMC effect as well. Regarding the x_B-dependence of the A_{LU} ratio, one can see that the bound protons have 20-40% smaller beam spin asymmetries than the free protons, and the anti-shadowing region seems to be absent in terms of the A_{LU} ratio. In case of the -t-dependence, one notices that the free and the bound protons appear to have compatible asymmetries as -t increases. These measurements disagree with the enhancement predicted by the simple impulse approximation of V. Guzey [92], as can be seen in chapter 1, figure 1.26. Also, our measured ratios are smaller than the measurement of HERMES (0.93 ± 0.23), and are not well predicted by the calculations of S. Liuti and K. Taneja [94].

More attention is needed in constructing the coherent A_{LU} ratio between ^{4}He and the free proton. One can see from figure 5.9 that the coherent experimental ranges of Q^2, x_B and $-t$ are limited compared to the incoherent channel especially in the $-t$-domain. The latter is due to the fact that the nuclear form factor of the ^{4}He has a steeper drop in $-t$ than the nucleonic one. Therefore, the free proton DVCS data sample was selected in the same coherent domains of Q^2, x_B, and $-t$. Then, both datasets, coherent and free proton, were binned into three bins in Q^2 integrated over the full domains of x_B and $-t$ to shows the Q^2-dependence of the coherent A_{LU} ratio. Similar procedures were performed to shows the x_B-dependence. For the dependence on $-t$, the data are integrated to one bin to optimize a more precise ratio. The results are presented in figure 6.9 along with the available theoretical predictions for this ratio. Our measurements shows a nuclear beam-spin asymmetry enhancement compared to the free proton, with almost no Q^2 dependence. The measured ratios do not match the measurement of HERMES collaboration [96] nor the calculations of Liuti and K. Taneja [94]. On the other hand, our measurements seems to agree with the enhancement predicted by V. Guzey [123]. Moreover, A.Kirchner and D. Mueller (KM model) [82], using their formalism of GPDs factorization, have predicted a constant beam-spin asymmetry ratio of 1.4 (0.35/0.25) for all different spin-zero nuclei at x_B= 0.3, E_b= 6GeV, -t= 0.25 GeV^2, and Q^2= 2.5 GeV^2, while the ratio is 0.2/0.25 for spin-one nuclear targets.

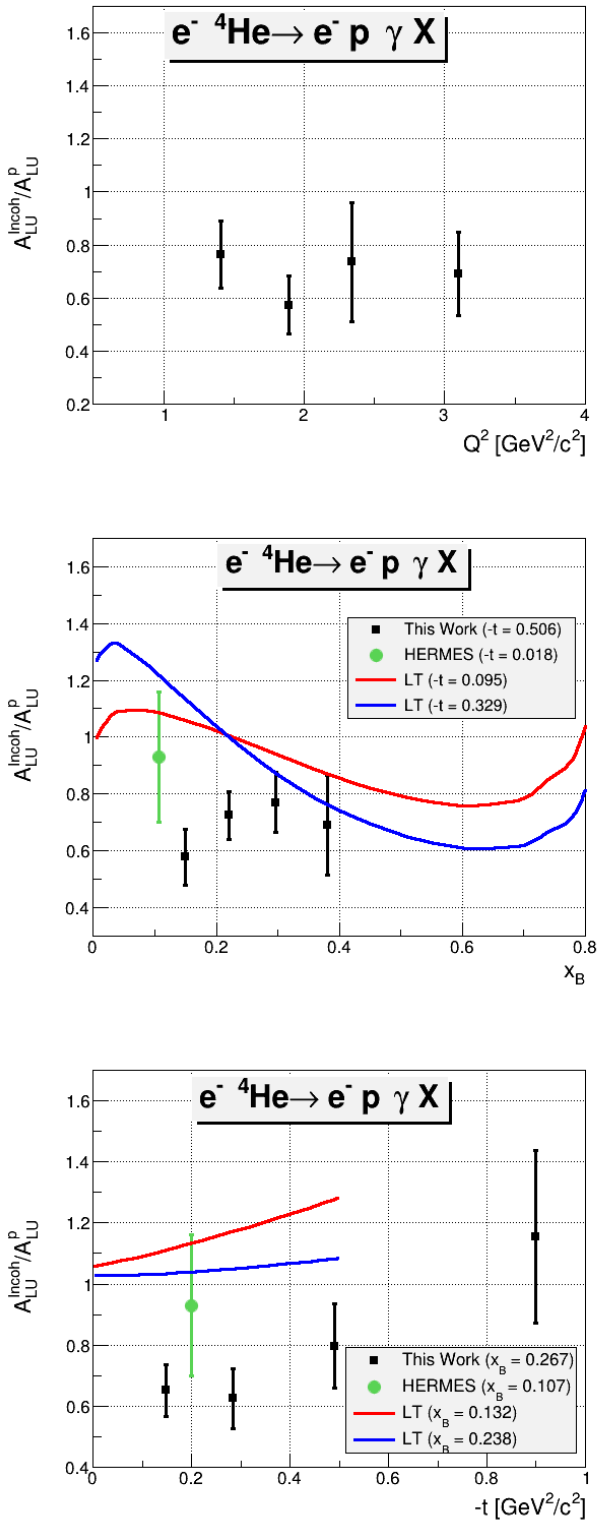

Figure 6.8: The A_{LU} ratio between the bound and the free proton at $\phi = 90°$, as a function of Q^2 (on the top), x_B (on the middle), and t (on the bottom). The green point in each plot present the HERMES inclusive measurement [96]. In the middle plot: the red and the blue curves are from the model of S. Liuti and K. Taneja [94] at two values of $-t$, 0.095 and 0.329 GeV^2/c^2, respectively. In the bottom plot: the red and the blue curves are the theoretical predictions from the same model at x_B= 0.132 and 0.238, respectively.

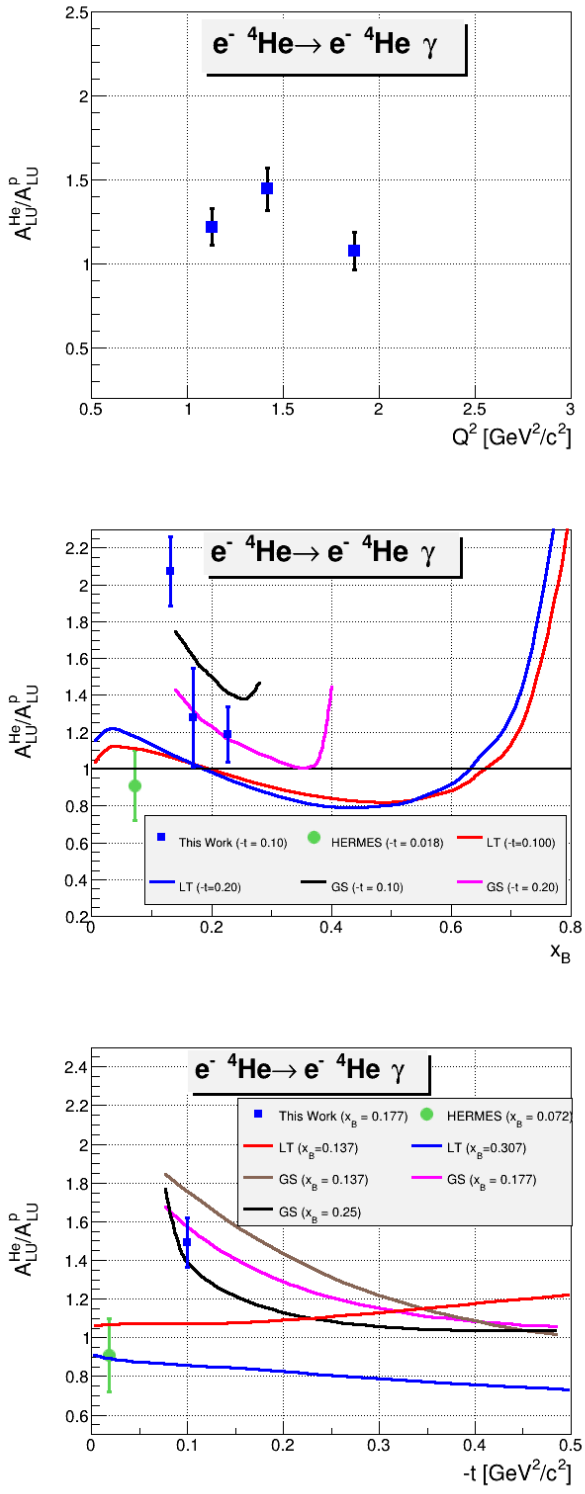

Figure 6.9: The A_{LU} ratio between ^{4}He and free proton at $\phi = 90^\circ$, as a function of Q^2 (on the top), x_B (on the middle), and $-t$ (on the bottom). The blue squares represent the results of this work, where the green points are the HERMES measurements [96]. These measurements are compared to theoretical predictions from S. Liuti and K. Taneja [94] (red and blue curves) and the model predictions from V. Guzey et al. [123] (black, pink, and brown curves).

Conclusions and perspectives

This thesis presented the first exclusive measurements of Deeply Virtual Compton Scattering (DVCS) off ^{4}He. The primary motivation of this study was to investigate the nuclear medium modifications through measuring the DVCS reactions: $e^4He \rightarrow (e^4He\gamma, ep\gamma X)$, within the framework of Generalized Parton Distributions (GPDs). The JLab-08-024 experiment was carried out in 2009 at Hall B of Jefferson Laboratory. During this experiment, two additional detectors were added to the CLAS spectrometer, a TPC that allows to detect low-energy nuclear recoils, and an inner calorimeter, which improves the detection of photons at very forward angle.

The calibration of the detectors was an important part of this work. For the RTPC, different techniques were investigated to calibrate the drift speed, the drift paths, and the gains of the readout collection elements. The drift speed and the drift paths have shown strong sensitivity to the changes of the conditions inside the RTPC, especially the proportions of the drift gas mixture. Regarding the extraction of the gains, we found that comparing real data to GEANT4 simulated one gives more precise gains than solving the Bethe-Bloch series of equations. For the IC, we improved its calibration via constructing the neutral pions from their two-photons decay channel. We observed non-negligible variations of the IC calibration over the experimental data taking period, and a dependence of the radial position inside the calorimeter.

We carried out a full analysis on our 6 GeV dataset, showing the feasibility of measuring exclusive nuclear DVCS reactions. The analysis included: the identification of the final-state particles, the DVCS event selection, the π^0 background subtraction. The beam-spin asymmetry was then extracted for both DVCS channels and compared to the ones of the free-proton DVCS reaction, and to theoretical predictions from two models. Finally, the real and the imaginary parts of the ^{4}He CFF $\mathcal{H}_A$ have been extracted.

Different levels of agreement were found between our measurements and the theoretical calculations. The coherent beam-spin asymmetry shows an enhancement compared to the free proton, which was predicted in an impulse approximation model based on combinatory arguments. The incoherent channel shows smaller beam-spin asymmetries than the free proton, and it shows an overall smaller asymmetry ratio than the measured inclusive ratio at HERMES. Also, our incoherent ratio disagrees with the enhancement predicted by the simple impulse approximation model, showing that additional nuclear effects have to be taken into account. Other comparisons were carried out between our results and a model based on the impulse approximation, using a realistic spectral function of the nucleus. The model predicted lower coherent, and higher incoherent asymmetries compared to our measurements. Regarding the ^{4}He CFF, the real and the imaginary parts have shown significant trends on the kinematical variables. More work is needed on the models to compare them with our results.

This analysis represents a unique source for the nuclear DVCS global dataset, which will be used to constrain GPD models. Further studies will be carried out to understand the new results in terms of partonic spatial and momentum degrees of freedom, giving rise to better understanding of the nuclear effects.

A promising DVCS program is planned for the future with the upgrade of the electron accelerator at Jefferson laboratory. Double of the previous beam energy will be provided to the

different experimental halls of the facility to obtain wider kinematical coverage with more precise measurements. An upgrade of CLAS has been designed for Hall B, named CLAS12, which will operate at an order of magnitude higher luminosity than CLAS. After the progress we achieved in measuring the exclusive nuclear DVCS reactions, a new ^{4}He DVCS experiment using CLAS12 and a new low energy recoil detector is under investigation in order to get better statistics and cover wider kinematical phase-space.

Chapter 7

French summary

7.1 Motivation physiques

Deux types de réactions avec la sonde électromagnétique ont principalement été utilisés pour étudier la structure des nucléons ces dernières décennies: les processus exclusifs comme la diffusion élastique (ES pour Elastic Scattering) et les processus inclusifs comme la diffusion inélastique profonde (DIS pour Deep Inelastic Scattering). L'ES permet de mesurer des fonctions de structure appelées "facteurs de forme". Dans un cadre où le nucléon va à la vitesse de la lumière dans une certaine direction, les transformées de Fourier des facteurs de forme fournissent des informations sur la distribution de charge à l'intérieur du nucléon dans le plan transverse à cette direction [14] [15]. Le DIS permet de mesurer les "fonctions de distribution des partons" qui procurent des informations sur l'impulsion longitudinale portée par les différents partons dans un nucléon. En 1983, la *European Muon Collaboration* (EMC) [8] a découvert que les fonctions de structure DIS des nucléons liés à l'intérieur des noyaux sont différentes de celles des nucléons libres. Pour comprendre les origines de cet effet, des études ont alors été menées au CERN [20, 39], SLAC [40], HERMES [41] et JLAB [42]. Des corrélations ont été observées entre cet effet et des propriétés nucléaires, telles que la masse et la densité nucléaires [42, 46], mais il n'y a toujours pas d'explications universellement acceptées pour ce phénomène.

En étudiant les corrélations entre position et impulsion des partons dans le nucléon, on peut espérer obtenir davantage d'informations qu'avec seulement les distributions d'impulsion mesurées dans le DIS. Ces corrélations sont accessibles via des fonctions de structure appelées distributions de partons généralisées (GPDs pour Generalized Parton Distributions). Ces GPDs sont accessibles par des réactions d'électro-production exclusives de méson ou de photon, en particulier le DVCS, qui est l'electro-prodction d'un photon réel. La figure 7.1 montre le diagramme du "sac-à-main" qui illustre le processus dominant pour le DVCS sur un nucléon.

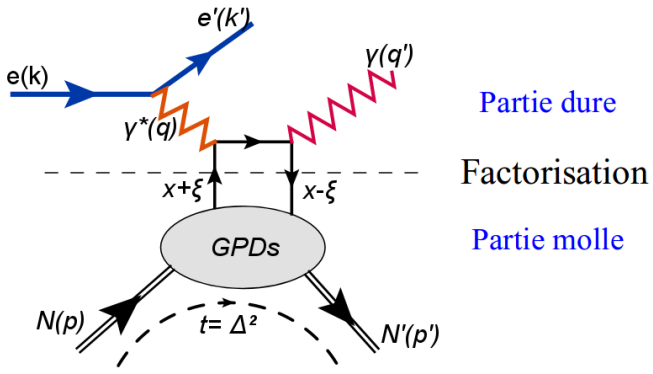

Figure 7.1: Diffusion Compton profondément virtuelle (DVCS) sur un nucléon.

Dans le DVCS, un photon virtuel (γ^*), rayonné par l'électron incident (e), interagit avec un quark du nucléon qui émet un photon réel (γ) avant de revenir dans le nucléon. Grâce au théorème de factorisation de QCD (Quantum ChromoDynamics), le processus peut être décomposé en deux parties: une partie dure et une partie molle. La partie dure se calcule par la QCD perturbative, tandis que la partie molle qui représente toute la complexité de la structure partonique du nucléon, est paramétrée en termes de GPD [32] [33].

Les GPDs dépendent de trois variables: x, ξ et t. $x+\xi$ est la fraction d'impulsion longitudinale du nucléon portée par le quark frappé par le photon virtuel, -2ξ est la composante d'impulsion longitudinale du transfert d'impulsion Δ (= $p' - p$) et t (=Δ^2) est le transfert de l'impulsion au carré entre l'état initial et l'état final du nucléon. Les GPD (x, ξ, t) peuvent être définies comme l'amplitude de probabilité de trouver un parton avec une impulsion longitudinale $x+\xi$ et de le remettre dans le nucléon avec l'impulsion longitudinale $x-\xi$, sans casser le nucléon, à un transfert d'impulsion carré t.

Pour un nucléon (spin 1/2), il y a quatre GPDs qui conserventla chiralité: H, E, $\widetilde{H}$ et $\widetilde{E}$. Dans le cas de cible de spin-zéro, teles que ^{4}He ^{12}C et ^{16}O, il y a seule GPD ($H_A(x,\xi,t)$) qui paramétrise leur structure partonique. Expérimentalement, nous ne pouvons mesurer que les variables ξ et t. Par conséquent, les GPDs ne sont pas directement mesurables à partir de l'expérience. En revanche, nous pouvons mesurer les facteurs de forme Compton (CFFs pour Compton Form Factors), qui sont des intégrales des GPDs sur x. Les GPDs sont aussi définies pour chaque saveur de quark q ($q = u, d, s$).

Expérimentalement, le DVCS est indiscernable du processus de Bethe-Heitler (BH) qui est la réaction où le photon final est émis par le lepton entrant ou sortant. Le BH n'est pas sensible aux GPDs. La section efficace de BH est calculable à partir des facteurs de forme de la cible. Par conséquent, la section efficace de $ep \to ep\gamma$ expérimentalement mesurée reçoit des contributions du BH, du DVCS et de l'interférence entre les deux processus.

Les cibles nucléaires permettent d'accéder à la mesure de deux canaux de DVCS: le cohérent et l'incohérent. Dans le canal cohérent, le noyau cible reste intacte et recule en émettant un photon réel ($eA \to e'A'\gamma$, où A représente le noyau-cible). Ce processus permet de mesurer les GPDs de la cible nucléaire contenant l'information sur les corrélations entre les partons dans le noyau. Dans le canal incohérent, le noyau se brise et le DVCS se passe sur le nucléon lié qui émet le photon final ($eA \to e'N'\gamma\ X$). Ce dernier canal permet de mesurer les GPDs, des nucléons liés et d'étudier les modifications des nucléons dans le milieu nucléaire. L'^{4}He est caractérisé par sa haute densité et par son système bien connu. Ces aspects font de l'^{4}He une cible idéal pour la compréhension des effets nucléaires au niveau partonique.

7.2 Appareillage expérimental

L'expérience présentée dans cette thèse a été réalisée dans le Hall B du Thomas Jefferson National Accelerator Facility (JLab), Virginie, USA. Le Hall B est équipé du spectromètre CLAS (CLAS pour CEBAF Large Acceptance Spectrometer). Notre expérience a été réalisée en 2009 avec un faisceau d'électrons polarisés longitudinalement de 6.064 GeV projeté sur une cible gazeuse d'^{4}He. L'accelérateur du JLab (illustré sur la figure 7.2) est constitué par un injecteur polarisé d'électrons et deux accélérateurs linéaires (linacs) reliés par des arcs de recirculation. Le faisceau peut être envoyé simultanément à trois Halls expérimentaux, A, B et C. L'injecteur produit des

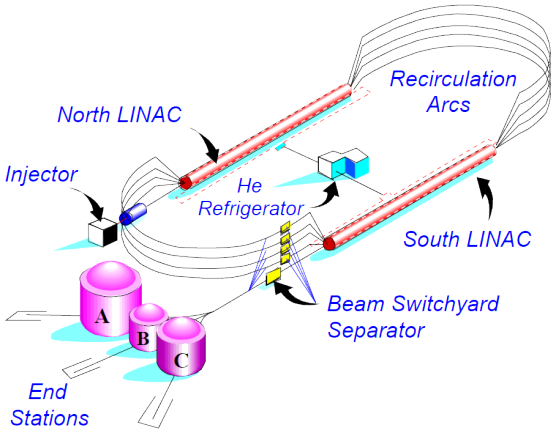

Figure 7.2: Schéma de l'accélérateur du JLab avec les trois halls expérimentalaux (A, B et C).

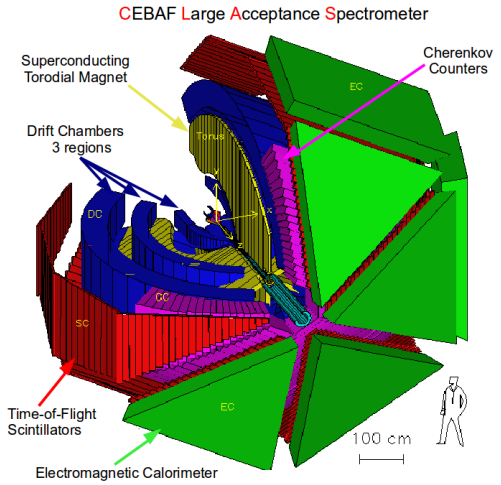

Figure 7.3: Représentation de l'appareillage de base du détecteur CLAS dans le Hall B.

électrons de 67 MeV en utilisant une photocathode polarisée. Ensuite, ces électrons sont injectés dans l'accélérateur linéaire pour être accélérée. Après cinq orbites successives, les électrons atteignent des énergies allant jusqu'à 6 GeV avec une polarisation pouvant aller jusqu'à 85%. Le système radiofréquence des linacs produit un faisceau à 1497 MHz soit 2 ns d'intervalle entre des paquets. Ainsi, après separation, chaque hall expérimental reçoit des paquets d'électrons à une fréquence de 499 MHz.

Le Hall B peut atteindre une luminosité de l'ordre de $10^{34}\text{cm}^{-2}\text{s}^{-1}$ avec son détecteur à grand angle solide CLAS. Le détecteur CLAS a été conçu pour utiliser des faisceaux d'électrons et de photons projetés sur des cibles fixes. La configuration de base du CLAS est montré sur la figure 7.3. Il est composé de trois régions de chambres à dérive (DCs pour Drift Chambers) pour la trajectographie des particules chargées, d'un aimant supraconducteur de forme toroïdale qui courbe les trajectoires des particules, de compteurs Cherenkov (CCs pour Cherenkov Counters) pour séparer les électrons des pions négatifs, de compteurs à scintillation (SCs pour Scintillation Counters) pour identifier les hadrons chargés par la mesure de leur temps de vol (TOF) et de Calorimètres électromagnétiques (ECs pour Electromagnetic Calorimeters) afin d'identifier et de mesurer les énergies des électrons, et des photons, et de détecter les neutrons.

Le cœur du système de détection de CLAS est un champ magnétique toroïdal qui permet la détection des particules chargées d'impulsion supérieure à 250 MeV/c. Le champ toroïdal est généré par un aimant constitué de six bobines supraconductrices. Le champ magnétique a une composante principale azimutale, par conséquent; les trajectoires s'approchent ou s'éloignent de la direction du faisceau en laissant l'azimut inchangé. La structure de l'aimant sépare l'ensemble du détecteur CLAS en six secteurs indépendants et identiques contenant les sous-détecteurs (DCs, CCs, SCs and ECs).

Pour garantir l'exclusivité de notre réaction de DVCS sur l'^4He ($e\ ^4He \rightarrow e\gamma^4He$), la configuration de base du CLAS a été améliorée avec une chambre à projection temporelle radiale (RTPC pour Radial Time Projection Chamber) pour détecter les noyaux d' énergies faibles, d'un calorimètre supplémentaire (IC pour Inner Calorimeter) pour détecter les photons réels

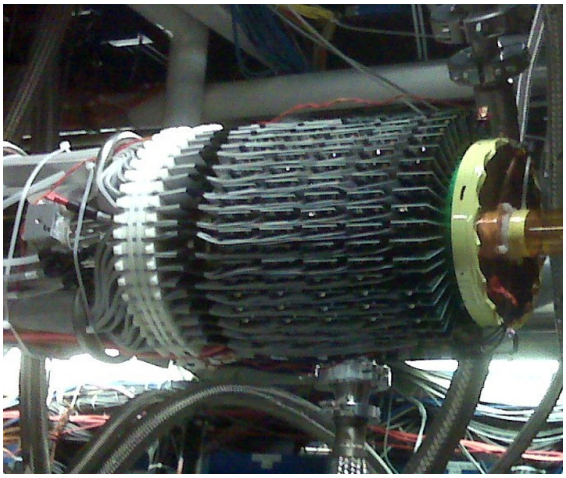

Figure 7.4: Une vue de la RTPC avant l'insertion dans le solénoïde. Le faisceau d'électrons incident vient de la gauche.

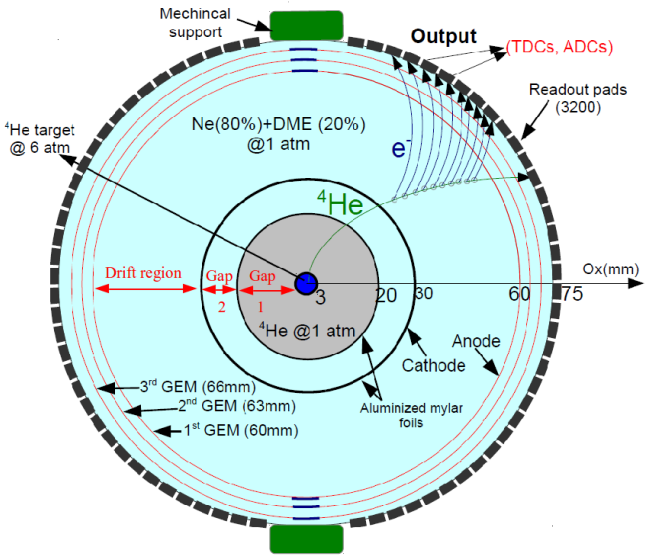

Figure 7.5: Schéma de la RTPC prise sur un plan perpendiculaire à la ligne de faisceau, avec une trace typique de ^{4}He.

emis vers l'avant, et d'un aimant solénoïde pour minimiser les effets du bruit de fond des électrons Møller (diffusion des électrons du faisceau sur les électrons du cortège atomique de la cible).

Pour un faisceau d'électron de 6 GeV, le noyau de recul a une impulsion moyenne d'environ 100 MeV/c. Pour détecter ces noyaux de faible énergie, une TPC radiale (RTPC) a été ajoutée à CLAS. La figure 7.4 montre une photo de la RTPC, et la figure 7.5 montre un dessin schématique de sa structure interne. La RTPC fait 200 mm de long et 150 mm de diamètre, elle est composée de deux modules séparés électroniquement, chacun couvrant environ 150° de l'angle azimutal. La RTPC détecte les particules chargées à travers l'ionisation provoquée par le noyau de recul en traversant le volume de détection rempli de gaz. Les électrons ionisés dérivent sous l'effet d'un champ électromagnétique, ils sont ensuite amplifiés par un système multiplicateur d'électrons à gaz (GEM) et ils sont enfin détectés sur un système de collecte. Le système de lecture enregistre les informations en fonction du temps. La charge est mesurée en unités analogique (ADC pour Analog-to-Digital-Converter), tandis que le temps est donné en Time-to-Digital unités de Converter (TDC). Chaque TDC est égal à 114 ns, et permet de mesurer le temps pris par l'électron pour dériver depuis son origine. Le temps d'arrivée des électrons fournit des informations sur la position de l'ionisation initiale dans la région de dérive, permettant de reconstruire la trajectoire de la particule. Les ADCs enregistrés quant à eux indiquent l'énergie déposée.

Dans la configuration de base du CLAS, les photons sont détectés par les ECs qui couvrent des angles polaires de 8° à 45°. Avec un faisceau d'électrons de 6 GeV, une grande partie des photons DVCS sont produits à des angles polaires en dessous de 8°. Depuis l'expérience CLAS-E1DVCS (2005) [105], CLAS a été amélioré avec l'ajout d'un calorimètre intérieur (IC). Ce calorimètre couvre des angles polaires entre 5° et 15°.

Avec un taux d'occupation de plus de 4%, l'efficacité des chambres à dérive commence à baisser et la résolution se dégrade. La première région de DC (R1) a une occupation plus élevée que les deux autres régions (R2 et R3), principalement à cause du bruit provenant des électrons

Møller. Pour réduire l'effet du bruit, CLAS a été amélioré par l'ajout d'un solénoïde qui entoure la cible [105]. L'aimant fournit un champ magnétique de 4,5 T centré sur la cible. Ce champ confine les électrons Møller à des très petits angles et empêche leur arrivée dans la première région de chambre à dérive. La présence du champ magnétique du solénoïde permet aussi de déduire l'impulsion des particules chargées grâce à la courbure de leur trajectoire dans la RTPC.

7.3 Analyse des données

L'état final d'un événement DVCS cohérent (incohérent) sur l'^{4}He est composé de trois particules: un électron, un ^{4}He (proton), et un photon réel. Pour identifier les événements DVCS, nous avons d'abord identifié, individuellement, ces différentes particules. Ensuite, les événements avec un bon électron, une bonne trajectoire dans la RTPC et au moins un bon photon, sont considérés comme de possibles événements DVCS cohérents. Même si la réaction DVCS a seulement un photon réel dans l'état final, les événements avec plus d'un bon photon ne sont pas rejetés à ce stade. Ceci est motivé par le fait que certains photons correspondent à des coïncidences aléatoires qui ne proviennent pas de la même reaction et qui peuvent etre retirés pas d'autres critères (cinématiques). Les événements avec un π^0, identifiés grace à la masse invariante des 2γ, sont par contre retirés de l'échantillon DVCS cohérent. Après cela, le photon le plus énergétique est choisi comme le photon DVCS. Pour considérer un événement comme étant un DVCS sur l'^4He, il doit passer deux type de coupures, celles caractérisant le DVCS et les coupures d'exclusivité.

Coupures DVCS

- $Q^2 > 1$ GeV^2: pour s'assurer que l'interaction se produit au niveau partonique et l'applicabilité de la factorisation sur le diagramme du sac-à-main DVCS.
- La masse invariante du système (W) supérieure à 2 GeV/c^2. Cette coupure permet d'éviter la région d'excitation du proton.
- $-t > -t_{min}$: l'impulsion transférée à l'^{4}He au carré doit être supérieure à une valeur minimale définie par la cinématique:

$$t_{min} = \frac{-Q^2 \cdot 2(1-x_A)(1+\varepsilon^2-\sqrt{1+\varepsilon^2})}{4x_A(1-x_A)+\varepsilon^2}, \tag{7.1}$$

  où $\varepsilon^2 = \frac{4M^2_{^4He}x^2_A}{Q^2}$, $x_A = \frac{M_p \cdot x_B}{M_{^4He}}$ et M_p ($M_{^4He}$) est la masse du proton (^4He).

  Dans le cas du DVCS incohérent, la variable x_A est remplacée par x_B dans la formule de t_{min}.

- $E_\gamma > 2$ GeV. Ceci est une coupure de nettoyage appliquée sur les distributions bleues dans la figure 7.6 pour le bruit dans l'échantillon DVCS avant les coupures d'exclusivité.

Coupures d'exclusivité

L'exclusivité de la réaction DVCS cohérente est assurée en imposant les lois de conservation suivantes:

- La coupure de coplanarité. En principe, le photon virtuel, le photon réel et le noyau hélium sont produits dans le même plan, qui est appelé le plan hadronique. $\Delta\phi$ est l'angle entre les plans (γ,γ^*) et (γ^*,^4He).
- Coupure sur l'énergie, la masse et l'impulsion transverse manquante ($p_X^T = \sqrt{(p_X^x)^2 + (p_X^y)^2}$) pour la configuration $\mathbf{P}_X^{e^4He \to e^4He\gamma\ X}$.
- Coupure sur la masse manquante pour les configurations $e^4He \to e^4HeX$ et $e^4He \to e\gamma X$.
- Coupure sur l'angle entre la direction du photon détecté et celle du photon calculé dans la configuration $e^4He \to e^4HeX$.

La figure 7.6 résume toutes les coupures d'exclusivité. Nous avons appliqué des coupures à 3σ autour de la valeur moyenne de chaque distribution. Les événements qui passent ces coupures sont considéres comme de bons événements DVCS cohérents.

Dans le canal incohérent, le processus DVCS se passe sur un proton lié. Ainsi, l'état final a un proton de recul au lieu d'un noyau d'hélium. Par conséquent, les événements avec un bon électron, un proton de recul, et au moins un photon réel sont les bons candidats. Pour le reste, nous suivons les mêmes étapes qui ont été presentées pour le canal DVCS cohérent. La figure 7.7 résume les coupures d'exclusivité pour le canal incohérent.

Même après avoir appliqué les lois de conservation, l'échantillon DVCS comporte encore un bruit de fond non exclusif. Dans notre région cinématique, la contamination principale vient de l'électroproduction de pions neutres. Lorsqu'un des photons de la décroissance à deux photons d'unπ^0 passe les coupures DVCS, il sera compté comme un événement DVCS. Ces événements doivent être soustraits. À cette fin, nous appliquons une technique dans laquelle nous combinons la mesure d'électroproduction exclusive de π^0 dans notre échantillon de données avec une simulation Monte-Carlo pour évaluer la quantité d'événements avec un π^0 restée dans l'échantillon DVCS sélectionné.

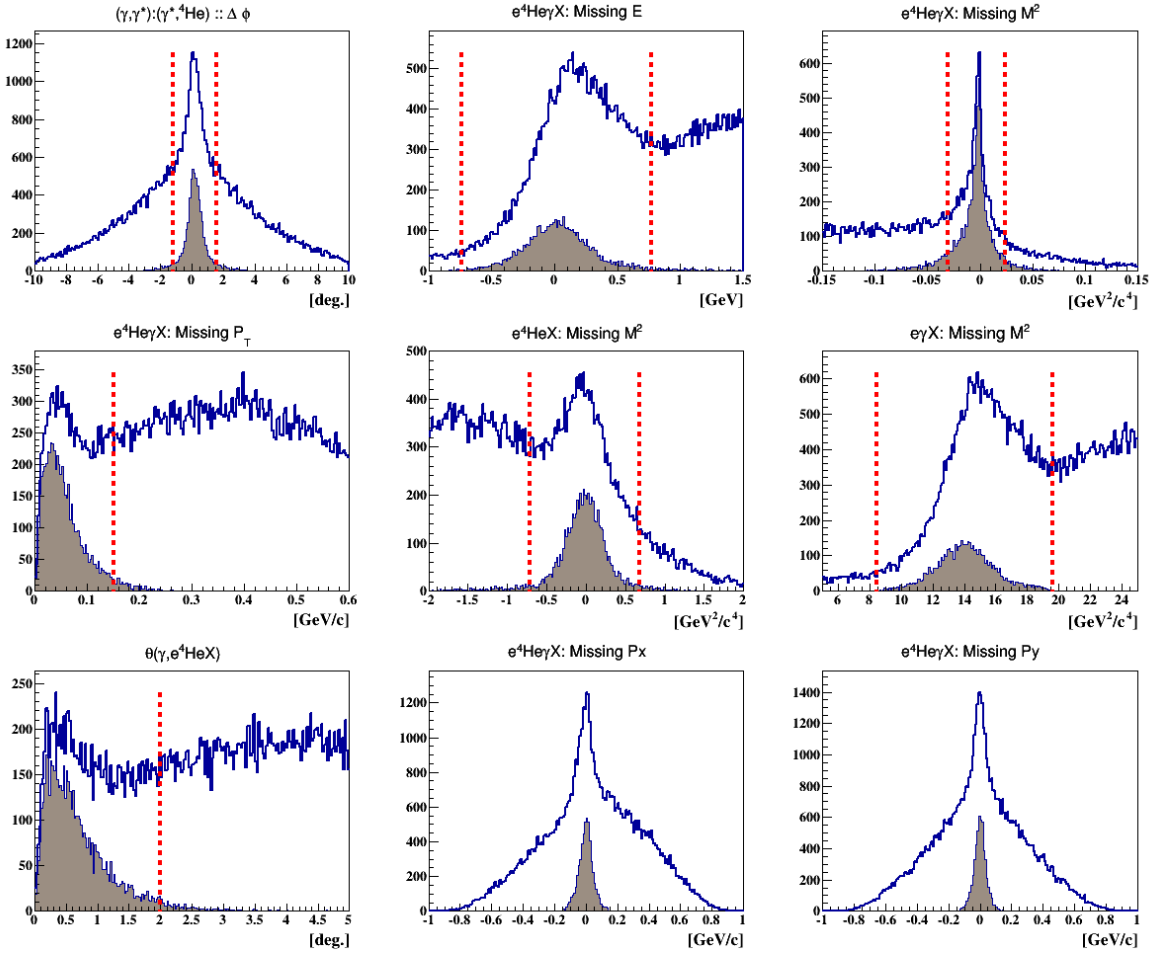

Figure 7.6: Les coupures d'exclusivité pour le DVCS cohérent. Les distributions bleues représentent les événements cohérents après les coupures DVCS et avant toutes les coupures d'exclusivité. Les distributions ombrées représentent les événements qui ont passé toutes les coupures d'exclusivité sauf celles de la quantité tracée. Les distributions de gauche à droite et de haut en bas sont: la coplanarité ^{4}He-photon, l'énergie manquante, la masse manquante au carré, l'impulsion transverse manquante à partir de $e^4He\gamma$, la masse manquante au carré e^4HeX, la masse manquante au carré $e\gamma$ X, l'angle entre la particule manquante dans e^4HeX et le photon mesuré, l'impulsion manquante P_x et P_y en $ep\gamma X$. Les lignes rouges verticales représentent les coupures à 3σ.

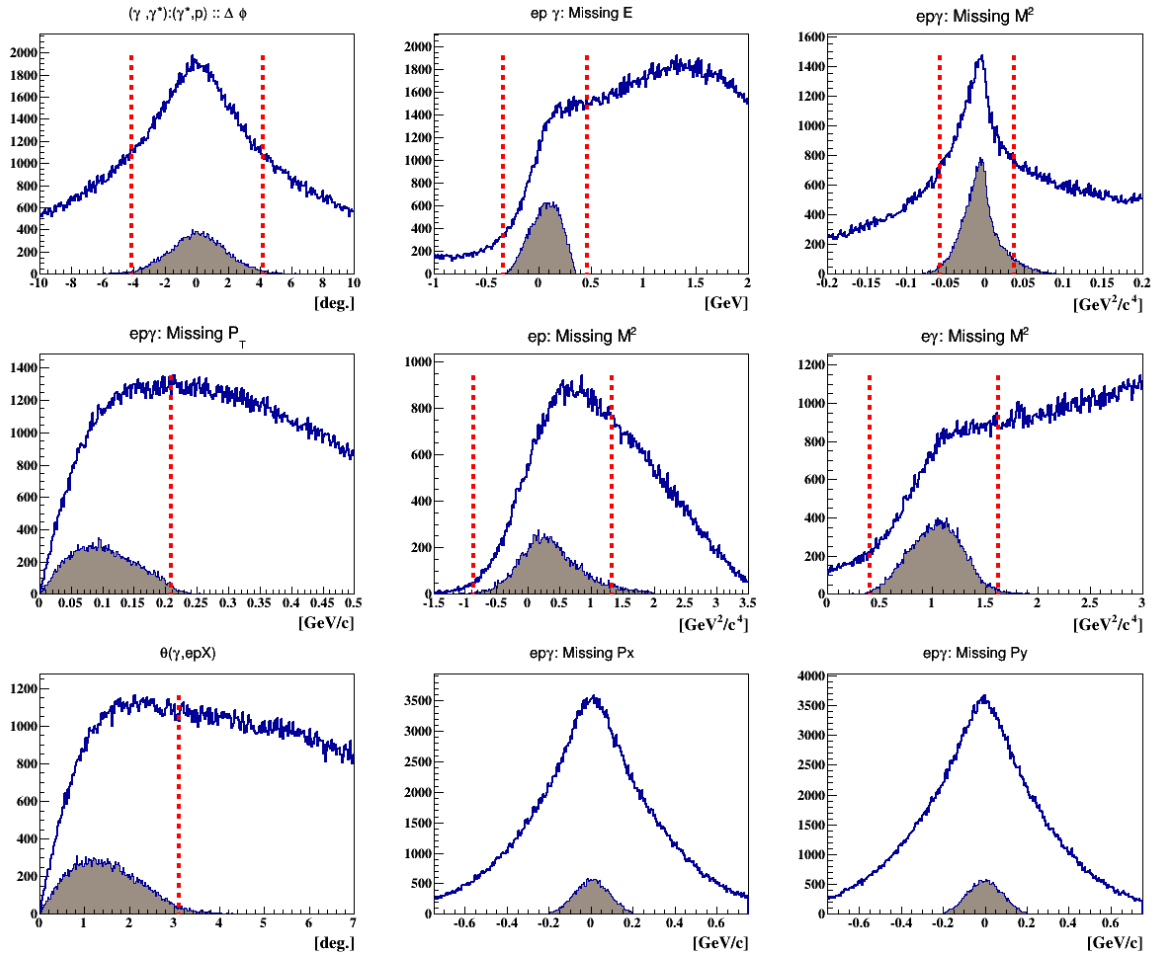

Figure 7.7: Les coupures d'exclusivité pour le DVCS incohérent. Les distributions ombrées montrent les événements DVCS incohérents qui passent toutes les coupures d'exclusivité, sauf celles de la quantité tracée. Les distributions de gauche à droite et de haut en bas sont: la coplanarité proton-photon, l'énergie manquante, la masse manquante au carré, l'impulsion transverse manquante à partir de $ep\gamma X$, la masse manquante au carré epX, la masse manquante au carré $e\gamma$ X, l'angle entre la particule manquante dans epX et le photon mesuré, l'impulsion manquante P_x et P_y en $ep\gamma X$. Les lignes rouges verticales représentent les coupures à 3σ.

7.4 Résultats

7.4.1 Asymétrie de spin du faisceau expérimentale

L'asymétrie de faisceau A_{LU} est définie comme:

$$A_{LU} = \frac{\sigma^+ - \sigma^-}{\sigma^+ + \sigma^-}, \tag{7.2}$$

où σ^+ (σ^-) est la section efficace d'électroproduction du photon avec hélicité positive (négative) de l'électron du faisceau.

Un avantage important de l'asymétrie de faisceau est que tous les facteurs de normalisation s'annulent durant le calcul de l'asymétrie. L'asymétrie de faisceau A_{LU} est définie comme:

$$A_{LU} = \frac{N^+ - N^-}{N^+ + N^-}, \tag{7.3}$$

où N^+ (N^-) est le nombre d'événements $e(^4He/p)\gamma$ avec hélicité positive (négative) de l'électron du faisceau, corrigé de la contamination des π^0.

Le processus DVCS dépend de quatre variables cinématiques: Q^2, x_B, t et ϕ. Le nombre d'événements DVCS cohérents (incohérents) identifiés est d'environ 5000 (30k). En raison de nos statistiques limitées, un binning seulement bidimensionnel est effectué dans cette analyse. Nous construisons les bins en deux dimensions comme il suit: les distributions en Q^2, x_B et $-t$ des événements candidats DVCS cohérents (incohérents) sélectionnés sont réparties statistiquement en trois (quatre) bins. Ensuite, les événements dans chaque bin en Q^2, x_B et $-t$, sont réparties en neuf bins en ϕ. Par conséquent, nous nous retrouvons avec des bins Q^2-ϕ intégrés sur tout le domaine en x_B et $-t$, des bins x_B-ϕ intégrés sur Q^2 et $-t$, et des bins $-t$-ϕ bins intégrés sur Q^2 et x_B. Par exemple, la figure 7.8 montre les bins unidimensionnels en Q^2 et les bins associés en ϕ.

Dans la figure 7.9, nous montrons les résultats de l'asymétrie du spin de faisceau du canal cohérent pour les bins en Q^2, x_B et $-t$ que nous avons obtenues. Sur la figure 7.10, nous montrons les résultats du canal incohérent.

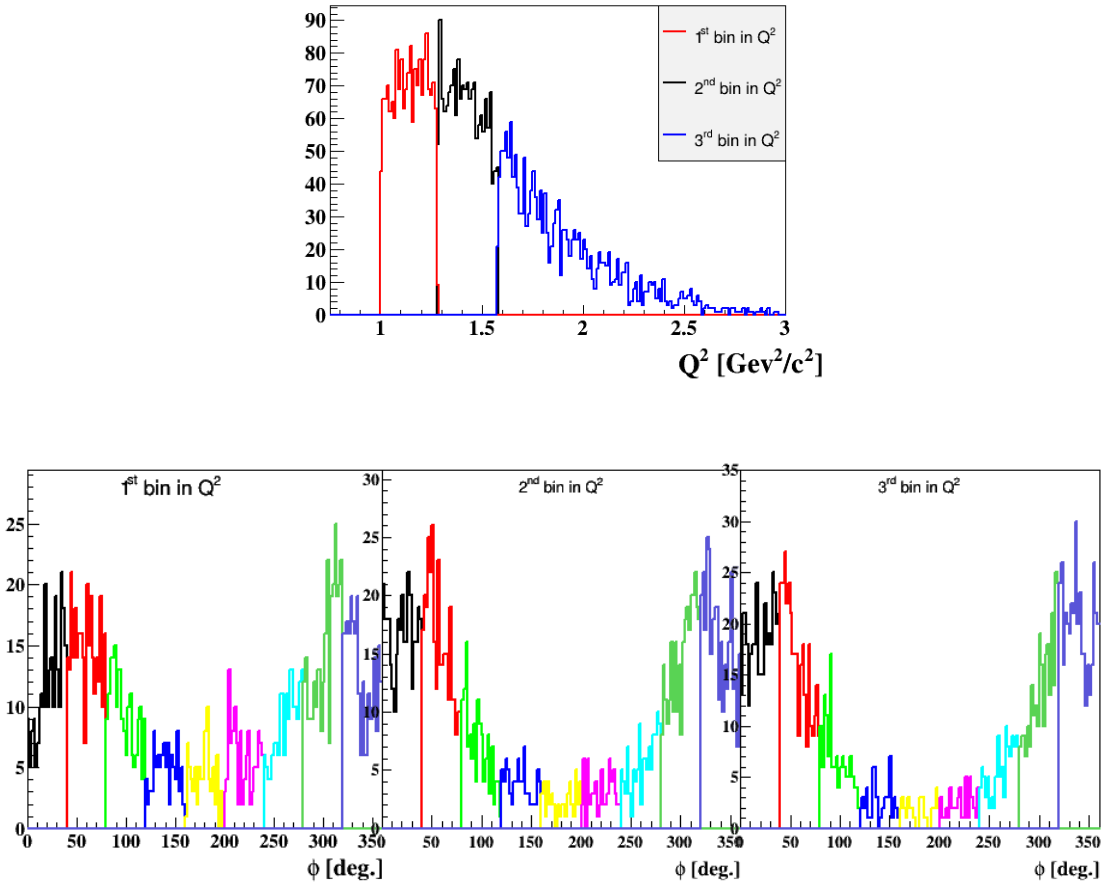

Figure 7.8: En haut: la distribution en Q^2 des événements DVCS cohérents. Les différentes couleurs indiquent les différents bins en Q^2 intégré sur tout le domaine en $-t$ et x_B. En bas: les distributions en ϕ des événements DVCS cohérents pour les bins en Q^2, qui sont présentés dans la figure du haut. Les différentes couleurs des distributions en ϕ représentent les neuf bins en ϕ.

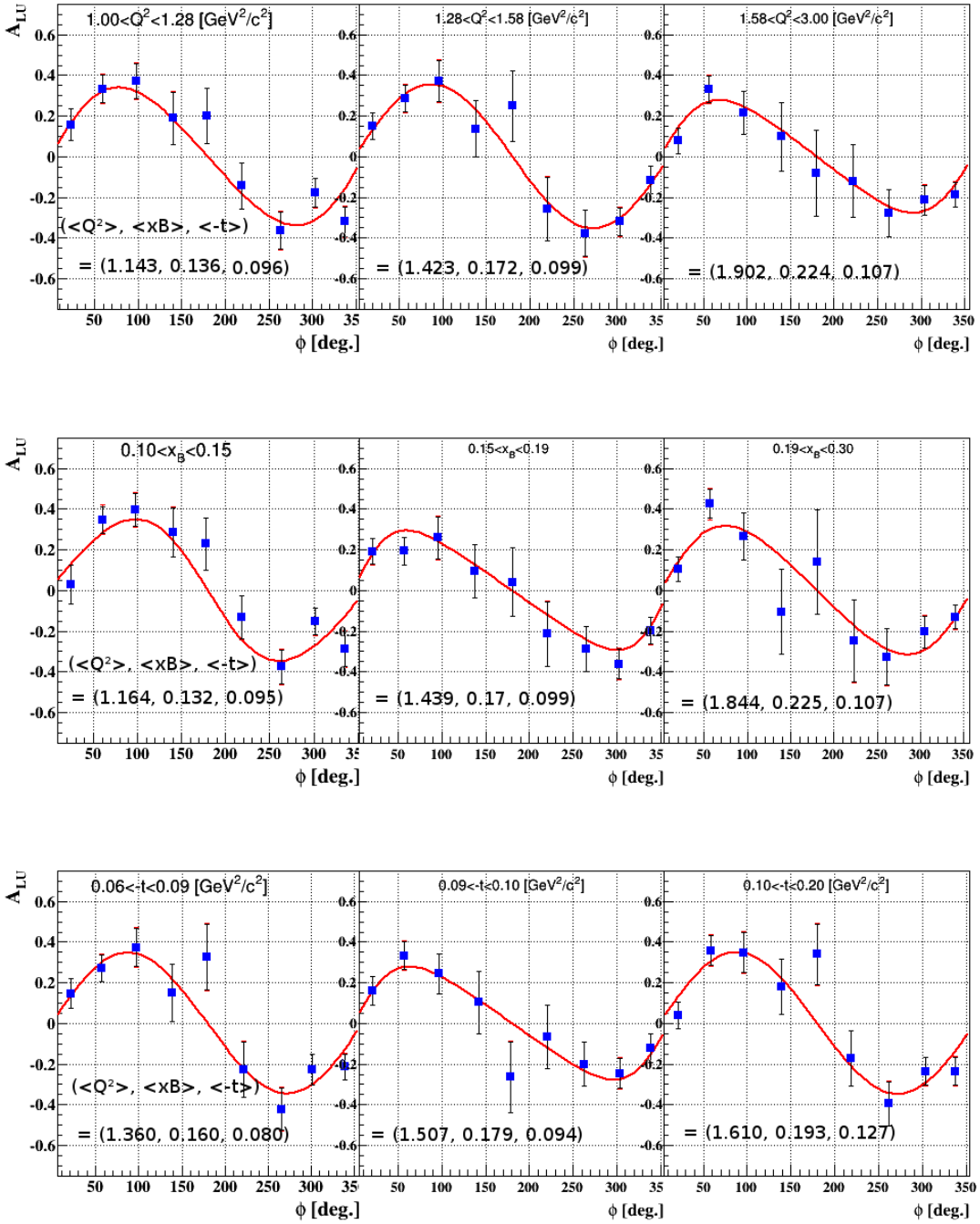

Figure 7.9: L'asymétrie du spin de faisceau A_{LU} du canal cohérent en fonction de ϕ pour les bins en Q^2, x_B et $-t$, de haut en bas. Les courbes rouges représentent des ajustements de la forme $\frac{\alpha \sin(\phi)}{1+\beta cos(\phi)}$.

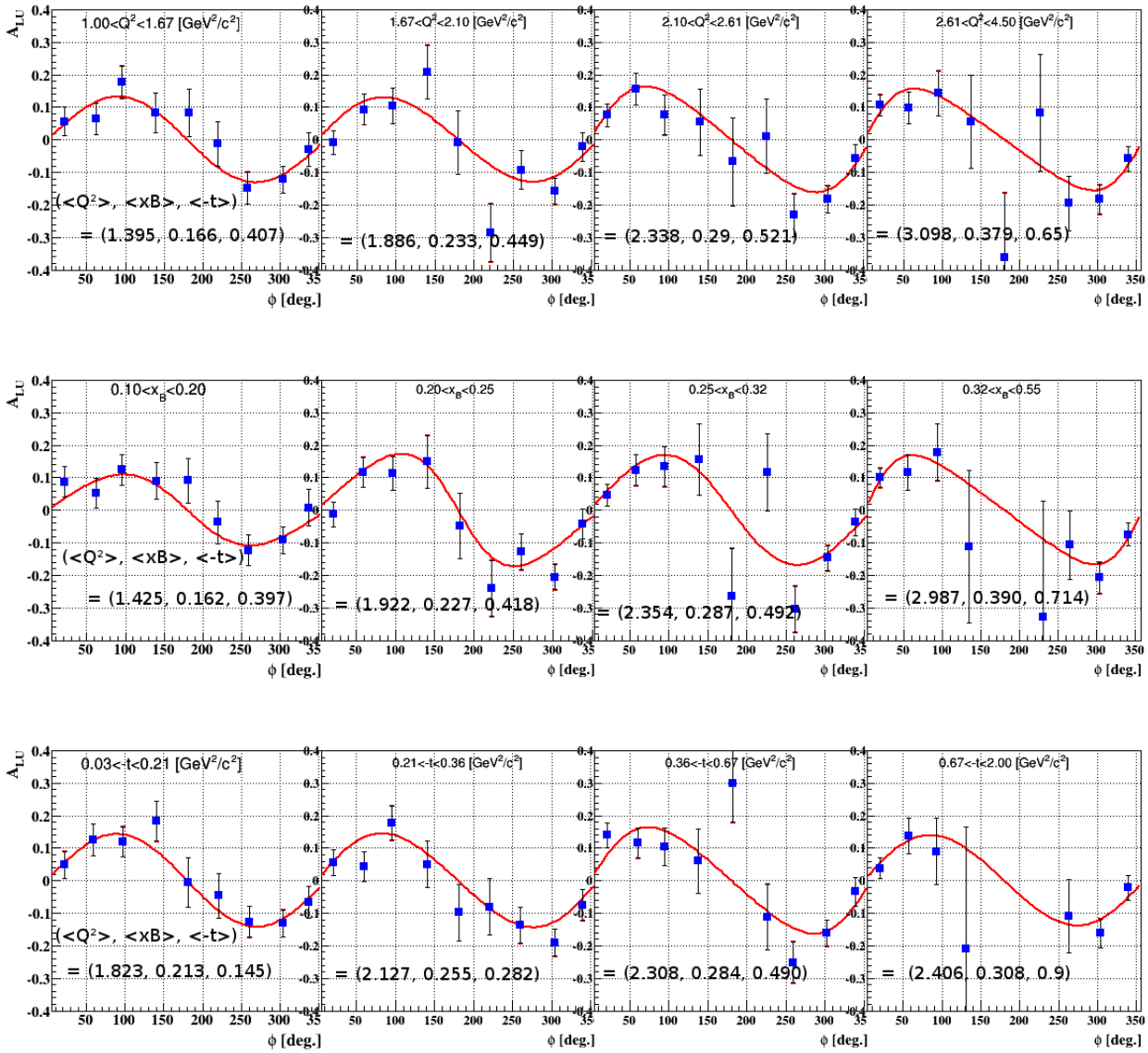

Figure 7.10: A_{LU} du canal incohérent en fonction de ϕ sur les bins en Q^2, x_B et $-t$, de haut en bas. Les courbes rouges représentent des ajustements de la forme $\frac{\alpha \sin(\phi)}{1+\beta cos(\phi)}$.

7.5 EMC généralisé

La comparaison de nos canaux de DVCS avec la réaction de DVCS sur proton libre nous permet d'étudier les effets nucléaires sur les GPDs. Une analyse similaire a été effectuée sur l'ensemble de données des DVCS sur proton libre au cours de l'expérience E1DVCS (parties 1 et 2). Les premiers résultats de la partie 1 ont été publiés dans [73, 76], mais pour des raisons pratiques, nous avons utilisé la partie 2 dans la suite de notre analyse basée sur le travail présenté dans les références [119, 120]. Les asymétries du spin de faisceau extraites dans les parties 1 et 2 de E1DVCS étant entièrement compatibles.

Les cinématiques explorées en Q^2, x_B et $-t$ des données du proton libre sont semblables à celles de notre canal incohérent. Les deux ensembles de données ont été acquis en utilisant des énergies de faisceau d'électrons similaires et la même configuration expérimentale. Par conséquent, nous avons extrait A_{LU} dans les mêmes bins pour les deux ensembles de données pour faire le rapport des A_{LU}. Les rapports pour le canal incohérent à ϕ= 90° sont présentés sur la figure 7.11 en fonction de Q^2, x_B et $-t$. Nous montrons aussi le point expérimental de la collaboration HERMES [96] et les deux prédictions théoriques aux valeurs cinématiques similaires.

Dans les incertitudes des données, notre rapport incohérent des A_{LU} ne montre pratiquement aucune dépendance en Q^2. Ceci est conforme à ce qui a été observé pour les rapports de fonctions de distribution de partons DIS, dont à été deduit l'effet ordinaire EMC. En ce qui concerne la dépendance en x_B, nous pouvons voir que les A_{LU} des protons liés sont de 20% à 40% plus petits que les A_{LU} des protons libres. Pour la dépendance en $-t$, nous remarquons que le proton libre et le proton lié semblent avoir des asymétries similaires quand $-t$ augmente. Ces mesures sont en désaccord avec l'augmentation prévue par le modèle de l'impulse approximation de V. Guzey [92]. On note aussi que nos rapports d'A_{LU} mesurés sont plus petits que la mesure par HERMES (0,93 $\pm$ 0,23), et ne sont pas bien prédits par les calculs de S. Liuti et K. Taneja [94].

Pour le rapport cohérent des A_{LU} entre ^{4}He et proton libre, nous pouvons le voir sur la figure 5.9 que les domaines en Q^2, x_B et $-t$ sont plus restreints par rapport du canal incohérent, en particulier dans le domaine en $-t$. Ceci est dû au fait que le facteur de forme nucléaire de l'^{4}He tombe plus vite en fonction de $-t$ que le facteur de forme nucléonique. L'ensemble de données, cohérent et protons libre, a été réparti en trois bins en Q^2 intégrés sur les domaines complets de x_B et $-t$ pour montrer la dépendance en Q^2 du rapport de A_{LU} cohérent. De même pour la dépendance en x_B. Pour la dépendance en $-t$, les données sont intégrées sur un seul bin afin d'obtenir un rapport plus précis. Les résultats sont présentés sur la figure 7.12 avec les prédictions théoriques. Nos rapports mesurés ne correspondent pas à la mesure de la collaboration HERMES [96] ni aux calculs de S. Liuti et K. Taneja [94], et semblent être en accord avec la prédiction de V. Guzey [123]. Par contre, A. Kirchner et D. Mueller (modèle KM) [82] prédit un rapport d'asymétrie constant de 1.4 (0.35/0.25) pour tous les noyaux de spin-zéro à x_B= 0.3, E_b= 6 GeV, -t= 0.25 GeV^2, et Q^2= 2.5 GeV^2, et un rapport égal à 0.2/0.25 pour les noyaux de spin-1.

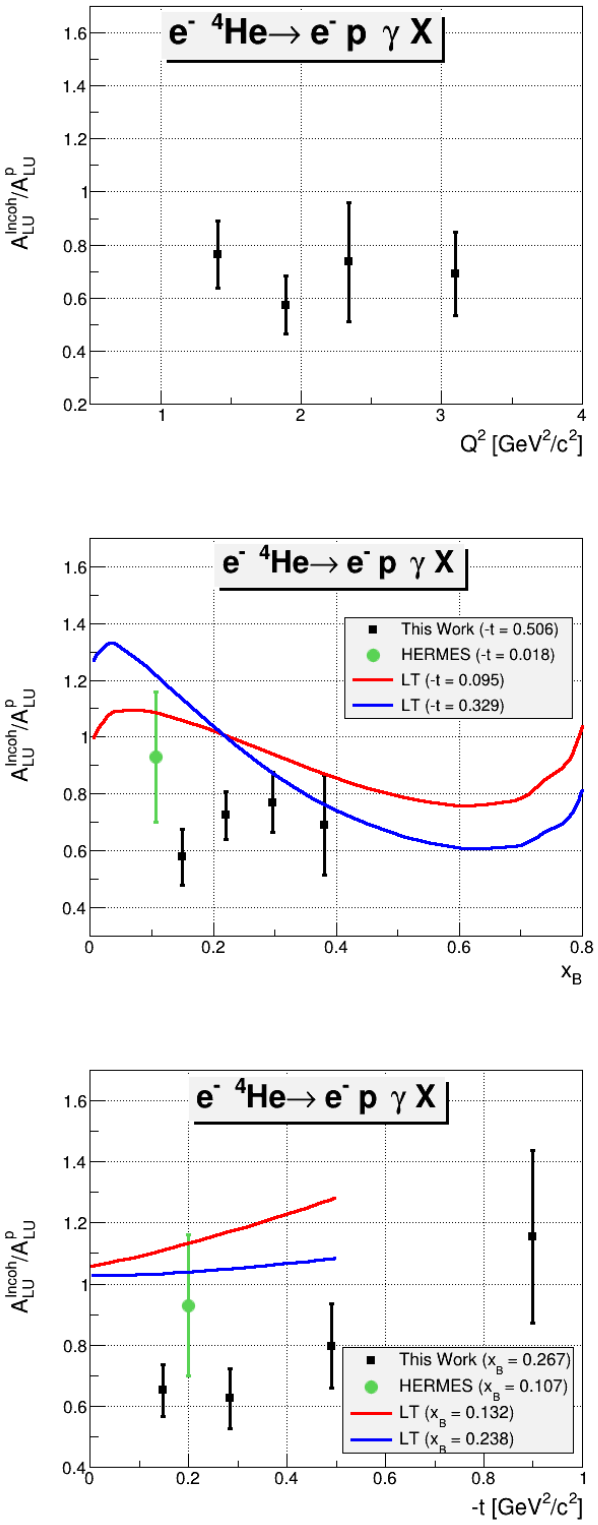

Figure 7.11: Le rapport des A_{LU} entre le proton lié et le proton libre à $\phi = 90°$, en fonction de Q^2 (haut), x_B (milieu), et $-t$ (bas). Le point vert dans chaque figure présente la mesure inclusive de HERMES [96]. Sur la figure du milieu, la courbe rouge et la bleue montrent le résultat du modèle de S. Liuti et K. Taneja [94] pour deux valeurs de $-t$= 0,095 et 0,329 GeV^2/c^2, respectivement. Dans le figure du bas: la courbe rouge et la bleue sont les prédictions théoriques du même modèle pour x_B= 0,132 et 0,238, respectivement.

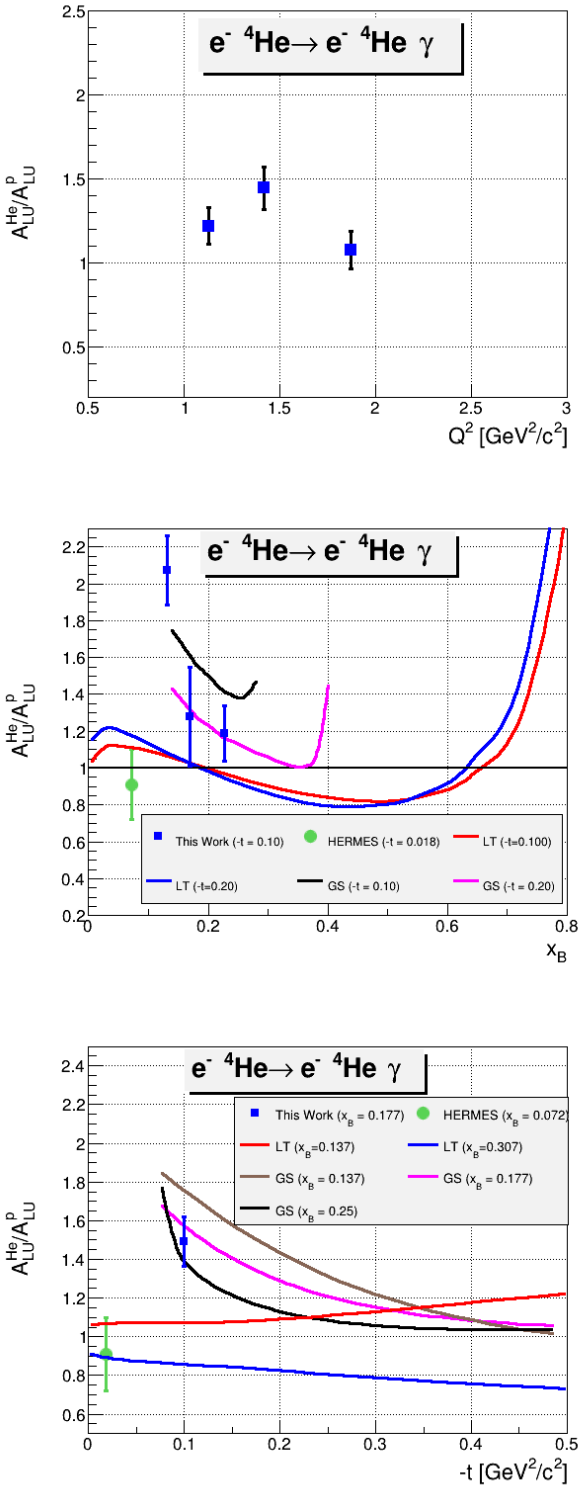

Figure 7.12: Le rapport des A_{LU} entre l'^{4}He et le proton libre à ϕ= 90°, en fonction de Q^2 (haut), x_B (milieu), et $-t$ (bas). Les carrés bleus représentent les résultats de ce travail, et les points verts sont les mesures d'HERMES [96]. Ces mesures sont comparées aux prédictions théoriques de S. Liuti et K. Taneja [94] (courbes rouges et bleues) et de V. Guzey et al. [123] (courbes noires, violetes et marrons).

Appendix A

$e\,^4He \to e\,^4He\,\gamma$ cross section

The differential cross section for a longitudinally-polarized electron beam ($\lambda = \pm 1$) and an unpolarized ^{4}He target can written as:

$$\frac{d^5\sigma^\lambda}{dx_A dQ^2 dt d\phi_e d\phi} = \frac{\alpha^3}{16\pi^2}\frac{x_A\, y^2}{Q^4\sqrt{1+\varepsilon^2}}\frac{|\mathcal{T}_{BH}|^2 + |\mathcal{T}^\lambda_{DVCS}|^2 + \mathcal{I}^\lambda_{BH*DVCS}}{e^6} \tag{A.1}$$

where $y = \frac{p\cdot q}{p\cdot k}$, $\varepsilon = \frac{2x_A M_A}{Q}$ and $x_A = \frac{Q^2}{2p\cdot q}$. The different amplitudes can be written as [82]:

$$|\mathcal{T}_{BH}|^2 = \frac{e^6(1+\varepsilon^2)^{-2}}{x_A^2 y^2 t\,\mathcal{P}_1(\phi)\mathcal{P}_2(\phi)}\left[c_0^{BH} + c_1^{BH}\cos(\phi) + c_2^{BH}\cos(2\phi)\right] \tag{A.2}$$

$$|\mathcal{T}_{DVCS}|^2 = \frac{e^6}{y^2Q^2}\left[c_0^{DVCS} + \sum_{n=1}^{2}\left(c_n^{DVCS}\cos(n\phi) + \lambda s_n^{DVCS}\sin(n\phi)\right)\right] \tag{A.3}$$

$$\mathcal{I}_{BH*DVCS} = \frac{\pm e^6}{x_A y^3 t\,\mathcal{P}_1(\phi)\mathcal{P}_2(\phi)}\left[c_0^{I} + \sum_{n=0}^{3}\left(c_n^{I}\cos(n\phi) + \lambda s_n^{I}\sin(n\phi)\right)\right] \tag{A.4}$$

where $\mathcal{P}_1(\phi)$ and $\mathcal{P}_2(\phi)$ are BH propagators and defined as:

$$\mathcal{P}_1(\phi) = \frac{(k-q')^2}{Q^2} = -\frac{1}{y(1+\varepsilon^2)}\left[J + 2K\cos(\phi)\right] \tag{A.5}$$

$$\mathcal{P}_2(\phi) = \frac{(k-\Delta)^2}{Q^2} = 1 + \frac{t}{Q^2} + \frac{1}{y(1+\varepsilon^2)}\left[J + 2K\cos(\phi)\right] \tag{A.6}$$

with,

$$J = \left(1 - y - \frac{y\varepsilon^2}{2}\right)\left(1 + \frac{t}{Q^2}\right) - (1-x_A)(2-y)\frac{t}{Q^2} \tag{A.7}$$

$$K^2 = -\delta t\,(1-x_A)\left(1 - y - \frac{y^2\varepsilon^2}{4}\right)\left\{\sqrt{1+\varepsilon^2} + \frac{4x_A(1-x_A)+\varepsilon^2}{4(1-x_A)}\delta t\right\} \tag{A.8}$$

$$\delta t = \frac{t - t_{min}}{Q^2} = \frac{t}{Q^2} + \frac{2(1-x_A)\left(1-\sqrt{1+\varepsilon^2}\right)+\varepsilon^2}{4x_A(1-x_A)+\varepsilon^2} \tag{A.9}$$

where t_{min} represents the kinematic boundary of the process and defined as:

$$t_{min} = Q^2\frac{2(1-x_A)(1-\sqrt{1+\varepsilon^2})+\varepsilon^2}{4x_A(1-x_A)+\varepsilon^2} \tag{A.10}$$

The Fourier coefficients, in equations A.2, A.3 and A.4, of a spin-0 target are defined as:

$$\begin{aligned} c_0^{BH} = & \Big[\left\{(2-y)^2 + y^2(1+\varepsilon^2)^2\right\}\left\{\frac{\varepsilon^2 Q^2}{t} + 4(1-x_A) + (4x_A+\varepsilon^2)\frac{t}{Q^2}\right\} \\ & +2\varepsilon^2\left\{4(1-y)(3+2\varepsilon^2) + y^2(2-\varepsilon^4)\right\} - 4x_A^2(2-y)^2(2+\varepsilon^2)\frac{t}{Q^2} \\ & +8K^2\frac{\varepsilon^2 Q^2}{t} \Big] F_A^2(t) \end{aligned} \tag{A.11}$$

$$c_1^{BH} = -8(2-y)K\left\{2x_A + \varepsilon^2 - \frac{\varepsilon^2 Q^2}{t}\right\} F_A^2(t) \tag{A.12}$$

$$c_2^{BH} = 8K^2\frac{\varepsilon^2 Q^2}{t} F_A^2(t) \tag{A.13}$$

where $F_A(t)$ is the electromagnetic form factor of the ^{4}He. At leading twist, the $|\mathcal{T}_{DVCS}|^2$ writes as a function of only one CFF according to

$$c_0^{DVCS} = 2(2-2y+y^2)\,\mathcal{H}_A\mathcal{H}_A^\star \tag{A.14}$$

and the interference amplitude coefficients are written as:

$$s_1^{INT} = 8Ky(2-y)F_A\,\Im m\{\mathcal{H}_A\} \tag{A.15}$$

$$\begin{aligned} c_0^{INT} = & -8(2-y)\frac{t}{Q^2}F_A\,\Re e\{\mathcal{H}_A\} \\ & \times \left\{(2-x_A)(1-y) - (1-x_A)(2-y)^2\left(1-\frac{t_{min}}{Q^2}\right)\right\} \end{aligned} \tag{A.16}$$

$$c_1^{INT} = 8K(2y-y^2-2)F_A\,\Re e\{\mathcal{H}_A\} \tag{A.17}$$

Appendix B

The parametrizations for the RTPC

- The parametrizations of the mean (μ) and the width (σ) of Δz distributions shown in figure 4.23, with L and R stand for the left and the right modules of the RTPC, and z in mm:

$$\mu^{L}_{\Delta z}(z) = 2.80051 - 0.0624556 * z + 0.00035567 * z^2 + 5.25789e-06 * z^3 \quad \text{(B.1)}$$
$$\sigma^{L}_{\Delta z}(z) = 7.48614 - 0.00776678 * z - 3.66892e-05 * z^2 \quad \text{(B.2)}$$
$$\mu^{R}_{\Delta z}(z) = -3.85725 - 0.061265 * z + 0.000324528 * z^2 + 4.28801e-06 * z^3 \quad \text{(B.3)}$$
$$\sigma^{R}_{\Delta z}(z) = 8.67335 - 0.00975138 * z + 8.01378e-05 * z^2 \quad \text{(B.4)}$$

- The parametrizations of the mean (μ) and the width (σ) of $\Delta\phi$ distributions shown in figure 3.12 are:

$$\mu^{L}_{\Delta\phi}(z) = 178.053 + 0.0298072 * z - 0.000362634 * z^2 - 2.32442e-07 * z^3 \quad \text{(B.5)}$$
$$\sigma^{L}_{\Delta\phi}(z) = 2.00365 + 0.0011081 * z + 4.1589e-05 * z^2 - 2.95347e-07 * z^3 \quad \text{(B.6)}$$
$$\mu^{R}_{\Delta\phi}(z) = 181.3 + 0.00749361 * z - 0.000338728 * z^2 + 6.37882e-06 * z^3 \quad \text{(B.7)}$$
$$\sigma^{R}_{\Delta\phi}(z) = 2.0939 + 9.59331e-05 * z + 2.16727e-05 * z^2 - 5.69296e-08 * z^3 \quad \text{(B.8)}$$

- The parametrizations of the mean (μ) and the width (σ) of $\Delta\theta$ distribution shown in figure 3.13 are:

$$\mu_{\Delta\theta}(z) = -1.02349 - 0.0487393 * z + 0.000219641 * z^2 + 3.84156e-06 * z^3 \quad \text{(B.9)}$$
$$\sigma_{\Delta\theta}(z) = 3.57854 + 0.00639663 * z \quad \text{(B.10)}$$

- The drift speed parametrization:

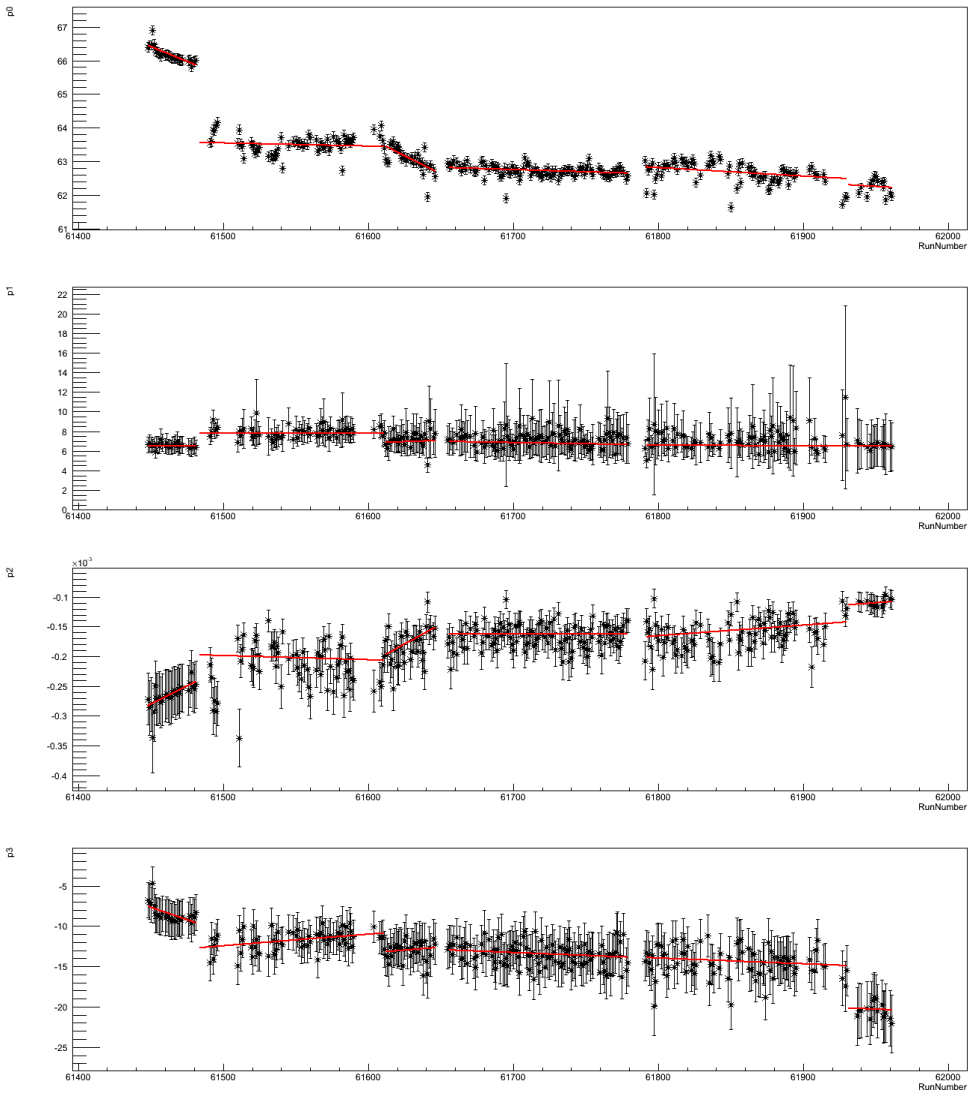

Figure B.1: The fit parameters: p_0, p_1, p_2, and p_3 for the individual runs. The red lines represent their piece-wise fits.

$$TDC_{max/2}(z) = p_0 + p_1 * e^{p_2*(z-p_3)^2} \tag{B.11}$$

run range	p_0 p_2	p_1 p_3
61448 - 61481	1.14312e+03 - 1.75217e-02 *r_N -7.55131e-02 + 1.22429e-06 *r_N	3.27339e+00 + 5.32577e-05 *r_N 3.76627e+03 - 6.14148e-02 *r_N
61483 - 61611	1.21405e+02 - 9.40705e-04 *r_N 4.09308e-03 - 6.97839e-08 *r_N	3.89644e+00 + 6.33813e-05 *r_N -9.04583e+02 + 1.45062e-02 *r_N
61612 - 61646	1.39733e+03 - 2.16496e-02 *r_N -8.23774e-02 + 1.33384e-06 *r_N	-3.07845e+02 + 5.10814e-03 *r_N -9.05752e+02 + 1.44872e-02 *r_N
61655 - 61779	1.45093e+02 - 1.33438e-03 *r_N -5.10501e-04 + 5.64359e-09 *r_N	1.63746e+02 - 2.54273e-03 *r_N 4.26282e+02 - 7.12408e-03 *r_N
61791 - 61930	2.18243e+02 - 2.51495e-03 *r_N -1.11909e-02 + 1.78407e-07 *r_N	4.92691e+01 - 6.90443e-04 *r_N 4.26297e+02 - 7.12383e-03 *r_N
61931 - 61961)	2.18152e+02 - 2.51641e-03 *r_N -1.11766e-02 + 1.78639e-07 *r_N	4.92921e+01 - 6.90070e-04 *r_N 4.23668e+02 - 7.16628e-03 *r_N

Table B.1: The parameters of $TDC_{max/2}$ used in EG6 experiment reconstruction codes.

- Drift paths' parametrization:

$$\Delta\phi(TDC, z) = \sum_{i=0}^{4} p_i(z) * TDC^i \tag{B.12}$$

Parameter	constant	*z	*z^2
p_0	0.14222	-6.52562e-05	4.06768e-06
p_1	-0.00147368	5.64924e-06	-7.31944e-07
p_2	0.000216222	6.25749e-09	1.8923e-08
p_3	-3.82450e-06	-6.29825e-09	-1.89627e-10
p_4	3.22973e-08	7.52017e-11	1.08564e-12

Table B.2: The drift paths extracted in the EG6 experiment.

Appendix C

The parametrization of the IC-photons energy corrections

- α parametrization $$\alpha(x) = c_0 + c_2 \left[e^{-c_3(x-c_1)} - e^{-c_4(x-c_1)} \right], \tag{C.1}$$

Fun_N	xmin	xmax	c_0	c_1	c_2	c_3	c_4
1	61510	61514	-0.00671929	61493	-0.00868856	-0.114874	-0.117953
2	61519	61525	-0.00160398	61585.7	-2.1e-09	0.38362	0.38362
3	61531	61545	-0.00956513	61876.8	-0.0295579	1.23958e-06	0.000704112
4	61546	61556	-0.000414459	61521.8	-0.0179471	-0.0316302	-0.030899
5	61558	61580	-0.00731749	61532.4	-0.465254	0.0200131	0.0193213
6	61581	61590	0.0604759	61561.7	-19.3314	0.0407449	0.0411026
7	61604	61608	-0.00320342	61521.1	-0.00074357	-0.018373	-0.0243743
8	61609	61622	-0.00205987	61649.1	5.94004e-05	0.0760846	-2.64412
9	61623	61637	-0.00153458	61640.7	-1.02541e-10	0.965545	0.959411
10	61638	61646	-0.000735223	61763.1	-0.00476067	0.0423013	0.0422956
11	61655	61675	-0.00123166	61561.1	-2.63733e-06	-0.159566	-0.159566
12	61678	61711	-0.00294886	61670.6	-0.0079126	0.052612	0.0252883
13	61712	61713	-0.00102705	61711.9	-0.0034062	-3.1972	-3.19763
14	61714	61724	-0.00109184	61731.2	-1.14221e-06	0.308061	-4.24803
15	61725	61729	-0.00915958	61716.6	-0.0240355	0.137179	0.0524492
16	61731	61779	-0.00295947	61669.4	0.0130552	0.00768358	0.0117274
17	61791	61796	-0.00117275	61791.9	-0.00210188	5.63266	5.63003
18	61797	61826	0.00155106	61787.7	-0.980189	0.0514066	0.0518518
19	61829	61843	-0.0015276	61826	-0.00204473	2.72258	0.275824
20	61848	61874	0.0265578	61973.2	-0.0249309	0.0010753	-0.186452
21	61876	61895	-0.00205642	61715.7	-3.3277e-05	-0.065808	-0.0658091
22	61904	61915	-0.00274984	62178.9	-0.107207	0.00976882	0.00977186
23	61925	61930	0.0064528	61924.8	-0.00849265	0.0278942	9.3268

Table C.1: α parametrization shown in figure 4.35.

- β parametrization

$$\beta(x) = p_0 + p_2 \left[e^{-p_3(x-p_1)} - e^{-p_4(x-p_1)} \right], \tag{C.2}$$

Fun_N	xmin	xmax	p_0	p_1	p_2	p_3	p_4
1	61510	61514	0.139127	61508.7	-0.00705827	-0.127	-0.163719
2	61519	61525	0.144057	61553.1	6.44528e-05	0.384066	0.384069
3	61531	61545	-0.238301	61487	-1.28623	0.0260483	0.011476
4	61546	61556	0.0904474	61545.1	-0.0367149	2.10481	-0.0186192
5	61558	61580	0.095243	61543.5	-0.197639	0.0280817	0.015222
6	61581	61590	0.0643454	61557.1	-0.394422	0.0358816	0.0212999
7	61604	61608	0.138436	61605.4	-0.0142253	-0.0323464	-0.0103419
8	61609	61622	0.135047	61605.8	-0.00856825	0.157423	0.0474859
9	61623	61637	0.137445	61646.8	-1.46307e-05	0.273975	-0.0770047
10	61638	61646	0.141909	61651.9	-0.103873	0.00713496	0.000949948
11	61655	61675	0.127712	61652.8	-0.00969769	0.220956	0.00215349
12	61678	61711	0.137774	61697.7	-9.15967e-05	0.237965	-0.158587
13	61712	61713	0.124706	61655.1	-3.72443e-05	-0.0443564	-0.100321
14	61714	61724	0.138057	61726.8	-0.000274029	0.234	-4.45937
15	61725	61729	0.108381	61721.3	-0.0289603	0.77633	-0.00285553
16	61731	61779	0.113727	61726	-0.0236114	0.243927	-0.00196355
17	61791	61791	0.136619	0.0	0.0	0.0	0.0
18	61792	61796	0.138708	61914.5	1.07991e-09	0.181595	0.181612
19	61797	61825	0.137559	61839.6	-0.000312349	0.160791	0.159434
20	61826	61843	0.0359758	61810.5	-0.10032	0.215911	-0.000529924
21	61848	61874	0.116396	61891.7	-0.385562	-0.0563216	-0.0479573
22	61876	61915	0.105816	61872.2	-0.0312028	0.384691	-0.00145868
23	61925	61930	0.137809	61927.5	-0.00071665	0.620419	0.222406

Table C.2: β parametrization shown in figure 4.35.

Appendix D

Exclusive π^0 events selection

The exclusive selection of the experimental $e^4He\pi^0$ and $ep\pi^0$ events require the detection of only one good electron, one good π^0 in the topology ICIC or ICEC, and one good ^4He track in the coherent channel or one good proton in the incoherent channel case. Furthermore, in order to ensure that this is a deep process we apply a set of initial requirements. The exclusivity of the reaction is ensured by a set of exclusivity cuts like for the DVCS channels. These requirements and exclusivity cuts are presented for the case of the coherent $e^4He\pi^0$ events are:

Initial criteria

These requirements are made to ensure that the selected events occurre at the partonic level:

- High virtuality of the exchanged photon (Q^2>1 GeV^2).
- High energy of the emitted π^0 (E_{π^0} > 2 GeV).
- The invariant mass of the virtual photon and the target proton is greater than 2 GeV^2/c^2 in order to avoid the baryons resonances region.
- The transfer momentum squared ($-t$) between the initial target and the recoil one is greater than the minimum allowed one (t_{min}) defined by the kinematics of the incoming and the scattered electrons. The definition of t_{min} for each channel can be found in the corresponding DVCS channel selection presented previously.

Exclusivity requirements

The exclusivity of the selected $e^4He\pi^0$ events is done with the following cuts:

- The coplanarity cut ($\Delta\phi$) between the recoil ^4He and the produced π^0.
- The missing energy, mass and transverse momentum cuts in the configuration $e^4He\pi^0X$.
- The missing mass cut in the configuration e^4HeX.
- The missing mass cut in the configuration $e\pi^0X$.
- The cone angle cut between e^4HeX and the reconstructed π^0.

The same procedure holds for the case of the incoherent $ep\pi^0$ events. In the following two subsections, the results of the two channels selection are presented.

D.1 $e^4He\pi^0$ exclusivity cuts

The events which pass the following exclusivity cuts are assumed to be good $e^4He\pi^0$ events.

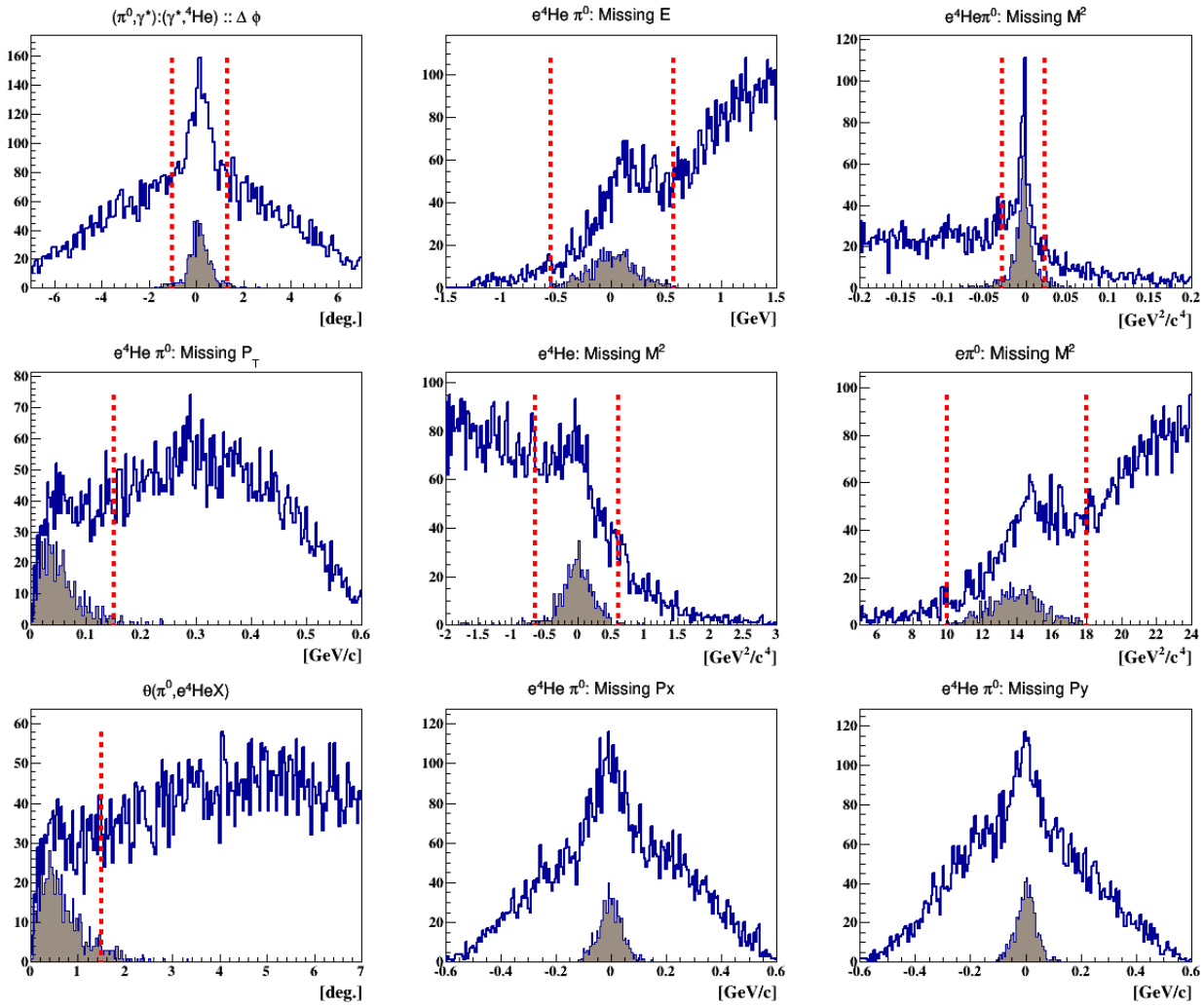

Figure D.1: The blue distributions represent all the $e^4He\pi^0$ events before the exclusivity cuts. The shaded distributions show the events which passed all the exclusivity cuts except for the quantity plotted. The red lines are 3σ cuts. The mean and sigma values of each distribution are listed in table E.2.

Comparison with simulation

As for the selection of the experimental $e^4He\pi^0$ events, the simulated events have to pass an equivalent set of exclusivity cuts in addition to the π^0 electroproduction criteria, presented at the beginning of this section. In this section, we show the comparison between the experimental and the simulated selected $e^4He\pi^0$ events as a function of the kinematic variables (Q^2, x_B, $-t$), figure D.2, and as a function of the variables used for the exclusivity cuts, figure D.3.

Even with low experimental statistics, figures D.2 and D.3 show a good match between the simulation and the experimental $e^4He\gamma$ events for the different kinematic variables, which is

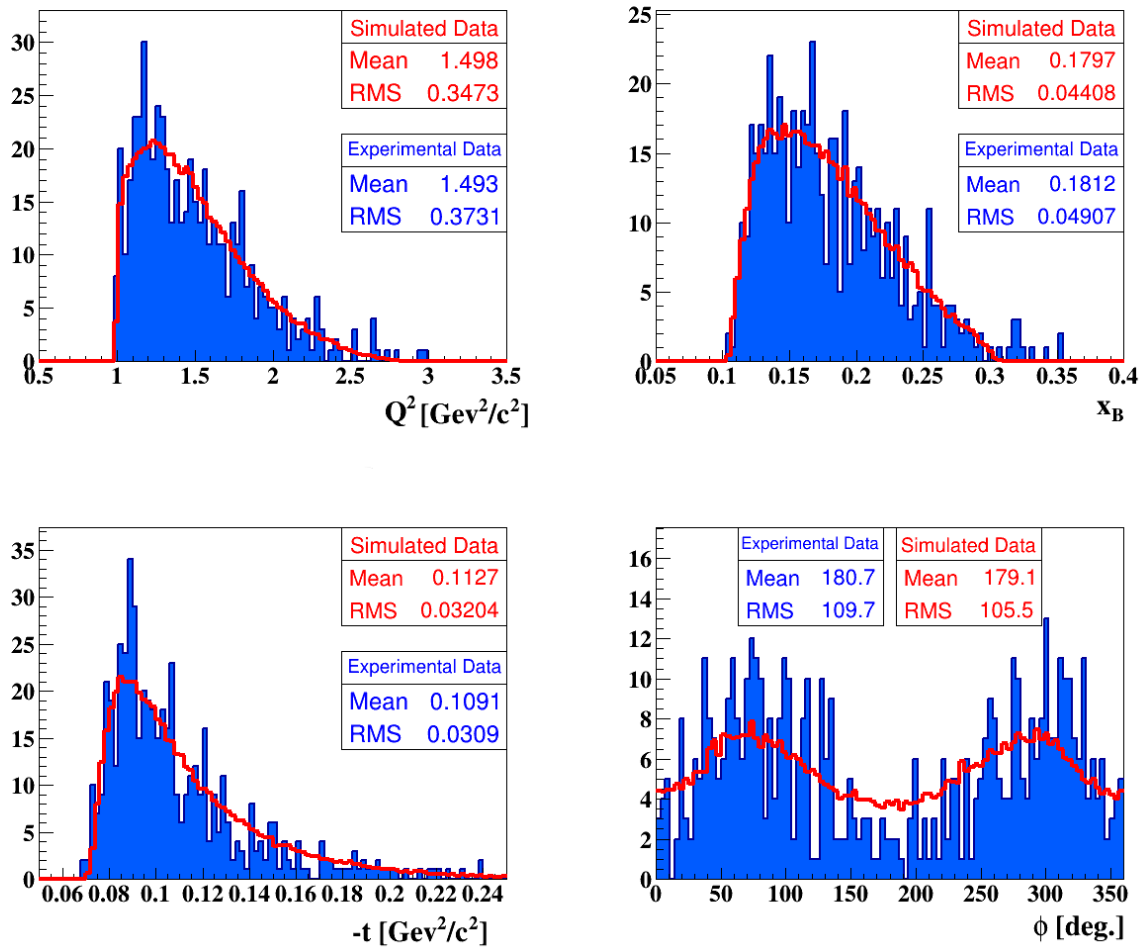

Figure D.2: Comparison between the simulated $e^4He\pi^0$ events (red lines) and the experimental events (blue shaded distributions) as a function of the kinematic variables: Q^2, x_B, $-t$ and ϕ_h respectively from top to right to right and from top to bottom.

satisfying for our background subtraction goal.

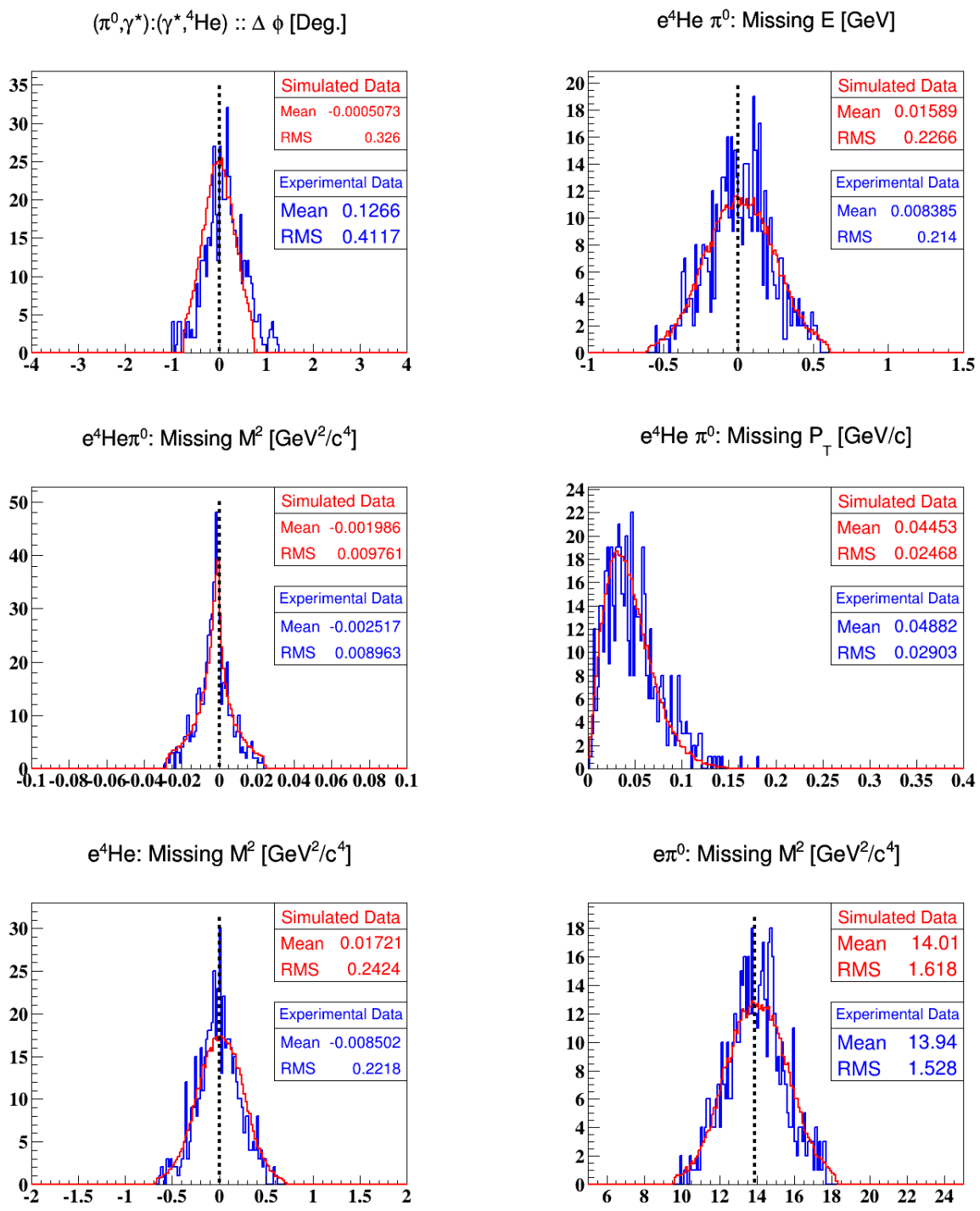

Figure D.3: Comparison between the simulated and experimental $e^4He\gamma$ events in terms of the exclusivity variables. The vertical black line indicates the theoretically expected value for each exclusive variable.

D.2 $ep\pi^0$ exclusivity cuts

The $ep\pi^0$ events which pass the initial deepness criteria and the exclusivity cuts, marked by the red vertical lines in the figure below, are considered as clean events.

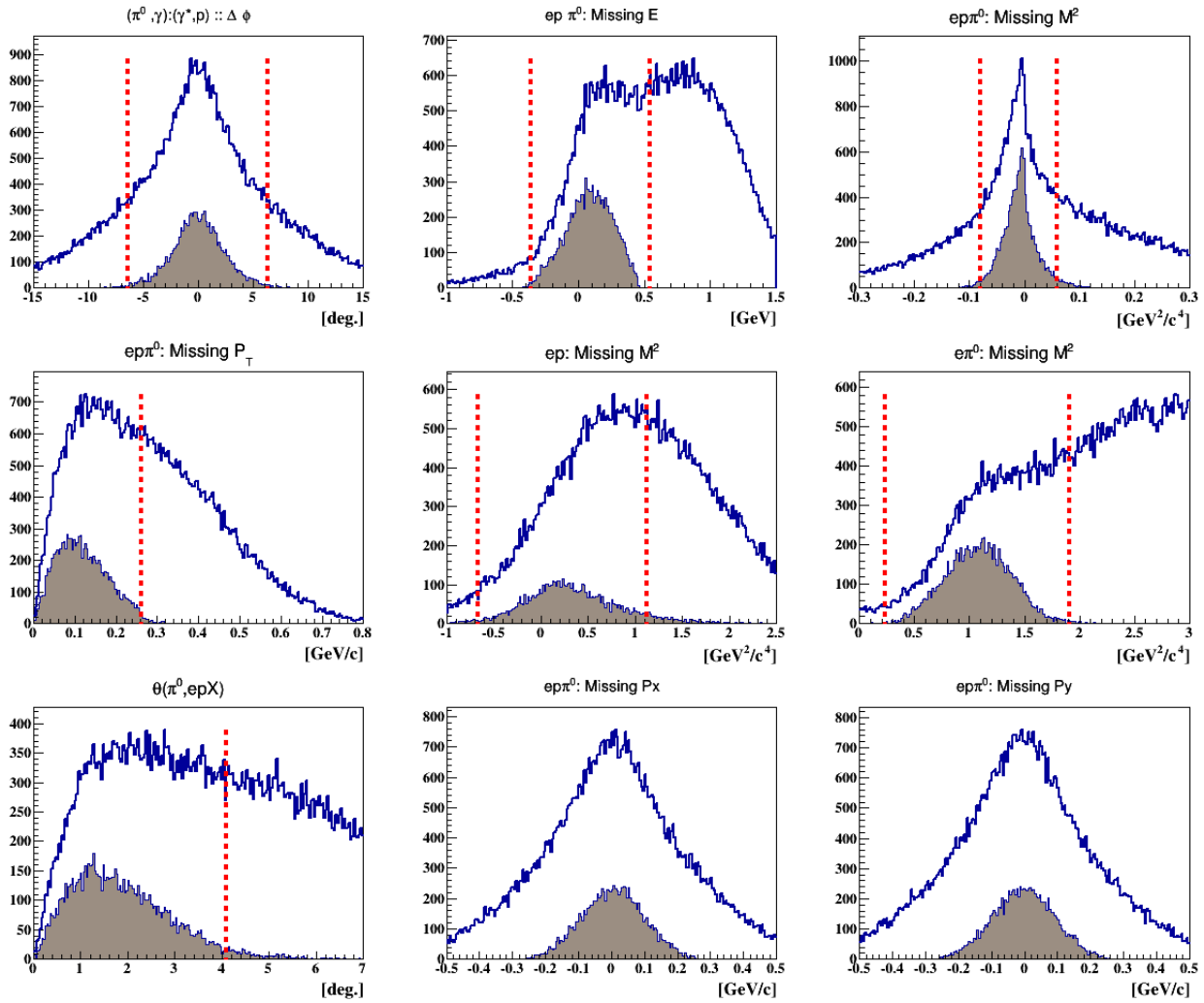

Figure D.4: The blue distributions represent all the $ep\pi^0$ events before any exclusive requirement. The shaded brown distributions show the events which passed all the exclusivity cuts except the quantity plotted. The vertical red lines represent 3σ cuts on the shaded distribution. The mean and sigma values of each distribution are listed in table E.4.

Comparison with simulation

In this section, the experimental selected $ep\pi^0$ events are compared to the Monte Carlo simulated events. Figure D.5 shows the comparison as a function of the kinematic variables. Figure D.6 shows the comparison in terms of the different exclusivity variables. One can see an agreement within some degrees of differences, which might come from the fact that our protons are bound ones and the physics of the nuclear process is not fully understood.

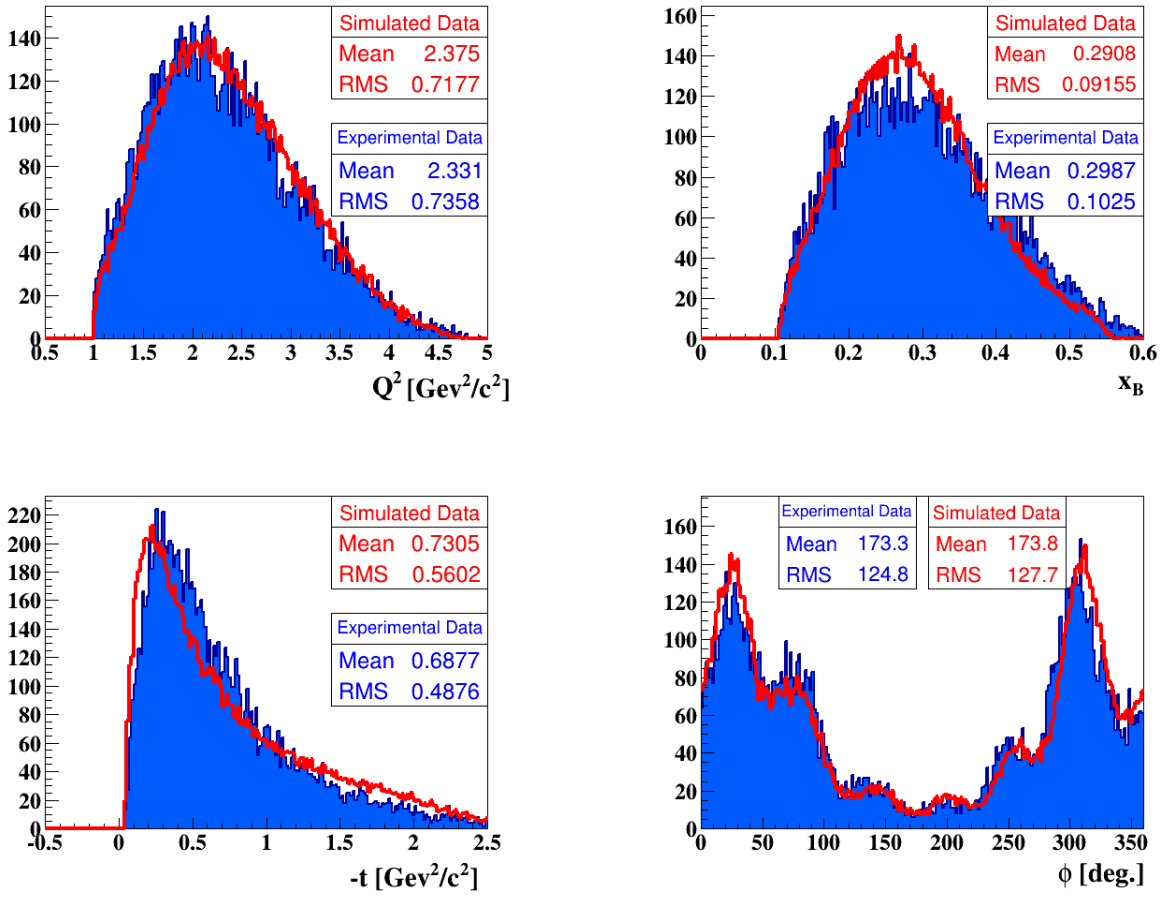

Figure D.5: Comparison between the Monte Carlo simulated $ep\pi^0$ events (red lines) and the experimental ones (blue shaded distributions) as a function of the kinematic variables: Q^2, x_B, $-t$, and ϕ, respectively from top to right to right and from top to bottom.

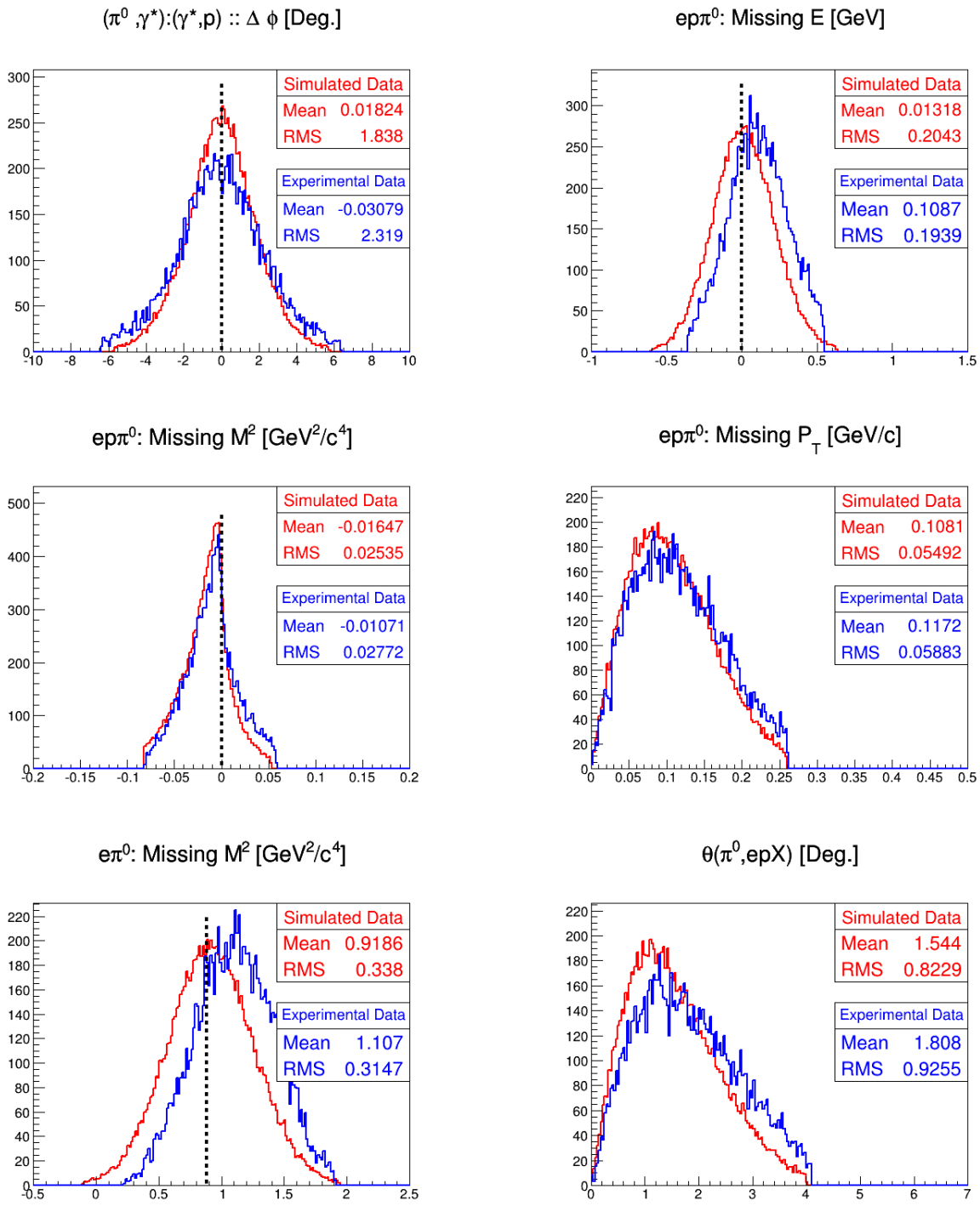

Figure D.6: Comparison between the simulated and experimental $ep\pi^0$ DVCS events as a function of the variables used for the exclusivity cuts. The simulated distributions are normalized with respect to the experimental ones. The vertical black lines indicate the theoretically expected values.

Appendix E

Tables list of the exclusive distributions

- Exclusive $e^4He\gamma$ distributions

The quantity	mean	σ
$\Delta\phi$	1.79405e-01	4.53791e-01
E_X ($e^4He\gamma X$)	1.56814e-02	2.51492e-01
M_X^2 ($e^4He\gamma X$)	-2.96869e-03	9.10158e-03
pt_X ($e^4He\gamma X$)	4.14664e-02	4.24914e-02
M_X^2 (e^4HeX)	-1.72013e-02	2.33988e-01
M_X^2 ($e\gamma X$)	1.40066e+01	1.85929
θ (γ,e^4HeX)	5.08070e-01	4.74883e-01
px_X ($e^4He\gamma X$)	-2.32102e-03	4.52945e-02
py_X ($e^4He\gamma X$)	-8.97351e-04	3.89937e-02

Table E.1: The mean and sigma values of the exclusive coherent quantities drawn in figure 5.2.

- Exclusive $e^4He\pi^0$ distributions

The quantity	mean	σ
$\Delta\phi$	1.41750e-01	3.84202e-01
E_X ($e^4He\pi^0X$)	7.80328e-03	1.85770e-01
M_X^2 ($e^4He\pi^0X$)	-2.31650e-03	8.65851e-03
pt_X ($e^4He\pi^0X$)	4.36619e-02	3.25254e-02
M_X^2 (e^4HeX)	-1.30346e-02	2.07791e-01
M_X^2 ($e\pi^0X$)	1.39835e+01	1.33781
θ (π^0,e^4HeX)	5.30001e-01	3.44745e-01
px_X ($e^4He\pi^0X$)	-3.79596e-03	4.20732e-02
py_X ($e^4He\pi^0X$)	9.41010e-04	3.50393e-02

Table E.2: The mean and sigma values of the exclusive coherent quantities drawn in figure D.1.

- Exclusive $ep\gamma$ distributions

The quantity	mean	σ
$\Delta\phi$	4.22584e-02	1.39413
E_X $(ep\gamma X)$	6.27739e-02	1.34499e-01
M_X^2 $(ep\gamma X)$	-1.00889e-02	1.58503e-02
pt_X $(ep\gamma X)$	8.03008e-02	4.28511e-02
M_X^2 (epX)	2.40257e-01	3.66321e-01
M_X^2 $(e\gamma X)$	1.01266	2.03835e-01
θ (γ, epX)	1.06788	6.76469e-01
px_X $(ep\gamma X)$	3.48024e-03	8.19527e-02
py_X $(ep\gamma X)$	-1.50911e-03	8.16219e-02

Table E.3: The mean and sigma values of the exclusive incoherent quantities drawn in figure 5.6.

- Exclusive $ep\pi^0$ distributions

The quantity	mean	σ
$\Delta\phi$	-3.25864e-02	2.11499
E_X $(ep\pi^0 X)$	9.23934e-02	1.50977e-01
M_X^2 $(ep\pi^0 X)$	-1.11900e-02	2.31963e-02
pt_X $(ep\pi^0 X)$	1.02247e-01	5.31387e-02
M_X^2 (epX)	2.27334e-01	2.98775e-01
M_X^2 $(e\pi^0 X)$	1.07125	2.79845e-01
θ (π^0, epX)	1.42739	8.89072e-01
px_X $(ep\pi^0 X)$	2.19686e-03	9.01343e-02
py_X $(ep\pi^0 X)$	-1.30580e-03	9.05090e-02

Table E.4: The mean and sigma values of the exclusive $ep\pi^0$ quantities drawn in shaded brown in figure D.4.

Bibliography

[1] R. Hofstadter, The electron-scattering method and its application to the structure of nuclei and nucleons, Nobel Lecture, December 11, 1961. (Cited on pages 9 and 13.)

[2] R. Hofstadter and R. W. McAllister, Electron Scattering from the Protons, Phys. Rev. 98, 217-218, 1955. (Cited on pages 9, 12 and 13.)

[3] M. Gell-Mann, A Schematic Model of Baryons and Mesons, Phys. Lett. 8, 214, 1964. (Cited on page 9.)

[4] G. Zweig, An SU(3) Model for Strong Interaction Symmetry and its Breaking, CERN Report No.8182/TH.401, 1964. (Cited on page 9.)

[5] J. I. Friedman and H. W. Kendall, Deep inelastic electron scattering, Annual Rev. of Nucl. Science, Vol. 22, 203-254, 1972. (Cited on pages 9 and 13.)

[6] R. P. Feynman, Very High-Energy Collisions of Hadrons Phys. Rev. Lett. 23, 1415, 1969. (Cited on page 9.)

[7] J. D. Bjorken and E. A. Paschos, Inelastic Electron-Proton and γ-Proton Scattering and the Structure of the Nucleon, Phys. Rev. 185, 1975, 1969. (Cited on page 9.)

[8] J. J. Aubert et al. (EMC Collaboration), The ratio of the nucleon structure functions F_N^2 for iron and deuterium, Phys. Lett. B 123, 275-278, 1983. (Cited on pages 9 and 131.)

[9] C. Amsler et al. (Particle Data Group), Review of Particle Physics, Phys. Lett. B 667, 1, 2008. (Cited on page 12.)

[10] M. N. Rosenbluth, HighEnergy Elastic Scattering of Electrons on Protons, Phys. Lett. 79, 615-619, 1950. (Cited on page 13.)

[11] C. F. Perdrisat, V. Punjabi and M. Vanderhaeghen, Nucleon Electromagnetic Form Factors, Prog. Part. Nucl. Phys. 59, 694-764, 2007. (Cited on page 14.)

[12] J. J. Kelly, Simple parametrization of nucleon form factors, Phys. Rev. Lett. C 70, 068202, 2004. (Cited on page 13.)

[13] R. Madey et al. (The Jefferson Laboratory E93-038 Collaboration), Measurements of G_E^n/G_M^n from the $^2H(e,en)^1H$ Reaction to Q^2=1.45 (GeV/c)^2, Phys. Rev. Lett. 91, 122002, 2003. (Cited on page 13.)

[14] C. E. Carlson and M. Vanderhaeghen, Empirical transverse charge densities in the nucleon and the nucleon-to-Delta transition, Phys. Rev. Lett. 100, 032004, 2008. (Cited on pages 13 and 131.)

[15] M. Vanderhaeghen and T. Walcher, Long Range Structure of the Nucleon, arXiv:1008.4225v1 [hep-ph], 2010. (Cited on pages 13 and 131.)

[16] S. D. Drell and J. D. Walecka, Electrodynamic Processes with Nuclear Targets, Annals Phys. Vol. 28, No. 1, 1964. (Cited on page 15.)

[17] A. Pich, Quantum Chromodynamics, arXiv:9505231 [hep-ph], 1994. (Cited on page 15.)

[18] Y. L. Dokshitzer, Calculation of the Structure Functions for Deep Inelastic Scattering and e^+e^- Annihilation by Perturbation Theory in Quantum Chromodynamics, Sov. Phys. JETP 46, 641–653, 1977. (Cited on page 15.)

[19] J. Beringer et al. (Particle Data Group), Structure Functions, Phys. Rev. D 86, 010001, page 241, 2012. (Cited on page 16.)

[20] T. Sloan, R. Voss and G. Smadja, The Quark Structure of the Nucleon from the CERN Muon Experiments, Phys. Rept. 162, 45-167, 2009. (Cited on pages 15, 19 and 131.)

[21] R. Placakyte et al. (H1 and ZEUS Collaborations), Parton Distribution Functions, arXiv:1111.5452 [hep-ph], 2010. (Cited on page 16.)

[22] A. Bacchetta et al., Semi-inclusive deep inelastic scattering at small transverse momentum, JHEP 0702:093, 2007. (Cited on page 17.)

[23] A. Airapetian et al. (HERMES Collaboration), Single-spin Azimuthal Asymmetries in Electroproduction of Neutral Pions in Semi-inclusive Deep-inelastic Scattering, Phys. Rev. Lett. 84, 4047, 2000. (Cited on page 17.)

[24] A. Airapetian et al. (HERMES Collaboration), Measurement of single-spin azimuthal asymmetries in semi-inclusive electroproduction of pions and kaons on a longitudinally polarised deuterium target, Phys. Lett. B 562, 182-192, arXiv:0212039 [hep-ph], 2003. (Cited on page 17.)

[25] H. Avagyan et al. (CLAS Collaboration), Measurement of Beam-Spin Asymmetries for Deep Inelastic π^+ Electroproduction, Phys. Rev. D 69, 112004, 2004. (Cited on page 17.)

[26] H. Avagyan et al. (CLAS Collaboration), Single Spin Asymmetries at CLAS, Phys. Part. Nucl. 35 S114-S120, invited talk at Conference: C 03-05-19, 2004. (Cited on page 17.)

[27] M. G. Alekseev et al. (COMPASS Collaboration), Measurement of the Collins and Sivers asymmetries on transversely polarised protons, Phys. Lett. B 692, 240; arXiv:1005.5609 [hep-ex], 2010. (Cited on page 17.)

[28] N. Makke, Transverse Momentum Effects in Unpolarised SIDIS at COMPASS, arXiv:1411.4244 [hep-ex], 2014. (Cited on page 17.)

[29] J. P. Chen et al., JLab E12-10-006: Target Single Spin Asymmetry in Semi-Inclusive Deep-Inelastic Electro Pion Production on a Trasversely Polarized ^3He Target at 8.8 and 11 GeV, An update to Phys. Rev. Lett. 12, 09-014, 2010. (Cited on page 17.)

[30] H. Avagyan et al. (CLAS Collaboration),
- JLab E12-06-112 : Probing the Proton's Quark Dynamics in Semi-Inclusive Pion Production at 12 GeV, 2006.
- JLab E12-07-107 : Studies of Spin-Orbit Correlations with Longitudinally Polarized Target, 2007.
- JLAB E12-09-007: Studies of partonic distributions using semi-inclusive production of kaons, 2009.
- JLab E12-09-008 : Studies of the Boer-Mulders Asymmetry in Kaon Electroproduction with Hydrogen and Deuterium Targets, 2009.

- JLab E12-09-009 : Studies of Spin-Orbit Correlations in Kaon Electroproduction in DIS with polarized hydrogen and deuterium targets, 2009. (Cited on page 17.)

[31] A. V. Radyushkin, Nonforward Parton Distributions, Phys. Rev. D 56, 5524-5557; arXiv:9704207 [hep-ph], 1997. (Cited on pages 17, 18 and 25.)

[32] A. Freund and J.C. Collins, Proof of Factorization for Deeply Virtual Compton Scattering in QCD, Phys. Rev. D 59, 074009; arXiv:9801262 [hep-ph], 1998. (Cited on pages 18 and 132.)

[33] X.-D. Ji and J. Osborne, One-Loop Corrections and All Order Factorization In Deeply Virtual Compton Scattering, Phys. Rev. D 58, 094018, 1998. (Cited on pages 18 and 132.)

[34] A.V. Belitsky, D. Müller and A. Kirchner, Theory of deeply virtual Compton scattering on the nucleon, Nucl. Phys. B 629, 323-392, 2002. Updated in: A. V. Belitsky and D. Müller, Exclusive electroproduction revisited: Treating kinematical effects, Phys. Rev. D 82, 074010, 2010. (Cited on pages 17 and 29.)

[35] R. L. Jaffe. Spin, twist and hadron structure in deep inelastic processes, Lecture Notes in Phys. Vol. 496, 178-249; arXiv:9602236 [hep-ph], 1977. (Cited on page 18.)

[36] C. Lorce, B. Pasquini and M. Vanderhaeghen, Unified framework for generalized and transverse-momentum dependent parton distributions within a 3Q light-cone picture of the nucleon, Jour. of High Energy Phys. 5:1-40, 2011. (Cited on page 19.)

[37] S. Meissner, A. Metz, M. Schlegel and K. Goeke, Generalized parton correlation functions for a spin-0 hadron, JHEP 0808:038; arXiv:0805.3165 [hep-ph], 2008. (Cited on page 19.)

[38] K. Kanazawa, C. Lorcé, A. Metz, B. Pasquini and M. Schlegel, Twist-2 generalized TMDs and the spin/orbital structure of the nucleon, Phys. Rev. D 90, 014028; arXiv:1403.5226 [hep-ph], 2014. (Cited on page 19.)

[39] J. Ashman et al. (EMC Collaboration), Measurement of the ratios of deep inelastic muon-nucleus cross sections on various nuclei compared to deuterium, Phys. Lett. B 202, 603, 1988. (Cited on pages 19 and 131.)

[40] J. Gomez et al. (SLAC-E139), Measurement of the A dependence of deep-inelastic electron scattering, Phys. Rev. D 49, 4348, 1994. (Cited on pages 19 and 131.)

[41] A. Airapetian et al. (HERMES Collaboration), Nuclear effects on R = σ_L/σ_T in deep-inelastic scattering, Phys. Lett. B 567, 339, 2003. (Cited on pages 19 and 131.)

[42] J. Seely et al., New Measurements of the European Muon Collaboration Effect in Very Light Nuclei, Phys. Rev. Lett. 103, 202301, 2009. (Cited on pages 19, 21 and 131.)

[43] D. Alde et al., Nuclear dependence of dimuon production at 800 GeV, Phys. Rev. Lett. 64, 2479, 1990. (Cited on page 19.)

[44] K. Rith, Present Status of the EMC effect, arXiv:1402.5000 [hep-ph], 2014. (Cited on page 20.)

[45] M. Ericson and A. W. Thomas, Evidence for an enhanced nuclear sea from the proton-nucleus Drell-Yan process, Phys. Lett. B 148, 191, 1984. (Cited on page 20.)

[46] J. Arrington et al., A detailed study of the nuclear dependence of the EMC effect and short-range correlations, Phys. Rev. C 86, 065204; arXiv:1206.6343v4 [nucl-ex], 2012. (Cited on pages 21 and 131.)

[47] N. Fomin et al., New Measurements of High-Momentum Nucleons and Short-Range Structures in Nuclei,Phys. Rev. Lett. 108, 092502, 2012. (Cited on page 22.)

[48] O. Hen et al., New data strengthen the connection between Short Range Correlations and the EMC effect, Phys. Rev. C 85, 047301; arXiv:1202.3452 [nucl-ex], 2012. (Cited on page 23.)

[49] M. Ericson and A. W. Thomas, Pionic corrections and the EMC enhancement of the sea in iron, Phys. Lett. B 128, 112, 1983. (Cited on page 22.)

[50] D. Gaskell et al., Measurement of longitudinal and transverse cross sections in the $^3He(e,e'\pi^+)^3H$ reaction at W= 1.6 GeV, Phys. Rev. C 65, 011001, 2002. (Cited on page 23.)

[51] S. V. Akulinichev, S. A. Kulagin and G. M. Vagradov, The Role of Nuclear Binding in Deep Inelastic Lepton Nucleon Scattering, Phys. Lett. B 158, 485, 1985. (Cited on page 23.)

[52] S. V. Akulinichev and S. Shlomo, Nuclear binding effect in deep-inelastic lepton scattering, Phys. Lett. B 234, 170, 1990. (Cited on page 23.)

[53] O. Benhar, Nuclear binding and deep inelastic scattering, V. Pandharipande and I. Sick, Phys. Lett. B410, 79, 1997. (Cited on page 23.)

[54] F. E. Close, R. G. Roberts and G. G. Ross, The Effect of Confinement Size on Nuclear Structure Functions, Phys. Lett. B 129, 346, 1983. (Cited on page 23.)

[55] K. Saito zt al., Nucleon and hadron structure changes in the nuclear medium and impact on observables, Prog. Part. Nucl. Phys. 58, 1, 2007. (Cited on page 23.)

[56] H. Mineo et al., Quark distributions in nuclear matter and the EMC effect, Nucl. Phys. A 735, 482, 2004. (Cited on page 23.)

[57] I. Cloët et al., Isovector EMC effect explains the NuTeV anomaly, Phys. Rev. Lett. 102, 252301; arXiv:0901.3559 [nucl-th], 2009. (Cited on page 23.)

[58] I. Cloët et al., Parity-violating DIS and the flavour dependence of the EMC effect, Phys. Rev. Lett. 109, 182301; arXiv:1202.6401 [nucl-th], 2012. (Cited on page 23.)

[59] M. Diehl, Generalized Parton Distributions with Helicity Flip, Eur. Phys. J. C 19, 485-492; arXiv:0101335 [hep-ph], 2001. (Cited on page 24.)

[60] X. Ji, Off-Forward Parton Distributions, J. Phys. G 24, 1181-1205; arXiv:9807358 [hep-ph], 1998. (Cited on pages 24, 25 and 26.)

[61] K. Goeke, M. V. Polyakov and M. Vanderhaeghen, Hard Exclusive Reactions and the Structure of Hadrons, Prog. Part. Nucl. Phys. 47, 401-515; arXiv:0106012 [hep-ph], 2001. (Cited on pages 25 and 27.)

[62] P. Hoodbhoy and X. Ji, Helicity-flip off-forward parton distributions of the nucleon, Phys. Rev. D 58, 054006, 1998. (Cited on page 25.)

[63] M. Diehl, Generalized parton distributions, arXiv:0307382 [hep-ph], 2003. DESY-THESIS,018, 2003. (Cited on pages 25, 27 and 33.)

[64] V. Bernard, N. Kaiser and Ulf-G. Meibner, Nucleon electroweak form factors: analysis of their spectral functions, LPT 96-15 TK 96 21, 1996. (Cited on page 26.)

[65] M. Guidal, Generalized Parton Distributions and deep virtual Compton scattering, Progress in Particle and Nuclear Physics, Vol. 61, Issue 1, 89-105, 2008. (Cited on page 26.)

[66] M. Guidal et al., Generalized Parton Distributions in the valence region from Deeply Virtual Compton Scattering, arXiv:1303.6600v1 [hep-ph], 2013. (Cited on pages 26, 28 and 35.)

[67] A.V. Belitsky and A.V. Radyushkin, Unraveling hadron structure with generalized parton distributions, Phys. Rep. vol. 418, Issues 1-6, Pages 1-387, 2005. (Cited on page 27.)

[68] Ji X., Gauge-Invariant Decomposition of Nucleon Spin and Its Spin-Off, Phys. Rev. Lett. 78, 610, 1997; Deeply Virtual Compton Scattering, Phys. Rev. D 55, 7114, 1997. (Cited on pages 26 and 27.)

[69] L. Mankiewicz et al., Hard exclusive meson production and nonforward parton distributions, Eur. Phys. J. C 5, 119, 1998. (Cited on page 27.)

[70] EMC collaboration, An investigation of the spin structure of the proton in deep inelastic scattering of polarised muons on polarised protons, Nucl. Phys. B 328, 1989. (Cited on page 27.)

[71] C. Lorce, Geometrical approach to the proton spin decomposition, Phys. Rev. D 87, 034031; arXiv:1205.6483 [hep-ph], 2012. (Cited on page 27.)

[72] A.V. Belitsky, D. Müller, L. Niedermeier and A. Schäfer, Leading twist asymmetries in deeply virtual Compton scattering, Nucl. Phys. B 593, 289, 2001. (Cited on page 29.)

[73] F.X. Girod et al. (CLAS Collaboration), Measurement of Deeply Virtual Compton Scattering Beam-Spin Asymmetries, Phys. Rev. Lett. 100, 162002, 2008. (Cited on pages 29, 124 and 143.)

[74] E. Seder, Longitudinal Target-Spin Asymmetries for Deeply Virtual Compton Scattering, Phys. Rev. Lett. 114, 032001, 2015. (Cited on page 29.)

[75] S. Pisano et al. (CLAS Collaboration), Single and double spin asymmetries for deeply virtual Compton scattering measured with CLAS and a longitudinally polarized proton target, Phys. Rev. D 91, 052014; arXiv:1501.07052, 2015. (Cited on page 29.)

[76] H.S. Jo et al. (CLAS Collaboration), Cross sections for the exclusive photon electroproduction on the proton and Generalized Parton Distributions, arXiv:1504.02009v1 [hep-ex], 2015. (Cited on pages 30, 124 and 143.)

[77] C. M. Camacho et al. (Jefferson Lab Hall A Collaboration), Scaling Tests of the Cross Section for Deeply Virtual Compton Scattering, Phys. Rev. Lett. 97, 262002, 2006. (Cited on page 30.)

[78] M. V. Polyakov, Generalized parton distributions and strong forces inside nucleons and nuclei, Phys. Lett. B 555, 57-62, 2003. (Cited on pages 31 and 32.)

[79] S. Liuti and K. Taneja, Nuclear Medium Modifications of Hadrons from Generalized Parton Distributions, Phys. Rev. C 72, 034902; arXiv:0504027v2 [hep-ph], 2005. (Cited on pages 31, 35 and 37.)

[80] E. R. Berger, F. Cano, M. Diehl and B. Pire, Generalized parton distributions in the deuteron, Phys. Rev. Lett. 87, 142302; arXiv:0106192 [hep-ph], 2001. (Cited on page 31.)

[81] F. Cano and B. Pire, Deep Electroproduction of Photons and Mesons on the Deuteron, Eur. Phys. J. A 19, 423; arXiv:0307231 [hep-ph], 2004. (Cited on page 31.)

[82] A. Kirchner and D. Müller, Deeply virtual Compton scattering off nuclei, Eur. Phys. J. C32, 347-375, 2003. (Cited on pages 31, 33, 34, 117, 118, 126, 143 and 147.)

[83] M. Vanderhaeghen, Gauge invariance of DVCS off an arbitrary spin hadron: the deuteron target case, Eur. Phys. J. A 8, 455, 2000. (Cited on page 31.)

[84] S. Liuti, Generalized parton distributions and transversity in nucleons and nuclei. Nucl. Phys. A 755, 565–570; arXiv:0503269 [hep-ph], 2005. (Cited on page 31.)

[85] S. Liuti, Exploring the transverse partonic structure of nuclei, Workshop on Hard Processes in Nuclei, ECT*, Trento, June 8-12, 2015. (Cited on page 32.)

[86] R. F. Frosch et al., Structure of the He-4 Nucleus from Elastic Electron Scattering, Phys. Rev. 160, 874, 1967. (Cited on page 33.)

[87] A. Camsonne et al. (Jefferson Lab Hall A Collaboration), JLab Measurement of the ^{4}He Charge Form Factor at Large Momentum Transfers, Phys. Rev. Lett. 112, 132503, 2014. (Cited on page 33.)

[88] K. Hafidi et al., Deeply virtual Comton scattering off ^4He, JLab proposal to PAC 33, 2007. (Cited on pages 34 and 49.)

[89] V. Guzey and M. Strikman, DVCS on spinless nuclear targets in impulse approximation, Phys. Rev. C 68, 015204; arXiv:0301216 [hep-ph], 2003. (Cited on page 34.)

[90] V. Guzey, Neutron contribution to nuclear DVCS asymmetries, Phys. Rev. C 78, 025211; arXiv: 0801.3235 [nucl-th], 2008. (Cited on pages 34 and 172.)

[91] I. V. Musatov and A. V. Radyushkin, Evolution and models for skewed parton distributions, Phys. Rev. D 61, 074027, 2000 (Cited on page 35.)

[92] V. Guzey, A.W. Thomas and K. Tsushima, Medium modifications of the bound nucleon GPDs and incoherent DVCS on nuclear targets, Phys. Lett. B 673, 9-14; arXiv:0806.3288 [nucl-th], 2009. (Cited on pages 35, 36, 126 and 143.)

[93] D. H. Lu et al., In-medium electron-nucleon scattering, Phys. Lett. B 417, 217, 1998. (Cited on page 35.)

[94] S. Liuti and K. Taneja, Microscopic Description of Deeply Virtual Compton Scattering off Spin-0 Nuclei, Phys. Rev. C 72, 032201; arXiv:0505123v1 [hep-ph], 2005. (Cited on pages 36, 119, 121, 123, 126, 127, 128, 143, 144 and 145.)

[95] J. Gomez et al., Measurement of the A-dependence of deep inelastic electron scattering. Phys. Rev. D 49, 4348-4372, 1994. (Cited on page 37.)

[96] A. Airapetian et al. (HERMES Collaboration), Nuclear-mass dependence of beam-helicity and beam-charge azimuthal asymmetries in DVCS, Phys. Rev. C 81, 035202, 2010. (Cited on pages 37, 38, 121, 123, 126, 127, 128, 143, 144 and 145.)

[97] J. Alcorn et al. (Hall-A Collaboration), Basic instrumentation for Hall A at Jefferson Lab, Nucl. Inst. and Meth. A 522, 294-346, 2004. (Cited on page 39.)

[98] G. Maclachlan, Ratio of Electric and Magnetic Proton Form Factors at $Q^2 = 1.13(GeV/c)^2$ via Recoil Polarimetry, Ph.D thesis, 2004. (Cited on page 39.)

[99] B.A. Mecking et al., The CEBAF large acceptance spectrometer, Nucl. Inst. and Meth. A 503, 513-553, 2003. (Cited on pages 39, 40, 44 and 70.)

[100] M.D. Mestayer et al., The CLAS drift chamber System, Nucl. Inst. and Meth. A 449, 81, 2000. (Cited on pages 42 and 75.)

[101] G. Adams et al., The CLAS Cerenkov detector, Nucl. Inst. and Meth. A 465, 414, 2001. (Cited on pages 43 and 74.)

[102] E.S. Smith et al., The time-of-flight system for CLAS, Nucl. Inst. and Meth. A 432, 265, 1999. (Cited on page 44.)

[103] M. Amarian et al., The CLAS forward electromagnetic calorimeter, Nucl. Inst. and Meth. A 460, 239, 2001. (Cited on page 44.)

[104] E. Hackett and W. Brooks, Neutron detection in the CLAS calorimeters: a first measurement, CLAS-NOTE-98-014, 1998. (Cited on page 45.)

[105] H. Avakain et al., Deeply Virtual Compton Scattering with CLAS at 6 GeV, Research Proposal to Jefferson Lab PAC 29, PR 06-003, 2005. (Cited on pages 45, 134 and 135.)

[106] Hyon-Suk Jo, Etude de la Diffusion Compton Profondément Virtuelle Sur le Nucléon avec le Détecteur CLAS de Jefferson Lab: Mesure des Sections Efficaces polarisées et non polarisées, IPNO-Thesis, 2007. (Cited on pages 45 and 47.)

[107] S. Tkachenko et al., Measurement of the nearly free neutron structure function using spectator tagging in inelastic $^2H(e,e'p)X$ scattering with CLAS, Phys. Rev. C 89, 045206, 2014. (Cited on page 49.)

[108] The PubChem Project. USA: National Center for Biotechnology Information, dimethyl ether - PubChem Public Chemical Database, http://pubchem.ncbi.nlm.nih.gov/compound/8254. (Cited on page 50.)

[109] N. Baillie et al., BoNus Experiment Analysis Note, CLAS internal analysis note. (Cited on page 51.)

[110] J. Beringer et al. (Particle Data Group), Particle detectors at accelerators, Phys. Rev. D 86, 010001, pages: 339-368, 2012. (Cited on page 51.)

[111] S. Biagi, Monte Carlo simulation of electron drift and diffusion in counting gases under the influence of electric and magnetic fields, Nucl. Inst. and Meth. in Phy. Res. A 421, pp. 234-240, 1999. (Cited on page 61.)

[112] N. Baltzell, New TPC Noise Reduction, https://clasweb.jlab.org/rungroups/lowq/wiki/index.php/New_TPC_Noise_Reduction (Not cited.)

[113] M. Osipenko et al., Matching between the electron candidate track and the Cherenkov counter hit, CLAS-NOTE-020, 2004. (Cited on page 74.)

[114] J. Beringer et al. (Particle Data Group), Electronic energy loss by heavy particles, Phys. Rev. D 86, 010001, 2012. (Cited on page 64.)

[115] F.X. Girod, Diffusion Compton profondément virtuelle avec le détecteur CLAS pour une étude des distributions de partons généralisées, Ph.D-Thesis, 2006. (Cited on pages 81, 86 and 118.)

[116] CLAS collaboration, CLAS GEANT3 simulation, http://nuclear.unh.edu/~maurik/gsim_info.shtml. (Cited on page 86.)

[117] Y. Perrin, Etude de la structure partonique du noyau d'hélium, Ph.D thesis, 2012. (Cited on page 113.)

[118] C. Moody and N. Baltzell, IC depth corrections for CLAS-EG6 experiment, https://clasweb.jlab.org/rungroups/lowq/wiki/index.php/IC_Depth_Correction_Investigation_Creating_a_new_depth_correction. (Cited on pages 93 and 95.)

[119] B. Guegan, Study of Generalized Parton Distributions and Deeply Virtual Compton Scattering on the nucleon with the CLAS and CLAS12, Ph.D-thesis, 2013. (Cited on pages 117, 124 and 143.)

[120] N. Saylor, A Measurement of Unpolarized Cross Sections and Polarized Cross Section Differences of Deeply Virtual Compton Scattering on the Proton at Jefferson Laboratory using CLAS, Ph.D-thesis, 2013. (Cited on pages 117, 124 and 143.)

[121] J. M. Grames et al., Unique electron polarimeter analysing power comparison and precision spin-based energy measurement, Phys. Rev. Spec. Topics - Accelerators and Beams, Vol.7 , 042802, 2004. (Cited on page 113.)

[122] A.V. Afanasev, M.I. Konchatnij and N.P. Merenkov, Single-spin asymmetries in the Bethe-Heitler process $e^- + p \to e^- + \gamma + p$ from QED radiative corrections, J. of Exp. and Theo. Phys. 102(2), 220-233, 2006. (Cited on page 114.)

[123] Private communication with V. Guzey based on his model presented in [90]. (Cited on pages 126, 128, 143 and 145.)